SISSA
Scuola Internazionale Superiore di Studi Avanzati

COMENIUS UNIVERSITY BRATISLAVA

Physics Area – PhD course in
Theory and Numerical Simulation of Condensed Matter

Towards Realistic Simulations of Structural Transformations in Solids by Metadynamics

Candidate: Matej Badin

Supervisor:
Prof. Roman Martoňák
Co-supervisor:
Prof. Giuseppe Santoro

Academic Year 2022-23

Comenius University
Faculty of Mathematics, Physics and Informatics

Towards Realistic Simulations of Structural Transformations in Solids by Metadynamics

Dissertation thesis

Study programme:	Physics of Condensed Matter and Acoustics
Field of study:	1122 Physics of Condensed Matter and Acoustics
Department:	Department of Experimental Physics
Supervisor:	prof. Ing. Roman Martoňák, DrSc.
Co-supervisor:	prof. Giuseppe Santoro

Bratislava, 2023 Mgr. Matej Badin

Comenius University Bratislava
Faculty of Mathematics, Physics and Informatics

THESIS ASSIGNMENT

Name and Surname:	Mgr. Matej Badin
Study programme:	Condensed Matter Physics and Acoustics (Single degree study, Ph.D. III. deg., full time form)
Field of Study:	Physics
Type of Thesis:	Dissertation thesis
Language of Thesis:	English
Secondary language:	Slovak

Title: Towards realistic simulations of structural transformations in solids by metadynamics

Annotation: Structural phase transitions in crystals, induced by pressure or temperature, are interesting for fundamental and practical reasons. Transforming the structure and all related physical properties, they offer a possibility of creating new materials with unusual properties, as demonstrated by the well-known graphite-to-carbon transformation in carbon. In spite of substantial progress in their modeling during past two decades there is still a significant gap in our understanding of the transformation pathways, especially under realistic conditions, such as presence of defects, non-hydrostatic stress, metastability, etc. This gap in fundamental understanding is clearly seen in our inability to predict the experimental outcome of structural transitions when strong kinetic effects are involved, such as e.g. decompression of the β-tin phase of Si. Perhaps even more importantly, from the practical point of view, the gap also directly impacts possible technological applications such as steering the transition towards creation of a desired phase with interesting/useful properties. The goal of this work is to develop new metadynamics-based methods, allowing more realistic simulations of these structural transformations. In order to allow an accurate and low-computational-cost description of the relevant systems we plan to employ potentials based on machine learning approaches.

Literature:
G. Bussi and A. Laio, Nat. Rev. Phys. 2, 200 (2020)
J. Behler, Chem. Rev. 2021, 121, 16, 10037–10072
Mark E. Tuckerman, Statistical Mechanics: Theory and Molecular Simulation, Oxford University Press 2010

Keywords: structural transformations, metadynamics, metastability

Tutor:	prof. Ing. Roman Martoňák, DrSc.
Consultant:	prof. Giuseppe Santoro
Department:	FMFI.KEF - Department of Experimental Physics
Head of department:	prof. Dr. Štefan Matejčík, DrSc.
Assigned:	23.01.2020

Approved: 23.08.2023 prof. Ing. Roman Martoňák, DrSc.
Guarantor of Study Programme

Comenius University Bratislava
Faculty of Mathematics, Physics and Informatics

....

Student Tutor

Univerzita Komenského v Bratislave
Fakulta matematiky, fyziky a informatiky

ZADANIE ZÁVEREČNEJ PRÁCE

Meno a priezvisko študenta: Mgr. Matej Badin
Študijný program: fyzika kondenzovaných látok a akustika (Jednoodborové štúdium, doktorandské III. st., denná forma)
Študijný odbor: fyzika
Typ záverečnej práce: dizertačná
Jazyk záverečnej práce: anglický
Sekundárny jazyk: slovenský

Názov: Towards realistic simulations of structural transformations in solids by metadynamics
Smerom k realistickým simuláciám štruktúrnych transformácií v tuhých látkach pomocou metadynamiky

Anotácia: Štruktúrne transformácie v kryštáloch indukované tlakom alebo teplotou sú zaujímavé z fundamentálneho aj praktického hľadiska. Transformácia štruktúry a príslušná zmena všetkých fyzikálnych vlastností poskytuje možnosť vytvorenia nových materiálov s neobyčajnými vlastnosťami, čo demonštruje dobre známy príklad premeny grafitu na diamant v uhlíku. Napriek podstatnému pokroku v ich modelovaní počas posledných dvoch desaťročí, naše chápanie transformačných ciest je stále nedostatočné, najmä za realistických podmienok, ako je prítomnosť defektov, nehydrostatického tlaku, metastability, apod. Táto medzera sa odráža v neschopnosti predpovedať experimentálny výsledok štruktúrnych prechodov, v ktorých hrajú podstatnú úlohu kinetické efekty, ako napr. dekompresia fázy typu β-cínu v Si. Z praktického hľadiska je pravdepodobne ešte dôležitejšie to, že toto neúplné chápanie nám neumožňuje dôležité technologické aplikácie, ako je riadenie transformačného procesu smerom k požadovanej fáze so zaujímavými a užitočnými vlastnosťami. Cieľom práce je vývoj nových metód umožňujúcich realistickejšie simulácie týchto štruktúrnych transformácií, založené na metadynamike. Za účelom presného popisu relevantných systémov s nízkou výpočtovou náročnosťou plánujeme využitie potenciálov založených na metódach strojového učenia.

Literatúra: G. Bussi and A. Laio, Nat. Rev. Phys. 2, 200 (2020)
J. Behler, Chem. Rev. 2021, 121, 16, 10037–10072
Mark E. Tuckerman, Statistical Mechanics: Theory and Molecular Simulation, Oxford University Press 2010

Kľúčové slová: štruktúrne transformácie, metadynamika, metastabilita

Školiteľ: prof. Ing. Roman Martoňák, DrSc.
Konzultant: prof. Giuseppe Santoro
Katedra: FMFI.KEF - Katedra experimentálnej fyziky
Vedúci katedry: prof. Dr. Štefan Matejčík, DrSc.

Dátum zadania: 23.01.2020

Dátum schválenia: 23.08.2023 prof. Ing. Roman Martoňák, DrSc.

Univerzita Komenského v Bratislave
Fakulta matematiky, fyziky a informatiky

garant študijného programu

.....

študent

.....

školiteľ

Acknowledgements

I would like to sincerely express my gratitude to my supervisor, prof. Roman Martoňák, for introducing me into the topic of enhanced sampling simulations and pressure-induced structural phase transitions in 2016, and for creating supporting conditions in his group.

I also deeply acknowledge the support from my co-supervisors prof. Giuseppe Santoro and (formerly) prof. Sandro Sorella, and sincerely express my gratitude for creating supporting conditions.

I also acknowledge the collaborations with prof. Alessandro Laio, prof. Stefano de Gironcoli, Dr. Yusuf Shaidu and prof. Ivan Oleynik, and their groups.

I also acknowledge PRACE for awarding access to the Fenix Infrastructure resources at Jülich Supercomputing Center, which are partially funded from the European Union's Horizon 2020 research and innovation programme through the ICEI project under the grant agreement No. 800858, as well as, the funding resources provided by Comenius University under Grant for Young Researchears No. UK/436/2021 and No. UK/454/2022, the support provided by the Slovak Research and Development Agency under Contracts No. APVV-15-0496 and No. APVV-19-0371, and by VEGA project 1/0640/20, the access to the SISSA Ulysses cluster and the computing resources at CINECA kindly provided by prof. Stefano de Gironcoli.

My gratitude is also aimed at my colleagues, Dušan Kavický, Lukáš Kopnický, Dominika Melicherová, Marián Ryník, Adam Škrlec, Ondrej Tóth and Gabriele Bellomia, Andrea Blason, Matteo Ferraretto, Neven Golenic, Ali Khosravi, Francesca Paoletti, Nishan Ranabhat, Pietro Torta and flatmates Martin Chudjak, Miroslav Psota, Juraj Surovčík, as well as to the contribution of friends not mentioned here, but who are not being forgotten. Among many, I would like to highlight the friendships with František Dráček, Adam Hložný, Dominik Rist and Boris Vavrík.

Last but not least, I would like to thank my parents and family for always supporting me along the path I have chosen.

Abstract

Structural phase transitions in crystals, induced by pressure or temperature, are interesting for fundamental and practical reasons. Transforming the structure and all related physical properties, they offer a possibility of creating new materials with unusual properties, as demonstrated by the well-known graphite-to-diamond transformation in carbon. In spite of substantial progress in their modelling during past two decades, there is still a significant gap in our understanding of the transformation pathways, especially under realistic conditions, such as the presence of defects, non-hydrostatic stress, metastability, etc. This gap in fundamental understanding is clearly seen in our inability to predict the experimental outcome of structural transitions when strong kinetic effects are involved, such as, e.g. decompression of the β-tin phase of Si. Perhaps even more importantly, from the practical point of view, the gap also directly impacts possible technological applications such as steering the transition towards the creation of a desired phase with interesting/useful properties. This thesis consists of six parts: (a) in the first part, we show an already published metadynamics scheme which can induce a nucleating regime in the solid-solid phase transitions and demonstrate it for the B1-B2 transition in NaCl, (b) in the second part, we move from the homogeneous nucleation and apply this scheme to the case of the nucleation on grain boundaries, (c) in the third part, we apply this scheme to the graphite to diamond transition in carbon, also studying dislocation loops, (d) in the fourth part, we show preliminary results of the application of the scheme to the post-diamond phases of carbon aiming to answer the question of how the BC8 phase can be synthesized and outline the construction of machine learning CVs aiming to answer this question, (e) in the fifth part, we apply a similar scheme to the α-ω and ω-α transitions in titanium, and finally (f) in the last part, we present an algorithm for the quantitative assessment of the suitability of the CVs in the metadynamics simulations.

Key words: structural transformations • metadynamics • metastability

Abstrakt

Štruktúrne transformácie v kryštáloch indukované tlakom alebo teplotou sú zaujímavé z fundamentálneho aj praktického hľadiska. Transformácia štruktúry a príslušná zmena všetkých fyzikálnych vlastností poskytuje možnosť vytvorenia nových materiálov s neobyčajnými vlastnosťami, čo demonštruje dobre známy príklad premeny grafitu na diamant v uhlíku. Napriek podstatnému pokroku v ich modelovaní počas posledných dvoch desaťročí, naše chápanie transformačných ciest je stále nedostatočné, najmä za realistických podmienok, ako je prítomnosť defektov, nehydrostatického tlaku, metastability, apod. Táto medzera sa odráža v neschopnosti predpovedať experimentálny výsledok štruktúrnych prechodov, v ktorých hrajú podstatnú úlohu kinetické efekty, ako napr. dekompresia fázy typu β-cínu v Si. Z praktického hľadiska je pravdepodobne ešte dôležitejšie to, že toto neúplné chápanie nám neumožňuje dôležité technologické aplikácie, ako je riadenie transformačného procesu smerom k požadovanej fáze so zaujímavými a užitočnými vlastnosťami. Táto dizertačná práca sa skladá zo šiestich častí: (a) v prvej časti demonštrujeme už publikovanú metadynamickú schému, ktorá dokáže indukovať nukleačný režim v štruktúrnom fázovom prechode a demonštrujeme jej aplikáciu na B1-B2 prechod v NaCl, (b) v druhej časti, aplikujeme túto schému na prípad heterogénej nukleácie na rozhraniach zŕn pre spomínaný prechod v NaCl, (c) v tretej časti, aplikujeme túto schému na prechod grafit-diamant, pričom študujeme aj nukleáciu na dislokačných slučkách, (d) v štvrtej časti prezentujeme predbežné výsledky aplikácie schémy na prechody v post-diamantových fázach uhlíka smerujúc k zodpovedaniu otázky, či a ako môže byť syntetizovaná fáza BC8. Taktiež ukazujeme náčrt kolektívnych premenných založených na metódach strojového učenia, ktoré plánujeme použiť na zodpovedanie tejto otázky. (e) V piatej kapitole aplikujeme podobnú metadynamickú schému na α-ω a ω-α prechody v titáne, a napokon (f) v poslednej časti, prezentujeme algoritmus umožňujúci kvantitatívne ohodnotenie vhodnosti kolektívnych premenných na metadynamické simulácie.

Kľúčové slová: štruktúrne transformácie • metadynamika • metastabilita

Contents

List of publications

[P1] **Nucleating a Different Coordination in a Crystal under Pressure: A Study of the $B1$-$B2$ Transition in NaCl by Metadynamics**
Matej Badin and Roman Martoňák
Phys. Rev. Lett. **127**, 105701, (2021), doi: 10.1103/PhysRevLett.127.105701

The following publications, done over the course of this PhD, have not been included in this thesis:

[P2] **Non-adiabatic corrections to chiral charge pumping in topological nodal semimetals**
Matej Badin
Phys. Rev. B **106**, 045146, (2022), doi: 10.1103/PhysRevB.106.045146

I Introduction

Structural phase transitions in crystals induced by pressure or temperature are complex phenomena of great fundamental and practical importance. Since the advent of quantum mechanics and electronic theory of solids in the 1920s, we understand that it is the structure of matter that determines its electronic, optic and structural properties. Consider, e.g., carbon which changes its form from graphite to diamond upon application of high pressure. The graphite is opaque, grey and easily ripped, while the diamond is translucent, lusty and is still considered as the hardest known natural material.

Pressure and temperature represent easily experimentally controllable external parameters that can drive structural phase transitions. Although undergraduate students of condensed matter courses are predominantly taught of examples of *second*-order structural phase transitions, e.g., note a canonically mentioned transition in $SrTiO_3$ [1] and the subsequent rise of popularity of the *soft-mode* concept in literature in the 1970s & 1980s [2], yet most of the structural phase transitions in crystals are actually *reconstructive* (*bond-breaking*) and thermodynamically first order [3].

The former makes the theoretical analysis of their atomistic mechanism challenging compared to the class of second-order structural phase transitions, even though their thermodynamics seems to be naively simple. The latter implies crossing of free-energy barriers via a non-trivial concerted motion of atoms, representing *a rare event*. We will return to the implications of the latter at the end of this introductory chapter.

The structural phase transitions give rise to a number of important phases with unique properties such as, e.g., mentioned diamond created from graphite at high-pressure conditions. In the process of synthesis of such phases, kinetics plays a key role in determining the outcome of the transition which might not necessarily be the thermodynamically most stable form, but rather a metastable one (e.g, after compression of silicon in the cubic-diamond structure to 11 GPa and decompression to atmospheric pressure, the BC8 phase is found) [4]. Pictographically this property is shown in Fig. I.1. This property is not unique to martensitic transitions (to be defined later) only, another example is nitrogen which should convert from its molecular crystal to a polymeric one around 40 GPa, but at room temperature, the transition does not happen [5], the presence of a barrier in the first order structural transitions makes the likelihood of finding a metastable form higher. Turning attention once again to carbon, the diamond should in principle at normal pressure return back to graphite, yet the barrier cannot be overcome at room temperature. Interestingly, one can find graphite, cubic diamond and hexagonal diamond to coexist in a large portion of the carbon phase diagram (up to $p < 15\,\mathrm{GPa}$ and $T < 1500\,\mathrm{K}$) [6]. Thus even the simplest compounds around us can possess a number of metastable phases.

Another important examples of elements and compounds with a number of metastable phases are e.g. silicon [7], germanium [8] or SiO_2 [9], to name a few. Recently (2021), Deng et al., [10] demonstrated that the critical superconductivity temperature can be increased in single

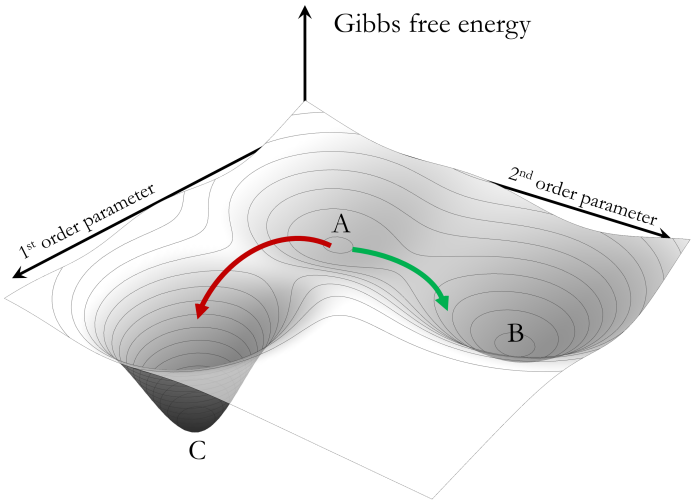

Figure I.1: Example of a hypotetical Gibbs free energy surface pictographically demonstrating the possible *metastability*. A system initially prepared in the state **A** proceeds into another state **B** even though the most optimal state is the state **C**, if the barrier $\mathbf{A} \rightarrow \mathbf{B}$ is lower than the barrier $\mathbf{A} \rightarrow \mathbf{C}$.

crystals of FeSe from $\sim 9\,\mathrm{K}$ to $\sim 37\,\mathrm{K}$ (at atmospheric pressure), after pressing the crystal in a diamond anvil cell to $\sim 4\,\mathrm{GPa}$ (the crystal undergoes a structural transition but does not return to an original structure). Even though this increase is possible only due to the fact $\sim 37\,\mathrm{K}$ is still clearly a low temperature to destroy the metastable phase, we believe such *a pressure quenching* procedure (atmospheric pressure $\rightarrow$ high-pressure $\rightarrow$ atmospheric pressure) could be useful in future in a synthesis of practical metastable phases of matter. We believe this undoubtedly motivates the fundamental research of computational techniques enabling the study of the first-order structural phase transitions.

In the past decades, large progress has been made in the prediction of crystalline phases due to the advent of methods such as *evolutionary search* [11], *random search* [12, 13], *particle swarm optimisation* [14], *minima hopping* [15], *a generalized solid-state nudged elastic band method* [16], etc. Although these approaches are able to very effectively identify stable and metastable structures as global or local minima of the enthalpy surface, understanding the mechanisms of the transitions, the free-energy barriers and the resulting kinetics still lag behind. This also motivates the need to computationally study (and develop methods enabling such study) the structural phase transitions.

First-order structural phase transitions are also "hidden" in literature under adjectives as *martensitic* or *diffusionless*. The latter suggests that the atoms do not diffuse over long ranges during the transition, the former refers to the *austenite* - *martensite* transition in iron upon addition of carbon. To avoid misunderstanding with the precise use of these words in literature, we review the proposed classification of structural phase transitions by Cohen, Olson and Clapp in 1979 [17] in Ch. II and from that point further, we follow this convention for the rest of this doctoral thesis.

The first-order structural phase transitions are not only interesting for the possibility of the synthesis of metastable phases. Martensitic phase-transitions can be found in shape memory alloys [18], steels [19] or in high-pressure conditions in planetary cores, e.g., see Refs. [20, 21]. Martensitic transitions are often used to improve materials properties, but their occurrence can also mean a possible limit of material performance. For instance, pure titanium undergoes

a structural phase transition from α-phase (hcp) $\rightarrow$ ω-phase (hexagonal) upon application of $\sim 9\,\mathrm{GPa}$ [22], but the ω-phase is thermodynamically metastable almost up to atmospheric pressure at $300\,\mathrm{K}$ [22]. This pressure-driven transition in pure titanium has significant technological implications for the aerospace industry since the ω-phase lowers toughness and ductility. Interestingly, simple oxygen impurities can significantly block this transition to happen [23]. We note that this problem has been studied exhaustively by other approaches (identifying common subgroups and collective transition mechanisms between those phases and evaluating barriers in them using ab-initio methods) [23–27] to our approach.

The first-order nature of structural/martensitic phase transitions implies that a transition proceeds through *nucleation*. However, the *nucleation of a solid inside another solid* is qualitatively far different from the *nucleation of a solid inside a melt*. The reason is simple. Why a surrounding liquid can easily flow away without resistance inside the melt, the same is not true in a solid. An emerging phase usually has a different density that causes a misfit of volumes. Both facts imply that a nucleus creates long-range ($\sim 1/r^3$) [3, 28–32] elastic strains in the parrent phase, originally pointed out by Nabarro in 1940 [28], where a comparable portion of elastic energy is stored in a surrounding matrix as in the nucleus itself [3, 32]. The ratio of elastic energy to surface energy determines the shape of the nucleus [33], which can hold even non-convex shapes [3, 32]. Not mentioning that the surface tension is highly anisotropic. All these "complications" imply non-trivial qualitative differences of nucleation, compared to a standard textbook discussion of nucleation in a melt or a droplet, as described thoroughly by Moran in 1996 [34]. Those are briefly reviewed in Ch. II.

Contrary to the *nucleation from a melt*, the *nucleation inside a solid* is also more complicated due to the unavoidable presence of *grain boundaries* [35–46], *defects* - such as *vacancies* [3, 30, 32, 47] or topological defects such as *dislocations* [48–55]. Today probably all undergraduate students of condensed matter physics are aware of the entropic argument on the existence of vacancies. However, the existence of dislocations raised more doubts, even they were originally independently proposed by Taylor, Orowan and Polanyi in 1934 [56]. Their existence was experimentally proven only in the 1950s and finally resolved the "mystery" of crystal growth[1] and plastic deformation in crystals. The nucleation on dislocations has been originally proposed by Cahn in 1957 [48] and studied by Cook [49], Olson [50, 51], Suezawa [52], or more recently by Li [53], Samanta [54] and Levitas [55] (certainly missing many others). Due to the initial high-energy cost needed to create a dislocation [56] and the unavoidable presence of them in a realistic material, the dislocations seems to be a suitable candidate to explain the transition mechanisms on a mesoscale - since the barrier for *homogenous nucleation* is in realistic materials $\gtrsim 100\,\mathrm{eV}$, even under modest overpressurization [57]. This value comes from our recent publication for the $B1$-$B2$ transition in NaCl. However, the original estimates for the nucleation barrier in the homogeneous nucleation for steels were as high as $6000\,\mathrm{eV}$ [58]. Both numbers imply that the homogeneous nucleation is certainly not possible to explain observed transitions.

The nucleation on grain boundaries was originally studied by Clemm and Fisher in 1955 [35] and studied subsequently by Cahn [36], Russel [37], Johnson et al. [38], Marth et al. [40], Aaronson et al. [41], Lange et al. [43, 44], in experiments e.g., by Park and Ardell [42], Offerman et al. [45] and Landheer et al. [46], in molecular dynamics e.g., in Refs. [59–66] or more recently by means of *phase field models* (see below) e.g., in Refs. [67–86].

[1] We note the argument from a classic condensed matter textbook - *Condensed Matter Physics* written by Marder [56] (see page 348). If a crystal is completely flat a single deposited new atom is likely to be highly unstable. Without the presence of screw dislocations penetrating a surface of a crystal, the calculated grow-rates of crystal in oversaturated conditions disagree by a factor of 10^{1000} with experimentally measured ones.

However, to our best knowledge, in an atomistic simulation community and free-energy calculations in the context of phase transitions, the presence of dislocations has been considered only by Samanta et al., 2014 [54] in the melting of copper and recently by Chen et al., 2022 [87]. Similarly, the only attempt to infer the free-energy barrier in the context of nucleation on grain boundaries has been done by Song and Hoyt in 2016 [62], who find the barrier to be of the order of 5 eV. In the problem of a first-order structural solid transition, there is no (to our best knowledge) study which quantifies how is a transition barrier lowered under the presence of them (dislocations or grain boundaries), e.g. using an enhanced sampling technique.

From the side of theory, the microscopic structural mechanism of first-order structural phase transitions remained for a long elusive. It was P. C. Clapp who in 1973 proposed a concept of what he called "*a localised soft-mode*"[2] upon which *Ginzburg-Landau-like* theories were gradually constructed to the 1990s. Those field theory models can also be found in the literature under term *phase-field models* [88, 89], even though the latter is more used in the context of spinodal decomposition in alloys (not to be confused with). We review the findings of Clapp [58, 90], Chu et. al [91], Falk and Konopka [92], Gooding [93], Guénin and Gobin [94], Heo and Chen [74], Krumhansl [95], Levitas et al. [33, 96–104] Moran [34], Olson [31], Roy [105], Reid [106], Shen [107], Wang et al. [108], Zhang et al. [109] in Ch. IV.

However, the construction of a realistic Ginzburg-Landau theory describing a particular transition is far from being trivial and often represent a rather challenging and cumbersome task as it requires to:

1. Identify common structural subgroups of parent and emerging phases.
2. Propose within every subgroup a possible collective mechanism and project it to a respective irreducible representation of that subgroup.
3. Identify secondary order parameters.
4. Account for anisotropy, gradient terms (e.g., see Ref. [110]) and all symmetry-allowed couplings between order parameters.
5. Measure/determine (e.g., from ab-initio methods) the dependence of all expansion coefficients as a function of temperature and pressure (which could be an ill-defined task).

Thus, even in the case of the simplest structural transitions, e.g., such as in a cubic to monoclinic transition of β-phase shape memory alloys studied by Falk and Konopka [92], the task of creating an effective Ginzburg-Landau theory represents a large amount of work, neither easily transferable to other systems nor even to another transition in that particular compound. But more importantly, it cannot be easily generalized to account for the possibility of *heterogeneous nucleation* on defects (e.g., such as grain boundaries or dislocations). This we believe, advocates

[2] In his words [58]: "*... the martensitic transformation is triggered by a strain induced elastic instability in special regions of the parent lattice, that the inclusion of anharmonic terms in the elastic free energy will considerably reduce the estimates of the nucleation barrier and that the lattice vibrations (or phonons) in these anomalous regions play an important role in the nucleation process.*" [58] To our best understanding, one should imagine a certain phonon at a specific wavevector $\mathbf{k}$ and think about the energy $\varepsilon(\mathbf{k}, A)$ corresponding to this phonon as the function of amplitude - A. At certain critical value of amplitude A_c, the anharmonic contribution starts to be negative (locally at places of high concentration of strain) and overall lowering the energy, so for $A > A_c : \varepsilon(A) < \varepsilon(A < A_c)$, or the frequency of phonon becomes completely imaginary ($A_c = 0$). Strictly speaking this hypothesis has never been (to our best knowledge) verified (and atomistic simulations can be a useful probe), rather a qualitative consequences were studied (in terms of field theories).

the use of *atomistic simulation techniques* as we state in Ch. V and our approach presented in Ch. VI.

Since the structural phase transitions are often activated by pressure, this subject is also interesting by means of *high-pressure chemistry* [111–113]. Pressure can *break existing bonds*, *create new ones*, *change a character of a bond*, or even *alter* chemistry by activating (semi)-core electrons of structure, unoccupied orbitals and even the non-atom-centred orbitals located on the interstitial sites [113]. A majority of known compounds usually respond to pressure by *becoming more homogeneous by compressing the longest and weakest bonds*, *increasing their coordination* [111, 112], *forming structures of higher symmetry* and *metallizing by delocalization of its electrons*, although the examples violating these empirical rules exist [113]. While it has been noted by Miao et al., 2020 [113] that examples violating the previous rules exist in the high-pressure world, yielding to atypical compounds and phenomena as e.g., *electrons detaching from atoms* [113] and *repopulation of the atomic orbitals changing the chemical identity of the atoms* [113], we are interested in the "*standard part*" of "*high-pressure world*" that fall into the section of *increase of coordination number upon pressure*.[3] This fourth empirical rule of Prewitt and Downs [111] was also the natural motivation for the choice of the so-called collective variable (order parameter) in our method [57]. For the reader's convenience, we show an example of diversity of local chemical environments which can be differentiated by the *coordination number* in Fig. I.2.

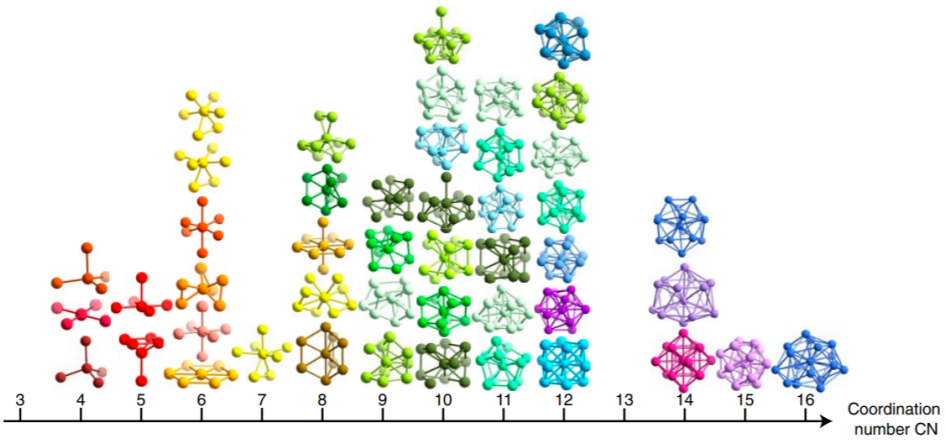

Figure I.2: Illustration of the diversity of local chemical environments present in crystals differentiated by *coordination number* within the first coordination sphere. Note that no claim is made on the exhaustiveness of this figure. Adapted and taken with a direct permission of S. C. Glotzer from Ref. [114]. Image is an intelectual property of J. Dshemuchadse.

While one can get much insightful information by studying field theories of nucleation in structural phase transitions, by the argument raised in one of the former paragraphs, it is clear that the practical applicability is rather cumbersome. With the advent of quantum mechanical and statistical mechanical computational methods such as (Kohn-Sham) *density functional theory* in 1965 [115], *molecular dynamics* at constant pressure and temperature in 1980 [116], Parrinello-Rahman method in 1980 [117, 118], Car-Parrinello method in 1985 [119] and *plane-wave DFT codes* in the 1990s, the problem of simulation of pressure-induced structural phase transitions became *in principle* tractable. However, the limit of *nucleation* and *growth* had still been for a long elusive and not accessible for those methods. The reason is simple, while molecular dynamics is

[3] Naturally, our method can also be used in structural transitions in which the coordination number decreases.

in principle an $\mathcal{O}(N)$ method, the density functional theory is *in principle* an $\mathcal{O}(N^3)$ method in the system size - N, and still quite demanding even with the modern linear approaches to DFT, e.g. see Ref. [120]. The necessity of simulation of large system sizes comes from the necessity to be able to accommodate an emerging nucleus[4] and it is due to the intrinsic nature of first-order solid-solid phase transitions, understandable by means of field theory [34].

The solution to the problem of scalability of *ab-initio* evaluation of forces had been solved by *machine learning potentials* by Behler and Parrinello in 2007 [121] and Bartók et al. in 2010 [122], while the progress still continues - see recent reviews [123–127]. We note that one of the early applications of metadynamics to structural phase transition (in silicon) has been also connected with neural network potentials [128]. A machine-learning potential here acts as "*a compress utility*" which after appropriate representation of positions and training, enables one to evaluate forces acting on nuclei as the function of their position faster than by *ab-initio* methods, thus saving the computational time by orders of magnitude. We note that recent interesting ideas to the development of machine learning potentials and the representation [127] of the physical structure have been raised recently by Zhang et al. [129] (DeepMD), Drautz et al. [130–138] (ACE), Xie et al. [139], Batzner et al. [140] (NequIP), Musaelian et al. [141] (Allegro), Batatia et al. [142, 143] (MACE) and also by many others, e.g. using recent powerful equivariant graph neural networks such as SE(3)-Transformers by Fuchs et al. [144] or Equiformer by Liao and Smidt [145].

But it is not only the necessity of the simulation of large system sizes but also the necessity of the large time scales as long as the structural phase transitions is *a rare event*, that makes simulation of structural phase transition computationally demanding. Even with simulations of systems of scale $\sim 10^6$ atoms, the probability of fluctuations yielding to a first-order transition are exponentially suppressed compared to the world around us ($\sim 10^{23}$), not mentioning the effect of defects and the need to be able to incorporate them into a simulation. With pure unbiased molecular dynamics, the typical times achievable ($\sim 100\,\mathrm{ns}$ - a few µs) are still not enough to observe the transition close to equilibrium conditions and much of this time would be spent in fluctuations near an initial free-energy minimum.

In the atomistic simulation community, the problem of nucleation in first-order structural transitions has been addressed by the so-called *seeding approach*, e.g., as in Ref. [146] (not mentioning an obvious way by overpressurisation if one wishes to observe a transition forcefully), where an initial nucleus is created "*manually*". However, it suffers from other drawbacks, as it requires creating an enormous number of structures where one needs to account for various shapes and sizes of nuclei of emerging phases and their relative crystal orientation with respect to the parent phase. Moreover, the emerging nuclei can have non-convex shapes, and one can easily introduce a systematic error if the bonds between emerging and parent phases are not relaxed properly. Even though such a task may be doable for the *homogenous nucleation*, e.g., such as in the case of the diamond from graphite nucleation in Ref. [146], it is not easily generalisable for the *heterogeneous nucleation* on dislocations, surfaces, grain boundaries, etc.

Other approaches (to phase transitions) represent *enhanced sampling methods* [147], and one possible example out of the family of these methods is *metadynamics* by Laio and Parrinello in 2002 [148, 149]. To be introduced in Ch. V, but let us explain it in a few sentences, based on the idea of pushing the system out of previously visited states while reconstructing a *free energy profile* as a function of so-called *collective variables*. Collective variables are usually a

[4] One can expect a typical size in the range of $10^4 - 10^6$ atoms (including the surrounding environment to fully relax long-range ($\sim 1/r^3$) elastic strains).

few functions of atomic coordinates which should be able to differentiate by means of their value the initial, final and all relevant transition states and pathways. The convergence of the metadynamics procedure was justified by Bussi et al., 2006 [150]. The problem of *automatic construction and choice of CVs* has been studied recently rather exhaustively in Refs. [129, 151–161]. For a recent complete overview of what representations (also used as collective variables not only as descriptors for machine learning potentials) see a recent review [127]. We also note that the use of metadynamics can be possibly motivated through of seminal work of Jarzynski (so-called *Jarzynski equality*) [150], who in 1997 demonstrated that it is possible to determine the free energy difference as a suitable average of the work done on the system by forcing the transition in a finite time. This observation is crucial since it tells us that extracting equilibrium information from a non-equilibrium process is possible.

The applications of metadynamics to the problem of structural phase transitions started by the work of Martoňák et al., 2003 [162] that used six independent components of a simulation supercell as collective variables [128, 163–174]. Applications of metadynamics to structural transitions not based on the supercell CV [162] include the use of *a coordination number* by Zipoli et al., 2004 [175], the *PIV metric* by Pipolo et al., 2017 [176], so-called *a path-CV* by Gimondi et al., 2017 [177], *a coordination number* and *transition path sampling* by Jobbins and Leoni in 2018 [178], *enthalpy* and *a pair approximation of entropy* by Mendels et al., 2018 [179], or *a neural network based on Behler-Parrinello descriptors* by Rogal et al., 2019 [180] or Yoo et al., 2021 [181].

Note that no approach before our recent work [57] (namely, see work of Stokes and Hatch [182, 183]) based on identifying common subgroups and geometric modelling and estimating energetic barriers per unit cell, also all publications [128, 163–174] following the methodology of Martoňák et al., 2003 [162] based on a simulation supercell as collective variable and all other applications of metadynamics to structural phase transitions based on other choices of collective variables [175–181] were not able to reach the nucleating limit and only collective mechanisms were observed. Thus they cannot determine the true nucleation barrier (as the reconstructed barrier scales in collective mechanism with system size). Thus up to our best knowledge, our recent work [57] is the first one to achieve the *nucleating limit* (in a solid-solid transition) without assuming it. However, we note that recently the approach based on the use of six independent components of a simulation supercell as collective variables by Santos-Florez et al. [184] was scaled to the system sizes of 500 000 atoms using a machine learning potential for a B4–B1 phase transition in GaN and observed the multiple nucleating events occurring at the same time.

Although "*there is nothing more practical than a good theory*"[5], the Gibbs free energy is not a directly measurable quantity. Yet what can be compared is the microscopic transition mechanism, which corresponds to the lowest Gibbs free energy barrier. In our recent publication [57], we have shown that simulating small systems (where nucleation cannot be observed) can lead to a wrong conclusion on the microscopic structural mechanism (identifiable by means of ultrafast X-ray diffraction). To be more specific, for the long-studied $B1$-$B2$ transition in NaCl [185], where there was a large dispute in the literature on the actual microscopic mechanism [182, 183, 186–195], we conclude that in thermodynamic limit the so-called Watanabe-Tokonami-Morimoto (WTM) mechanism [188] is observed contrary to the Buerger-like mechanism [187] observed in small systems (in simulations). This is due to the presence of the boundary between the emerging and parent phases that shifts the relative cost of different mechanisms. The experimental study of the $B1$-$B2$ transition in KCl [196] revealed the WTM mechanism by means of ultrafast X-ray diffraction in the thermodynamic limit.

[5] Kurt Lewin.

This **doctoral thesis** is organised as follows. In Ch. II, we review the current state of understanding of *martensitic* structural phase transitions in terms of high-pressure chemistry, their kinetics and the analysis of their corresponding microscopic structural mechanisms via experimental techniques such as e.g., ultrafast X-ray diffraction.

In Ch. III, we focus on the review of the current state of knowledge about aspects of nucleation in solid-solid structural phase transitions. This chapter also reviews concepts of *homogenous* and *heterogenous* nucleation considered in literature in this context while bringing the attention of the reader to qualitative differences in the *nucleation of a solid inside another solid* from the *nucleation from a melt*.

In Ch. IV, we review, in a chronological order, the development of theoretical understanding of microscopic structural mechanism of martensitic transitions from a simple *Landau-like* thermodynamic analysis to detailed and sophisticated *Ginzburg-Landau* theories developed between the 1970s and the 1990s. However, to our subjective evaluation, no complete Ginzburg-Landau theory accounting for all complexities at all has been ever constructed for a martensitic transition.

In Ch. V, having introduced the reader to the enormous complexity of the construction of a realistic theory of martensitic transitions, we briefly advocate the use of *atomistic simulation techniques* to the problem of their realistic study (including the ability to describe the nucleation, the nucleation in presence of defects, etc.). We try to convince the reader that recent progress from the 1990s to the 2010s in atomistic simulation techniques, the availability of computing power and development of experimental techniques created a *"window of opportunity"* in the 2020s to finally, both theoretically and experimentally, answer "*easy-to-ask;hard-to-quantitatively-answer*" questions such as:

- *What does a structural mechanism of a structural phase transition look like?*
- *What is the free-energy barrier?*
- *What is the quantitative role of structural defects (e.g., dislocations or grain boundaries)?*

In Ch. VI, we demonstrate the use of our recently published method [57] for the B1-B2 transition in NaCl. The results presented in this chapter incorporate those presented in Ref. [57] as well as the unpublished results for the nucleation on grain boundaries.

In Ch. VII, we present the unpublished results obtained for the application of the method presented in Ref. [57] to the graphite to diamond transition in carbon based on the use of the machine learning potential [197] of Shaidu et al.

Ch. VIII tries to answer a question with an elusive answer, if and how the BC8 phase of carbon can be synthesized, employing the recent machine learning potential of Willman et al. [198].

In Ch. IX we present the results obtained by the application of method similar to those presented in Ref. [57] to the $\alpha \rightarrow \omega$ and $\omega \rightarrow \alpha$ transitions in titanium.

Finally, the Ch. X presents the unpublished results for a project done in collaboration with A. Laio - a method for critical assessment of the suitability of collective variables for metadynamics simulations using their diffusivity.

II Structural phase transitions in solids

In this chapter, we briefly review essential aspects of *first-order structural phase transitions*, starting with their classification proposed by Cohen, Olson and Clapp in 1979 [17], a standard textbook description of their thermodynamics, high-pressure chemistry, and a brief state of the current limits (2023) of experimental techniques used to probe them. For in-depth reviews, please see a book of Kostorz, 2001 [3] or a recent book of Fultz, 2020 [32]. The purpose of this chapter is only to define the terms used later and give the reader "*a glimpse*" of this complex subject.

II.1 Introduction

Cohen, Olson and Clapp in 1979 [17] divided (first-order) *structural phase transitions*, see Fig. II.1, to subclasses in which interfacial energy dominates strain energy or the difference in chemical potentials of phases (driving energy) dominates a potential energy contribution caused by strain.

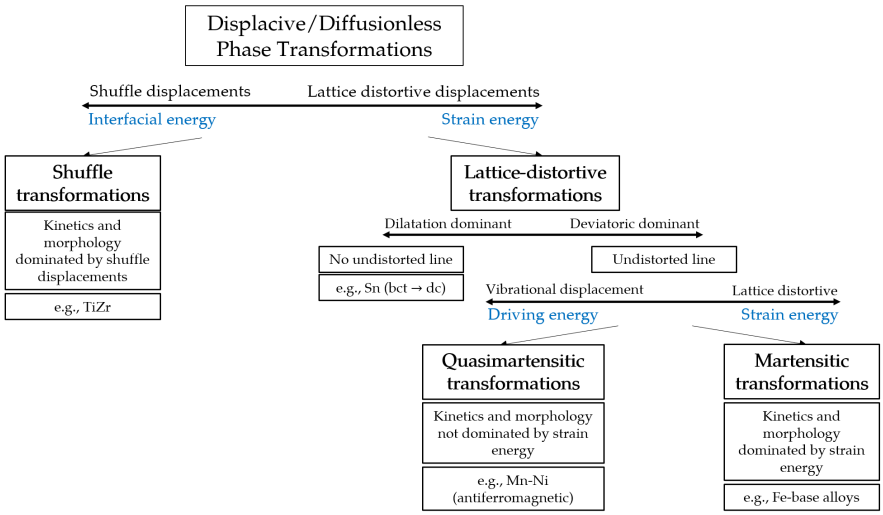

Figure II.1: Classification scheme proposed by Cohen, Olson and Clapp in 1979 [17]. Figure adapted from Fig. 2 in Ref. [17].

A *shuffle transition* happens when in the contribution to the Gibbs free energy of emerging nuclei an interfacial (potential) energy[1] dominates over a strain energy contribution. Cohen et al. define the *shuffle* as "*a coordinated shift of atoms within a unit cell which in itself does not produce a homogeneous lattice-distortive strain*" [17].

When the latter dominates, Cohen et al. call those transitions *lattice-distortive*. In *lattice-*

[1] Microscopically the potential energy of bonds at an interface of two phases.

distortive transitions, the microscopic structural mechanism corresponds to *homogeneous lattice deformations*. A *lattice deformation* is defined by Cohen et al. as "*a homogeneous strain which converts one Bravais lattice to another. This is the same as a Bain strain or Bain distortion - the term originally adopted in iron-base martensitic transformations*" [17].

If the transformation involves both shuffle and lattice deformations, Cohen et al. divide the transition according to which type of displacement dominates. Thus, the shuffle transformations include transitions involving additional lattice-distortive displacements (to shuffle displacements) as long as these are "*small enough not to significantly alter the kinetic and morphological character of the transformation*" [17].

Examples of shuffle transformations include the mentioned $\alpha \rightarrow \omega$ transition in pure titanium [22], but also the $\beta \rightarrow \omega$ transitions in its or Zr-alloys. The example of shuffle transformations according to the classification of Cohen et al. is also the $B1$-$B2$ transitions in NaCl studied recently by us [57] (so-called WTM-like mechanism [188]), or other $B1$-$B2$ transitions, e.g., as in MgO [199].

The lattice-distortive transitions can be further divided according to the fact that if the *dilatation* is present or not. If no distorted line in a lattice-distortive transformation, they regard it as *dilatation-dominant*. If a distorted line does result from the transformation, they regard it as *deviatoric-dominant*.

The latter ones are further divided by Cohen et al. according to the comparison of displacement of atoms during the transition with equilibrium root mean square vibrational displacement of atoms. If the displacements are small, the transitions are usually second-order (or approach second-order character) and are called by Cohen et al. as *quasimartensitic*. If the lattice distortion is significant Cohen et al. call these transitions *martensitic*, to which the original martensite-austenite transition in iron falls.

Note that whether one concludes the transformation to be *shuffle* or *martensitic/lattice distortive* can depend on the realized microscopic structural mechanism (in the thermodynamic limit). Note that in the problem of $B1$-$B2$ transition in NaCl [57] the one class of proposed mechanisms falls within the shuffle transformations (so-called WTM-like mechanisms [183, 188, 189, 194]), the others involving more strain (so-called Buerger-like mechanisms [182, 186, 187]) into the class of dilational-dominant mechanisms.

However, as already pointed out by Cohen et al. in 1979 "*... the various energies at play (interfacial energy, strain energy, transformational driving force, etc.) are generally not known in the same quantitative detail as are the atomic displacements...*" - the precise conclusion of the transformation mechanism cannot be made without the precise knowledge of the "*all costs*" (namely, contribution to the potential energy) altering the Gibbs free energy. Therefore the atomistic simulation methods represent a suitable approach that can effectively identify those contributions easily just from the chemistry itself.

For the completeness of the overview, we include an adapted table from the book of Kostorz [3], see Fig. II.2, which nicely reviews the thermodynamical character of transitions corresponding to the classification of Cohen et al. [17].

Characteristics → / Type of diffusionless transformation ↓	Structural change		Pure lattice deformation		
			Principial strains		Volume change
	Type	Thermodynamic order	Sign	Value	
Shuffle	Discontinuous or Continuous	First order Second order	All zero	Zero	Zero up to 10^{-5}
Dilatational	Discontinuous	First order	All positive or All negative	Large	Large ~ 10^{-1}
Quasi-martensitic	Discontinuous or Continuous	First order Second order	Mixed sign	Small	Small ~ 10^{-4} - 10^{-3}
Martensitic	Discontinuous	First order	Mixed sign or Zero and +,-	Large	Small or large 10^{-2} - 10^{-1}

Figure II.2: Adapted table (Tab 9.1) from the book of Kostorz [3] showing the complexity of *diffusionless transformations*.

II.2 Kinetics and Metastability

As already stated in Ch. I, the thermodynamics of first-order structural phase transitions seems to be trivially simple, explainable through a canonical figure present in every statistical physics or condensed matter textbook, see Fig. II.3. Yet what is not simple is to create a field theory consistent with the thermodynamics of first-order structural phase transitions, nucleation and that gives a correct microscopic spatial mechanism of how the atoms shuffle and the lattice is strained during the transition. The summary of what is known on this subject is reviewed in Ch. IV. The first-order nature of structural phase transformations implies the transition to proceed via *nucleation*, whose aspects are reviewed in Ch. III.

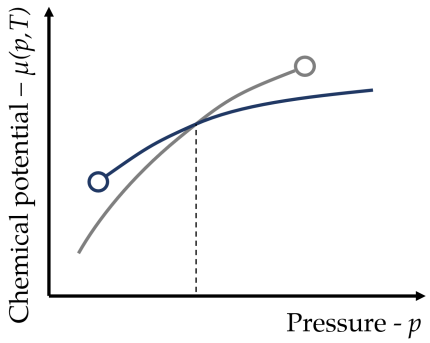

Figure II.3: A canonical figure demonstrating a chemical potential - $\mu(p,T) = G(p,T)/N$ of two phases as a function of pressure. The vertical dashed line notes the point of an equilibrium transition pressure and the blank circles denote the loss of stability of the two phases. Note that the nucleation barrier in free energy at the equilibrium pressure always diverges. Thus the transition is never observed at the equilibrium transition pressure in experiment leading to *hysteresis* and *metastability*.

Note that, as the chemical potentials (of bulk phases) can be written in the form $\mu = e - Ts + pv$, where e is the intensive potential energy (per atom), s is the intensive entropy (per atom) and v is the volume density, so it is not easy to computationally *a priori* calculate the difference of chemical potentials between two phases at a given temperature and pressure even with the knowledge of *ab-initio* forces acting on nuclei. The reason is the entropic contribution to the Gibbs free energy.

The standard solution to the evaluation of the free energy differences are methods as e.g.,

umbrella sampling, *thermodynamical integration*, methods based on *quasiharmonic calculations*, etc.. However, all of them cannot calculate the true barriers (obviously not the same as the difference of free energy minima) as long as they assume some collective transformation mechanisms, or "*can evaluate only what has been inserted*". This can induce *systematic bias* as the relative costs of different mechanisms change with the presence of an interface (due to induced strain and interfacial energies) [57]. Therefore a free-energy method capable of discovering the transition mechanism is needed and of large importance.

II.3 High-pressure chemistry

As stated in Ch. I, structural phase transitions in solids are often activated by pressure, where *high-pressure chemistry* [111–113] is different from the chemistry at zero pressure. A majority of known compounds usually respond to pressure according to the following set of empirical rules of Prewitt and Downs [111]:

1. *A structure usually compresses by displaying the greatest distortion between atoms separated by the weakest bonds.*
2. *Short bonds are the strongest, and long bonds are the weakest.*
3. *As a given bond compresses, it becomes more covalent.*
4. ***Increasing pressure increases coordination number.***
5. *The oxygen atom is more compressible than the cations.*
6. *Angle bending is dependent upon coordination.*
7. *O-O packing interactions are important.*
8. *High-pressure structures tend to be composed of a closest-packed array of atoms.*
9. *Elements behave at high pressures like the elements below them in the periodic table at lower pressures,*

where **the fourth rule** is the inspiration for our choice of collective variable in our method [57], see Ch. VI.

We note that the "*high-pressure world*" [113] is far more complex than what is described by the rules of Prewitt and Downs [111]. Consider e.g., a recent publication of Zong et al. [200] which showed that at high pressures the liquid potassium possesses a liquid-liquid transition in which electrons "*detach*" from nuclei and form a so-called *electride*, leading to a state where a liquid is denser than a close-packed solid. However, within this doctoral thesis is enough to restrict oneself to these "*standard*" empirical rules of high-pressure chemistry.

II.4 Experimental techniques

For the sake of completeness, we briefly state here the current limits of a few state-of-the-art methods used to probe first-order structural methods. The discussion is limited to *diamond anvill cells*, *laser ramp compression* and *ultrafast X-ray diffraction*, while many other methods can

be also employed to detect a structural transition (*neutron powder diffraction*, *NMR*, *IR* or *Raman spectroscopy*, etc.).

The achievable pressures in static **diamond anvil cells** are $\sim 300\,\mathrm{GPa}$, while being laser-heated they can reach temperatures up to $\sim 6000\,\mathrm{K}$ [201]. Thanks to the transparency of diamond in a wide range of wavelengths, it is possible to use it together with visible light (for sample visualization and spectroscopic methods), infrared light (IR; as heat source) and X and γ-rays (for determination of atomic, phononic, electronic and magnetic structure) [201]. The achievable pressures in **laser ramp compression** are of order $5\,\mathrm{TPa}$ which are achieved in $\sim 10\,\mathrm{ns}$ [202]. The laser ramp compression is often used together with **ultrafast X-ray diffraction**, e.g. as in Ref. [196], where pulses of duration of tens of picoseconds are separated in range of nanoseconds [203].

III Nucleation in structural phase transitions

The *nucleation of a solid inside another solid* is qualitatively far different from the *nucleation of a solid inside a melt* described by *classical nucleation theory*. This chapter aims to introduce the reader to the complexity of the nucleation of a solid inside another solid. As already mentioned in the introduction - Ch. I, the reason for this complexity is threefold. The first two are the misfit of volumes of an emerging and a parent phase that creates long-range ($\sim 1/r^3$) [3, 28–32] elastic strains and the anisotropy of elastic properties of a solid. Both are later complicated even in the case of homogenous nucleation (without the presence of defects) due to the non-linear nature of elasticity of any realistic solid resulting in complex field theories reviewed in Ch. IV. The third reason is the unavoidable presence of defects in solids, such as dislocations and grain boundaries, potentially significantly lowering a nucleation barrier. This chapter reviews what is known about all these "*complexities*".

III.1 Classical nucleation theory (CNT)

Classical nucleation theory of an emerging solid from melt or a liquid droplet from vapour is a standard textbook topic accessible with its level of discussion even to a high-school student. Consider, e.g. an undercooled vapour, the chemical potential difference $\Delta\mu$ of liquid to vapour is then negative $\Delta\mu < 0$ - creating a so-called driving force for a transition. Yet, the transition has to start somewhere - e.g. the fluctuations need to "simultaneously join" to create a small droplet of radius r. The presence of an interface between the liquid and vapour creates an additional energy cost due to *surface tension* - σ. The Gibbs free energy of a droplet of solid or liquid is then

$$\Delta G(r) = -4/3\pi|\Delta\mu|r^3 + 4\pi\sigma r^2\,, \tag{III.1}$$

the droplet grows when it is thermodynamically favourable ($\Delta G < 0$ for $r > r_c$). The critical radius of the droplet - r_c is clearly $r_c = 2\sigma/|\Delta\mu|$ with the nucleation barrier of $\Delta G_{\text{barrier}} = \Delta G(r = r_c) = 16\pi\sigma^3/3|\Delta\mu|^2$.

Note that the classical nucleation theory does not contain any information about the *point of stability* (where the metastable phase completely losses its stability to the stable phase). In particular, this situation will change for the nucleation of a solid inside a solid after the inclusion of elastic energy in a proper field theory applied to this problem, see Section III.2.3.

III.2 Nonclassical nucleation theory

III.2.1 Elastic energy

In a solid, a surrounding material cannot flow away to make space for a growing nucleus. Therefore, the elastic strains are not only present inside the nucleus but also in a parent phase

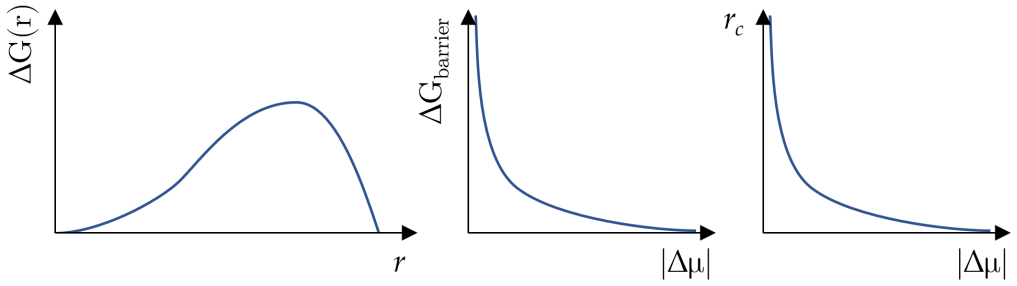

Figure III.1: Canonical picture of classical nucleation theory everyone has in a mind. Both the critical radius r_c and the barrier $\Delta G_{barrier}$ diverge when the pressure or temperature approaches the equilibrium transition pressure or temperature - $|\Delta\mu| \to 0$.

around it. Probably the first to realise this and solve the problem for the case of an *isotropic* solid was Nabarro in 1940 [28], who was interested in the calculation of strains created during precipitation in alloys. The solution and elastic fields were later studied in greater detail by Eshelby in 1957 [29], also for the case of an isotropic medium. Here we summarize the *qualitative* nature of elastic energy contribution to the nucleation of a barrier as found in the book of Fultz, 2020 [32], following the solutions of Nabarro and Eshelby. We note that the calculation of elastic energy for a non-ellipsoidal inclusion (which can emerge as a result of a complex interplay between the anisotropic interfacial and elastic energy) in a not-isotropically-elastic solid is a non-trivial task and a no *closed-form solution* exists in general [204] even within the "*world of linear elasticity*".

Elastic energy stored in a surrounding matrix

For simplicity, consider a homogeneous elastically isotropic material, in which a *bubble* of emerging phase appears with higher volume density as the parent phase (similar to the discussion in Section III.1). Outside the spherical bubble, but in the vicinity of it, the displacements are purely radial $u_r = \Delta V/4\pi r^2$ [28], where $\Delta V < 0$. Causing the strains in the form $e_{ij} = \delta_{ij}/r^3 - 3x_i x_j/r^5$, as noted by Fultz [32], the total dilatational strain outside the spherical bubble is zero ($e_{xx} + e_{yy} + e_{zz} = 0$). Hence the strain outside the bubble is pure shear. The shear stress (in spherical coordinates) has the form of $\sigma_{rr} = -G\Delta V/\pi r^3$, where G is the shear modulus [28, 29]. This result can be easily generalized to elliptical bubbles [29]. The energy stored in a surrounding matrix is equal to the work done by the normal forces at the surface of the nucleus $W \propto -\int \sigma_{rr} u_r \mathrm{dS}$ yielding an expression

$$E_{\mathrm{elastic-matrix}} = G(\Delta V)^2/2\pi R^3\,, \tag{III.2}$$

where R is the radius of the bubble. Note that for small relative changes of volume $\Delta V/V \sim 3\Delta R/R \equiv 3\delta_R$, where ΔV is the difference in the volume of the bubble included in a matrix compared to the previous volume of space filled by the parent phase, hence the elastic energy stored in a surrounding matrix is proportional to the volume of the bubble ($E_{\mathrm{elastic-matrix}} \sim GV\delta_R^2$).

Elastic energy stored inside a nucleus

On contrary to the surrounding matrix, in the case of isotropic medium, the strains inside the spherical bubble are purely dilatational. Thus the energy is determined by the bulk modulus - B [32]. The acting forces on the surface of the nucleus need to be equal from both sides, which creates an interesting analogy to a problem with two springs connected in series [32]. Therefore the ratio of energies stored inside a nucleus to energy stored in a surrounding matrix - $E_{\mathrm{elastic-inside\,nucleus}}/E_{\mathrm{elastic-matrix}}$ is given by $4G/3B$ [32] (in the case of a spherical bubble in an isotropic medium). Hence both the elastic energy stored inside and outside scales with the volume of the bubble and the overall elastic energy becomes [32]

$$E_{\mathrm{elastic}} = E_{\mathrm{elastic-matrix}} + E_{\mathrm{elastic-inside\,nucleus}} = \frac{2GB}{3B+4G} V \delta_R \,. \tag{III.3}$$

As pointed out by Nabarro already in 1940 [28] the elastic energy is the largest for a sphere and smaller for disks ("*pancakes*") and cylinders, opposite to the case of interfacial energy. Also, observe that the elastic energy is always positive and volume proportional, thus effectively lowering the effect of the difference of chemical potentials - $\Delta\mu$, making the barrier larger.

III.2.2 Interfacial energy

While it is easy to write a general expression for interface energy such as $\oint_S \sigma(\mathbf{n})\mathrm{dS}$, there is no usefulness of it without having in mind a particular transition and thus an ansatz or a model for $\sigma(\mathbf{n})$. Hence we restrict to a few points we would like to emphasize and find nontrivial. The effect of interfacial energy was studied, and probably the most in-depth study of the morphology of critical nuclei in solid-solid nucleation has been performed by Zhang et al., 2007 [33], whose findings we briefly mention.

Zhang et al., 2007 [33] used a simple phase-field model/Ginzburg-Landau theory (to be described later) with a single scalar order parameter modelling the first-order transition using a simple Landau functional for bulk free energy. Using a realistic ansatz for interfacial energy of a cubic crystal (see Eq. 1 in Ref. [33]), they were able to show a variety of different shapes for critical nuclei as variational solutions of functional, for a reproduced figure see Fig. III.3.

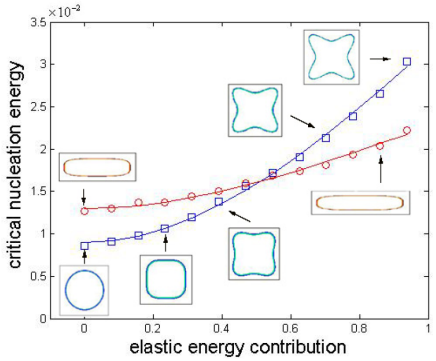

Figure III.2: The shape of critical nucleus depends on the ratio between the elastic and interfacial energy as well as on the overall barrier itself. Adapted from Ref. [33].

The important "*moral*" of their work is that the well-known Wulff construction used to determine equilibrium shapes of a nucleus of crystal in another phase (which accounts for

anisotropy of surface tension/interfacial energy) fails as long as it does not take into account elastic energy contribution. This leads to even non-convex shapes. Another moral of their work is that the critical nucleus can have even lower symmetry than the parent and emerging phase.

III.2.3 Nonclassical nucleation theory of Moran et al., 1996

To be able to describe *qualitatively* the unique features of nucleation of a solid inside a solid, a *minimal field theory* is needed. In this subsection, a minimal model of purely dilatational first-order solid-solid transition of Moran et al., 1996 [34] is presented (*in medias res*), even though an in-depth review (in chronological order and a gradual increase of complexity) of field theories and phase-field models is subject of the following Ch. IV.

Consider an elastically isotropic solid undergoing a pure dilatational transition (and spherically symmetric deformation) induced by pressure[1] described by a single scalar order parameter $\eta \equiv \varepsilon_{kk}/\overline{\varepsilon_{kk}}$, where ε_{ij} is defined as usual as $\varepsilon_{ij} \equiv (1/2)(\partial u_i/\partial x_j + \partial u_j/\partial x_i)$ with u being a standard displacement field and $\overline{\varepsilon_{kk}}$ is the dilatational strain in an emerging phase assuming the strain to be zero in a parent phase. Then the material is assumed to be governed by a Ginzburg-Landau free energy functional of a form[2] [34],

$$\Delta G_{\mathrm{barrier}}[\eta] = 4\pi \int_0^\infty r^2 \mathrm{d}r \left[g(\eta, p) + (2G/3)\eta^2 + (\kappa/2)\left(\nabla\eta\right)^2 \right], \tag{III.4}$$

where $g(\eta, p) = A(p)\eta^2 - B(p)\eta^3 + C(p)\eta^4$, G is the shear modulus, and the coefficient $\kappa > 0$. The first term represents bulk free energy density, the second term elastic energy density, and the third term comes from extending a continuum description into the atomic scale and represents the interfacial energy, hence the coefficient κ also determines the effective length scale.

The difference of chemical potentials (or so-called driving force) is then $\Delta\mu(p) = \Delta g(p) = g(1,p) - g(0,p) = g(1,p) < 0$ as $g(0,p) = 0$ by construction. Moran et al., 1996 [34] conveniently defines a normalized difference of chemical potentials $\alpha \equiv \Delta g(p)/\Delta g_{\mathrm{loss}}$, where $\Delta g_{\mathrm{loss}} = \Delta g(1, p_{\mathrm{loss}})$ is the difference of chemical potentials at the *point of complete loss of stability* of parent phase (where its bulk modulus vanishes) corresponding to a pressure p_{loss}.

Moran et al., 1996 [34] then proposed a simple ansatz for coefficients in Landau functional A, B and C leading to a first-order transition in p,

$$\begin{aligned} A(p) &= 16\Delta e_{\mathrm{eq}}(1 - \alpha(p)) \\ B(p) &= 32\Delta e_{\mathrm{eq}}(1 - \alpha(p)) - 4\alpha(p)\Delta g_{\mathrm{loss}} \\ C(p) &= 16\Delta e_{\mathrm{eq}}(1 - \alpha(p)) - 3\alpha(p)\Delta g_{\mathrm{loss}} \\ \alpha(p) &= (p - p_{\mathrm{eq}})/(p_{\mathrm{loss}} - p_{\mathrm{eq}}), \end{aligned} \tag{III.5}$$

where Δe_{eq} is the energy density barrier at *equilibrium transition pressure* - p_{eq}. The critical nucleus profile of η is then found by solving the corresponding Euler-Lagrange equation,

$$\kappa\frac{\mathrm{d}^2\eta}{\mathrm{d}r^2} + \frac{2\kappa}{r}\frac{\mathrm{d}\eta}{\mathrm{d}r} = \frac{\mathrm{d}g}{\mathrm{d}\eta} + \frac{4G}{3}\eta, \tag{III.6}$$

[1] Moran et al., 1996 [34] discuss a transition induced by temperature but without the loss of generality, we can change it.

[2] This functional is the most general functional assuming spherical symmetry and the lowest-order of strain-gradient energy terms.

with boundary conditions $\eta(r=0)=1$, $\eta(r\to\infty)=0$, and $(\mathrm{d}\eta/\mathrm{d}r)r^2|_{r=\infty}=0$. No closed-form solution of Eq. (III.6) exists, but the asymptotics of solutions close to the equilibrium transition pressure ($p\to p_{\mathrm{eq}}$) and close to the point where the bulk modulus of parent phase vanishes ($p\to p_{\mathrm{loss}}$) can be inferred [34]. Since this is a continuous model, the critical radius of bubble r_c is defined as a point of the maximal derivative of η (a point with the maximal contribution to interfacial energy).

In the limit $p\to p_{\mathrm{loss}}$ [34] ,

$$\Delta G_{\mathrm{barrier}}\sim(p_{\mathrm{loss}}-p)^{3/2} \tag{III.7}$$

$$r_c\sim(p_{\mathrm{loss}}-p)^{-1/2}\,. \tag{III.8}$$

Observe that CNT, see Section III.1, does not contain any information about the *point of complete loss of stability*. Thus $\Delta G_{\mathrm{barrier}}$ approaches zero with exponent -2 compared to $3/2$ here. Also observe that contrary to CNT, the radius of critical nucleus also diverges as one approaches p_{loss} with exponent $-1/2$, whereas in CNT the radius decreases continuously to zero.

In the limit $p\to p_{\mathrm{eq}}$ [34] ,

$$\Delta G_{\mathrm{barrier}}\sim(p-p_{\mathrm{eq}})^{-2} \tag{III.9}$$

$$r_c\sim(p-p_{\mathrm{eq}})^{-1}\,, \tag{III.10}$$

consistent with CNT (if $|\Delta\mu|\propto p$), see Section III.1. The full behaviour of theory of Moran et al., 1996 [34] given by Eq. (III.4) can be *qualitatively* depicted as in Fig. III.3. For precise numerical solutions see Ref. [34].

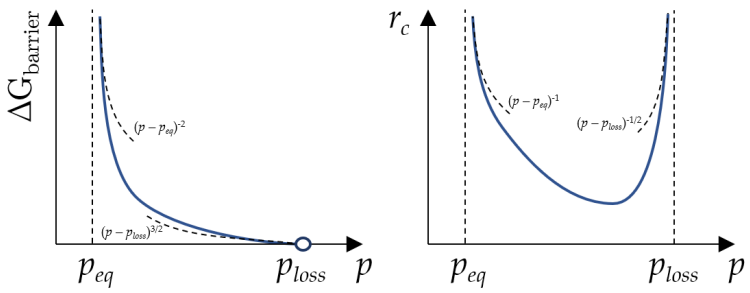

Figure III.3: A *pictographically* depicted *qualitative* dependencies of free energy barrier $\Delta G_{\mathrm{barrier}}$ and the radius of critical nucleus r_c in nonclassical nucleation theory of Moran et al., 1996 [34].

This behaviour, including its exponents, is consistent with the result in a seminal work of Cahn and Hillard, 1959 [205], on *spinodal decomposition in two-component fluids*, namely see Fig. 6 in Ref. [205]. Due to the mathematical equivalence of the Ginzburg-Landau functionals, P. C. Clapp also proposed the term "*spinodal decomposition of strains*" [58, 90].

However, while the insights presented here are undoubtedly useful, the functional in Eq. (III.4) is still far away from a realistic description of a structural transition in solid as it misses nonlinear elasticity, coupling to other modes (shuffling of atoms), anisotropy of elastic properties, and models the nucleation only in the homogeneous limit. The summary to what extent these has been included in literature is the subject of Ch. IV.

III.3 Nucleation on defects

Since the presence of *vacancies* would merely decrease nucleation barriers by a scale of nucleation barrier comparable to e.g., $100\,\mathrm{eV}$ as found in the case of NaCl [57], see Ch. VI, for instance, think about a vacancy as an elastic defect in the spirit of Section III.2.1. We focus purely on defects that can significantly lower the Gibbs free energy barrier and start the process of nucleation. These need to already accommodate a large portion of the energy in long-range elastic deformations of a solid such as *dislocations* or a large portion of energy must be stored in misfitting surfaces or edges as is the case for *grain boundaries*.

III.3.1 Nucleation on dislocations

The nucleation on dislocations was originally proposed by Cahn in 1957 [48], soon after their experimental confirmation, and studied by Cook [49], Olson [50, 51], Suezawa [52], or more recently by Li [53], Samanta [54] and Levitas [55] (possibly missing others). In this subsection, we review their findings.

Cahn in 1957 [48] was the first one to propose the idea of nucleation on dislocation to lower the nucleation barrier. Cahn discussed a simple model of an infinitely long dislocation line and nucleus starting to grow in a radial direction to the dislocation core. Cahn [48] discussed a simple Landau free-energy functional of a form

$$F[r] = -A\log r + 2\pi\sigma r - \pi\left|\Delta\mu\right| r^2\,, \tag{III.11}$$

where the first term accounts for dislocation self-energy ($A = Gb^2/4\pi(1-\upsilon)$ for edge dislocations and $Gb^2/4\pi$ for screw dislocations; G being shear modulus, b Buergers vector, υ Poisson ratio), the second term accounts for interfacial energy with σ being the surface tension and the third accounts for bulk free energy in which $\Delta\mu$ is the density of difference of chemical potentials (per unit of length). Cahn [48] then solved a simple variational problem of cylindrical symmetry - the critical nucleus profile $r(z)$ as the function of distance z along the infinite dislocation core.

Using his analysis, he found that the barrier for nucleation is present if the ratio

$$\alpha \equiv \frac{2A\left|\Delta\mu\right|}{\pi\sigma^2} \tag{III.12}$$

is less than one. If it is greater than one, then there is no barrier for nucleation, and further analysis does not make sense since one would not find such dislocation with an embryo of emerging phase. For the case when $\alpha < 1$, Cahn solved the variational problem to find the equilibrium value of r_0,

$$r_0 = \frac{A}{2\pi\sigma}\left[2\alpha^{-1}\left(1-\sqrt{1-\alpha}\right)\right]\,, \tag{III.13}$$

which he then calls an embryo of emerging phase, and a critical value of r_c, which corresponds to critical cylindrical nucleus radius. The barrier for nucleation is then defined as $\Delta G_{barrier} = L\left(F[r_c] - F[r_0]\right)$, where L is the length of dislocation. Unfortunately, $\Delta G_{barrier}$ cannot be expressed analytically. Cahn [48] plotted the ratio of this barrier to the barrier found for the homogeneous nucleation ($16\pi\sigma^3/3|\Delta\mu|^2$) as a function of the ratio α, see Fig. 3 in Ref. [48]. The ratio goes to zero as $\alpha \to 1$ almost linearly. Cahn [48] concluded his discussion by giving an order of magnitude estimate of nucleation rate, finding that his discussions provide a suitable order of magnitude for realistic data - "*The model predicts a significant nucleation rate at values of*

the parameters which are within the limits of the assumptions. " [48]. The solution for Cahn thus provides an order of magnitude justification for the relevance of dislocations to nucleation.

Cook in 1973 [49] created a simple lattice-site free energy model of an isotropic solid as a function of displacements of individual atoms for a simple $\mathrm{bcc} \rightarrow \mathrm{fcc}$ transition, with a simple nearest-neighbour coupling (so-called Born-Huang atomic force constant). Solving his model numerically, he then discussed the nucleation on dislocations. However, he concludes his discussion that the dislocations expectedly lower the barrier without providing much quantitative detail for a realistic transition.

Olson and Cohen in 1976 [39, 50, 51] proposed for the classes of $\mathrm{fcc} \rightarrow \mathrm{bcc}$, $\mathrm{bcc} \rightarrow \mathrm{fcc}$, and $\mathrm{bcc} \rightarrow \mathrm{hcp}$ transformations a general mechanism of nucleation by faulting from groups of existing dislocations. However, much of the discussion in Ref. [50] is only on a qualitative level concluding that such a process is energetically possible. Ref. [51] then applies these considerations to mentioned classes of structural transitions, concluding that the proposed mechanism of nucleation is possible within certain examples in material, however, also without providing much quantitative detail. Ref. [39] finally generalizes the analysis to a case of finite *dislocation loops* which are created from a "*forest*" of dislocation lines intersected by embryos growing in the fault planes. Olson and Cohen conclude such a process to be able to explain the observed nucleation rates by an order of magnitude qualitative estimate. Olson and Cohen are probably the first ones to realize the importance of *finite dislocation loops*.

Suezawa and Cook in 1979 [52] generalize the method presented by Cook in 1973 [49] to a nucleation on a screw dislocation in a martensitic transition in Fe – Ni system at $250\,\mathrm{K}$. Using a simple Landau functional, with empirically deduced constant accounting for elastic energy, and model presented in Ref. [49] they insert spherical embryos of various shapes to find a critical embryo that interacts with a pileup of dislocations by its growth. However, they still found the critical nucleus to consist of around ~ 1000 atoms of a barrier around $50 k_B T$ [52].

Li et al., 2004 [53] perform a series of molecular dynamics (MD) simulations at $100\,\mathrm{K}$ assuming various lattice defects such as a single edge dislocation, various dislocation configurations or a low-angle grain boundary using a classical EAM potential for Ni-Al alloy. However, their conclusions are somehow limited, as they conclude that the defects play a role, but by using an unbiased MD, they could not draw any conclusion on the energetics of such transition.

Recently, Levitas et al., 2018 [55] used also simple unbiased MD with a classical Tersoff potential for silicon to study the effects of dislocation on pressure-induced phase transformation. He performed simulations of 8 000 - 4 096 000 atoms under uniaxial stress at $1\,\mathrm{K}$, however, the conclusions are also somehow limited as they concluded that the reduction of phase transitions pressure is observed to be around 30%.

We note that we are not aware (to our best knowledge) of any other publications **theoretically discussing** or modelling an **effect of dislocations in** the problem of **nucleation in a structural phase transition**, while on the contrary, many experimental works exist, e.g., see the citing articles of seminal work of Cahn [48].

In a similar problem of the melting of copper, Samanta et al., 2014 [54] used an alternative approach to metadynamics [148, 149] so-called adiabatic free energy dynamics (AFED) [206] with classical EAM potential for copper. The simulations were performed in supercells of 32 000 & 256 000 atoms. They showed that the presence of dislocation can reduce the barrier for melting in overheated solid by approximately one half, see Fig. 2D in Ref. [54], assuming closed

dislocation loops.

III.3.2 Nucleation on grain boundaries

The nucleation on grain boundaries was studied by Clemm and Fisher in 1955 [35] and studied subsequently by Cahn [36], Russel [37], Johnson et al. [38], Marth et al. [40], Aaronson et al. [41], Lange et al. [43, 44], in experiments e.g., by Park and Ardell [42], Offerman et al. [45] and Landheer et al. [46], in molecular dynamics e.g., by Lazerev et al. [59], Uehara et al. [60], Zong et al. [61], Song and Hoyt [62, 63], Meiser and Urbassek [64, 65], Zhang et al. [66], or more recently by means of phase field models by Jin et al. [67], Artemev et al. [68], Sutou et al. [69], Cui et al. [70], Yamanaka et al. [71], Cho et al. [72], Malik et al. [73], Heo et al. [74], Mamivand et al. [75], Schoof et al. [76], Yeddu et al. [77], Shchyglo et al. [78], Zhu et al. [79], Ciss et al. [80], Xi et al. [81], Xu et al. [82], Paliwal et al. [83], Fan et al. [84], Basak [85] and Babaei et al. [86] (certainly missing many others).

In this subsection, we review their findings as well as the simple modification of CNT.

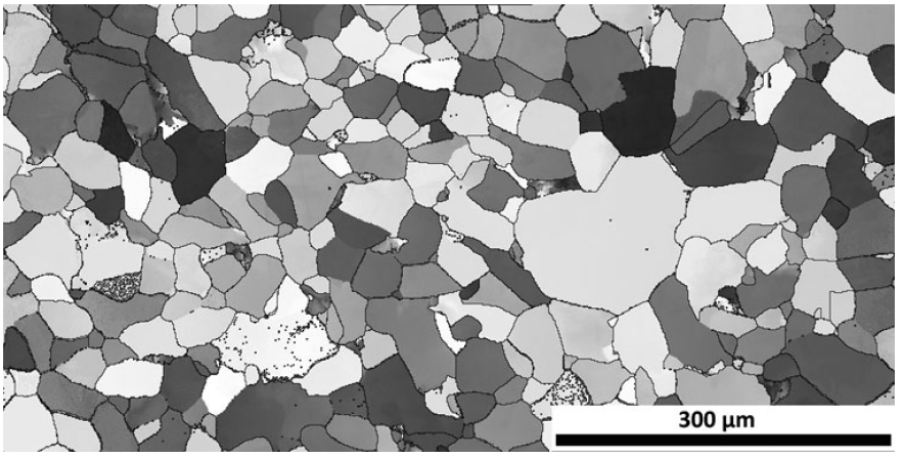

Figure III.4: Electron backscatter diffraction image showing individual crystals in a polycrystalline sample of a slowly cooled carbon steel. Adapted from the Fig. 11.6 presented in Ref. [32].

In the presence of a grain boundary, the standard CNT analysis changes in the following way [32]. Consider a double spherical cap consisting of the forming β phase having a contact angle θ (see Fig. III.5) sitting at the boundary of the two grains of the α phase assuming isotropic surface energy for the α–β interface. The spherical cap has a surface area of $4\pi(1-\cos\theta)r^2$ and its volume is $2\pi(2-3\cos\theta+\cos^3\theta)r^3/3$, where r is the radius of the cap. We note that the assumption of local sphericity comes from the fact that atoms far from the boundary should be unaware of it [32]. The Gibbs free energy of the β-nucleus is then

$$\Delta G(r) = -2/3\pi|\Delta\mu|(2-3\cos\theta+\cos^3\theta)r^3 + 4\pi(1-\cos\theta)\sigma r^2 - \pi\sin^2\theta\sigma_{gb}r^2\,, \qquad \text{(III.14)}$$

where σ_{gb} is the surface energy of the grain boundary and creates an additional factor which lowers the free energy barrier. Since this term is not present in the CNT, it prefers the nucleation on grain boundary over the homogeneous nucleation as described by CNT. The critical radius r_c is found as $r_c = \frac{4(1-\cos\theta)\sigma-\sin^2\theta\sigma_{gb}}{|\Delta\mu|(2-3\cos\theta+\cos^3\theta)}$, plugging this result back we find $\Delta G_{\text{barrier}} \propto \sigma^3/|\Delta\mu|^2$ as in CNT, but with a lower barrier. The angle θ must (in equilibrium) fulfill the relationship $\sigma_{gb} = 2\sigma\cos\theta$. A realistic nucleus of lead crystal sitting at the boundary of two aluminium crystals is shown in Fig. III.6. Note that contrary to the simplified analysis presented above, the

shape of the lead crystals respects the anisotropy of the lead-aluminium surface energy.

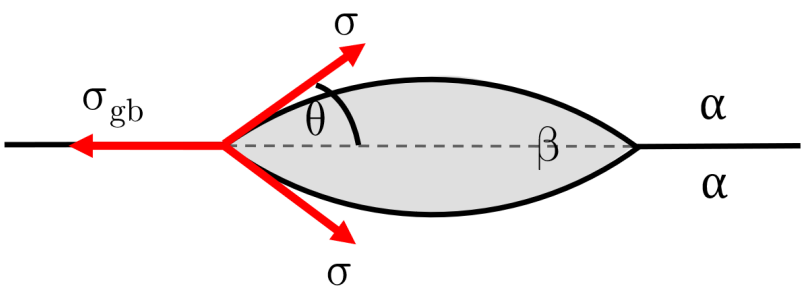

Figure III.5: Emerging β phase at the grain boundary of α phase.

It is also worth to note that in a realistic material, the grain boundaries form a three-dimensional network through a polycrystalline sample of the material. Contrary to the nucleation on a surface presented above, this network offers edges of several grains joining together as well as the corners of the grains as possible nucleation sites. This fact also motivates the use of atomistic simulation techniques, to be introduced in Ch. V, for study of the role of grain boundaries as it is probably more natural to consider them in atomistic simulation than in a phase-field model, see Ch. IV.

Clemm and Fisher in 1955 [37] examined the case of nucleation on junctions of two, three and four grains for the nucleation of ferrite from austenite. They found the barrier for the nucleation on three-grain junctions to be approximately five times smaller than that for the nucleation on two grain junctions. Similarly, the barrier for the nucleation on four-grain junctions was found to be approximately 25 times smaller than that for the nucleation on two-grain junctions.

Cahn in 1956 [36] generalized their result and calculated the nucleation rates for the nucleation on junction of two (planes), three (edges) and four grains (corners). The analysis was based on the idea that the nucleation rate is not determined only by the energetics of the specific path (which favours four-grain junctions) but also by the number of available nucleation sites (which is the lowest for the nucleation on four-grain junctions). His important observation is that there exist conditions under which the nucleations on sites of lower dimensionality are not observed because the undercooling (in a case of temperature induced transition) might place the transformation into the conditions when nucleation in bulk dominates.

Russel [37] calculated nucleation rate factors and incubation times for the nucleation on grain boundaries. He found a quantitatively good agreement for the case of SiO_2.

Johnson et al. [38] generalized the modification of CNT on a grain boundary presented above to the case when the shape of nuclei is not a spherical cap but rather is facetted due to a realistic surface tension anisotropy. They found that the facetted shape decreases the barrier. Marth et al. [40] and Aaronson et al. [41] applied it to a problem of precipitation at grain boundaries in alloys. Lange et al. [43] measured maximal and steady state nucleation rate at grain boundaries using photographs from transmission electron microscopy for the nucleation of ferrite from austenite, however they found that regardless of the expression for the facet energy, all of these models (modifications of CNT in the spirit presented above) predicted steady state nucleation rates from 10 to 10^6 times lower than those observed in all studied alloys. For a critical review

of measured nucleation rates in experiments and their comparison with theoretical predictions (for the case of nucleation on grain boundaries) one is referred to Ref. [44].

Park and Ardell [42] studied boundary precipitation in a commercial alloy 7075 Al using transmission electron microscopy and experimentally found a tendency of the nuclei to establish a crystallographic orientation relationship with respect to only one grain.

Landheer et al. [46] experimentally studied nucleation of ferrite in austenite. They found that that the specific orientation relationships between emerging and parent phase play a dominant role during nucleation. However, the ferrite grains nucleate on grain faces independently of the misorientation between austenite grains. They also found that different types of nucleation mechanisms are found to be active during transformation.

Offerman et al. [45] studied experimentally the austenite-ferrite transition. Based on their measurements, they found that the activation energy for grain nucleation is at least two orders of magnitude smaller than those predicted by thermodynamic models.

Lazarev et al. [59] studied martensitic transition in Ni-Al shape memory alloy using classical MEAM potential in perfect crystal as well as a system with grain boundary to find that in the latter the transition starts at the grain boundary.

Uehara et al. [60] also studied martensitic transition in Ni-Al alloy using classical MEAM potential. However, their system was quasi 2D periodic (the supercell was of size 40 x 40 x 5 multiplications of unit cell, of total size of 31 000 atoms). They found the transition to start at the grain boundaries. However, no inference of barrier was performed.

Zong et al. [61] studied the effects of grain boundaries on the $\alpha \rightarrow \omega$ phase transition in titanium using molecular dynamics and proposed that the coherent twin boundary assists the transformation under shock loadings.

Song and Hoyt [62, 63] studied nucleation of iron ferrite phase from its austenite phase by means of unbiased molecular dynamics under presence of grain boundaries. They performed simulations using a classical Fe-Cu MEAM potential of Ackland et al. [207] in a quasi-2D settings (in z-direction the supercell consisted of 9 atomic unit cell, while in x and y directions the sample was of size $650\,\text{Å}$ x $650\,\text{Å}$ large containing 4 austenite grains, thus totalling to supercells of approximately 380 000 atoms). In order to induce the nucleation process, they performed a questionable so-called *potential switch process* [208]. In agreement with experiment, the most favorable nucleation sites were the junctions of three grains, followed by the surfaces of grains. However, another drawback, besides the potential switch process, was that part of the atoms in the supercell were constrained to be fixed, while the atoms in the other regions were allowed to evolve freely. By counting the atoms in the interface layer and in the transformed bulk, using CNT, they were able to determine the barrier for the critical nucleus of size $38\,\text{Å}$ to be 5 eV. In the second work [63] the simulations were performed in the full 3D sample of size $45 \times 45 \times 9\,\text{nm}^3$ (1 382 400 atoms) with a similar conclusion of preference of three grains junction as a nucleating site, however, with no attempt to infer the barrier.

Meiser and Urbassek [64] simulated a martensitic transition in pure iron using a classical Meyer-Entel potential. Their simulation box contained two equally sized fcc crystallites which were separated by a symmetric tilt grain boundary. The sample contained around 96 000 atoms. They found evidence for switching between the so-called Pitsch and the Kurdjumov-Sachs pathways. In their second work [65], they show that under their studied conditions the

transition does not proceed without the presence of grain boundary and that the transition temperature decreases approximately linearly with the grain boundary energy.

Zhang et al. [66] performed molecular dynamics simulations using classical MEAM potential for iron under shock loadings and the presence of three kinds of grain boundaries. They found that all three grain boundaries provide a nucleation site for the transitions in shock-loaded samples.

The nucleation on grain boundaries has been studied rather extensively also by means of phase field models, see Ch. IV, for instance, in Refs. [67–86, 209]. The phase field models are able to describe several stages of the growth of nuclei - parabolic growth, delayed nucleation and growth, temporary shrinkage, partial shrinkage, complete shrinkage, coarsening, accelerated growth in the transformation as well as plastic deformation accommodating transformation-induced stress or post-transformation tweed formation, while the typical size of the simulation cell can represent as large boxes as 0.8 x 0.8 x $0.8\mathrm{mm}^3$, comparable with sizes of samples in experiments. They also allow to study the influences of the parent microstructure (grain-size distribution). For instance, Babaei et al. [86] recently studied the transformation between cubic Si I to tetragonal Si II phases in samples of 55 and 910 grains. They found that in contrast to a single crystal, the local mechanical instabilities are stabilized at the macroscale by arresting/slowing the growth of Si II regions by the grain boundaries. However, the phase field models can have their own peculiarities, such as the problem of convergence in respect to the mesh size or potential elastic instabilities leading to strain localization and divergences of solution [86].

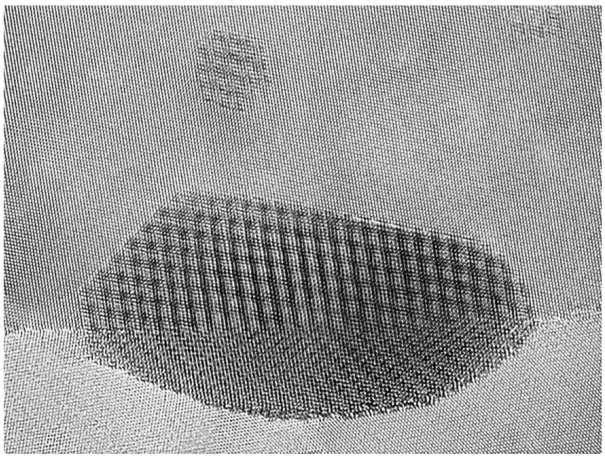

Figure III.6: A high-resolution transmission electron micrograph of a lead crystal at the grain boundary of two aluminum crystals. Adapted from Ref. [32].

We note that we are not aware (to our best knowledge) of any other publications theoretically discussing or modelling the effect of grain boundaries in the problem of **nucleation in a structural phase transition**, in the sense that the work would quantify the barrier for such process (using an enhanced sampling technique).

IV Field theories of first order structural phase transitions

In previous Ch. III we have seen that the nucleation of a solid inside a solid is quite different from standard classical nucleation theory. Unique features of the nucleation in structural phase transition have been revealed due to the field theory of Moran et al., 1996 [34].

This chapter reviews the findings of literature that led to this work and also the subsequent works. The purpose of this chapter is to exhaustively summarise all insights, as well as, to show that creating such *a realistic field theory/phase-field model* is far from being trivial. The attention is put on *nucleation* and predictions of *nucleation precursor effects*. For reviews of *phase-field models* with applications also to structural phase transitions in solids, see Refs. [88, 89].

IV.1 "Spinodal decomposition of strain" of P. C. Clapp, 1973

P. C. Clapp proposed in 1973 his idea of "*a localized soft mode*" [58] for martensitic transformations. This idea can be summarized as "*... the martensitic transformation is triggered by a strain-induced elastic instability in special regions of the parent lattice, that the inclusion of anharmonic terms in the elastic free energy will considerably reduce the estimates of the nucleation barrier and that the lattice vibrations (or phonons) in these anomalous regions play an important role in the nucleation process.*" [58]. The motivation behind this idea was the lack of experimental evidence for the so-called *embryo hypothesis*[1]. For a bcc $\rightarrow$ fcc transformation immersed in a cubic lattice, Clapp wrote a most general full strain free-energy Landau functional with all up to third-order terms allowed by cubic symmetry. He then investigates the stability of free energy generalising well-known Born stability criteria. Using empirically determined elastic constants, he finds solutions for Li, Na and CuZn representing a *spinodal* [2]. He concludes his analysis by postulating that sufficient initial "*displacements*" in strain can be achieved near defects. Clapp [58] also mentions the possibility that a high concentration of strains can "*locally*" soften the phonons easing locally the possibility of larger displacements, thus implicitly pointing to the importance of *strain-phonon coupling* or let us say *strain - shuffle displacements* coupling.

In 1979 Clapp extended his idea of "*strain spinodal decomposition*" by giving predictions on the experimental implications of his hypothesis, see Ref. [90]. Namely, he predicts the ultrasonic acoustic attenuation and velocity changes due to the existence of regions of high strain and compares them to experiments for Ti−Ni, In−Tl and Fe−Ni alloys. He observes a good *qualitative* correlation between the predicted dependencies of ultrasonic acoustic attenuation and velocity changes given by his model with the experimental data, concluding that the volume fraction of "soft mode" (high strain) regions can be, *in principle*, measured using these experiments. Hence it suggests that if his hypothesis is correct for all first-order displacive transformations then it can be verified using careful ultrasonic measurements, or they may show

[1] *Homogeneous nucleation hypothesis* would be saved if the nucleus start to grown on preexisting embryos as it is the case of rain in clouds.

[2] A surface of instability in a six-imensional strain space.

up in X-ray or neutron scattering experiments as anomalous contributions to the Debye-Waller factor [90].

In 1981 in Ref. [210], Clapp further extended his predictions by explicitly evaluating implications of his hypothesis to *inelastic neutron scattering*, *ultrasonic acoustic attenuation* and *Mössbauer resonance absorption* experiments. Though the anomalous scattering had not been observed by 1981 in neutron scattering experiments, similar anomalous effects brought the motivation of Clapp to further push his analysis. The significance of the work of Clapp [210] is that his "*strain spinodal*" hypothesis implies precursor effects not normally expected with a first-order transition, since they do not *in general* display critical fluctuation phenomena [210].

Guénin and Gobin [94], used a similar Landau functional as Clapp [58] to describe a $\mathrm{bcc} \rightarrow 9\mathrm{R}$ martensitic transition in Cu–Zn–Al alloy. They found through the experimentally determined third-order elastic constants that the combination $(C_{11} - C_{12})$ of elastic constants (in the bcc phase) is highly sensitive to $\langle 011 \rangle$ shear strains, finding that around dislocations the combination softens dramatically [94]. Interestingly, as in our case of NaCl [57], several geometrical models are possible differing in the amount of strain compared to shuffles of atoms. Guénin and Gobin quantitatively discuss the implication of functional when the dislocations play a role, proposing a suitable nucleating model [94] comparing their predictions with other nucleation models such as Olson and Cohen [51] (see Section III.3), concluding that their model is also able to approximately describe experimental values.

IV.2 Towards a nonclassical nucleation theory

Olson and Cohen in 1982 [31] (see also their work in Section III.3) proposed a toy model of nonclassical nucleation theory almost of the form of the isotropic and of radial symmetry model of Moran et al., 1996[34] (see Section III.2.3), differing only that the model of Olson and Cohen was a toy-model on a semi-infinite line. We note that they were the first to introduce gradient terms, thus accounting for interfacial energy too. Comparing the order of magnitude estimates of this model to their former predictions for nucleation on dislocation [51] they found the latter to be preferable.

In 1988, Barsch and Krumhansl [211] proposed a rather exhaustive analysis of Ginzburg-Landau functional applied to a $O_h - D_{4h}$ (cubic-tetragonal) ferroelastic transition in $\mathrm{In}_{1-x}\mathrm{Tl}_x$ alloys, which as they stressed does not rely on a concept of *soft mode*. They provide one of the most insightful discussions of nonlinear and nonlocal elasticity. The result of their work is the prediction of a spatially modulated precursor pattern, consistent with the experimental observations. We note that the dependence of spatial precourse period (wavelength) has the same qualitative dependence as a function of temperature as the radius of the critical bubble in the field theory of Moran et al., 1996 [34], see Section III.2.3 and Fig. 4 in Ref. [211].

Gooding and Krumhansl in 1989 [93] analysed a $\mathrm{B2} \rightarrow 7\mathrm{R}$ martensitic transition in $\mathrm{Ni}_x\mathrm{Al}_{1-x}$ alloy. They suggest that the transition may be attributed to the $\Sigma_4\langle 011 \rangle$ phonons and homogeneous strains associated with the softening of $(C_{11} - C_{12})$ elastic constant as in Ref. [94]. They show that there must be a wave-vector dependence (coupling) of the Landau coefficient appearing in a Landau functional for free energy. Their theory predicts strains compatible with those observed experimentally and is consistent via strong dependence of the elastic constant $(C_{11} - C_{12})$ on temperature with the strong first-order character of the transition. We note that this is the only work presented in this overview, which explicitly took into account a coupling

with phonon modes ("*shuffling of atoms not explainable through pure strain*") in a Landau functional, see Eq. 6 in Ref. [93]. However, Gooding and Krumhansl used only a Landau functional without strain gradient (interfacial energy) terms, thus no conclusion was drawn on nucleation itself.

Krumahnsl and Gooding [212], then pushed the analysis further, still accounting for a coupling between the strain subspace and phonons discussing ω phase transformations in Zr-alloys pointing to a strong precursor effects far above the transition temperatures. The second motivation of this work of them was to show how static and phenomenological free energy can be related to many-body phonon perturbation theory.

Falk and Konopka in 1990 [92], provided (in our subjective point of view) the most detailed analysis of all possible symmetry-allowed terms for a cubic-monoclinic phase transition of β-phase shape memory alloys by studying irreducible representations of O_h group acting on a six-dimensional strain space. By this geometrical construction, they found all possible strain invariants[3] up to the sixth order. Inferring the experimental temperature dependence of all nonlinear elastic constants, they determined the precise numerical form of Landau functional in Cu−Al−Ni alloys. Unfortunately, their analysis ends here, without the inclusion of strain energy terms, thus without any useful solution to the problem of nucleation.

Schwabl and Täuber [213] investigated in 1991 how the statics and dynamics of elastic phase transitions are influenced by defects. They developed a theory for a finite concentration of randomly distributed defects, based on a one-dimensional Ginzburg-Landau functional. Their work is the first work that attempts to solve also the dynamics of the Ginzburg-Landau functional by inserting the functional derivative of the field into an effective Langevin-type equation with thermal white noise and effective diffusion constant. The latter is (in our opinion) probably the largest weakness of such approaches, as long as, there is no *a priori* way how to relate the effective diffusion constant in the dynamics of effective order parameter to the microscopic parameters of a solid (mass density, etc.) Their quantitative conclusions are limited.

In 1992, Krumhansl in his review paper [95] discussed the question "*Are soft modes needed for structural phase transitions?*" advocating to abandon a common taste in the literature to study soft mode transitions and "willingness" to explain every structural phase transitions through the soft-mode concept pointing to several unique features of first-order structural transitions nonexplainable through soft-mode concept.

In 1996, Moran, Chu and Olson [34] proposed their toy model for homogenous nucleation in dilatational transition already presented in Section III.1 in Ch. III.

Chu et al., 2000 [91] presented another model for nonclassical nucleation, which is a further generalisation of the nonclassical model of Moran et al., 1996 [34]. This model is extended by introducing driving-force dependencies into the interfacial free energy, the misfit strain energy, and the nucleus chemical free-energy change to capture the nonclassical nucleation phenomena, which enables the modification of the exponents of critical nucleus and nucleation barrier as a function of driving force. Then they applied the model to a cubic-tetragonal transformation in Fe−Co alloy, determing the critical nucleus size and shape, however still finding that the nucleation barrier is of the order of $40k_BT$.

[3] As the free energy expansion can be function of strain invariants only.

IV.3 Nucleation and transformation precursor effects

Kartha et al., 1991 [214] pointed to the fact that despite many displacive solid-solid transformations, despite being first order, show pronounced precursor effects, such as the mesoscopic, "*tweed*" pattern seen in shape-memory alloys. They modelled the tweed using a nonlinear, nonlocal elastic free energy from which an effective version of the random-field version of Sherrington-Kirkpatrick model emerged [214]. Their model predicts the appearance of tweed precursor patterns in 2D martensite.

In 1993, Clapp [47] studied static and dynamic precursor effects of displacive transformations near crystalline defects. In the framework of Ginzburg-Landau functionals, of the form as in Ref. [31] he calculated the exact nucleation energy for nucleation in strain fields of planar defects and calculated metastable precursor strain profiles in the vicinity of such defects.

Saxena and Barsch in 1993 [215] studied pretransformation structural modulations in $O_h - D_{4h}$ (cubic-tetragonal) transformation as metastable fluctuations stabilized by defects. However, not many quantitative conlusions are made.

In 1995, Kartha et al., [216] studied disorder-driven pretransitional tweed patterns in martensitic transformations observed by *transmission electron microscopy* in many first-order solid-solid displacive transitions. Using a simple Ginzburg-Landau functional accounting for three order parameters of a 2D solid, they predict a tweed pattern consistent with experiments. Moreover, their predictions on diffraction patterns, namely modification of Bragg points, agree very well with experimental data. We note that they provided quite a careful analysis of physically realizable Ginzburg-Landau functionals with physically realizable couplings due to long-range elastic interactions, linear order parameter coupling, coupling to gradients of disorder and coupling to bulk dilation.

IV.4 Bringing external pressure to play

Fradkin in 1994 [217] as the first one, left the world of temperature-induced phase transformations and discussed also the studied Landau functionals for the case of pressure-induced phase transitions in the cases of hydrostatic and uniaxial pressures. He found that the nonlinearity of thermal expansion implies a special relationship between the shear strain and volume change that can lead to the transformation from an fcc lattice to a bcc as in iron alloys. The nucleation limit is not studied as long as Fradkin discusses a Landau-like functional only.

IV.5 Modern phase-field models

Wang and Khachaturyan [108] in 1997 created a three-dimensional continuum stochastic field kinetic model of martensitic transformations which explicitly takes into account the transformation-induced elastic strain. The model can predict the major structural characteristics during the transition including nucleation, growth and eventually the formation of internally twinned plates which are in thermoelastic equilibrium with the parent phase by simulation in a 3D cubic computational cell with a 64 x 64 x 64 mesh. Their work represents the first 3D continuum field kinetic model of martensitic transformations being able to predict the structural characteristics of the nucleus.

Roy et al., 1998 [105], studied nucleation in a phase-field model in 2D to calculate with a

Ginzburg-Landau functional as in many others previously mentioned works here, also using an effective Langevin equation for the simulation of the model time evolution. They determined how the spatially nonlocal interactions affect both droplet morphology and nucleation rate. However, their quantitative conclusions are also limited.

In 1999, Reid, Olson and Moran [106] developed a model for the determination of the stress and strain fields of an array of dislocation effects in the two-dimensional elastic medium of a highly nonlinear and nonlocal functional. The model is then solved using a finite element method. They found that in the presence of a suitable dislocation array, fully-formed embryos arise from the effect of the dislocation geometry on the nonlinear elasticity of the matrix.

In 2002, Levitas et al., 2002 [96–98] created a fully three-dimensional Ginzburg-Landau functional for stress-induced martensitic phase transitions, using an effective Langevin equation for the simulation of its time evolution, also accounting for full anisotropy in interfacial energy and full anisotropy of applied pressure. First, in Ref. [96], they applied the methodology to austenite-martensite transitions, then generalising it to a generic martensitic transition in Ref. [97]. Their theory accounts for the stress-strain curves with constant transformation strain and constant, or weakly temperature-dependent, stress hysteresis, as well as nonzero tangent elastic moduli at the phase transformation point and allows for the inclusion of all temperature-dependent thermo-mechanical properties of both phases. In Ref. [98], alternative Landau potentials for the description of stress- and temperature-induced martensitic phase transformations under arbitrary three-dimensional loading are obtained. The unique features of the potentials are pointed out and a detailed comparison of the potentials is made for NiAl alloy.

Shen, Li, Wang in 2007 [107] used a *nudged elastic band method* together with a Ginzburg-Landau functional for a cubic to tetragonal transformation in both 2D and 3D. They calculated the activation energy and the shape of the critical nucleus, accounting for full anisotropy of interfacial energy. However, the nucleation in presence of dislocations has not been considered.

In 2013, She, Liu, Wang [99], presented a solution of a phase-field model to the case of heterogeneous nucleation in a cubic to tetragonal transition in the presence of different types of microscopic defects (voids, stress-concentration site, inertial inclusion and pre-existing nucleus). However, the discussion of results is limited to the *qualitative* figures of the time evolution of emerging spatial patterns on mesoscale for those cases.

In 2014, Levitas et al., [100] generalized their approach to the case of large strais and interface stresses.

In 2016, Levitas et al., [101] generalized their approach for the case with the anisotropic interface (gradient) energy (e.g. an energy density that depends both on the magnitude and direction of the gradients in the phase fields).

In 2017, Levitas et al., [102] employed a continuum/atomistic approach to prediction of the lattice instability during crystal-crystal phase transformations for the general loading with an arbitrary stress tensor and large strains.

IV.6 Summary

It is clear that the task of creating a *realistic* Ginzburg-Landau theory for a first-order structural transition is highly nontrivial.

First, one needs to identify all possible subgroups of parent and emerging phases and then propose within every considered subgroup a possible collective mechanism, and project it to a respective irreducible representation of that subgroup. This task was solved by Stokes and Hatch in 2002 [182] who created a computer program that automatically identifies all possible candidates. Then one needs to identify/propose all secondary order parameters which play a role of "*shuffle*" degrees of freedom, see the classification of Cohen, et al., 1979 [17]. Next, one needs to account for the anisotropy in externally applied stress, see e.g., Ref. [96], gradient terms, solved e.g., by Hatch et al., 1996 [110] as well as to account for all allowed couplings between the order parameters. Obviously, all couplings and expansion coefficients need to be determined, e.g. empirically from experiments, as well as with their temperature and pressure dependence (which may represent still an underdetermined/an ill-defined problem [92]).

Having done all this, one still finds *a static* Ginzburg-Landau theory. To simulate its real-time evolution, one needs to introduce kinetic term to a corresponding Lagrangian or use a Langevin-type equation with an effective diffusion coefficient (or a matrix), as in Refs. [96–98, 100–102, 105–108]. The latter obviously represents a set of free parameters of the theory, which also need to be determined, and it is (in our opinion) not clear, how to obtain them for a crystal of more than one chemical element.

Having done all this, one is still able to simulate only the nucleation and growth of the emerging phase in the homogeneous limit. Although the heterogeneous nucleation can be studied by insertion of defects as a suitable initial condition to the set of partial differential equations, all relevant of them need to be studied separately.

Having done all this, one is still able to describe *a single particular transition* for *a single particular compound*, despite the immense intellectual complexity of this task. We also note that we are unaware of any work in which all these subtleties (including also the analysis of secondary order parameters as in Ref. [182]) as well as the anisotropy of interfacial energy terms and external pressure as in Ref. [96], together with the consideration of heterogeneous nucleation, as in Ref. [99], were put together all at once.

V Methods

We have seen that the construction of a realistic and exhaustive field theory (Ch. IV) for the problem of nucleation in structural phase transitions in solids (Ch. III), under the presence of defects (Section III.3), represents an inefficient and "*tremendous*" amount of work. The possible *effective* solution to the problem of realistic simulation of structural phase transition represents *atomistic simulation methods* that enable the simulation of the transition and infer all its details as the result of pure statistical emergence in a large system.

V.1 Molecular dynamics at constant pressure and temperature

One of the reasons why the construction of effective field theory of a first-order transition is so hard is that there are still too many relevant degrees of freedom (and their couplings). The possible solution to this problem may be not to try to solve it at all! If our understanding of nature is correct, all properties of a solid at mesoscale *emerge* from a microscopic theory as a property of a system of a large number of atoms and its structure. Thus *in principle*, it is enough to study large systems having a precise description of effective interactions between the atoms (in *Born–Oppenheimer approximation*).

Since experimentally, we can easily control pressure and temperature, it is natural to consider a NPT ensemble. The time integration of system evolution from knowledge of forces acting on nuclei is performed by *molecular dynamics*, where the simulation in the NPT ensemble is addressed by e.g., Nosé–Hoover thermostats and barostats [218, 219] with Martyna-Tobias-Klein correction term [220]. For a review of molecular dynamics methods, we refer the reader to the classical books [221–223]. We note that since we have in mind applications where *nuclear quantum effects* do not play a role, no method able to incorporate their effects is employed.

V.2 Density functional theory

However, the application of molecular dynamics is limited by the precision of the so-called *force field*. For long, applications of molecular dynamics have been limited by the use of empirical force fields/interatomic potentials such as Tersoff potential for silicon [224], (M)EAM potentials for metals [225, 226] or Born-Mayer-Huggins-Fumi-Tosi potentials [227, 228] for alkali halides, etc. The solution to the accurate quantum-mechanical description of interactions at the *mean-field* level of electronic correlation is given, e.g., by Kohn-Sham *density functional theory* [115].

However, the quality of the solution is hidden in the quality of used exchange-correlation functional, where the research continues, e.g., see *a strongly constrained and appropriately normed (SCAN) functional* by Sun et al., 2015 [229], *regularised SCAN functional* of Bartók and Yates [230], *a modified Vydrov and Van Voorhis functional* accounting for *nonlocal van der Waals interactions* (rVV10) by Sabatini et al., 2013 [231], a recently proposed *machine learning functional* by Kirkpatrick

et al., 2021 [232] enabling one to obtain a solution of CCSDT quality as a SCF solution of corresponding Kohn-Sham equations, etc. For the overview of density functional methods see Refs. [233–237] or the classical books [238–240].

V.3 Enhanced sampling - Metadynamics

As already mentioned in Introduction (Ch. I) the limiting factor of the use of molecular dynamics or ab-initio molecular dynamics is the achievable time scale in simulations ($\sim 100\,\mathrm{ns}$ - a few µs) which is still not enough to observe a rare event such as a structural phase transition. The solution to this problem is *enhanced sampling* [147], namely *free-energy methods*, and within them one such example is *metadynamics* [148, 149].

V.3.1 Overview

Metadynamics [148, 149] is an *enhanced sampling method* based on the idea of "*pushing out*" the system in an abstract space of *collective variables* (to be described later)[1] (defined as a function of atomic coordinates) from previously visited states. This is done during the course of molecular dynamics simulation in a controlled manner, thus enabling the system *in principle* to explore all states. Metadynamics thus construct a free energy profile as a function of chosen collective variables. This procedure is achieved by the modification of potential energy of the system $U(\mathbf{R})$ to the form $U(\mathbf{R}) \to U(\mathbf{R}) + V_\mathrm{B}(\mathbf{s}(\mathbf{R}), t)$, where $\mathbf{R}$ are the atomic coordinates, $\mathbf{s}(\mathbf{R})$ are the collective variables (functions of atomic coordinates) and V_B is the bias potential (see below).

The bias potential is chosen in the form such that in the long time limit of simulation ($t \to \infty$), the bias potential converges to the negative of free energy $V_\mathrm{B}(\mathbf{s}, t \to \infty) \to -F(\mathbf{s}) + C$, where C is an additive constant and F is the (Helmholtz/Gibbs)[2] free energy. The bias potential $V_\mathrm{B}(\mathbf{s}(\mathbf{R}), t)$ is chosen as

$$V_\mathrm{B}(\mathbf{s}(\mathbf{R}), t) = \sum_{t_i < t} h \exp\left(- \sum_{i=1}^{d} \frac{\left(s_i(\mathbf{R}) - s_i(\mathbf{R}(t_i))\right)^2}{2w_i^2} \right), \tag{V.1}$$

where t_i is the time of deposition of i-th Gaussian (which are deposited periodically with a period t_d), h and w_i are the free parameters of the method, and $s_i(\mathbf{R})$ is the i-th collective variable (out of d). The convergence of this method was proven by Bussi et al., 2006 [150]. Moreover, it was shown that the modification of this method called *well-tempered metadynamics* leads always to convergence [241]. Since, for the applications outlined in this doctoral thesis, we are interested in the as fastest as possible escape from the initial free energy minimum, we employ a non-well-tempered version of metadynamics (Eq. (V.1)). For the recent review see Ref. [149].

V.3.2 Choice and construction of collective variables

Note that there is no *a priori* guarantee that the metadynamics procedure will work as it requires suitably chosen values of its free parameters (which allow the system to *quasi-equilibrate* other degrees of freedom during the period t_b) as well as the suitable choice of collective variables,

[1] One can imagine under term "*collective variable*" an *order parameter*, though there can be not necesserily a suitable Landau/Ginzburg-Landau functional in which they act *really* as the order parameters.

[2] Depending upon the ensemble in which molecular dynamics is performed.

which enables to distinguish by their value **all** relevant transition states, transition pathways and the initial and the final (and metastable) states.

The problem of *automatic construction and choice of CVs* has been studied recently rather exhaustively in Refs. [129, 151–161]. However, note that the automatic constructed CV is as good as a proposed ansatz for it. Moreover, as we noted in our recent publication [57], simulating only small systems can induce a systematic bias to the deduced structural mechanism. For a recent complete overview of possible choices of collective variables see the recent review [127].

Note that there is no a priori guarantee that the chosen CVs will work and hence the construction of the CVs is to a large extent a trial and error procedure. In the Ch. X we provide our proposed algorithm for the quantitative assessment of the suitability of the CVs, possibly enriching the way in the future how the CVs are automatically constructed.

Note that the application of collective variables for the simulation of structural phase transitions is rather limited as it involves, *a supercell* as CV by Martoňák et al., 2003 [162], *a coordination number* by Zipoli et al., 2004 [175], the *PIV metric* by Pipolo et al., 2017 [176], so-called *a path-CV* by Gimondi et al., 2017 [177], *a coordination number* and *transition path sampling* by Jobbins and Leoni in 2018 [178], *enthalpy* and *a pair approximation of entropy* by Mendels et al., 2018 [179], or *a neural network based on Behler-Parrinello descriptors* by Rogal et al., 2019 [180] or Yoo et al., 2021 [181].

V.4 Machine learning potentials

A typical DFT calculation becomes *practically* prohibitive at the scale of hundreds of atoms. For the reader's imagination, assuming the atoms to be part of a cubic lattice implying a spatial scale of $\sim$ 3 - 8 lattice constants ($\sim$ 10 - 40Å). It is commonly believed that the interactions on the atomic scale are important up to the range of $\sim$ 10 Å [130] implying that the system at the spatial prohibitive limit can suffer from artificial correlations through periodic boundary conditions. Moreover, as stated in Introduction (Ch. I), a typical nucleus in structural solid transitions needs a structure of $\sim 10^4$ - 10^6 atoms (also to accommodate the induced elastic strains) [57]. On the contrary, classical force fields are usually fitted to reproduce properties near equilibria of corresponding phases but usually fail in describing transition states as it physically involves breaking of chemical bonds and creating the new ones (at least most of the commonly known potentials). Fortunately, the problem of length-scale of DFT (or more precise post-DFT) methods can be overcome by so-called *machine learning potentials*.

Originally, two main different approaches arose. Behler and Parrinello in 2007 introduced, see Ref. [121], a limited set of descriptors which were able to distinguish the chemical environments by two body functions based on radial distance and three-body functions dependent on a relative angle and distance, inspired by the original work of Tersoff [224], upon which a standard fully-connected neural network is to be built to create a neural network potential [121].

Bartók, Payne, Kondor and Csányi in 2010 created so-called *GAP potentials* [122] on the idea of so-called *Gaussian Process*, expressing the chemical environment in spherical harmonics and using the *bispectrum* a kernel of similarity to reference structures (also found under the name *SOAP descriptor* in literature). This procedure does not require a learning procedure as neural networks, which can make it however rather slow and also as standard BP networks [121] GAP potentials suffer from a degeneracy problem [242] as the bispectrum is *in principle* equivalent to three body BP descriptors.

For the recent reviews see Refs. [123–127], namely for the review of different representation of physical structure see Ref. [127].

Other recent approaches to the problem of machine learning potentials have been proposed by e.g., Zhang et al. [129] (DeepMD) based on two types of subsequent neural networks - the first ones used to create the set of descriptors based on a translational and rotational invariant, the other being a standard fully-connected neural network, or Drautz [130–133, 138] ("*atomic cluster expansion*"), who in 2019 generalised the expression of the geometric position of neighbouring atoms using ideas from cluster expansion in lattice models and representation theory of SO(3) group to any order of the geometrical correlation, or Batzner et al. [140] (NequIP) who joined ideas from graph neural networks with the class of group equivariant neural networks (in regard to SO(3) group). The other recent approaches are made on modifications of ACE or NequIP approaches, such as Allegro by Musaelian et al. [141] or MACE by Batatia et al. [142]. Research also continues in the line of SE(3)-equivariant graph neural networks such as SE(3)-Transformers by Fuchs et al. [144] or Equiformer by Liao and Smidt [145].

VI The B1-B2 transition in NaCl

This chapter is based on the results published in Ref. [57] as well as the unpublished results for nucleation on grain boundaries. The results of this chapter shall be viewed as the benchmark of our method and the demonstration of what is achievable by means of our method [57] (what kind of information can be infered). As a model for a martensitic transition, we have chosen the well-studied B1-B2 transition in NaCl [182, 183, 186–195].

VI.1 Summary of previous studies

The B1/B2 transition in NaCl represents a paradigmatic martensitic transition, which was extensively studied in the literature [182, 183, 186–195]. It occurs at room temperature at $p = 26.6\,\mathrm{GPa}$ and involves a volume drop of 5% [185]. We note that this transition is also present in 31 other binary compounds [194]. The B1/B2 transitions often proceed via intermediate B33 or B16 structures depending on the particular compound [194].

Several theoretical collective mechanisms were proposed for this transition, falling essentially into two groups. The ones by Shoji [186], Buerger [187] and Stokes & Hatch [182] are mainly driven by lattice strain, while the other class by Hyde & O'Keeffe [189], Watanabe *et al.* (WTM) [188] and Toledáno *et al.* [194] involves more shuffling of atoms [183]. Computational studies include overpressurised variable-cell MD [190, 191] and transition path sampling by Zahn & Leoni [195].

Sims et al. [193] performed a similar study at various level of accuracy (DFT, HF and post-HF) and concluded that both the WTM mechanism and the Buerger's mechanism have close activation energies. In the case of NaCl, they found that the activation energy for the Buerger's mechanism has an activation energy 0.2 kJ/mol lower than that for the WTM mechanism.

Stokes & Hatch [182] provided an exhaustive and complete list of all common subgroups of B1 ($\mathrm{Fm\bar{3}m}$) and B2 ($\mathrm{Pm\bar{3}m}$) structures and presented a method to find the optimal reaction pathway within each subgroup. They found that the WTM mechanism and the Buerger mechanism have significantly lower enthalpy barrier with respect to the other ones and in case of NaCl the Buerger mechanism was found to be preferred. Moreover, they found that a modification of the Buerger mechanism, which introduces a monoclinic distortion along the reaction pathway, can further lower the barrier.

Tolédano et al. [194] combined previous ideas of identifying common subgroups of B1 and B2 lattices and proposed a modified phenomenological Landau theory for the 1$^{\mathrm{st}}$ order phase transition. They suggested that for several alkali halides (e.g. PbS) the B1/B2 transition proceeds via intermediate B16 or B33 (bulk) phases and this pathway has lower enthalpic barrier than that of a direct B1/B2 transition. However, they concluded that this is not the case for NaCl since no B33 phase was experimentally observed.

Stokes et al. [183] revisited the results from their previous work [182] inspired by the results of Tolédano et al. [194]. They showed that the pathway proposed by Tolédano et al. is basically a modification of the WTM mechanism. For NaCl, they found both the "modified Buerger" mechanism (in our work [57] and Ref. [195] referred to as the "Stokes and Hatch mechanism") and the Tolédano et al. mechanism to proceed via the same B33 structure. At the DFT level of accuracy, they found at 24.4 GPa the Tolédano et al. pathway to have slightly lower enthalpic barrier than the "modified Buerger" one (see Fig. 5 in Ref. [183]).

Dynamical studies include an overpressurised (at 60 GPa) variable cell MD study [191] by Nga & Ong and a transition-path-sampling (TPS) study by Zahn & Leoni [195]. The former study used two different constant-pressure algorithms (modified Andersen (MA) and Parrinello-Rahman (PR)) and found both Buerger-like (PR) and WTM-like mechanisms (MA) in system of 216 atoms. The latter TPS study employed two system sizes (270 and 216 pairs of ions) and observed the transition to proceed via a WTM-like mechanism with an intermediate B33 structure (Tolédano et al. mechanism [194] proposed in 2003). We note that both studies used the same force field as our study.

VI.2 Model

To model the interactions, we used a classical force field - the pair **Born-Mayer-Huggins-Fumi-Tosi (BMHFT) potential** [227, 228]

$$U(i,j) = \frac{q_i q_j}{r_{ij}} + \mathrm{A}_{ij} \exp\left(-\mathrm{B} r_{ij}\right) - \frac{\mathrm{C}_{ij}}{r_{ij}^6} - \frac{\mathrm{D}_{ij}}{r_{ij}^8}, \tag{VI.1}$$

which accounts for Coulomb, an effective short-range Pauli repulsive interaction and van der Waals interaction (dipole-dipole & dipole-quadrupole terms).

The parameters of the potential are provided in Tab. VI.1. They were taken from a study of the melting point of NaCl from Ref. [243] and are based on the original Fumi-Tosi parameters [227, 228]. We also note that the force field parameters are the same as in the TPS study [195]. The potential satisfactorily reproduces the basic properties of the solid phases of NaCl (lattice constant, compressibility, cohesive energy) [227, 228].

	A_{ij} [eV]	B $\left[\text{Å}^{-1}\right]$	C_{ij} $\left[\text{Å}^6\text{eV}\right]$	D_{ij} $\left[\text{Å}^8\text{eV}\right]$
Na^+-Na^+	424.097	3.1546	1.05	0.499
Na^+-Cl^-	1265.31	3.1546	7.0	8.676
Cl^--Cl^-	3488.998	3.1546	72.5	145.427

Table VI.1: Parameters of the BHMFT potential.

The reason for this choice of force field was twofold. First, it allows us to compare our results with previous ones, e.g. those obtained in the TPS study [195]. Second, the classical force field description is computationally cheap ($\sim$ 100s ns/day on PC) and provides a realistic, yet simple model for the development of new metadynamics-based schemes.

In Fig. VI.1, we provide the enthalpy curves for B1, B2 and B33 phases. From them we conclude that the equilibrium transition pressure (between B1 & B2) is $p_{\mathrm{eq}} = 19.25\,\mathrm{GPa}$. Including entropic effects in the quasiharmonic approximation (phonon spectra were calculated for this

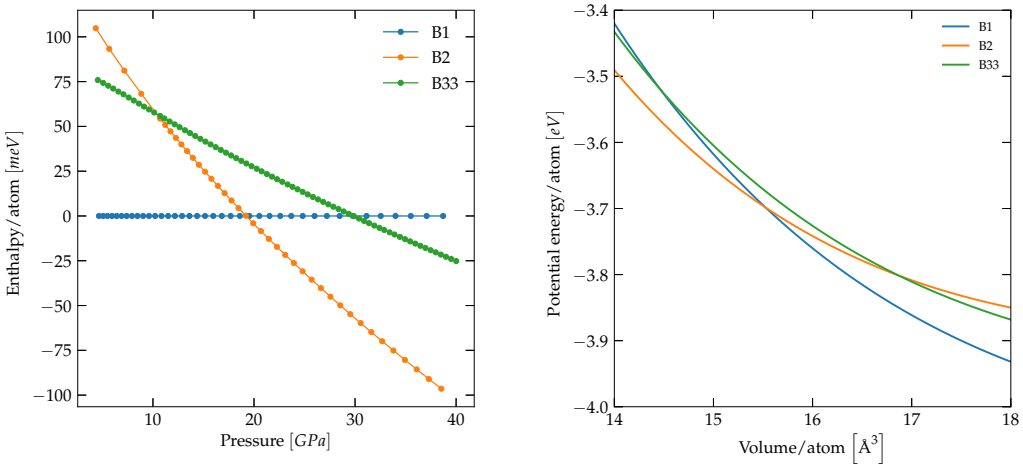

Figure VI.1: (Left) Relative enthalpy curves (with respect to the B1 phase) for B1, B2 & B33 phases as functions of pressure. Note relatively small differences in enthalpy for B33 with respect to B1 & B2. (Right) Potential energy vs volume for the B1, B2 & B33 phases of NaCl.

potential by means of the frozen-phonon approach) does not change this value significantly ($p_{\text{eq}} = 18.9\,\text{GPa}$ @ $T = 300\,\text{K}$), showing that the Gibbs free energy is dominated by enthalpy.

The point of loss of dynamical stability for overpressurisation of the B1 phase at $T = 300\,\text{K}$ is found at $p_{\text{loss}} = 60\,\text{GPa}$ in unbiased NPT MD when the pressure is raised by the rate 0.05 GPa/ps.

The B33 (Cmcm/#63) structure were obtained by a direct search at fixed pressures of interest (0 - 60 GPa). The B33 structures can be fully described by five parameters, where three determine the supercell and two represent the internal coordinates of atoms. All five parameters were used to minimise the enthalpy of the B33 structure at given pressure. We note that these structures are not dynamically stable at $T = 300\,\text{K}$. We agree with Ref. [195] that B33-like structures appear only as transient structures since we observed them only during transitions in smaller systems (up to 4 096 atoms), in supercells which were under a significant macroscopic strain. Thus, we rule out the possibility of nucleation of an intermediate bulk B33 phase, which plays a role in other B1/B2 transitions [194]. In simulations larger than 4 096 atoms, we observed nucleation of the B2 phase covered by a 7-coordinated layer, which in general does not resemble the B33 phase.

The attention in the literature was devoted to the systematic analysis of common sub-groups of the B1 and B2 phases and identification of the collective mechanism [182, 183, 186–189, 192–194]. While these results provide valuable insights, it is clear that they provide only upper estimates to free energy barriers of transition. In our work [57], we showed that the inclusion of interfacial energy and/or elastic energy of nuclei can change the relative costs of collective mechanisms. Hence the results from collective mechanisms, where no interface is considered and therefore the interfacial energy and elastic energy of nuclei and surrounding lattice is omitted, can lead to a wrong conclusion also at the level of transition mechanisms inside critical nuclei. For comparison with the metadynamics results, we calculated the barrier of the idealised Buerger's mechanism by means of a static calculation, see Fig. VI.2.

The Buerger's mechanism can be sampled as follows [193]. Both the B1 phase the B2

phase can be immersed into the triclinic point group $\mathrm{R\bar{3}m}$. The unit cell of $\mathrm{R\bar{3}m}$ is defined by $(a, a, a, \alpha, \alpha, \alpha)$. The fractional coordinates of the Na and Cl ions within this unit cell are $(0, 0, 0)$ and $(1/2, 1/2, 1/2)$, respectively. The B1 phase corresponds to the choice $(a, a, a, \pi/3, \pi/3, \pi/3)$, while the B2 phase to the choice $(b, b, b, \pi/2, \pi/2, \pi/2)$. The reaction pathway thus creates a two-dimensional space in coordinates (a, α). We choose the $\alpha \in \{\pi/3, \pi/2\}$ to be the reaction coordinate and optimise the volume of the crystal by optimising a to maintain the pressure of interest p at every choice of α.

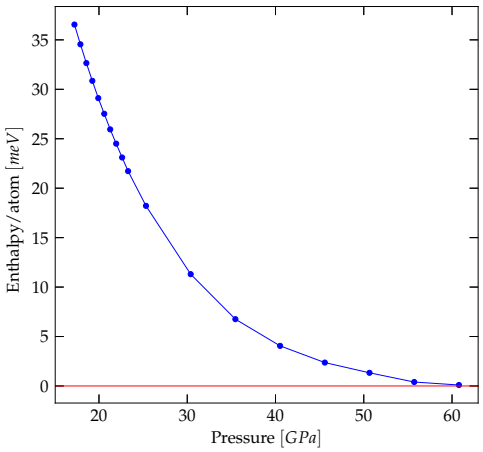

Figure VI.2: Pressure dependence of the enthalpy barrier between the B1 and the B2 phase of NaCl within the Buerger's mechanism for the BHMFT potential at T = 0.

VI.3 Choice of collective variables

In our work [57], we advocated the use of coordination number (CN) and volume (V) for a solid-solid metadynamics simulation as a simple and general scheme involving collective variables with a good physical underlying motivation. Here, we briefly review our arguments.

Firstly, the choice of coordination number, originally proposed as a reaction coordinate in constrained MD in Ref. [244], and also employed at early metadynamics study of a structural transition in carbon [175] or in a metadynamics study of the B1/B2 transition in colloidal clusters [245], can be motivated by one of the generic rules of high-pressure chemistry formulated by Prewitt and Downs [111–113], which states that pressure-induced transitions are typically accompanied by an increase of CN in the 1$^{\mathrm{st}}$ coordination sphere, see also Section II.3.

Secondly, the choice of volume can be motivated by the fact that we aim to study first-order phase transition, accompanied with a jump in volume from a few % up to as large as 10-20%.

In our work [57], we also provide a following crucial insight. Structurally, the B1/B2 transition in NaCl is accompanied by the transfer of 2 ions with opposite charges from the 2$^{\mathrm{nd}}$ to the 1$^{\mathrm{st}}$ coordination shell, increasing the CN from 6 in B1 to 8 in B2. The average CN between the Na^+ and Cl^- ions can be calculated by means of a switching function as

$$\mathrm{CN} = \frac{2}{N} \sum_{\substack{i \in \mathrm{Na}^+ \\ j \in \mathrm{Cl}^-}} \left(1 + \left(\frac{r_{ij} - d_0}{r_0} \right)^6 \right)^{-1}, \tag{VI.2}$$

where r_{ij} is the distance between the i-th cation and the j-th anion and N is the total number of atoms. Since the switching function involved the calculation of coordination number effectively mediates the transfer of 2 ions from the 2nd to the 1st coordination shell, the choice of d_0 and r_0 is crucial [57]. The switching function should allow to clearly differentiate between the initial state (e.g. B1), the transition state and the final state (e.g B2) [149]. Moreover, its slope should be sufficiently high at the positions of the radial distribution function (RDF) peaks of the B1 phase corresponding to the 1st and the 2nd coordination sphere in order to drive an easy exchange of ions between the two spheres. A suitable switching function meeting both requirements, which was used in our work [57] is shown in Fig. VI.3.

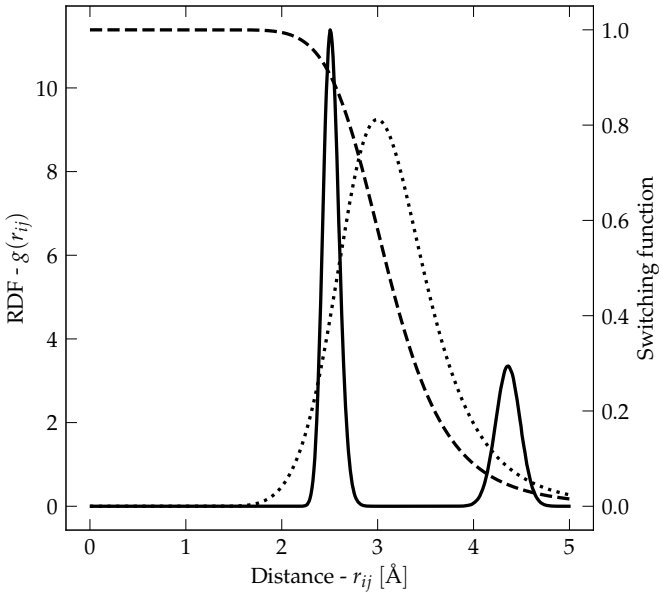

Figure VI.3: The Na^+-Cl^- RDF (full) of the B1 phase at $p = 20\,\mathrm{GPa}$ and $T = 300\,\mathrm{K}$, shown together with the switching function employed (dashed) and the absolute value of its derivative (dotted). Note the overlap of the derivative with the 1st and 2nd coordination spheres. The parameters of the switching function are $d_0 = 1.3\,\text{Å}$ and $r_0 = 2.1\,\text{Å}$.

In our work [57], we compared the two simulations (a) using the CN as the only CV and (b) using the CN and V as both CVs. We used the following results to advocate that the use of CN and V as the both CVs is inevitable.

At first, we run a metadynamics simulation which uses CN as the only CV. The parameters of the switching function were set to $d_0 = 1.3\,\text{Å}$ and $r_0 = 2.1\,\text{Å}$, the Gaussian height was set to $0.41\,\mathrm{meV/atom}$, the Gaussian width was set to 0.02 along CN, and the Gaussians were deposited every 1000 MD steps ($2\,\mathrm{ps}$), see Figs. VI.4 and VI.5.

Secondly, we run a metadynamics simulation which uses both CN and Volume as CVs. The parameters of the switching function were set to $d_0 = 1.3\,\text{Å}$ and $r_0 = 2.1\,\text{Å}$, the Gaussian height was set to $0.41\,\mathrm{meV/atom}$, the Gaussian width was set to 0.03 along CN and 0.03^3 along V, and the Gaussians were deposited every 1000 MD steps ($2\,\mathrm{ps}$), see Figs. VI.6 and VI.7.

It is clear that in both versions, both forward and reverse transitions can be seen, see Figs. VI.4 to VI.7. However, the character of the CN evolution in the two cases is different. When only the CN is used as CV, even after the 1st forward and reverse transitions, the system continues to

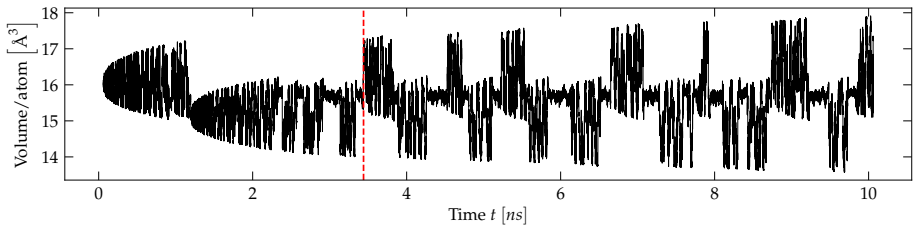

Figure VI.4: Time evolution of V in the MetaD simulation using CN as the only CV. The red dashed line denotes the time when both the B1 and B2 basins were filled.

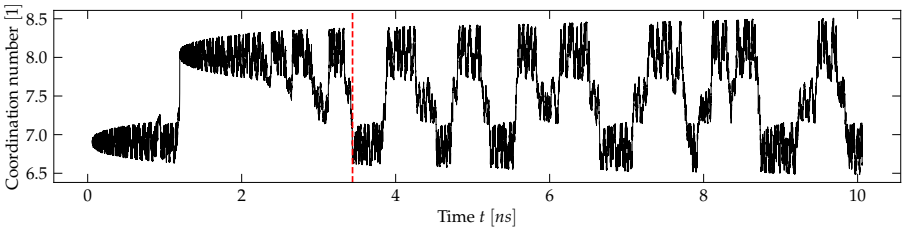

Figure VI.5: Time evolution of CN in the MetaD simulation using CN as the only CV. The red dashed line denotes the time when both the B1 and B2 basin were filled.

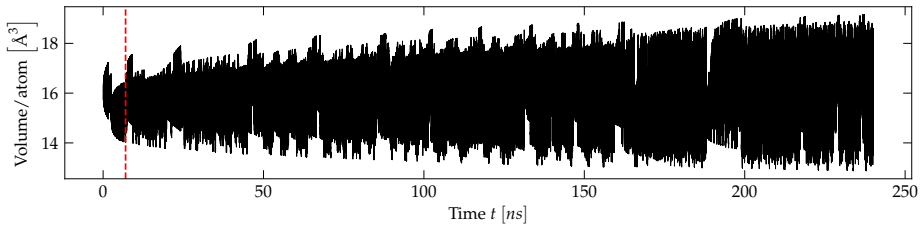

Figure VI.6: Time evolution of V in the MetaD simulation using CN & V as CVs. The red dashed line denotes the time when both the B1 and B2 basin were filled.

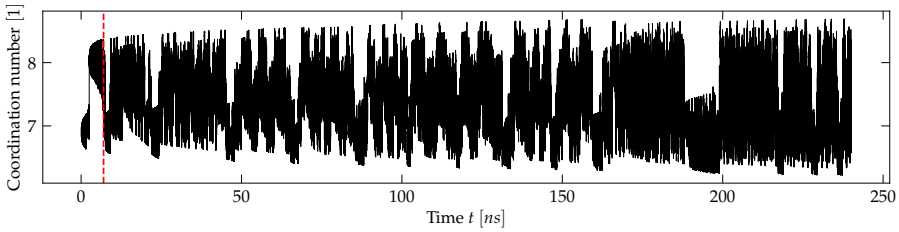

Figure VI.7: Time evolution of CN in the MetaD simulation using CN & V as CVs. The red dashed line denotes the time when both the B1 and B2 basin were filled.

jump between the two phases indicating that the CN does not have full control over the system. On the other hand, when V is added, the evolution of CN & V after the 1st transitions becomes much more diffusive, see also Ch. X for a quantitative evaluation of this phenomenon.

We concluded [57] that CN & V thus represent a good choice of CVs. We also provided an underlying physical explanation, why we believe the CN & V to be a good set of CVs. Physically, the addition of volume as a CV helps to disentangle changes induced by the "breathing" mode of the crystal (isotropic fluctuations of volume) from those representing structural changes.

However, since the switching function parameters are constant (not scaled with volume), the coupling between CN and volume manifests itself in the slope and shape of valleys of the B1 and B2 basins which are rather long and narrow, see the reconstructed FES in Fig. VI.8.

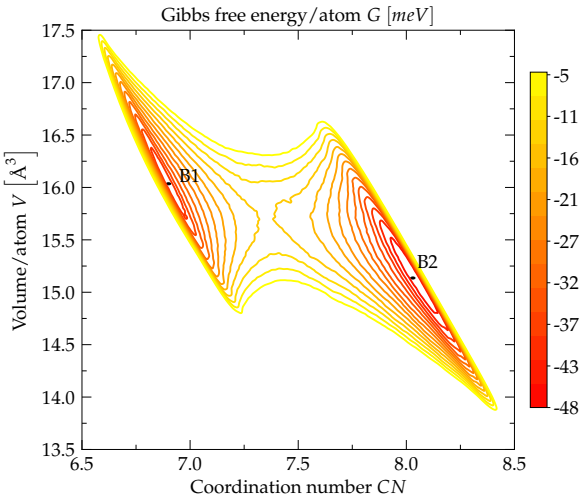

Figure VI.8: Reconstructed FES from 100 ns MetaD simulation of a 512 atoms system, using CN & V as CVs, at $T = 300\,\mathrm{K}$ and $p = 20\,\mathrm{GPa}$. Gaussians of height $0.41\,\mathrm{meV/atom}$ and width of 0.02 along the CN and $0.02\,^3$ along the volume CV respectively, were used. The positions of the B1 and B2 phases are denoted.

Further, to improve the sampling of such shaped FES, we introduced a rotation of CVs [57] with origin at the equilibrium point $[\overline{\mathrm{CN}}_{\mathrm{B1}}, \overline{V}_{\mathrm{B1}}](p,T)$ of B1. Deposited Gaussians thus respect the shape of the valleys - being wide in the direction along the prolongated shape of valleys (which we call *soft*) and narrow in the perpendicular one (which we call *hard*). We first rescaled CN & V with respect to B1,

$$\begin{aligned} \delta_V &\equiv (V - \overline{V}_{\mathrm{B1}})/\overline{V}_{\mathrm{B1}} \\ \delta_{\mathrm{CN}} &\equiv (\mathrm{CN} - \overline{\mathrm{CN}}_{\mathrm{B1}})/\overline{\mathrm{CN}}_{\mathrm{B1}}\,, \end{aligned} \tag{VI.3}$$

and then rotate the rescaled coordinates $[\delta_{\mathrm{CN}}, \delta_{\mathrm{V}}]$ by an orthogonal transformation (similar to Ref. [246]), whose components are unit-length eigenvectors of the covariance matrix of the rescaled coordinates.

$$\begin{aligned} \delta_{\mathrm{soft}} &\equiv \mathrm{e}_{\mathrm{soft},V}\delta_V + \mathrm{e}_{\mathrm{soft},CN}\delta_{\mathrm{CN}} \\ \delta_{\mathrm{hard}} &\equiv \mathrm{e}_{\mathrm{hard},V}\delta_V + \mathrm{e}_{\mathrm{hard},CN}\delta_{\mathrm{CN}}\,. \end{aligned} \tag{VI.4}$$

The covariance matrix is obtained from a short 200 ps unbiased NPT MD simulation at given pressure p and temperature T in the B1 phase [57]. Values of $\overline{\mathrm{CN}}$, $\overline{V}$ and $\mathrm{e}_{\alpha,i}$ are provided in Tab. VI.2. Such rotated Gaussians respect the shape of the narrow and long valleys of the B1 and the B2 phase, thus reducing the possibility of overfilling by inappropriately rotated/or wide Gaussians in the original coordinates.

We noted [57] that this construction is completely general, and the only *a priori* information it requires is the information about the CV fluctuations around the starting phase/structure. We would like to stress that it does not make any assumption about the transition pathway in the CV space, the structural transition mechanism in the real space (being local, collective,

p [GPa]	T [K]	$\overline{CN}_{\mathrm{B1}}$	$\overline{V}_{\mathrm{B1}}$	$\mathbf{e}_{\mathrm{soft,V}}$	$\mathbf{e}_{\mathrm{soft,CN}}$	$\mathbf{e}_{\mathrm{hard,V}}$	$\mathbf{e}_{\mathrm{hard,CN}}$
15	300	6.72	16.84	-0.87	0.49	0.49	0.87
20	300	6.92	15.97	-0.87	0.50	0.50	0.87
25	300	7.10	15.28	-0.86	0.51	0.51	0.86
30	300	7.26	14.70	-0.86	0.52	0.52	0.86
35	300	7.41	14.21	-0.85	0.53	0.53	0.85
40	300	7.55	13.79	-0.84	0.55	0.55	0.84
45	300	7.69	13.42	-0.83	0.55	0.55	0.83
50	300	7.82	13.11	-0.82	0.57	0.57	0.82
55	300	7.95	12.79	-0.81	0.59	0.59	0.81

Table VI.2: $\overline{CN}_{\mathrm{B1}}$, $\overline{V}_{\mathrm{B1}}$ and the eigenvectors of the covariance matrix of their fluctuations.

r_0 [Å]	0.9	1.3	1.7	2.1	2.5	2.9	3.3	3.7
d_0 [Å]	2.43	2.06	1.68	1.3	0.92	0.54	0.16	-0.21
Maximum $\left[^{-1}\right]$	1.71	1.19	0.91	0.73	0.62	0.53	0.47	0.42

Table VI.3: Maxima of absolute values of switching functions derivatives.

nucleation, etc.) or the transition state in the CV or the real space. Importantly, it does not make any assumption about the final state and thus can also be used in the search for new crystalline phases accessible via the lowest Gibbs free energy barrier from the parent phase. Exploration of the Gibbs free energy profile thus can be employed for crystal structure prediction, e.g. to search for phases that are metastable or stabilised by entropy (unreachable by standard $T = 0$ crystal structure prediction methods).

VI.4 Details of construction of switching function

For the metadynamics simulation which uses CN as the only CV ($N = 512$, $p = 20\,\mathrm{GPa}$ and $T = 300\,\mathrm{K}$), we demonstrated [57] that the proper choice of parameters for the switching function (d_0 & r_0) is important to avoid artefacts in the estimate of the free energy barrier.

The purpose of the switching function is twofold. First, it distinguishes by its value the coordination of the B1 phase (6), B2 phase (8) and the transition state between the two. The sharpest distinction of coordination will be achieved if the switching function is a step function with the centre in the middle between the 1st and 2nd coordination shells (see Fig. VI.9). Second, the switching function also has to induce force on atoms in the 1st and 2nd coordination shells during metadynamics simulation. This requires a sufficiently large slope of the switching function at the positions of the 1st and 2nd shells. Clearly, both requirements cannot be fulfilled at the same time so we have to choose a compromise.

In the left part of Fig. VI.9, we show different switching functions (for their parameters see Tab. VI.3), which are equally centred, but differ in softness. If the switching function becomes too soft (the lower four dashed lines in the right part of the Fig. VI.9), the first requirement breaks and CN starts to fail to distinguish the phases (the labelling of CN becomes "degenerate"). On the contrary, if the switching function is too sharp, the basin of B1 in the FES becomes very narrow requiring the use of Gaussians with tiny width w [57].

In the right part of Fig. VI.9, we show different switching functions (for their parameters

r_0 [Å]	2.1	2.1	2.1	2.1	2.1	2.1
d_0 [Å]	0.9	1.1	1.3	1.5	1.7	1.9
Maximum [Å]	2.885	3.085	3.285	3.485	3.685	3.885

Table VI.4: Positions of maxima of the absolute values of the switching functions derivatives.

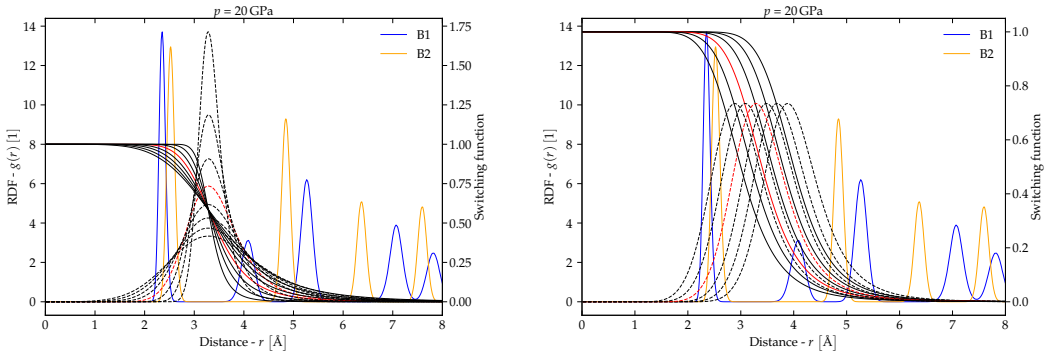

Figure VI.9: (Left) RDF of the B1 and the B2 phase at $p = 20\,\mathrm{GPa}$ and different switching functions (solid) equally centred but having different maximal slopes of their derivatives ("softness"). Curves of the absolute values of the switching function derivatives are denoted by dashed lines. For the parameters of switching functions see Tab. VI.3. (Right) RDF of the B1 and the B2 phase at $p = 20\,\mathrm{GPa}$ and different switching functions (solid) having the same maximal slope ("softness") but centred at different positions. Curves of the absolute value of the switching function first derivative are denoted by dashed lines. For the parameters of the switching functions see Tab. VI.4.

see Tab. VI.4), whose first derivatives reach the same maximal value $\left(0.73\,\text{Å}^{-1}\right)$, but are centred at different positions. Similarly to softness, a wrong choice of the centre can result in problems with metadynamics sampling [57].

In Fig. VI.10 we show that for both parameters d_0 and r_0, there exists a plateau of the reconstructed free energy barrier which corresponds to the proper reconstruction of the free energy [57].

VI.5 Simulation details

MetaD simulations were carried out using LAMMPS [247, 248] and PLUMED [249, 250]. Integration time step was set to $2\,\mathrm{fs}$. Nosé-Hoover barostats and thermostats of chain length 3 with MTK correction terms [220] were used. The relaxation times of the barostat and thermostat were set to $0.5\,\mathrm{ps}$ and $0.25\,\mathrm{ps}$, respectively. The cutoff for long-range interaction was set to $8\,\text{Å}$. Coulomb interactions were evaluated using the Ewald or PPPM method (depending on system size) with relative precision 10^{-5}. All input configurations were thermalised at the given temperature and pressure in 200 ps long unbiased MD runs.

In simulations for all system sizes and pressures which were used for the determination of barrier height (Fig. VI.11), the scaled and rotated version of CVs given by the Eq. (VI.4) was used. The parameters of Gaussian height can be found in Tab. VI.5, Gaussian width was in all simulation $15 \cdot 10^{-4}$ in the soft direction and 10^{-4} in the hard direction. The Gaussian deposit rate was set in all simulations to 2 ps.

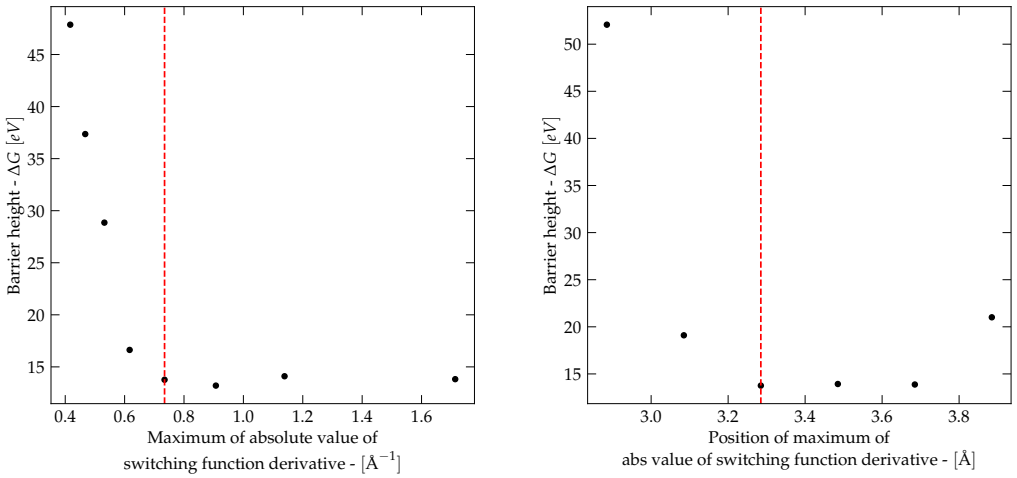

Figure VI.10: Dependence of the reconstructed barriers after the 1st transition (B1 → B2) on the softness (left) and centering (right) of the switching function. The vertical red dashed line denotes the parameter of the switching function employed in our calculations. See Tabs. VI.3 and VI.4 for the parameters of the switching functions and Fig. VI.9 for their visualisation. The final choice of the switching function is denoted together with its absolute value of its derivative in red. Parameters of Gaussians were not changed during these experiments (Gaussian height - $0.41\,\mathrm{meV/atom}$, widths of 0.02 along the CN and 0.02^3 along the volume directions, respectively).

p [GPa]	T [K]	System size N	Gaussian height [meV]
30	300	512	52
30	300	4 096	310
30	300	13 824	520
40	300	512	26
40	300	4 096	210
40	300	13 824	310
40	300	32 768	520
40	300	64 000	620

Table VI.5: Metadynamics parameters in all presented simulations. Gaussian heights are presented *per system* not *per atom*.

VI.6 Homogeneous nucleation

In this subsection, we review our findings on the case of homogeneous nucleation presented in our work [57]. In Fig. VI.11 we show the evolution of the transition barrier as a function of system size for two values of pressure. The barrier height was determined from Gaussians accumulated in metadynamics up to the 1st transition. For $p = 30\,\mathrm{GPa}$ the curve appears to grow in a nearly linear manner up to $N = 13\,824$ indicating that even at this moderate overpressurisation very large system sizes are necessary to properly accommodate the large critical nucleus. For systems smaller than $4\,096$ atoms, the barrier per atom well agrees with the estimate based on the static Buerger's mechanism, see Fig. VI.2, showing that the transition proceeds via a collective mechanism. The barrier height in the thermodynamic limit must be larger than $100\,\mathrm{eV}$, revealing that homogeneous nucleation in such a regime is physically impossible [57]. At the higher pressure of $40\,\mathrm{GPa}$ the curve appears to eventually converge to a value above $90\,\mathrm{eV}$, still too high for a physical transition [57].

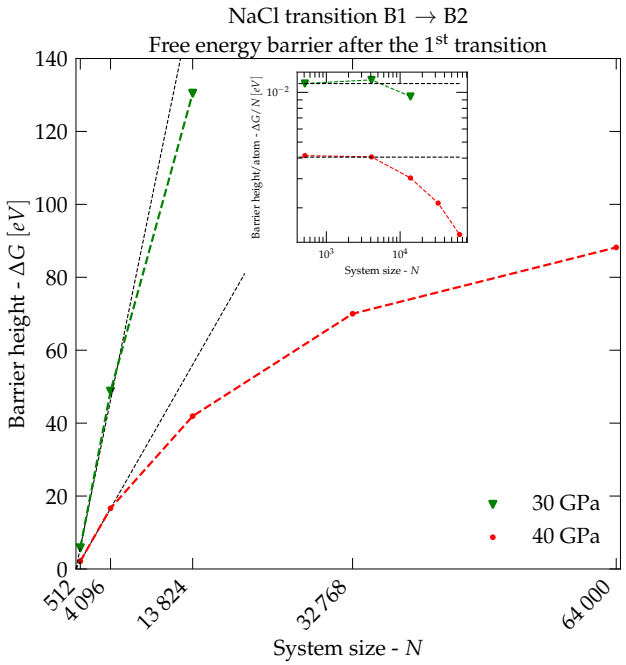

Figure VI.11: Barrier heights (from the B1 phase) for various system sizes at $T = 300\,\mathrm{K}$ & $p = 30\,\&40\,\mathrm{GPa}$. Straight dotted lines represent the values of the barrier from Buerger's collective mechanism. The inset shows the barrier height divided by the system size - $\Delta G/N$ vs the system size N on a log-log plot, highlighting the deviations from the linear scaling characteristic of the collective regime. For larger systems, transformation via nucleation and growth proceeds via lower barrier than for the collective mechanism.

Since experimentally the transition at 300 K occurs at $p = 26.6\,\mathrm{GPa}$ [185], it must be assisted by extrinsic factors such as lattice defects [3, 30, 32, 47, 146], dislocations [48–55], grain boundaries [39], surfaces [3, 30, 32] or non-hydrostatic pressure [251, 252]. This observation is similar to the one found for nucleation of melting [54], crystallisation of ice [253] and transformation of graphite to diamond [146]. The slow convergence of the barriers can be explained by the presence of long-range ($\sim 1/r^3$) elastic strain fields [3, 28–32].

Note that in section Section VI.7 we provide yet unpublished results on the case of nucleation on grain boundaries, which significantly lower the barriers.

We noted [57] that the elastic energy of the nucleus and surrounding lattice [3, 30–32] is taken into account in non-classical nucleation theory [31, 34, 58, 74, 90–95, 105–109] but is missing in standard static approaches [182, 183, 186–189, 192–194] which assume a strictly collective character of the transformation with no interface between the parent and the new phase.

VI.6.1 Crossover of local transformation mechanism

Further, in our work [57] we demonstrated the crossover of local transformation mechanism with respect to system size indicating that the presence of interface between the parent and the emerging phase can change the relative energetic cost of the mechanism. We present our results also here.

As stated in our work [57], the local transformation mechanism of a selected atom A in the simulation cell can be easily quantified by the angle $\sphericalangle$BAC where B,C are two atoms

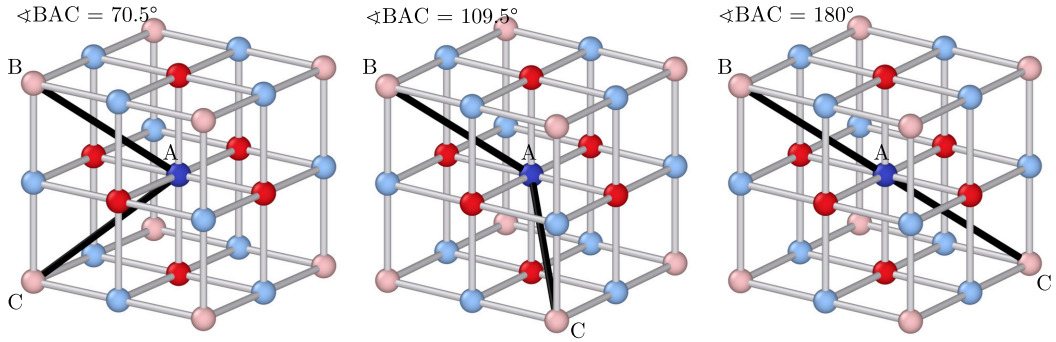

Figure VI.12: Three possibilities for the relative angle ◁BAC of two atoms (B and C) and the central atom (A). Central atom (A) (dark blue), its 1st coordination shell (dark red) and 2nd coordination shell (light red) including ions of the same charge as the central one in the 2nd coordination shell (light blue) in the B1 phase.

entering from the 2nd into the 1st coordination shell. There are only three possibilities for this angle, see Fig. VI.12. The value $\sphericalangle\mathrm{BAC} = 70.5°$ corresponds to WTM-like mechanisms and $\sphericalangle\mathrm{BAC} = 180°$ to Buerger's-like mechanisms. There is also a third possibility for the angle $\sphericalangle\mathrm{BAC} = 109.5°$; however, we have observed this mechanism only in the simulation of $p = 30\,\mathrm{GPa}$ and system size of $N = 13\,824$ atoms, and only in a locally distorted B2 structures in the atoms lying at the twin boundary between three domains.

In Figs. VI.13 and VI.14 we provide the histograms of this angle from simulations of various system sizes and pressures. For the histograms, we considered only perfectly eight-coordinated atoms in the resulting B2 phase and identified which two out of eight atoms entered from the 2nd coordination shell of the B1 phase. Atoms having coordination smaller or larger than 8 in the B2 phase (defects) were not considered, as well as the (typically few) atoms (also defects) towards which the two extra atoms did not come from the 2nd but from the 3rd coordination shell. The histograms reveal that in the simulations at $p = 40\,\mathrm{GPa}$, the crossover between the Buerger's-like and the WTM-like mechanisms occurs at the system size of 4 096 atoms. The situation is similar at $p = 30\,\mathrm{GPa}$, where the crossover at the system size of 4 096 atoms is sharper in favour to the WTM-like mechanism. We note that at $p = 30\,\mathrm{GPa}$ and $N = 13\,824$, few atoms are found to proceed via the mechanism with angle $\sphericalangle\mathrm{BAC} = 109.5°$.

Furthermore, in order to distinguish the original Buerger's and WTM mechanisms from their modified versions (Buerger's → modified Buerger's (Stokes & Hatch), WTM → Toledáno mechanism) proceeding through 7-coordinated structures, one can take into account whether the two additional atoms enter the 1st shell at the same time or at distinct times. The difference between those mechanisms can be easily demonstrated by plotting distances to ions of opposite charge from the 1st and the 2st coordination shell of the selected atom. In Figs. VI.15 and VI.16 we provide diagrams of those distances to ions in the 1st and 2st coordination shells of selected atoms transforming via WTM-like or Buerger's-like mechanisms. While we observe these local mechanisms (proceeding via 7-coordinated structures) in all system sizes and both pressures considered ($p = 30$ and $40\,\mathrm{GPa}$), they resemble the B33 structure only in systems smaller than 4 096 atoms.

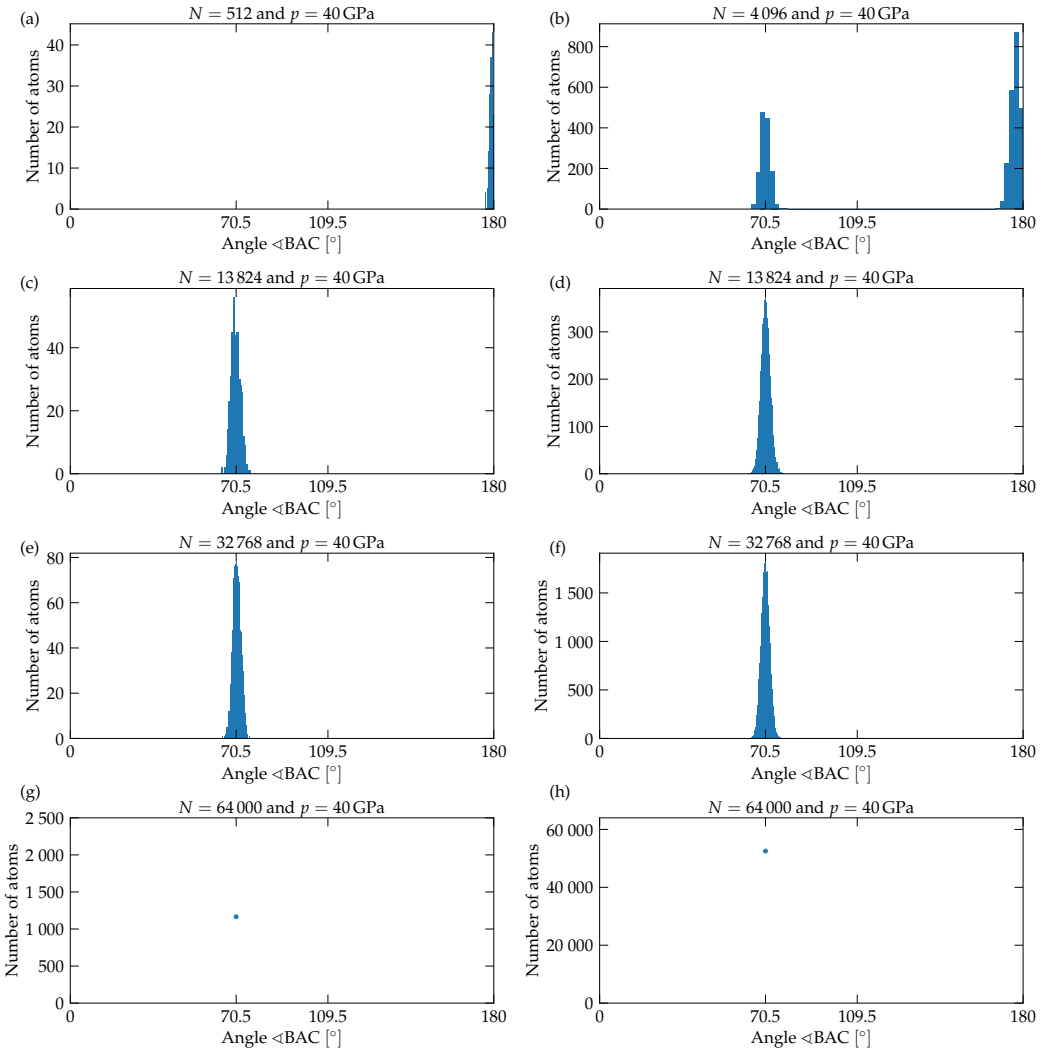

Figure VI.13: Histograms of the relative observed angle - $\sphericalangle\mathrm{BAC}$ measured from simulations at $p = 40\,\mathrm{GPa}$. (a) In the smallest system all atoms in the bulk proceed via the Buerger's-like mechanism. (b) In simulation of $N = 4\,096$ a significant part of the system locally proceed via the WTM-like mechanism. (c) The WTM-like mechanism in system of $N = 13\,824$, atoms creating the critical nucleus. (d) The WTM-like mechanism in the system of $N = 13\,824$, all atoms after the whole system proceed into the B2 phase. (e) The WTM-like mechanism in the system of $N = 32\,768$, only the atoms creating the critical nucleus. (f) The WTM-like mechanism in the system of $N = 32\,768$, after the whole system proceeds into the B2 phase. (g) The WTM-like mechanism in the system of $N = 64\,000$, only the atoms creating the critical nucleus. The distribution is so sharp that, within the accuracy to one digit after the decimal point, it makes all data lie on a single point. (h) The WTM-like mechanism in the system of $N = 64\,000$, all atoms in the system are considered. The distribution is so sharp that, within the accuracy to one digit after the decimal point, it makes all data lie on a single point.

VI.6.2 Shape and size of critical nuclei

For the identification of the *critical frame*, we performed [57] a binary search in the trajectory for the first frame, from which the system proceeds into the B2 phase in an unbiased MD simulation. By *critical nucleus/nuclei* we refer to the nucleus/nuclei in the *critical frame*, if nucleation is observed. Nuclei in the critical frame were identified as follows [57]. First, we identified all atoms in the frame with coordination larger than 6.5. Second, we identified all connected components and removed those which consisted of less than 5 atoms, thus removing isolated fluctuations of coordination in the neighbourhood of large nuclei induced by elastic

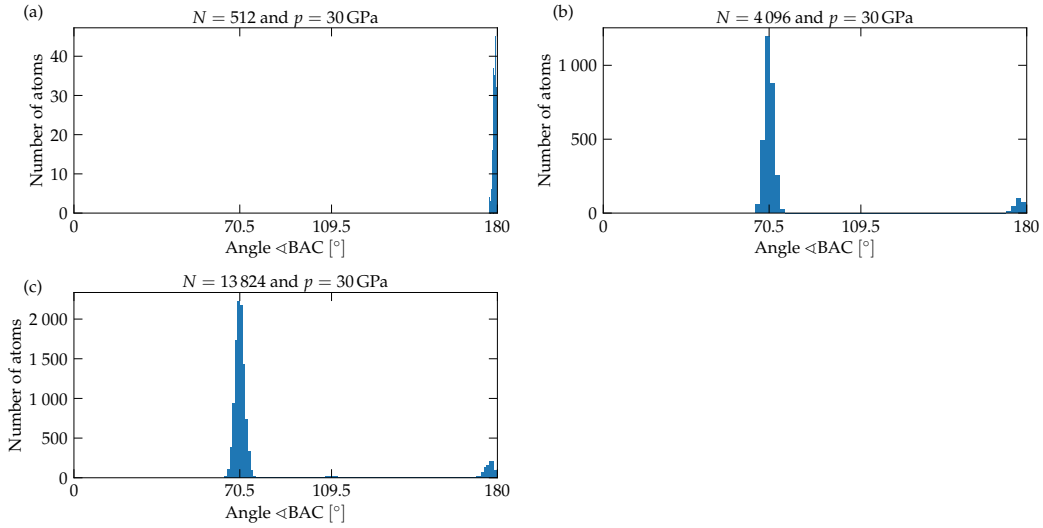

Figure VI.14: Histograms of the relative observed angle - $\sphericalangle\mathrm{BAC}$ measured from simulations at $p = 30\,\mathrm{GPa}$. (a) In the smallest system all atoms in the bulk proceed via the Buerger's-like mechanism. (b) In the simulation of $N = 4\,096$ a majority of the system locally proceeds via the WTM-like mechanism. (c) In the simulation of $N = 13\,824$ atoms locally proceed via the WTM-like mechanism with the minority of the atoms proceeding via Buerger's-like mechanism and the third possible mechanism of $\sphericalangle\mathrm{BAC} = 109.5°$.

deformation of the surrounding lattice. Next, we identified centroids of nuclei and calculated the inertia tensors with respect to them. By the diagonalisation of the inertia tensors, we found the corresponding semi-axes in the case of ellipsoids and the semi-axes of the cylinder base and its length in the case of cylinders.

For systems of sizes $\leq 4\,096$ atoms, it does not make sense to define *critical nuclei* since no nucleation is observed. For systems of sizes $> 4\,096$ atoms, for $p = 30 \text{ and } 40\,\mathrm{GPa}$ we summarise below the observed size and shape of the nuclei.

At $p = 40\,\mathrm{GPa}$, for $N = 13\,824$ we observed in the critical frame two ellipsoids with 427 and 549 atoms. Their semiaxes were $14.1\,\text{Å}$, $11.7\,\text{Å}$ & $10.7\,\text{Å}$ and $14.8\,\text{Å}$, $11.7\,\text{Å}$ & $12.5\,\text{Å}$. For $N = 32868$ we observed two ellipsoids and one thin cylinder. Their sizes were 1571, 95 & 129 atoms, respectively. The semiaxes of the ellipsoids were $18.1\,\text{Å}$, $20.2\,\text{Å}$ & $15.8\,\text{Å}$ and $7.2\,\text{Å}$, $14.5\,\text{Å}$ & $13.3\,\text{Å}$. The cylinder had length of $69.3\,\text{Å}$. At $N = 64000$, the critical frame consisted of a single cylinder with 2442 atoms, length of $92.7\,\text{Å}$ and the semi-axes of $11.0\,\text{Å}$ and $11.6\,\text{Å}$.

At $p = 30\,\mathrm{GPa}$, for $N = 13824$ we also observed in the critical frame two ellipsoids, with 392 and 411 atoms. Their semiaxes were $11.2\,\text{Å}$, $10.7\,\text{Å}$ & $13.5\,\text{Å}$ and $12.1\,\text{Å}$, $10.4\,\text{Å}$ & $13.7\,\text{Å}$, respectively.

VI.7 Nucleation on grain boundaries

In this section we briefly state our unpublished results on the nucleation on grain boundaries for the B1-B2 transition in NaCl. First, we briefly describe the procedure for creating samples involving grains and second, we briefly summarize our results.

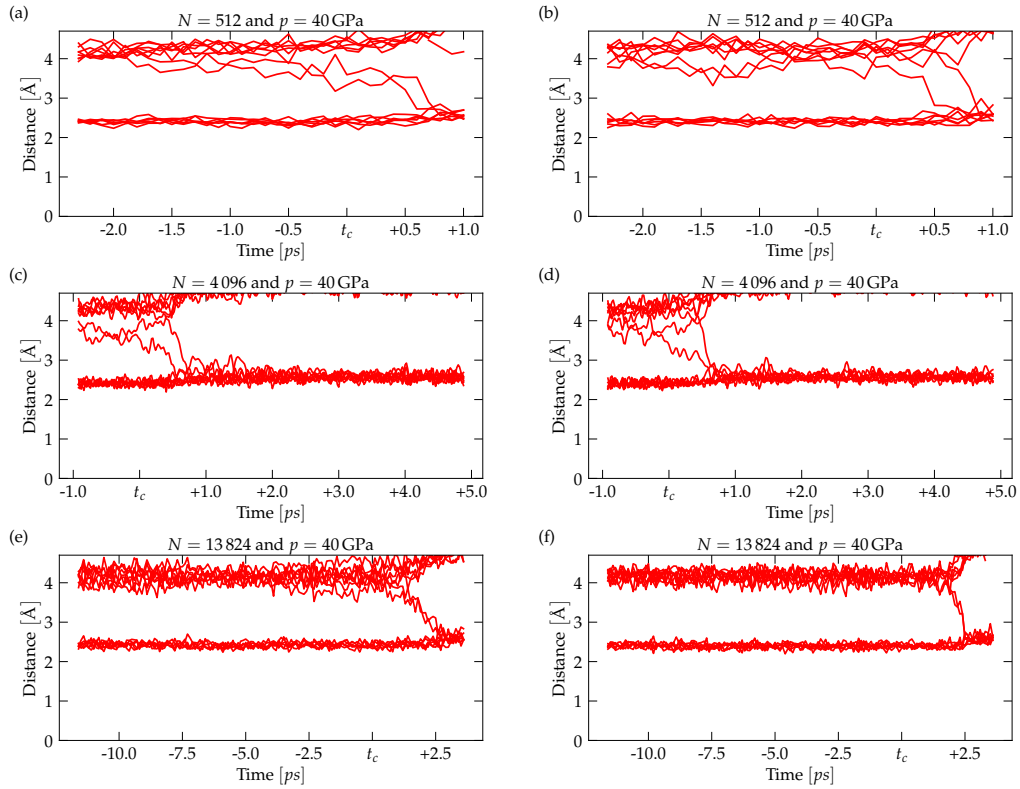

Figure VI.15: Distances to nearest neighbors (NN) and next nearest neighbors (NNN) of selected typical atoms in simulations with given system size and pressure. (a-b) Simulation for $N = 512$. Atoms from two different layers show that the transition mechanism is not layer-dependent and in both cases the two extra atoms from the 2$^{\text{nd}}$ shell enter the 1$^{\text{st}}$ shell with the time difference of 0.2 - 0.5 ps. (c-d) Simulation for $N = 4\,096$ atoms. Atoms from different layers (B2 (c) and B33-like (d), the time difference here is around 0.2 - 0.5 ps. (e-f) Simulation for $N = 13\,824$ atoms. (e) - an atom near the critical nucleus. (f) - an atom far from the critical nucleus. One can see that in the final phase of the formation of the B2 phase, the original WTM mechanism is preferred to its modified version (Toledáno).

VI.7.1 Creation of samples

First, we use Atomsk software [254] to create samples close to 0 GPa at 0 K. We first fix the side of the supercell e.g., to 110 Å and the lattice spacing of the NaCl unit cell, e.g., to 5.4 Å and then call the Atomsk to fill the supercell with the grains of the respective lattice spacing fixing the number of the grains (the number is also provided to the Atomsk software). The Atomsk then creates a supercell containing randomly orientated grains which fill the supercell using the Voronoi tesselation. Repeating the procedure once again for the same parameters (size of the supercells, lattice spacing and the number of grains) yields to a different sample as long as the random number generator is involved in the creation of positions of the centres of the respective grains.

Since the filling of the Voronoi cells is random procedure it is possible that the total number of the Na^+ ions does not equal the total number of Cl^- ions leading to overall charge imbalance. Also, it is possible that some atom pairs, in particular at the grain boundaries, are too close to each other. The latter can create an instability in terms of the force field, see Eq. (VI.1), where if the atoms are too close to each other, they can overcome the maximum of the short-range Pauli repulsion term and an unphysical attractive force acts on them. To ensure this does not happen, we remove all atom pairs that are closer than 1.75 Å. Note that this number was chosen arbitrarily ensuring that is larger than the maximum in the force acting on a pair of ions for

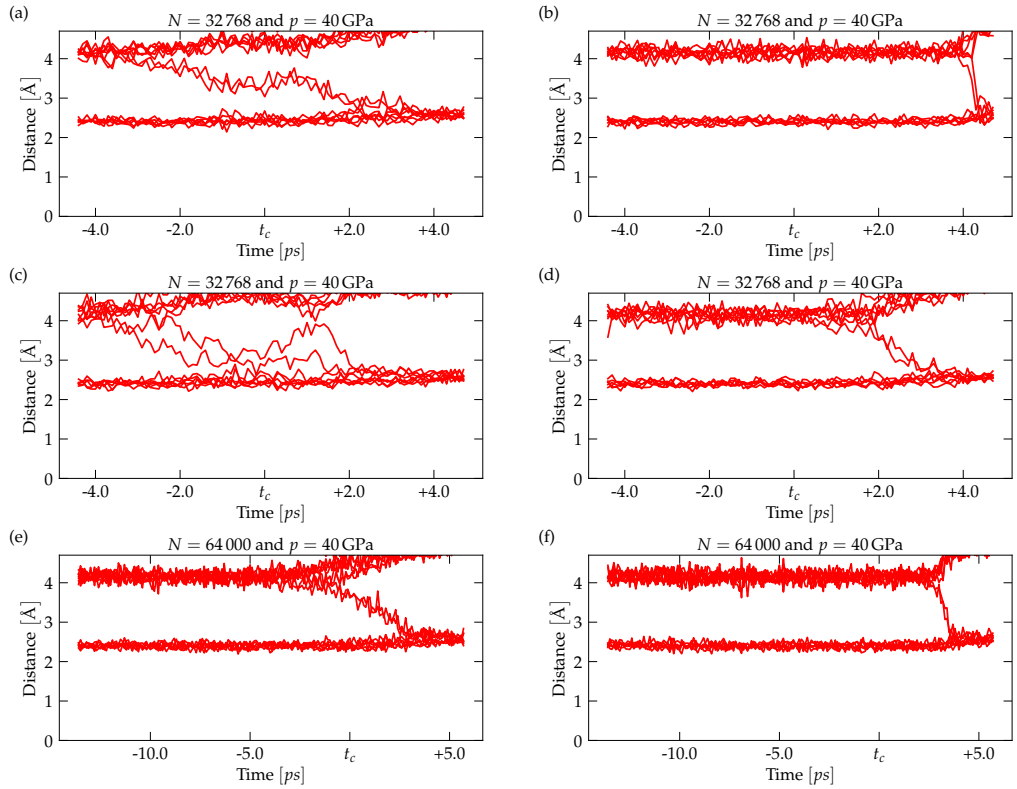

Figure VI.16: Distances to NN and NNN of selected typical atoms in simulations with given system size and pressure. (a-d) Simulation for $N = 32\,768$ atoms. (a-b) - atoms near the first (critical) nuclei. (c) An atom from the secondary nucleus. (d) An atom far from the nuclei. Note that in all cases the conclusion is the same as in smaller systems; there is clear time distinction of 0.2 - 0.5 ps in the subsequent increase of coordination of a given atom. (e-f) Simulation for $N = 64\,000$ atoms. (e) - an atom near the critical nucleus (cylinder), (f) - an atom far from the critical nucleus.

every type of the three possible interactions. Also note that, in reality, we do not know how close the atoms can actually be on the grain boundaries.

Summarizing all the steps so far, it is almost certain that charge imbalance is present in the system. To ensure the charge neutrality of the supercell, we further remove either randomly selected Na^+ or Cl^- ions, depending on which number of them is bigger in order to equalize their numbers.

Lastly, we thermalize the sample. We heat the sample from 0 K to 1 000 K in 20 ps run, then we thermalize/anneal it at 1 000 K and 0 GPa for 100 ps, and subsequentially compress it from 0 GPa to the pressure of interest while cooling it from 1 000 K to 300 K at the same time in 20 ps run.

VI.7.2 Results

We decided to work at three pressures of interests - 30 GPa, 35 GPa and 40 GPa, all at temperature of 300 K. The simulation cells varied from around 64k to 256k atoms. At 30 GPa the simulation did not proceed in the given time window, indicating that the barrier is at least of an order 100 eV (estimated as a lower bound from the simulations of length 5 ns) thus still too high to be activated by the temperature (at 300 K).

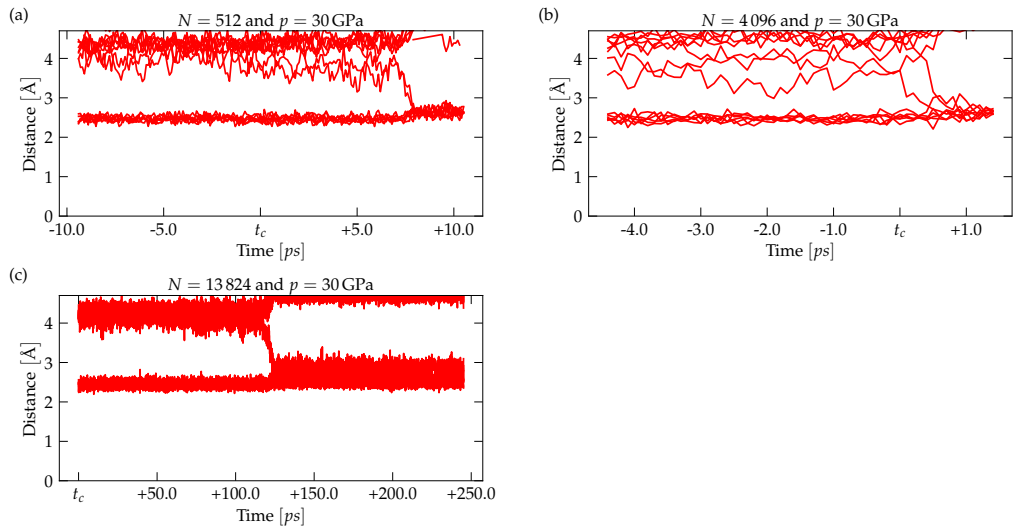

Figure VI.17: Distances to NN and NNN of selected typical atoms in simulations with given system size and pressure (a) Simulation for $N = 512$. The increase of coordination occurs in two steps with the time difference of 0.2 ps between two incoming ions from the 2nd coordination shell. (b) Simulation for $N = 4\,096$. The increase of coordination occurs in two steps with the time difference of 0.5 ps between two incoming ions from the 2nd coordination shell. (c) Simulation for $N = 13\,824$. The atom between two critical nuclei which merge into a single bulk B2 layer. Due to the creation of the bulk B2 layer extending across the PBC along two dimensions, the subsequent fall into the B2 basin on the FES in this simulation is much slower comparing to other simulations.

System size N	Number of grains	Barrier height [eV]
65 180	6	30.609
65 300	6	26.652
65 312	5	33.015
65 378	5	17.754
65 470	4	4.973
65 494	4	23.108
65 494	3	26.284
65 588	2	18.415
65 652	3	7.519
66 030	2	116.218
121 496	5	31.462
121 624	5	30.427
121 834	2	7.174
121 992	3	18.151
122 138	3	92.284
122 582	2	174.982

Table VI.6: Free energy barriers found for the simulation with several grain boundaries at 35 GPa and 300 K.

.

At the 35 GPa the barrier height varied from around 5 eV found for simulation of size of 64k atoms and 4 grains up to 174 eV for simulation of size of 122k atoms and two grains. A detailed statistics is provided in Tab. VI.6. At the 40 GPa the barrier height varied from as low as 0.075 eV for system size of 65k atoms and 6 grains up to 44.76 eV for system size of 267k atoms and 3 grains. A detailed statistics is provided in Tab. VI.7.

System size N	Number of grains	Barrier height [eV]
65 078	6	0.077
65 142	6	0.077
65 234	5	2.423
65 356	5	0.075
65 532	3	0.504
65 560	4	0.078
65 598	4	0.077
65 700	3	0.109
65 936	2	0.085
66 004	2	0.445
121 176	8	1.243
121 562	5	2.033
121 662	4	1.243
122 180	3	18.39
122 340	2	1.723
122 756	2	4.928
265 560	8	2.498
265 604	8	2.496
265 780	6	2.487
266 148	6	4.309
266 178	2	3.966
266 206	5	5.153
266 758	5	43.939
267 764	3	2.487
267 834	3	44.766
269 002	2	13.729

Table VI.7: Free energy barriers found for the simulation with several grain boundaries at 40 GPa and 300 K.

.

These numbers require some attention and also caution in terms of their interpretation. First, the surprisingly low values at 40 GPa were verified by running simulations with Gaussians of height of one half, one fourth and one eight of the initial height of used Gaussians. Here, the value of the barrier is so low than typically few tens of Gaussians can induce the transition. If the value of the barrier from the simulations with Gaussians of various heights differed, we provided the lowest value. Thus the value of the barriers at 40 GPa represents actually an upper estimate of the barrier. The second point which requires our attention is the height of these barriers. Actually, the barriers for the system size of 65k atoms at 40 GPa are so low, that the transition can also proceed in unbiased NPT dynamics, when one waits for sufficiently long time. We explicitly verified that the transitions can be observed in unbiased NPT dynamics in these structures with 65k atoms and all number of grains. The last point which requires the attention is the relative variance of these barriers between different simulations. It is plausible that this is caused by the interplay of (strong) periodic boundary conditions effects and the actual topology of the grain boundaries in the supercell (which generally differ from the one implied by Voronization due to annealing step and that can be implied by the elastic interaction of the boundaries itself). This indicates that these simulations should be rather viewed as the *proof of concept* as they probably do not involve realistic sizes of grains (too small or too many)

and one should run simulations of much larger system size.

These results show that while the grain boundaries significantly lower the pressure of the dynamical instability from 60 GPa to 40 GPa (at 300 K), and also significantly lower the barrier at 35 GPa, they still cannot explain the experimental observation of the transition at 26.6 GPa. Thus other defects, such as dislocations together with grain boundaries (or grain boundaries at even larger systems) are needed to explain this value.

VII The Graphite to Diamond transition in Carbon

This chapter summarises the unpublished results obtained for the graphite to diamond transition in carbon during the collaboration with prof. Stefano de Gironcoli and Dr. Yusuf Shaidu based on the use of their machine learning potential [197].

VII.1 Summary of previous studies

The synthesis of diamond from graphite can happen under the presence of catalysts or can be catalyst-free [6]. In our work, we focus purely on catalyst-free transformations of graphite into diamond, hence we will restrict only to the review of catalyst-free transformations. Diamond is metastable under ambient conditions and does not graphitise noticeably until near 1800 K in the absence of oxygen at zero pressure, while graphite is stable to 15–30 GPa at room temperature [6]. Thus, in a large portion of the carbon phase diagram both graphite, cubic and hexagonal diamond are (meta)stable, see Fig. VIII.1.

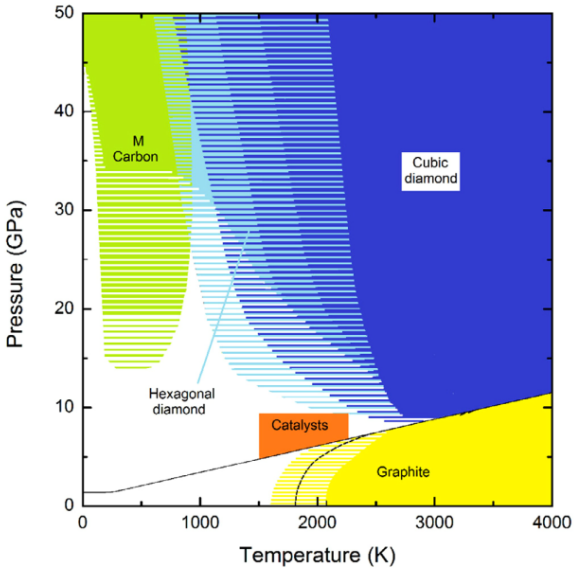

Figure VII.1: Phase diagram of carbon showing large portion of phase diagram (white area) where both graphite, cubic and hexagonal diamond are stable. Full line is the graphite–diamond equilibrium line, dashed curve approximate stability limit for diamond. Adapted from Ref. [6].

Direct conversion of graphite into cubic diamond was first reported from shock experiments at estimated pressures near 30 GPa [255]. Later, a synthesis at pressures between 12 and 18 GPa and temperatures probably above 3000 K was reported [256]. The direct synthesis have been repeated and verified by many groups [257–262]. It has been concluded [255, 259] that the conversion into diamond is preceded by a transformation of graphite from hexagonal (AB) to rhombohedral (ABC stacking), see Fig. VII.2 for visualisations of different stackings.

Experimental works also found that well-ordered graphite is more difficult to convert into diamond than strongly disordered carbon. To be more concrete, at 15 GPa the transition proceeds at 1400 K for strongly disordered material and more than 2100 K for well-ordered graphite [6]. It has to be also noted that hexagonal diamond is often found as reaction product [262–265] at temperatures below those yielding cubic diamond, while hexagonal and cubic diamonds can also be produced from graphite in shock experiments or explosions [6, 21, 266–269].

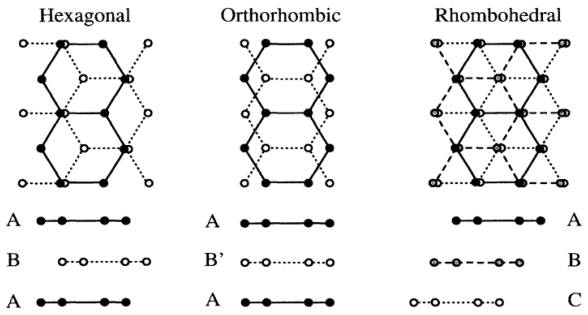

Figure VII.2: Different stackings of graphite. Adapted from Ref. [270].

For a recent review of experimental as well as theoretical works, the reader is referred to the work of Sundqvist [6]. Here, we put more attention into the recent side of theory, starting by work of Scandolo et al. [270].

Scandolo et al. [270] performed a constant-pressure ab initio molecular dynamics in supercells of 48 and 64 atoms starting from hexagonal graphite and found that the transformation path proceeds through sliding of graphite planes into the orthorhombic stacking, see Fig. VII.2, with subsequent buckling of the planes which leads to a comparable proportion of cubic and hexagonal diamond. The transition path found by Scandolo et al. was consistent with the mutual orientation observed in shock-wave experiments. The transition to diamond was observed to happen at 90 GPa at 1000 K.

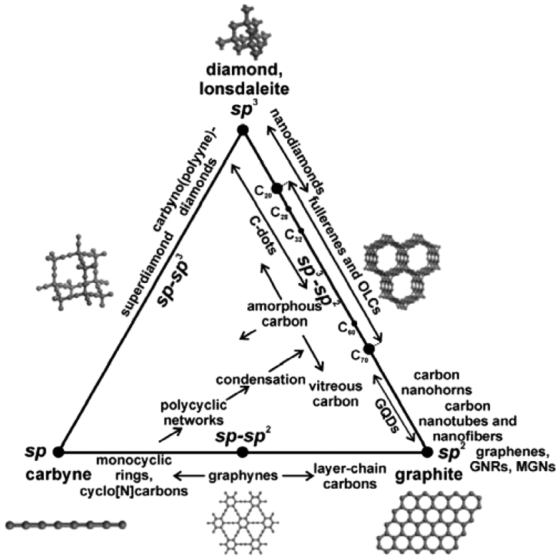

Figure VII.3: Hybridization states of carbon. Adapted from Ref. [6].

Tateyama et al. [271] investigated the activation barriers and the intermediate paths of the transformation to cubic diamond and hexagonal diamond from graphite under pressure using a

method of finding a saddle point of the potential surface automatically from constant-pressure ab-initio molecular dynamics. They found the barrier from graphite to cubic diamond to be ~ 70 meV/atom lower than that to hexagonal diamond. Thus they conclude that when the collective slide of graphite is allowed, the transformation to cubic diamond is preferred.

Zipoli et al. [175] performed metadynamics calculation based on coordination number and constant-pressure molecular dynamics using a tight-binding description supplemented by an empirical two-body van der Waals interaction. Calculations were performed with a supercell containing 128 atoms initially arranged in the ABAB (hexagonal) stacking. They observed the transition to proceed at 129 GPa at 1000K in unbiased simulation. The metadynamics calculation was performed at 15 GPa and 300 K where a mixed phase of cubic and hexagonal diamond in phase transition was observed, but contrary to Ref. [270] without orthorhombic transition state.

Mundy et al. [272] performed ab initio molecular dynamics of shock compression of graphite normal to basal planes. They found a novel short lived diamond intermediate phase formed within a fraction of picoseconds upon shock loading corresponding to longitudinal stress larger than 130 GPa followed by formation of cubic diamond. They observed the transition to proceed also without the orthorhombic transition state by buckling of graphitic planes, instead a layered diamond state, that was a mixture of hexagonal and cubic diamond, was observed.

Khaliullin et al. [146] studied direct nucleation of diamond from graphite using seeding approach inside a periodic - 100Åx 100Åx 100Åsupercell of 145 000 atoms using a machine learning potential based on Behler-Parrinello descriptors. Hexagonal and rhombohedral graphite lattices were used as initial structures for the formation of hexagonal and cubic diamond nuclei. They observed buckling of basal planes into the chair conformation in the rhombohedral graphite leading to cubic diamond and the boat buckling of the hexagonal graphite leading to hexagonal diamond. The enthalpy barrier for nucleation at the 20 GPa was found to be in order of 560 - 630 eV, and of order 125 eV for nucleation at 30 GPa. The results were verified using calculations for a 200 Å× 200Å× 200Åsimulation cell.

Wang et al. [273] presented a comprehensive study of the energetics and kinetics for the phase conversion of graphite under a wide pressure range of 5–25 GPa and found a new sp^3-orthorhombic Pnma structure employing a climbing image nudged elastic band method. However, at 15 GPa the lowest barrier was still that corresponding to the transition to cubic diamond.

Boulfelfel et al. [274] performed transition path sampling simulations to both cubic and hexagonal diamond from graphite, to find the barrier to be of order 0.2 eV/atom employing a density functional tight binding approach for force field description.

Xiao et al. [275] employed a generalized solid-state nudged elastic band method for study of reaction pathways between graphite and diamond using a simulation cell containing 40 atoms. They found the barrier from graphite to hexagonal diamond to be lower than to cubic diamond at 15 GPa. The corresponding barriers were found to be of order 0.15 eV/atom for transformation into cubic diamond and 0.1 eV/atom for transformation into hexagonal diamond.

Dong et al. [276] compared the transition paths from graphite to two types of diamond using the variable cell nudged elastic band method employing an ab-initio description of forces. At 10 GPa, they found the barrier to be of an order of 0.21 eV/atom favouring the transition to cubic diamond from hexagonal graphite.

Xie et al. [277] performed classical molecular dynamics transition with a local bond order potential (LCBOPII) for a study of a direct graphite to diamond transition. They found a new "wave-like buckling and slipping" mechanism, which controls the transformation from hexagonal graphite to cubic diamond.

Qiu et al. [278] found a barrier 2.42 eV/atom at 7 GPa using ab-initio calculations for transition between hexagonal graphite and cubic diamond.

Xie et al. [279] employed stochastic surface walking method and reported seven types of low energy intermediate structures at the atomic level for graphite to diamond transition. They showed that hexagonal diamond has an easier initial nucleation mechanism inside graphite matrix and faster propagation kinetics owing to the presence of three coherent graphite - hexagonal diamond interfaces and that the growth of cubic diamond is at least 40 times slower. As the force field descriptions they used the environment-dependent interatomic potential (EDIP). They found the barrier of an order of 0.75 - 0.9 eV/interface for graphite to cubic diamond transition at 15 GPa.

Kroonblawd and Goldman [280] predicted the formation of heterogeneous diamond structures from rapid uniaxial compression of graphite using ab-initio tight-binding molecular dynamics. However, without any conclusion on free energy barrier.

Signetti et al. [281] obtained Hugoniot curves of shock-compressed graphite (8–900 GPa) by MD simulations employing classical AIREBO-M potential.

Zhu et al. [79] performed molecular dynamics simulation using angular dependent potential of graphite-diamond transition under the presence of several grain boundaries (system size of 1 226 000 atoms) to observe that the major product was cubic diamond, with hexagonal diamond present at defects (grain boundaries of cubic diamond grains). The observed transition pressure was 40 GPa at 1500 K.

Luo et al. [282] performed molecular dynamics simulations using a local bond order potential (LCBOP) in supercell containing 192 000 atoms at 2000 K to find an intermediate orthorhombic graphite phase. Furthermore, they observed that quenchable orthorhombic and rhombohedra graphites are stabilised in buckled graphite at lower temperatures and these intermediate phases are further converted into hexagonal and cubic diamond at higher temperatures following favourable pathways in the order: graphite $\rightarrow$ orthorhombic graphite $\rightarrow$ hexagonal diamond, graphite $\rightarrow$ orthorhombic graphite $\rightarrow$ cubic diamond, and graphite $\rightarrow$ rhombohedral graphite $\rightarrow$ cubic diamond.

Wang et al. [283] recently created a Deep-MD potential for carbon, however the attention was focused on amorphous carbon and no information about energetics for graphite-diamond transition was provided.

Srinivasan2022 [284] created an automated framework that calculates a metastable phase diagram for carbon phases using quasiharmonic approximation employed on top of ab-initio calculations and machine learning techniques.

Qamar et al. [138] very recently (June 2023) published an ACE potential for carbon trained on ab-initio data described by PBE functional with additional additive vdW corrections (D2). The published ACE parametrisation comprises 488 basis functions containing terms up to the fifth body order leading to a comparable RMSE error on forces as PANNA potential [197], and also

leading to a comparable barrier height between the graphite to diamond transition as PANNA potential ($\sim$ 0.3 eV/atom).

VII.2 Model

The machine-learning potential of Shaidu et al. [197] is based on the radial and angular Behler-Parrinello descriptors of the following form, which yield together a set of 144 descriptors,

$$G_{\text{rad}} = \sum_{i \neq j} e^{-\eta(R_{ij}-R_s)^2} f_c(R_{ij}) \,, \tag{VII.1}$$

$$G_{\text{ang}} = 2^{-22} \sum_{i \neq j,k} (1 + \cos(\theta_{ijk} - \theta_s))^{23} e^{-\eta(R_{ij}/2+R_{ik}/2-R_s)^2} f_c(R_{ij}) f_c(R_{ik}) \,, \tag{VII.2}$$

where

$$f_c(R_{ij}) = \begin{cases} \frac{1}{2}\left[1 + \cos\left(\frac{\pi R_{ij}}{R_c}\right)\right], & R_{ij} \leq R_c \\ 0, & R_{ij} > R_c \,, \end{cases} \tag{VII.3}$$

and where R_{ij}, R_{ik} are the distances to neighbouring atoms, θ_{ijk} is the relative angle between the two neighbours and the central atom and R_s, R_c, θ_s and η are the free parameters, for their values see Ref. [197]. Upon the 144 descriptors a feed-forward neural network is placed with two hidden layers comprising 64 and 32 neurons, which uses a Gaussian activation function ($\exp(-x^2)$). The dataset used to train the network comprised a rich set of 60 000 structures in sp, sp^2 and sp^3 hybridizations [197]. The DFT energy and forces were calculated with the *modified Vydrov and Van Voorhis functional* (rVV10) [231] accounting for van der Waals interactions.

The model equilibrium transition pressure between the cubic diamond and the rhombohedral graphite is 10 GPa, see Fig. VII.4. The model instability pressure is 80 GPa at 1 000 K, as found in unbiased molecular dynamics by the subsequent increase of pressure at the rate 0.16 GPa/ps.

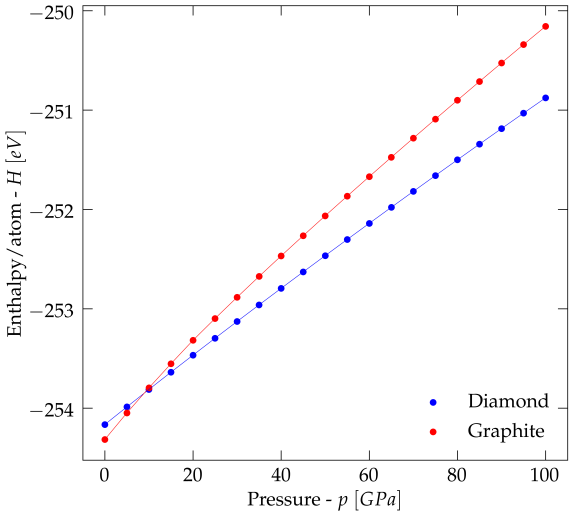

Figure VII.4: Enthalpy curve for the cubic diamond and the rhombohedral graphite as predicted by the machine learning potential of Shaidu et al. [197].

Since the dataset does not contain graphitic structures at negative pressures, we employed so-

called `upper walls` (on the volume at 7.75 $\text{Å}^3/\text{atom}$) and `lower walls` (on the coordination number, see later, at 1.25) constraints in PLUMED during the metadynamics calculations to prevent the system from exploring the part of the graphitic basin with the large volumes (negative pressures). This also speeded up the sampling of the graphitic phase and helped to decrease the timed needed to fill the initial (graphitic) free energy basin. The coefficient κ in the upper or lower walls ($1/2\kappa x^2$, where x stands for volume/atom or average coordination) were set in both cases to 1 000 eV.

We have also identified that the major computational bottleneck of the model presented above is the use of Gaussian activation function in the neural network and the exponential in the radial and angular descriptors. In collaboration with Dr. Yusuf Shaidu, we tried to replace the exponentials by polynomial kernels with finite support. However, even while this replacement provided a speed-up of the evaluation of forces by an order of magnitude, the final networks (models) deviated largely when compared to the original network presented in Ref. [197]. Namely, in terms of model's equilibrium transition pressure and model instability pressures at 1 000 K. Therefore, we stuck to the use of the original network presented in Ref. [197], even though this practically prohibited calculations of systems larger than 64 000 atoms, see Section VII.5.

VII.2.1 Verification of the model

We found that the transient structures between graphite and diamond in the system of 128 atoms lie in the extrapolating regime of the original dataset/network. Therefore, we performed the verification of the neural network and calculated the energy of the transient structures discovered by the metadynamics, see Section VII.3. The transient structures were calculated with the same parameters for DFT as the original dataset (the cutoff for kinetic energy and charge densitiy being 80 and 480 Ry, respectively; and the Brillouin zone sampling with the resolution 0.034 $\times 2/\pi$ Å^{-1} were used.) The comparison is presented in Fig. VII.5. We conclude that even though the transient structures lie in the extrapolating regime of the original neural network, the neural network behaves reasonably good and is able to describe the structures in this part of phase diagram.

VII.3 Choice of collective variables

Inspired by the work of Zippoli et al. [175] (which used a coordination number) and our work for NaCl [57] we employed the coordination number and volume as the collective variables. The coordination number was calculated using the same switching function, see Eq. (VII.4), as in the case of NaCl, see Section VI.3.

$$\mathrm{CN} = \frac{1}{N}\sum_{i\neq j}\left(1+\left(\frac{r_{ij}-d_0}{r_0}\right)^6\right)^{-1}. \tag{VII.4}$$

The parameters of the switching function were chosen as $d_0 = 0$ and $r_0 = 2.2$ Å. We note that this choice was also originally made by Zippoli et al. [175]. The parameter d_0 were varied in the interval $\langle -1; +1\rangle$Å, to find out that the value $d_0 = 0$ yields to an optimal position of the centre of maximum derivative of switching function, in respect to the reconstructed barrier, see Fig. VII.7, and in the respect to the positions of the 1$^{\text{st}}$ and the 4$^{\text{th}}$ peak of the radial distribution function,

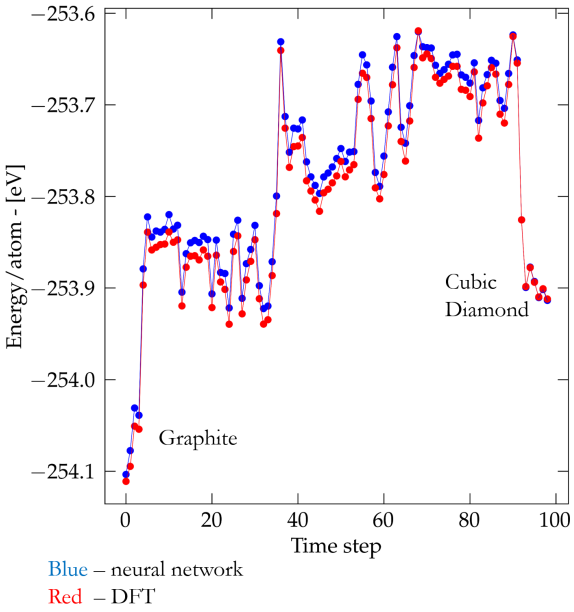

Figure VII.5: The comparison of the energies of transient structures between the graphite and the diamond. (Blue) the prediction of the original neural network [197], (red) the ground truth based on DFT calculations with the same parameters as the original dataset.

see Fig. VII.6. We note a similar insight as for the case of NaCl. In the case of NaCl, the B1-B2 transition is accompanied by the transfer of two ions from the second into the first coordination shell. The graphite to diamond transition is accompanied by the transfer of one ion from the fourth (out of plane) coordination shell into the first coordination shell of graphite. Therefore, as in the case for NaCl, in order to be able to induce this transfer effectively a suitable switching function is needed whose derivative has a significant overlap with the first and the fourth coordination peak of RDF.

We note that in the work of Zippoli et al. [175] only the out of plane atoms are considered for the calculation of the coordination number. The coordination number of the Zippoli et al. approach does not take into account the atoms sitting in the first, second and third coordination shell of graphite (which contains in-plane atoms). We also experimented with this choice of calculation of coordination number, however, we did not find any significant influence of such choice to the values of reconstructed barriers, see Section VII.5. Therefore, we stuck to the mean of calculation of the coordination number which does not distinguish between the in-plane and out-of-plane atoms.

We have also tested another version of the calculation of coordination number, namely using a so-called `more than` keyword in PLUMED (or in respective private modifications of the PLUMED code). In this approach, the value of the coordination number calculated as in Eq. (VII.4) is passed to another switching function which leads to the value 1, if the calculated coordination is higher than a certain value (e.g., value found in equilibrium in the graphitic phase) and is zero, if the value is smaller than the given threshold. We experimented with this approach since, as it will be shown in Section VII.5 we were not able to induce nucleation, in the system sizes which were computationally feasible to simulate. This approach has the advantage that the gradient from the free energy "flows" only to the atoms whose coordination is larger than the given threshold, thus expectedly promoting the rise of nucleus. However, even with this approach, we were not able to achieve the nucleating limit, see Section VII.5.

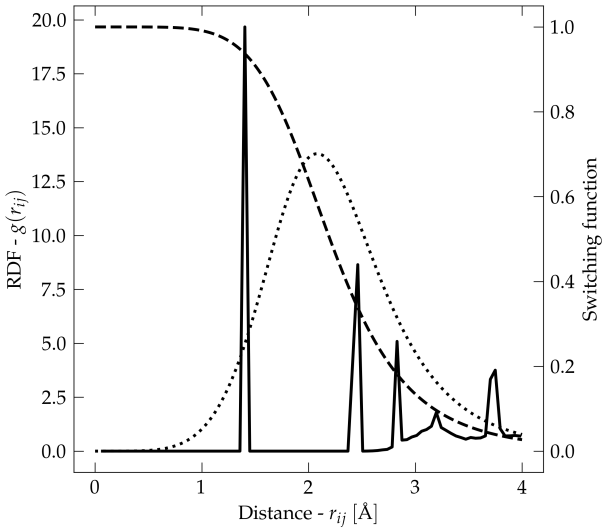

Figure VII.6: (Full) The radial distribution function of graphite at 20 GPa and 1 000 K. The first three peaks corresponds to the in-plane nearest neighbours of an atom in the graphene sheet. The fourth peak corresponds to the first peak containing out-of-plane neighbours of the atom, from which one atom is needed to create a diamond structure. (Dashed) the switching function with parameters $d_0 = 0$ and $r_0 = 2.2$ Å, (dotted) the absolute value of the derivative of the switching function.

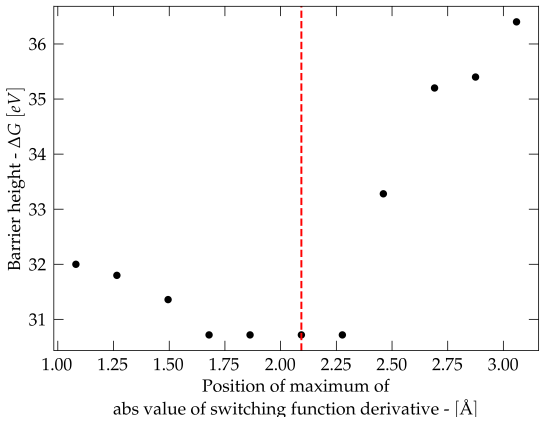

Figure VII.7: The reconstructed barriers for the graphite $\rightarrow$ diamond transition at 40 GPa and 1000 K in the system size of 128 atoms using different switching functions, where the parameter d_0 is varied to change the position of the maximum of the absolute value of the derivative of the switching function.

System size	Height [meV/atom]	Width in CN direction	Width in volume [Å^3/atom]
128	0.41	0.2	0.15
1 024	0.41	0.2	0.15
8 192	0.41	0.2	0.15
65 536	0.41	0.2	0.15

Table VII.1: Parameters of Gaussians used for simulation of graphite → diamond transition.

VII.4 Simulation details

Simulations were performed using LAMMPS [247, 248] and PLUMED [249, 250]. The integration step was set to 1 fs. Nosé-Hoover barostats and thermostats of chain length 3 with MTK correction terms [220] were used. The relaxation times of the barostat and thermostat were set to $0.5\,\mathrm{ps}$ and $0.25\,\mathrm{ps}$, respectively. For parameters of Gaussians, see Tab. VII.1. The Gaussians were deposited every 500 MD steps.

VII.5 Results

We performed simulations at various pressures 15 - 70 GPa and temperatures 500 - 2 000 K for system sizes of 128, 1 024, 8 192 and 65 536 atoms, see Fig. VII.8 for the values of the barrier for the graphite → cubic diamond transition after the first transition.

However, at all studied pressures and temperatures the computationally feasible system sizes[1] were too small to capture a nucleating event. At all studied pressures and temperatures there is still some "collectivity" of transition present in the compression of the structures perpendicular to the graphitic planes. Contrary to the Ref. [170] which studied transitions by ab-initio metadynamics in BN, no temperature dependence is found in the outcome of the graphite → diamond transition, which is always found to be the cubic diamond. Similarly, the cubic diamond is found to be preferred over hexagonal diamond at all studied pressures.

We also observed, that if one does not start from rhombohedral graphite (ABC stacking), but from hexagonal or orthorhombic graphite, the system tries to prefer the rhombohedral graphite (at 1 000 K) and subsequentially moves into it or tries to move into it in the simulation which are not commensurate with the rhombohedral graphite. The transition apparently closest to nucleation is found at the system size of 65 536 atoms, 40 GPa and 1 000 K, where after the initial compression in the direction perpendicular to the graphitic planes the cubic diamond starts to grow from three independent sites, see Fig. VII.9. We note that this transition proceeded after 0.5 ns of filling the initial graphitic phase, therefore the behaviour (tendency to compress the structure) cannot be explained by too high Gaussians, as their choice were rather conservative. This was also tested by running an independent simulation, with a different Gaussian height, to find that the time needed to fill the initial graphitic free-energy basin was inversely proportional to Gaussian height. Therefore we expect to be in a regime which does not suffer from the artefacts of too high Gaussians.

At all temperatures and pressures the transition proceeds locally through rhombohedral graphite (ABC stacking) and chair puckering, with the boat buckling and hexagonal diamond found as the outcome only as a defect between the grains of the cubic diamond.

[1] The simulation at system size of 65 536 atoms required more than 200 000 core CPU hours.

For the transition mechanism at 40 GPa, 1 000 K and system size of 65 536 atoms, see Fig. VII.9. For the visualisation of the microscopic transition mechanism, see Fig. VII.10. For the metadynamics parameters see Tab. VII.1.

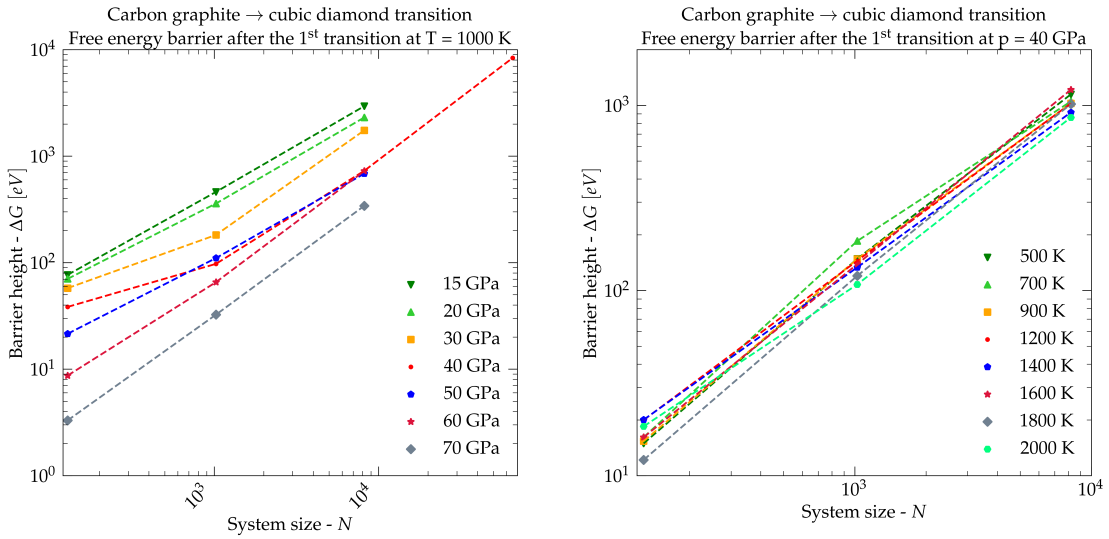

Figure VII.8: (Left) The barriers after the first transition from the graphite → cubic diamond phase as found by metadynamics at various pressures as a function of the system size. (Right) The barriers afte the first transition from the graphite → cubic diamond phase as found by metadynamics at various temperatures as a function of the system size. Note that in both cases, contrary to the results for NaCl, we do not see any deviation from the linear scaling which correlates with the overall compression of the system in the direction perpendicular to the graphitic planes.

VII.5.1 Nucleation on dislocations

Although the studied system sizes were too small to capture a nucleating event, we tried to incorporate structural defects into the largest system sizes studied (65 536 atoms; 1 000 K and at modest overpressurization - 40 GPa) to see (a) if they are able to induce nucleation at this system size (b) to see if they are able to reasonable lower the barrier. We focused on finite dislocation loops created either by condensed vacancy defects or as additional circular graphitic plates, see Fig. VII.11.

Experimentally, dislocations in graphite were studied by Amelinckx and Delavignette [285, 286] by means of transmission electron microscopy. They found dislocation loops to be present in graphite, see Fig. VII.11 for the sketch, and Fig. VII.12 for the transmission electron photograph of the dislocation loops present in the material after the annealing procedure at 1 500 K. At a mesoscale, they found the dislocations to form a ribbon network, see Fig. VII.12 suggesting that a realistic simulation of graphite must consider its presence in the simulation. Therefore, a realistic simulation in the system sizes larger than 65 536 must not only contain graphite grains, but also this network of ribbons to sufficiently mimic the real structure of the graphite. However, we did not include their presence as the supercell of size of 65 536 is still too small to fully accommodate them in the structures and we restricted to the dislocation loops such as those depicted in Fig. VII.11.

However, even the dislocation loops present as additional circular flakes or circular holes cannot alone provide barriers which can be overcome by thermal fluctuations at 1 000 K and 40 GPa. Their presence lowers the barriers by factor of 1/4 - 1/2, however, they remain still of an

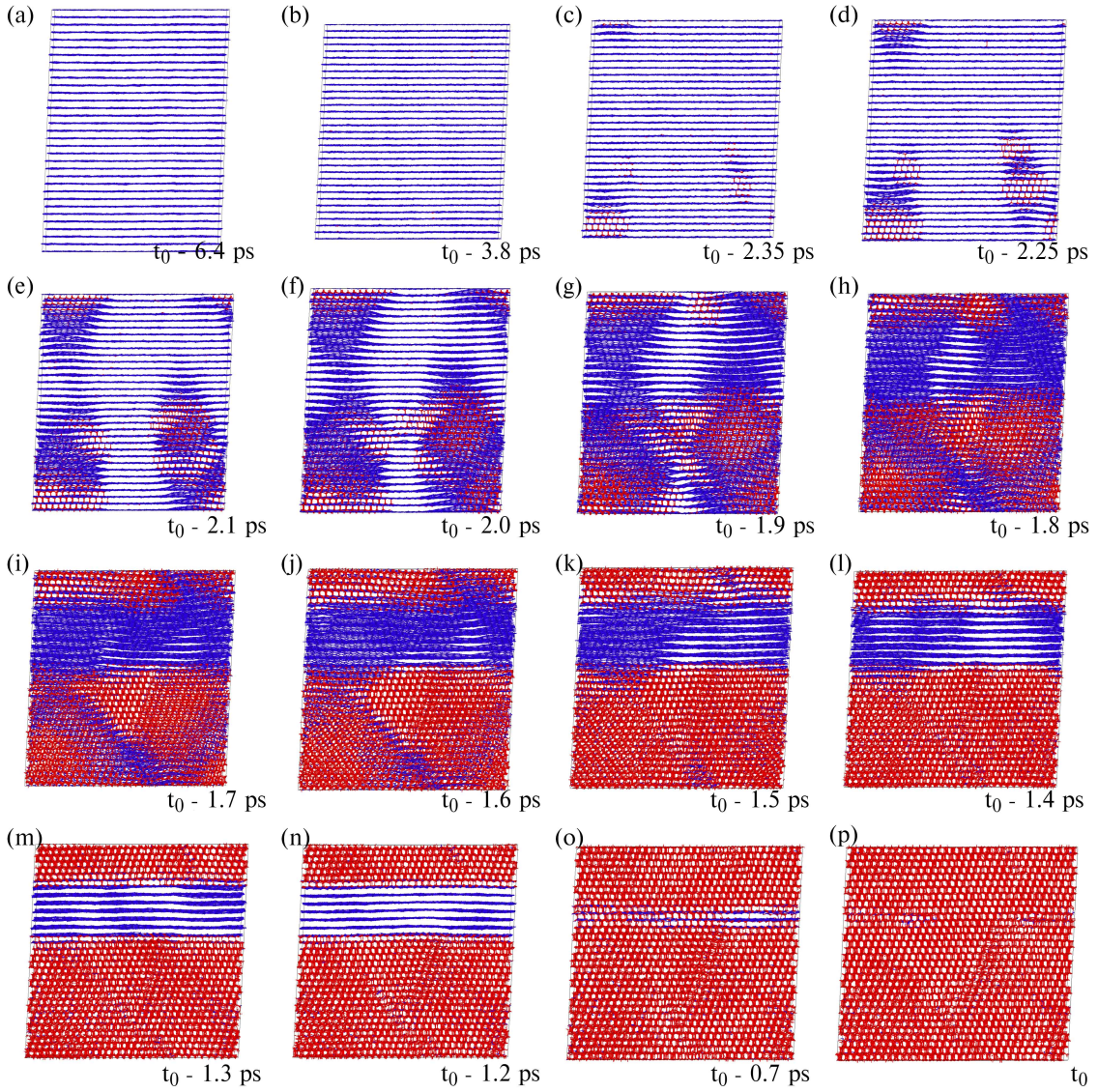

Figure VII.9: Evolution of the system of the size of 65 536 atoms near the point of the transition. (Blue) three coordinated atoms (red) four coordinated atoms.

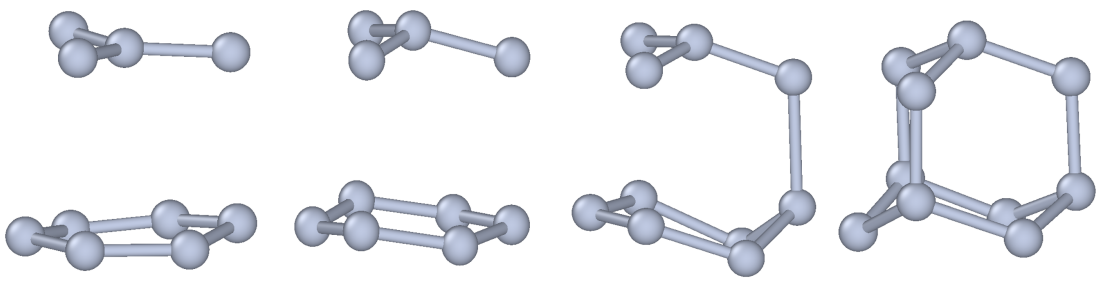

Figure VII.10: Observed atomistic transformation mechanism.

order of thousands of eV. Therefore, probably the realistic simulation of graphite to diamond transitions needs to consider the structure of graphite at mesoscale - the presence of dislocation ribbons, see Fig. VII.12. Unfortunately, the system sizes needed for such simulations were beyond the reach of the resources we had access to.

For the transition mechanism at 40 GPa, 1 000 K and system size of 65 536 atoms with the presence of an additional circular flake of radius 15 Å, see Fig. VII.14.

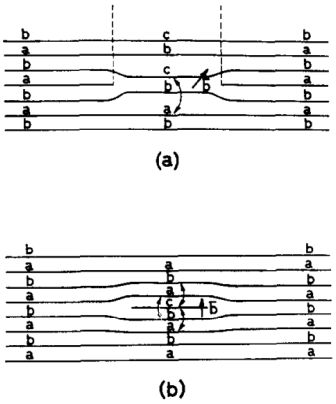

Fig. 68. Schematic view of prismatic loops. a) Loops due to the precipitation of vacancies; the Burgers vector is inclined with respect to the c-plane; b) Loops due to the precipitation of interstitials. The Burgers vector is perpendicular to the c-plane.

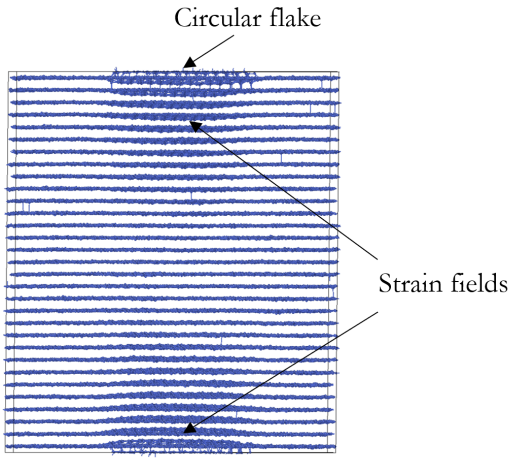

Figure VII.11: (Left) Schematic view of prismatic finite dislocation loop due to (a) missing circular flake (precipitation of vacancies) (b) an additional plane in the shape of circular flake. Adapted from Ref. [286]. (Right) Example of initial structure used in our simulations. Note the induced upper and lower strain fields by the presence of additional layer in the form of a circular flake.

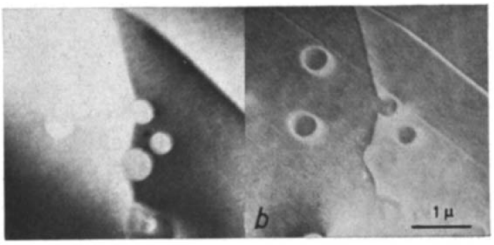

Fig. 69. Quenched-in dislocation loops. a) normal image but inverted contrast; b) Dark field image using the (11$\bar{2}$0) reflection. The dislocation lines show inverted contrast except for one loop, which has its Burgers vector in the (11$\bar{2}$0) plane used.)

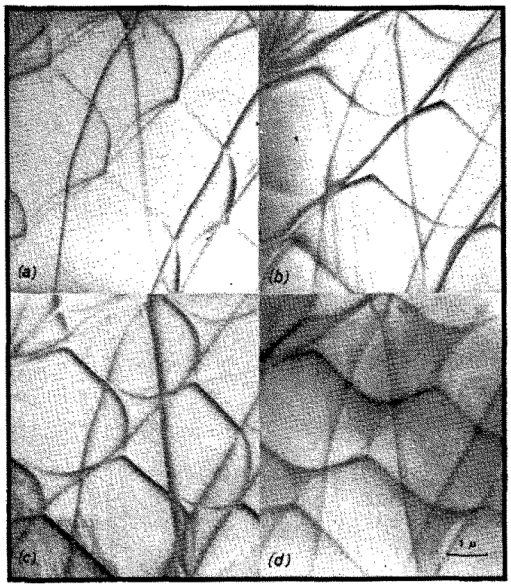

FIG. 5. Number of dislocation nodes. The sequence of photographs shows the disappearance of contrast for each one of the three families of partials, while the fourth photograph shows the stacking fault contrast inside the extended nodes. From these photographs and the corresponding diffraction patterns the Burgers vectors can be determined unambiguously.

Figure VII.12: (Left) Dislocation loops found in graphite layers visulalised using transmission electron microscopy. The samples were prepared from single crystals of pure natural graphite and heated in vacuum by electron bombardment with peak temperature 3 300 K, and subsequentially cooled in vacuum. The dislocation loops were not found after initial heating, only after annealing to 1 500 K [286]. Figure adapted from Ref. [286]. (Right) The dislocation ribbon network found in experiment. Figure adapted from Ref. [285].

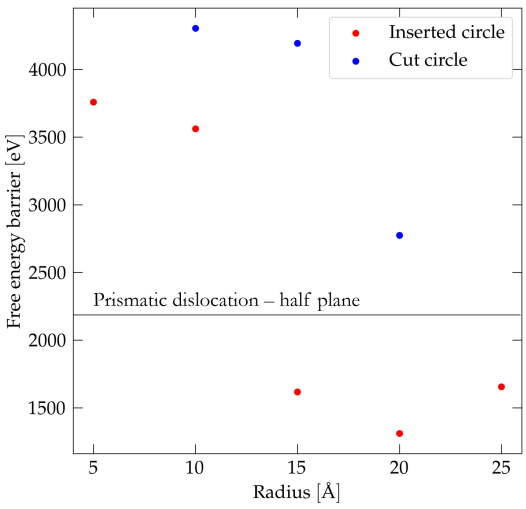

Figure VII.13: The height of barrier for three cases (a) infinite prismatic dislocation in a form of inserted half plane (b) inserted circular flakes (c) missing circles in a plane (holes) as a function of the radius of the respective circular flakes / circular holes. Note that the barriers are smaller with respect to the case of simulation of 65k atoms without defects by the factor of 1/4 - 1/2. However, also note that the structures for large radii suffer from strong periodic boundary conditions artefacts, which probably explain rapid decrease of the barrier with the increase of the radius of the flake/hole.

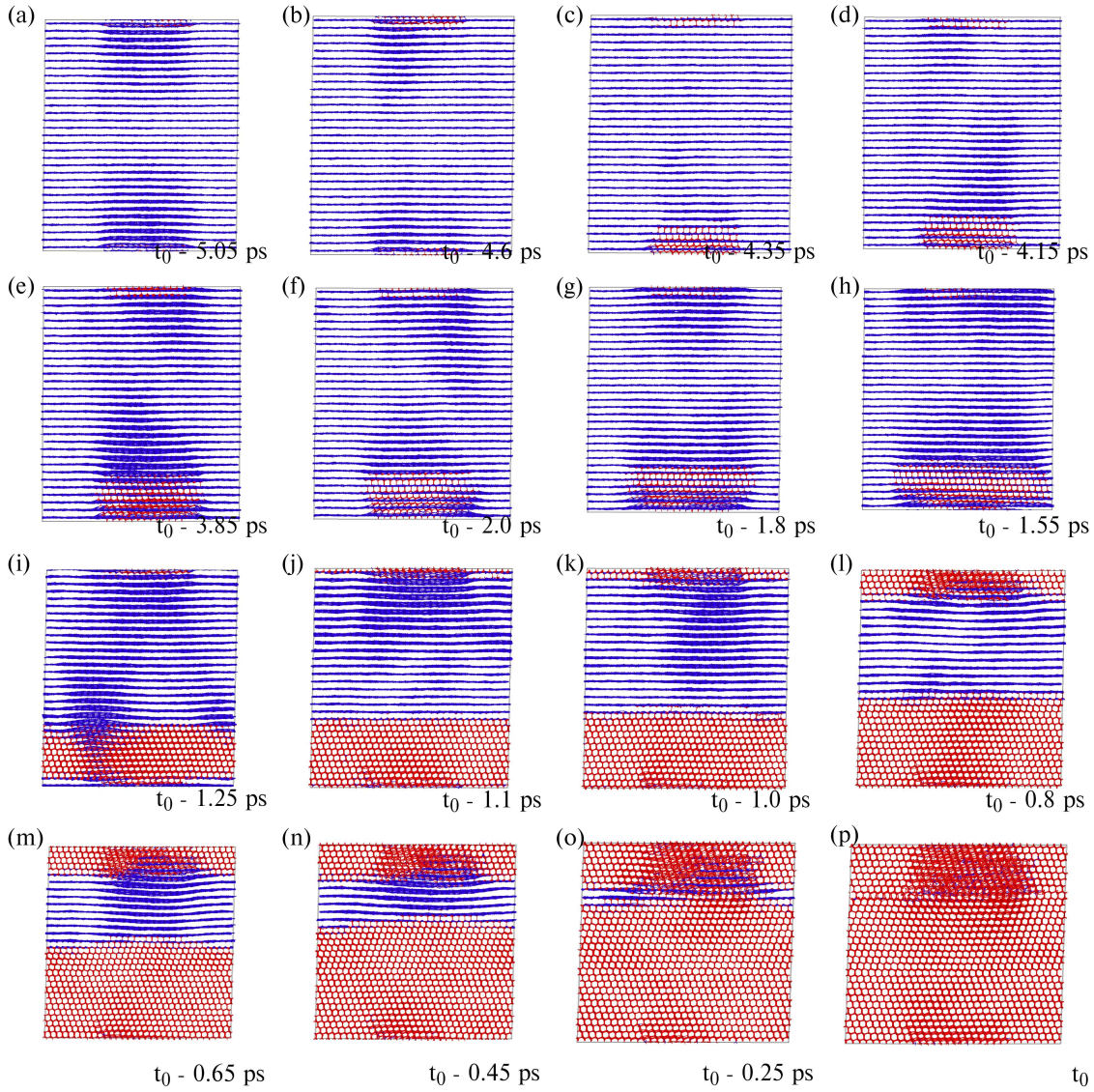

Figure VII.14: Evolution of the system of the size of 65 536 atoms with the additional defect (circular flake) near the point of the transition. (Blue) three coordinated atoms (red) four coordinated atoms.

VII Transitions in the post-diamond phases of Carbon

In this chapter we summarises the unpublished results obtained by the application of metadynamics techniques presented in Ch. VI to the transitions in post-diamond phases of carbon, namely BC8 and simple cubic phases. These results have been obtained in collaboration with the group of prof. Ivan Oleynik, who kindly provided us with their recent machine learning potential [198] developed for this part of carbon phase diagram.

VIII.1 Summary of previous studies

In this subsection, we briefly review the findings of experimental and theoretical works aiming at the post-diamond phases of carbon.

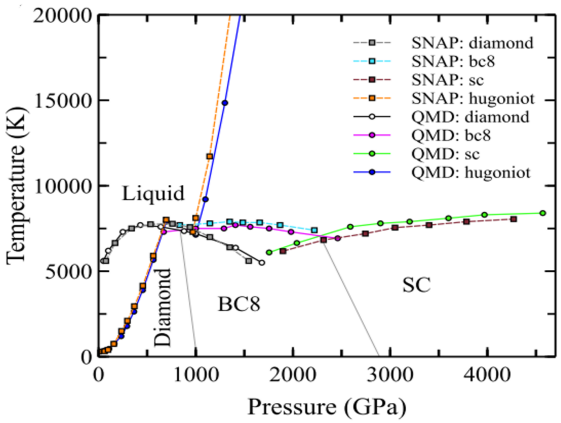

Figure VIII.1: Phase diagram of carbon up to 4 TPa and 20 000 K as reproduced by SNAP potential [198]. Adapted from Ref. [198].

Yin and Cohen predicted in 1983 [287] the transformation of diamond into simple cubic phase at 2.3 TPa (no phase transformation to any other structure below this value was predicted) using ab-initio calculations with a LDA exchange functional to find a year later [288] that diamond should transform at 1.2 TPa to the BC8 phase.

Biswas et al. [289] calculated the properties of BC8 phase of carbon using ab-initio calculations, and found BC8 phase to be stable above 1.2 TPa.

Fahy et al. [290] found the transition to proceed at a slightly lower value of 1.1 TPa using ab-initio calculations employing local orbitals.

Galli et al. [291] performed an ab-initio molecular dynamics of melting of diamond in supercell of 64 atoms at pressures greater than 1 TPa to find out that the melting temperature of diamond increases with pressure, opposite to the case of silicon and germanium, in agreement with experiments.

Mailhiot and McMahan [292] investigated the stability of BC8 with respect to graphite, cubic and hexagonal diamond via high-symmetry paths, namely via $Ibca$, $Pbca$ and $R\bar{3}$ space groups. They systematically evaluated all possible transformation paths from the BC8 phase to the diamond and graphite phases which involved 16 or fewer atoms per supercell. They identified barriers as follows, 0.25 eV/atom towards hexagonal diamond (with breaking of one bond), 1.5 eV/atom towards cubic diamond (with breaking of 1.5 bonds) and the smallest being 0.2 eV/atom towards graphite (with breaking of one bond). They conclude that the BC8 phase should be metastable at atmospheric pressure. However, they performed no calculation of phonons at ambient pressure and the metastability was concluded by means of collective transformation mechanisms.

Clark et al. [293] found that diamond structure should be unstable towards tetrahedrally coordinated structure (R8) at 0.5 TPa. Based on the analogy with silicon they conjectured that the decompression from the R8 phase might result in the formation of BC8 phase of carbon at pressures lower than 0.24 TPa. However, no information about the barriers were provided.

Scandolo et al. [294] observed the transition of diamond into the sixfold coordinated SC4 structure at 3 TPa using ab-initio molecular dynamics, while no transition to BC8 phase has been observed. For the diamond to BC8 transition path proposed by Mailhiot and McMahan [292] (to be more precise for the inverse path) they recalculated the energy barrier at 1.8 TPa and found value of 4 eV/atom.

Grumbach and Martin [295] also performed ab-initio molecular dynamics to find the melting of simple cubic phase at 3.4 - 4 TPa at 4000 K and the melting of BC8 phase at 2.2 TPa at temperatures higher than 6000 K.

Gogotsi, Kailer and Nickel [296] reported in 1998 an experimental observation of a phase transformations in diamond. However, the transformations were observed by indentation and scratching of diamond surface and not in bulk.

Nellis, Mitchell, McMahan [297] reported in 2001 the single-shock Hugoniot equation of state for shock-compressed graphite at pressures up to 0.76 TPa. They observed graphite to be completely transformed into diamond at pressures below 80 GPa, and found that diamond to be preserved to pressures at least 0.6 TPa.

Wang, Scandolo and Car [298] computed the free energy of solid and liquid diamond at ab-initio level of accuracy using thermodynamic integration, to find an excellent agreement with the experimental estimate and their calculated melting curve, including the position of graphite-diamond-liquid triple point.

Correa, Bonev and Galli [299] presented in 2006 predictions of melting lines of diamond and BC8 phase, and found a triple point between the phases at 0.85 TPa and 7 400 K.

Correa et al. [300] constructed a phase diagram for carbon in the range 0 - 2.5 TPa and 0 - 10 000 K describing the stability of diamond, BC8 and liquid phase using ab-initio calculations and quasiharmonic approximation.

Hicks et al. [301] measured the diamond Hugoniot curve at pressures between 6 and 1.9 TPa.

Sun, Klug and Martoňák [167] performed ab initio metadynamics calculations with supercell as the collective variable and observed the transformation of diamond to simple cubic structure at

2 TPa and 4 000 K. They also observed the transformation into the BC8 phase from decompression of simple cubic structure at 1 TPa and 5 000 K. At 1 TPa and 3 000 K, they observed decompression of simple cubic phase into two new metastable tetrahedrally coordinated structures, MP8 and OP8.

Bradley et al. [302] presented in 2009 a new ramp compression technique and reported stability of cubic diamond up to 0.8 TPa.

Martinez-Canales, Pickard and Needs [303] reported a study of phases of carbon up to 1 PPa using ab-initio calculations, reporting a sequence of transitions of the form diamond $\rightarrow$ (at 1 TPa) BC8 $\rightarrow$ (at 2.9 TPa) simple cubic phase, followed by the sequence, simple cubic $\rightarrow$ (at 6.4 TPa) simple hexagonal $\rightarrow$ (at 21 TPa) fcc $\rightarrow$ (at 270 TPa) dhcp $\rightarrow$ bcc (at 650 TPa) phase.

Smith et al. [202] reported a ramp compression of diamond up to 5 TPa, without evidence for the transition to another phase. Lazicki et al. [304] reported a ramp compression of diamond up to 2 TPa, also without evidence for the transition to another phase.

NguyenCong et al. [305] performed a billion-atom molecular dynamics simulation of carbon using a recent SNAP potential [198] and observed transition into BC8 phase at 1.2 TPa and 5 000 K starting, however, from amorphous carbon and not from cubic diamond.

VIII.2 Model

To model the carbon BC8, simple cubic and cubic diamond phases, we worked with the recent SNAP potential [198] of Willman et al. In the SNAP potential the total energy of the system is as in other machine-learning approaches sum of individual atomic contributions $E = \sum_i E_i$, the individual atomic contributions E_i are a quadratic function of the so-called *bispectrum coefficients* $\mathbf{B}_i$ of the local neighbour density, with the parameters which are subject to optimisation during learning being the symmetric matrix α and the vector β.

$$E_i = \beta \cdot \mathbf{B}_i + \frac{1}{2}\mathbf{B}_i \cdot \alpha \cdot \mathbf{B}_i \,. \tag{VIII.1}$$

The bispectrum coefficients are calculated as follows [305]. First, a local neighbour density of the i-th atom is projected on 3-sphere (lying in a four-dimensional space), hence the local neighbour density is projected using four-dimensional hyperspherical harmonic functions as

$$U_j = \sum_k f_c(r_{ik}) u_j(a,b) \,, \tag{VIII.2}$$

where f_c is a suitable switching function, u_j is a Wigner U-matrix, and a, b are Cayley-Klein parameters - mappings of vector $\mathbf{r}_{ik}$ onto the 3-sphere and where index j take half-integer values. The bispectrum coefficients are calculated from U_j as follows

$$\mathbf{B}_{j_1 j_2 j} = U_{j_1} \otimes^{j}_{j_1 j_2} U_{j_2} : U^*_j \,, \tag{VIII.3}$$

where $\otimes^{j}_{j_1 j_2}$ is a Clebsch-Gordan product of matrices and : is a element-wise scalar product of two matrices of equal rank. The vector $\mathbf{B}_i$ is a flattened list of elements $\mathbf{B}_{j_1 j_2 j}$. In the SNAP potential [305] the total number of elements is 55.

For the H-p and E-V curves see Fig. VIII.2. Both cubic diamond and simple cubic phases

are stable against overpressurisation or underpressurisation in molecular dynamics and do not proceed to the BC8 phase, instead simple cubic transforms into cubic diamond and vice-versa.

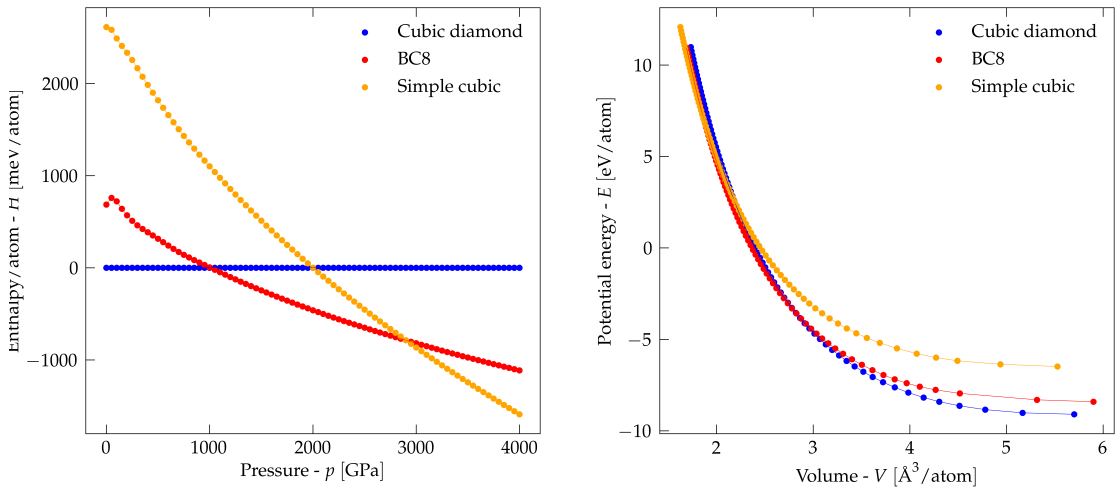

Figure VIII.2: (Left) The H-p curve for carbon BC8, simple cubic and cubic diamond phases for the SNAP potential [198]. (Right) The E-V curve for carbon BC8, simple cubic and cubic diamond phases for the SNAP potential [198].

VIII.3 Results

In this section we summarize the preliminary results obtained so far by applications of metadynamics to the post-diamond phases of carbon using the SNAP potential [198].

VIII.3.1 Coordination number and volume as CVs

It may be surprising to try to use coordination number and volume as CVs for the transition in post-diamond phases of carbon, since both cubic diamond and the BC8 phase are four coordinated and there seems to be no change of coordination number. However, this is not completely true, since the transition from the BC8 phase into the cubic diamond involves breaking of the chemical bond [292], even though both structures are equally coordinated. Therefore, we also experimented with the use of coordination number and volume as CVs and indeed observed transitions between the BC8, cubic diamond and simple cubic phases. The radial distribution function of the respective phases is depicted in Fig. VIII.3. As for the case of NaCl the coordination number is calculated following the switching function,

$$\mathrm{CN} = \frac{1}{N}\sum_{i\neq j}\left(1+\left(\frac{r_{ij}-d_0}{r_0}\right)^6\right)^{-1}, \tag{VIII.4}$$

where the free parameters are chosen as $d_0 = 0.7\,\text{Å}$ and $r_0 = 0.8\,\text{Å}$. The switching function is also depicted in Fig. VIII.3. We report a few representative examples of the observed phase transitions using these CVs below in this subsection.

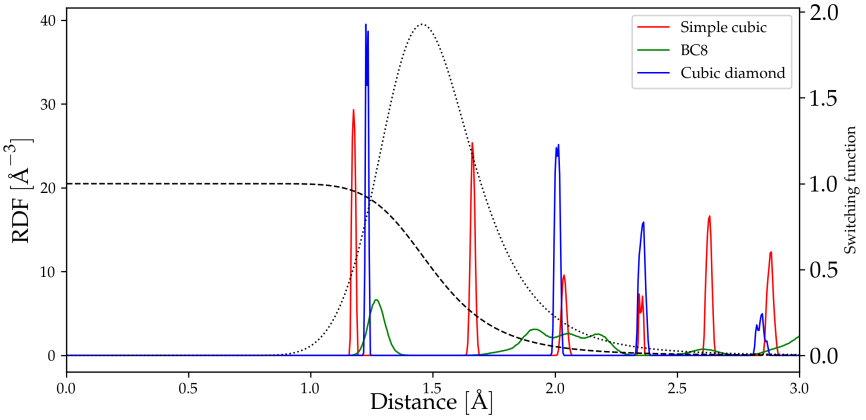

Figure VIII.3: Radial distribution function of simple cubic phase at 1 000 K and 4 TPa (red), BC8 phase at 1 000 K and 1 TPa (green), cubic diamond phase at 1000 K and 1 TPa (blue) and employed switching function used for the calculation of CN (dashed) and the absolute value of its derivative (dotted).

BC8 decompression at 250 GPa

We start with the simulation of decompression of the BC8 phase at 250 GPa and 5 000 K. The temperature may seem too high for the simulation of the decompression as it will be probably far away from the actual condition under which the decompression would be performed in the experiment. We are aware of that. The reason for this choice was the fact that using the coordination number and volume as the CVs the transition did not proceed at lower temperatures, however, this is not true for the tetrahedral order parameter, see later.

Here, the simulation proceeds fast (after $\sim$ 90 ps) to a highly distorted structure from which the cubic diamond eventually emerges after (after $\sim$ 20 ps), see Fig. VIII.4. One initial bond is broken. The corresponding barrier is approximately 1.5 eV/atom. For comparison the Ref. [292] observed a similar value of the barrier. For the time evolution of the CVs see Fig. VIII.11.

Gaussian width was set to 0.1 in the CN direction, 0.5 Å^3/atom in the volume direction and the height of Gaussians was set to 2.02 meV/atom, Gaussians were deposited every 0.5 ps. The system size was set to 128 atoms.

Cubic diamond compression at 1 500 GPa

The simulation of the cubic diamond compression at 1 500 GPa and 300 K proceeds after $\sim$ 9.5 ns into the distorted simple cubic phase Fig. VIII.5, here the transient structures lives approximately 0.5 ps. The free energy barrier is approximately 3 eV/atom. For the time evolution of the CVs see Fig. VIII.11. However, note that the observed transition is unphysical, since at 1 500 GPa the simple cubic phase has bigger enthalpy than cubic diamond.

Gaussian width was set to 0.1 in the CN direction, 0.5 Å^3/atom in the volume direction and the height of Gaussians was set to 0.81 meV/atom, Gaussians were deposited every 0.5 ps.

Simple cubic decompression at 2 250 GPa

The simulation of the decompression of the simple cubic phase at 2 250 GPa and 1 000 K proceeds after $\sim$ 1.1 ns, even though three attempts to a highly distorted cubic diamond precede, see Fig. VIII.6. The corresponding barrier is approximately 3 eV/atom. For the time evolution of the CVs see Fig. VIII.11. However, note that the observed transition is unphysical, since at 2 250 GPa the cubic diamond phase has bigger enthalpy than simple cubic phase.

Gaussian width was set to 0.5 in the CN direction, 0.5 Å^3/atom in the volume direction and the height of Gaussians was set to 2.02 meV/atom, Gaussians were deposited every 0.5 ps.

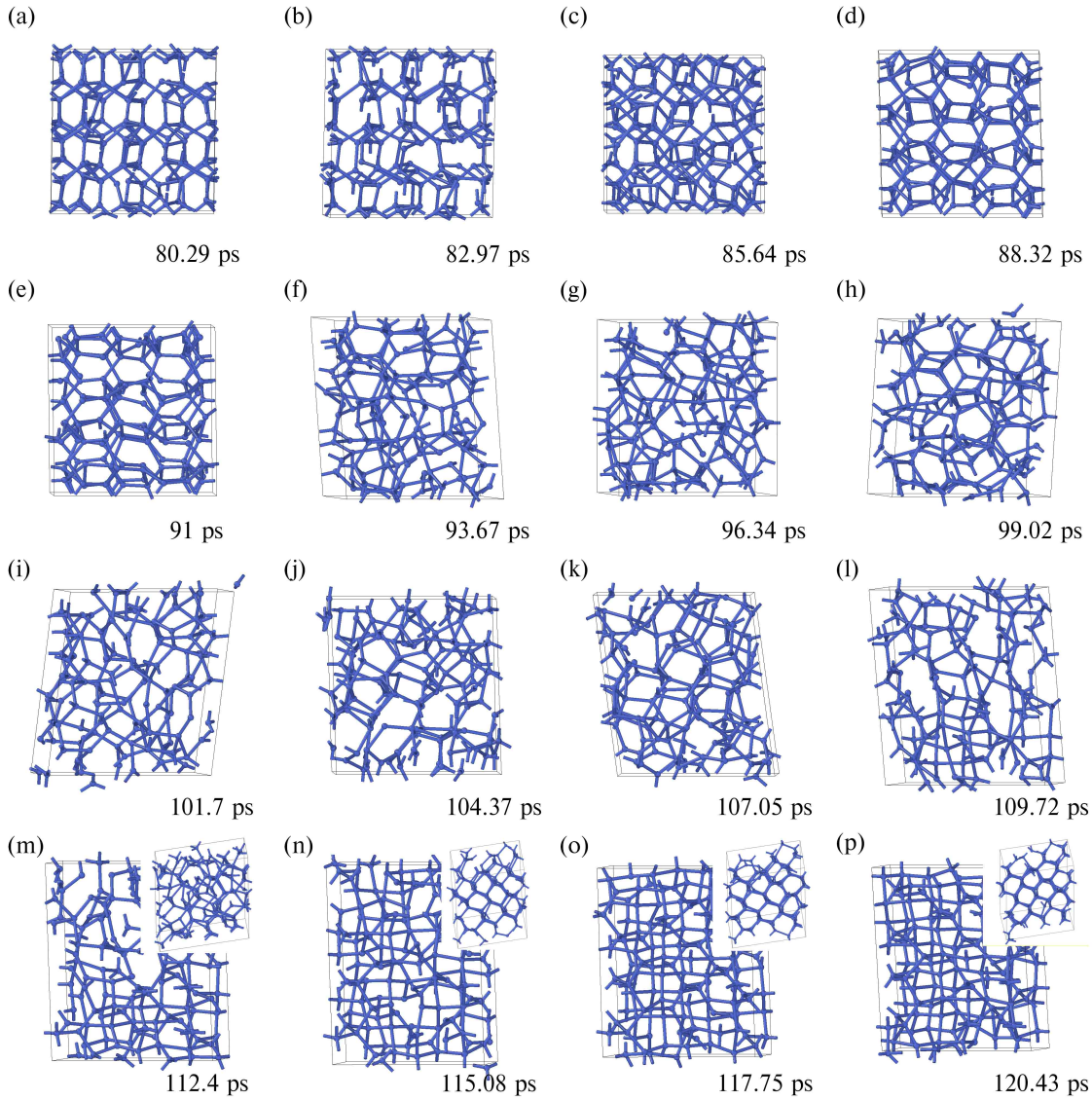

Figure VIII.4: Transformation from the BC8 phase to the cubic diamond phase, when using the coordination number & volume as the CVs. The simulation was run at 250 GPa and 5 000 K. For the time evolution of the CVs see Fig. VIII.11. Note that the point of view is fixed in all snapshots. To persuade the reader of the presence of cubic diamond, snapshots from different point of view are inserted into the last four snapshots.

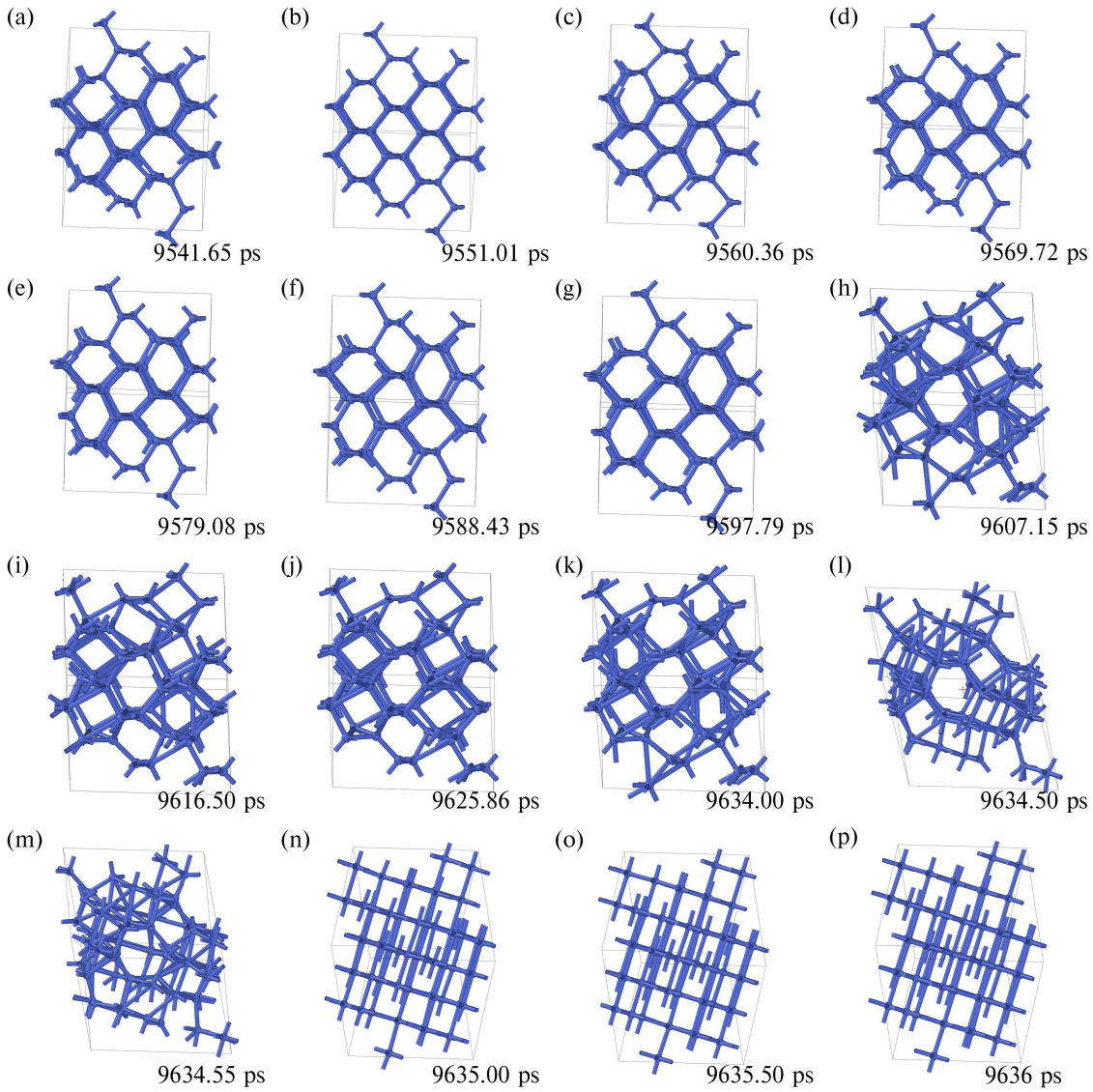

Figure VIII.5: The compression of cubic diamond at 1 500 GPa and 300 K using the coordination number & volume as the CVs. The simulation proceeds to the simple cubic phase. For the time evolution of the CVs see Fig. VIII.11.

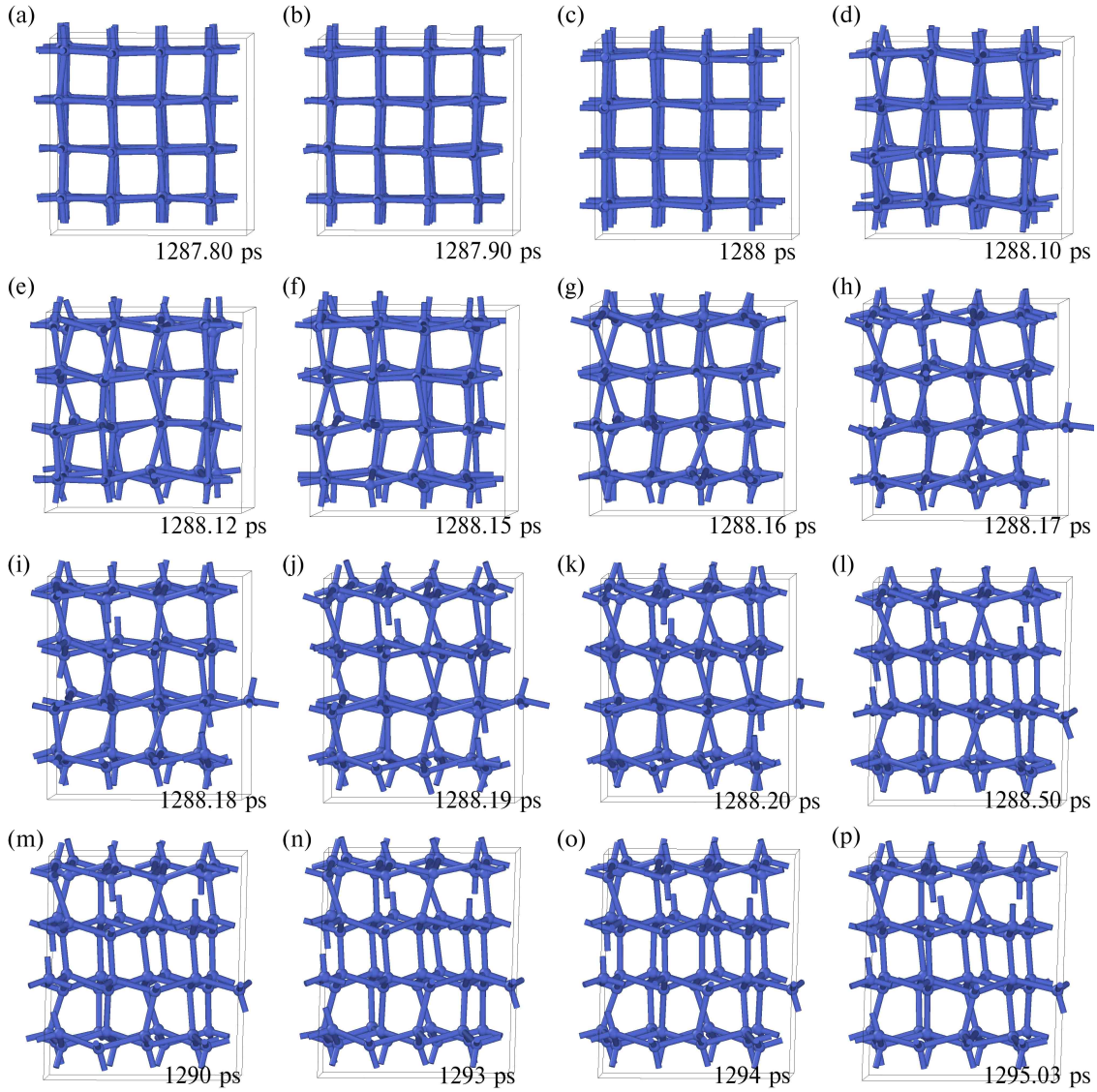

Figure VIII.6: The decompression of the simple cubic phase at 2 250 GPa and 1 000 K using the coordination number & volume as the CVs. The simulation proceeds to the cubic diamond phase. For the time evolution of the CVs see Fig. VIII.11.

VIII.3.2 Tetrahedral order parameter and volume as CVs

In order to see if we are able to steer the transitions from or into the BC8 phase we took the inspiration by the work Chau and Hardwick [306] and the fact that bond angles in the BC8 phase deviate largely from the tetrahedral angle found in cubic diamond structure, see e.g. ADF depicted in Fig. VIII.7. Thus, we employed the following tetrahedral order parameter [306] together with volume as CVs (we implemented the following relationship for tetrahedral order parameter as CV in PLUMED),

$$\chi = \frac{1}{N} \sum_{i \neq j \neq k} f_c(r_{ij}) f_c(r_{ik}) \left(\cos \theta_{ijk} + \frac{1}{3} \right)^2 , \tag{VIII.5}$$

where N is the number of atoms in the system. The switching function f_c ensures that only the triplet of atoms, where atoms are creating a bond with the central atom are considered (atoms closer than 2 Å are considered). The switching function was chosen to have the following form

$$f_c(r) = \left(1 + \left(\frac{r_{ij} - d_0}{r_0} \right)^6 \right)^{-1} , \tag{VIII.6}$$

with parameters d_0 and r_0 chosen as $d_0 = 1.5$ Å and $r_0 = 0.1$ Å. We report a few representative examples of the observed phase transitions using these CVs below in this subsection.

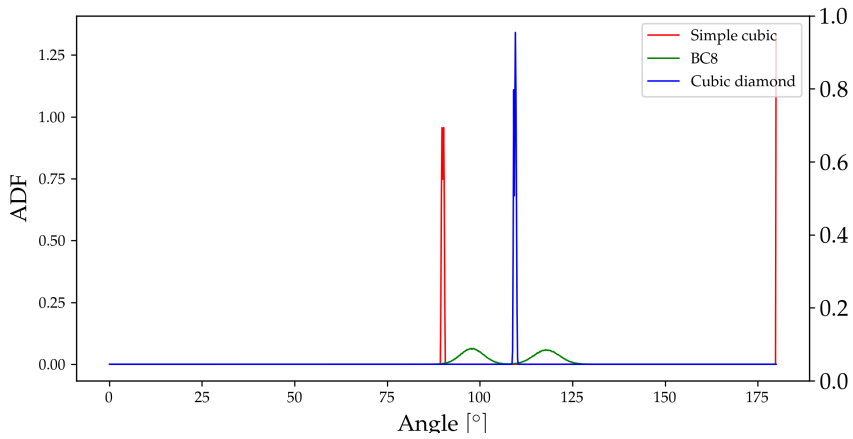

Figure VIII.7: Angular distribution function of simple cubic phase at 1 000 K and 4 TPa (red), BC8 phase at 1 000 K and 1 TPa (green), cubic diamond phase at 1000 K and 1 TPa (blue).

BC8 decompression at 250 GPa

We continue with a few examples of simulation using the tetrahedral order parameter and volume as CVs. Contrary to the simulation which uses CN and volume, here the simulation of decompression of the BC8 phase is performed at 1 000 K.

Here, the simulation proceeds (after $\sim$ 646.8 ps) to a transient structure when one of the initial bonds is broken, see Fig. VIII.8. This structure has the value of tetrahedral order parameter lower as the intial value of the BC8 phase, however, still higher than the cubic diamond. After approximately 300 ps the free energy basin of this structure is filled and the transition finally proceeds to the cubic diamond. The free energy barrier is approximately 0.8 eV/atom. For the time evolution of the CVs see Fig. VIII.11.

Gaussian width was set to 0.025 in the χ direction, 0.5 Å^3/atom in the volume direction and the height of Gaussians was set to 2.02 meV/atom, Gaussians were deposited every 0.5 ps.

Cubic diamond compression at 2250 GPa

The simulation of the cubic diamond compression at 2 250 GPa and 1 000 K proceeds after $\sim$ 2.5 ns into the distorted simple cubic phase, see Fig. VIII.9. The corresponding barrier is approximately 2 eV/atom. For the time evolution of the CVs see Fig. VIII.11.

Gaussian width was set to 0.125 in the χ direction, 0.5 Å^3/atom in the volume direction and the height of Gaussians was set to 4.05 meV/atom, Gaussians were deposited every 0.5 ps.

Simple cubic decompression at 1250 GPa

The simulation of the simple cubic decompression at 1 250 GPa and 1 000 K proceeds after $\sim$ 280 ps into the distorted cubic diamond phase containing two grains which in the following $\sim$ 100 ps transforms into the perfect cubic diamond phase, see Fig. VIII.9. The corresponding barrier is approximately 0.5 eV/atom. For the time evolution of the CVs see Fig. VIII.11.

Gaussian width was set to 0.125 in the χ direction, 0.5 Å^3/atom in the volume direction and the height of Gaussians was set to 4.05 meV/atom, Gaussians were deposited every 0.5 ps.

VIII.3.3 Machine learning CVs

So far, we have shown the results in which we observed the transitions from the cubic diamond into the simple cubic phase, skipping the BC8 phase and vice versa, the transitions from the simple cubic phase into the cubic diamond phase also skipping the BC8 phase. The latter is a bit surprising since the work of Sun, Klug and Martoňák [167] observed the BC8 phase upon decompression from the simple cubic phase.

To be able to steer the transitions towards the BC8 phase from the cubic diamond and simple cubic phases and to answer the questions, if the barrier towards the BC8 phase is higher upon decompression from the simple cubic phase than towards cubic diamond, and correspondingly, if the barrier towards simple cubic phase is lower upon compression from the cubic diamond phase than towards BC8 we are currently creating a set of machine learning CVs. We summarised the outline of their construction here, despite the fact that we currently do not have the results yet from the metadynamics which are run with these machine learning CVs.

Inspired by the work of Rogal et al., 2019 [180], Yoo et al., 2021 [181] and the master thesis of Ondrej Bilý [307] who created a neural network discriminator based on Behler-Parrinello descriptors for the phases of germanium, we take a similar approach, but with some differences which are stressed below. The machine learning CVs are created using a simple feed-forward neural network discriminator applied upon the Behler-Parrinello descriptors. We employ the following set of 102 Behler-Parrinello descriptors incorporating the radial and angular part. In the angular part, we modify the usual form of the so-called G_5 descriptor, namely the part with the cosine function and replace it with more sharper exponential (in the terms of the angle θ_{ijk}).

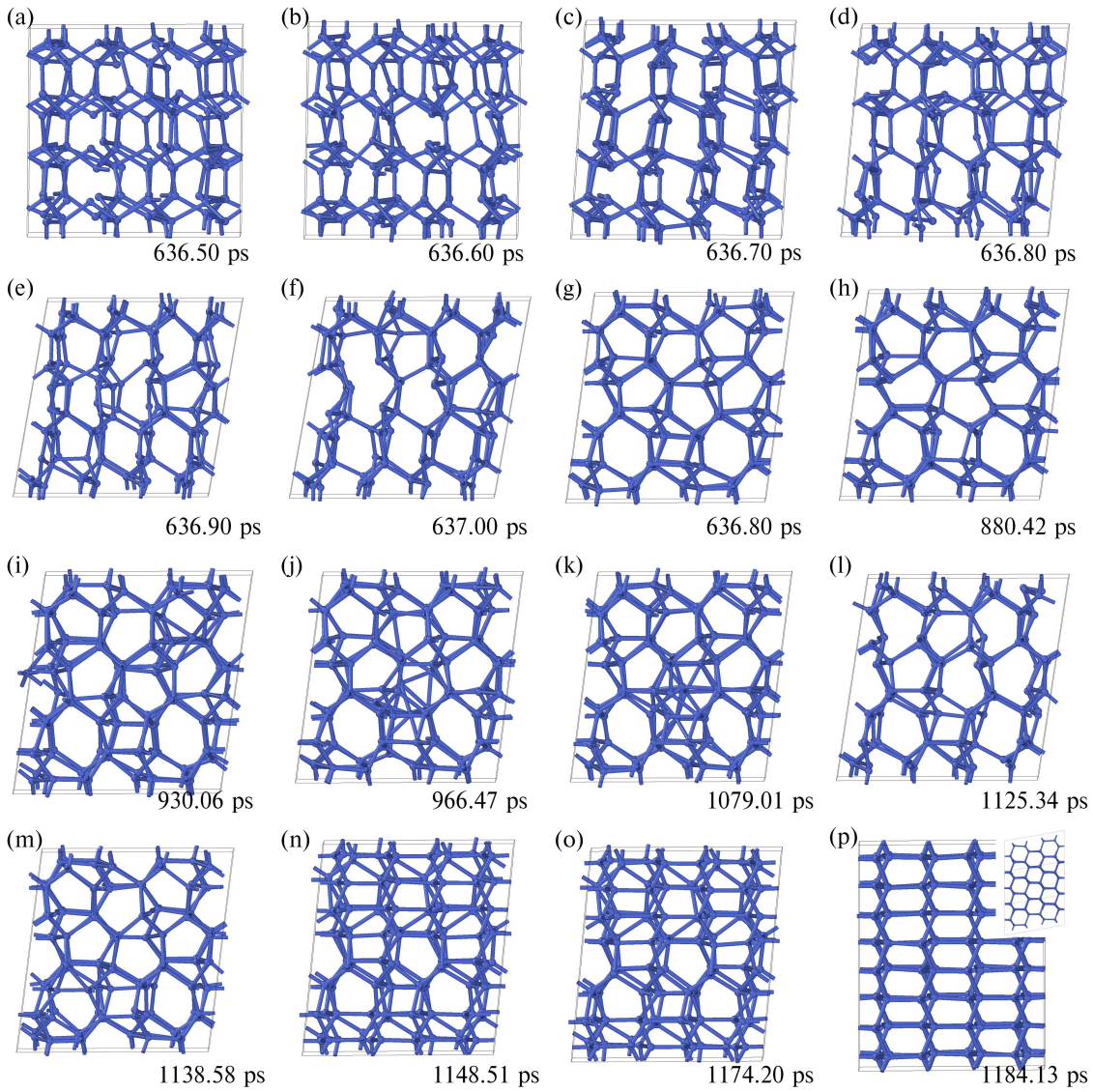

Figure VIII.8: Transformation of the BC8 phase into the cubic diamond phase at 250 GPa and 1 000 K using the tetrahedral order parameter and volume as the CVs. For the time evolution of the CVs see Fig. VIII.11.

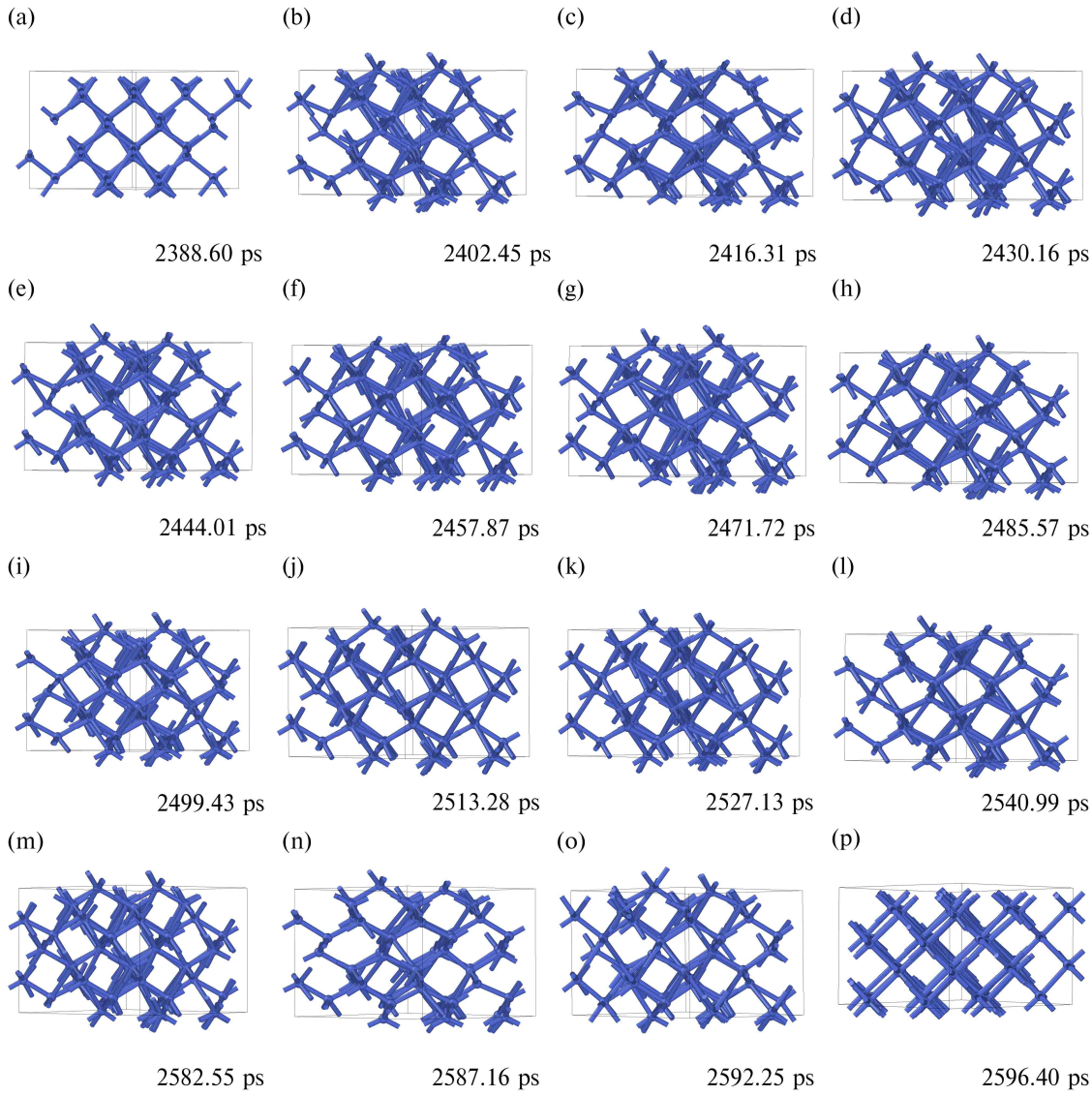

Figure VIII.9: The compression of the cubic diamond phase at 2 250 GPa and 1 000 K using the tetrahedral order parameter and volume as the CVs. The simulation cell transforms into the simple cubic phase. For the time evolution of the CVs see Fig. VIII.11.

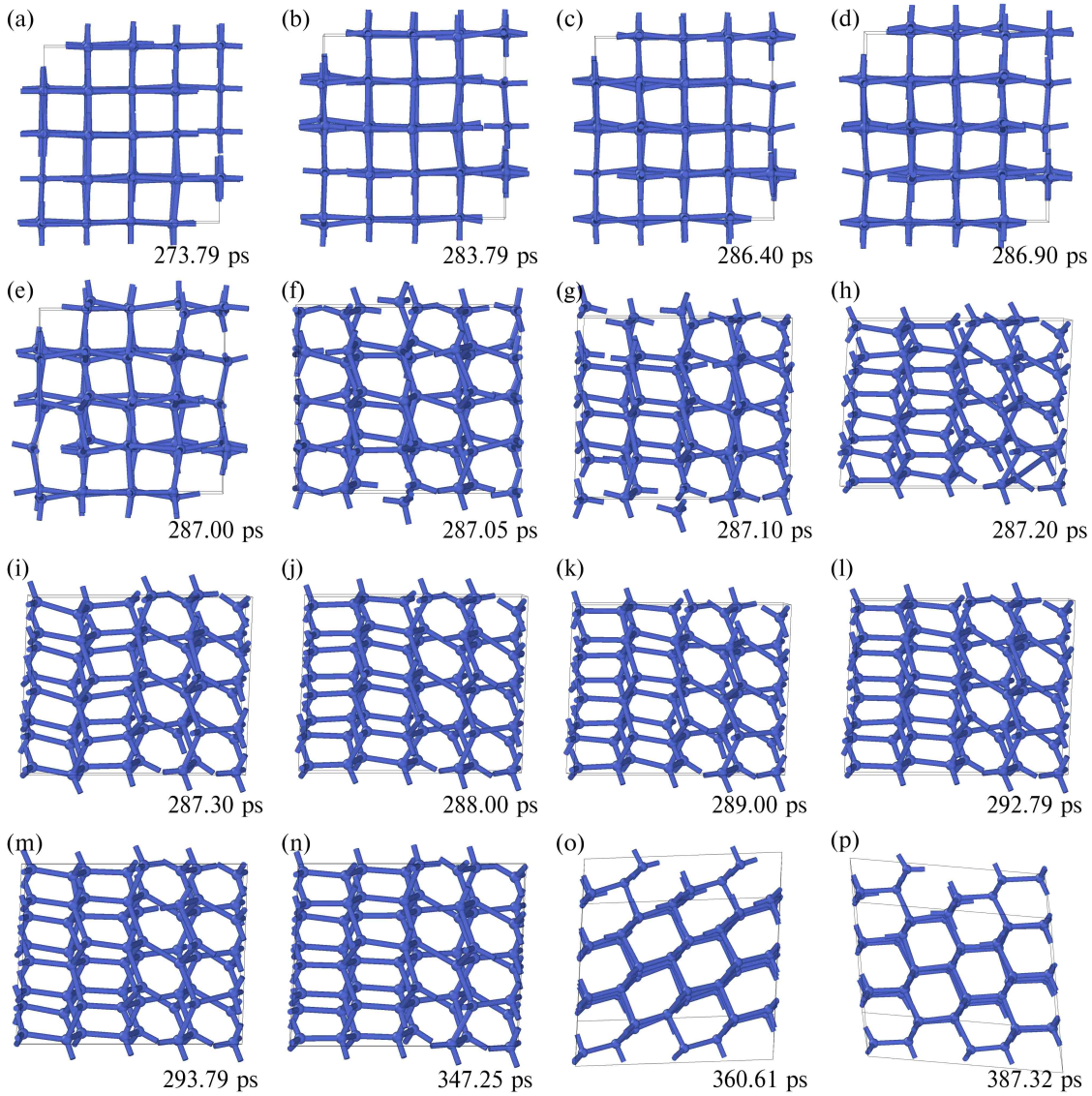

Figure VIII.10: The decompression of the simple cubic phase at 1 250 GPa and 1 000 K using the tetrahedral order parameter and volume as the CVs. The simulation cell transforms into the cubic diamond phase. Note that for the last two snapshots the point of view was rotated. For the time evolution of the CVs see Fig. VIII.11.

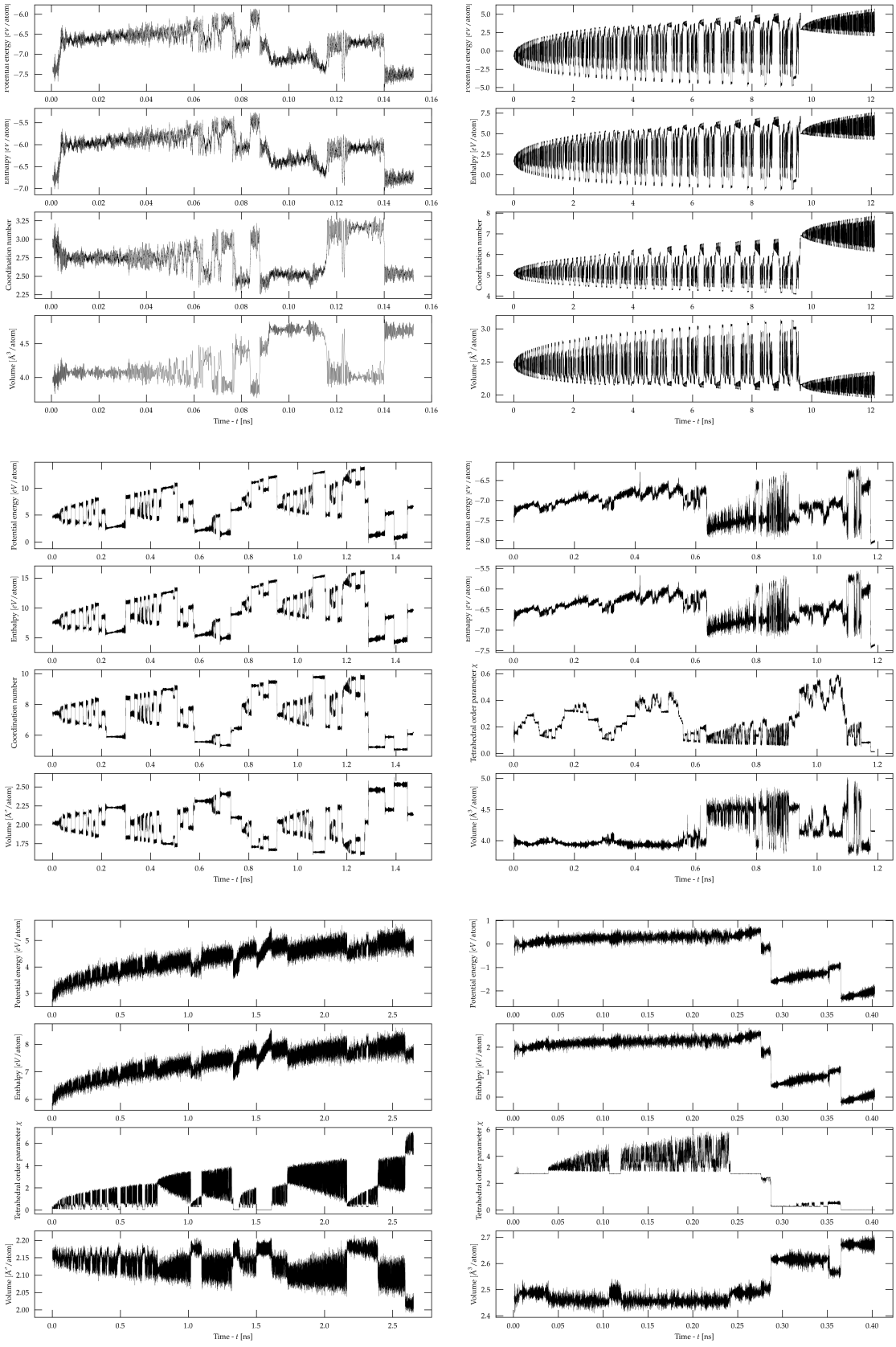

Figure VIII.11: [Upper left] Simualtion using CN & V as the CVs starting from the BC8 phase. [Upper right] Simualtion using CN & V as the CVs starting from the cubic diamond phase. [Middle left] Simualtion using CN & V as the CVs starting from the simple cubic phase. [Middle right] Simualtion using χ & V as the CVs starting from the BC8 phase. [Lower left] Simualtion using χ & V as the CVs starting from the cubic diamond phase. [Lower right] Simualtion using χ & V as the CVs starting from the simple cubic phase.

$$G_2 = \sum_{i \neq j} e^{-\eta(R_{ij}-R_s)^2} f_c(R_{ij}) \,, \tag{VIII.7}$$

$$G_5^{\mathrm{mod}} = \sum_{i \neq j,k} e^{-\eta_{\mathrm{ang}}\left(\theta_{ijk}-\theta_s\right)^2} e^{-\eta(R_{ij}/2+R_{ik}/2-R_s)^2} f_c(R_{ij}) f_c(R_{ik}) \,, \tag{VIII.8}$$

where

$$f_c(R_{ij}) = \begin{cases} \frac{1}{2}\left[1+\cos\left(\frac{\pi R_{ij}}{R_c}\right)\right], & R_{ij} \leq R_c \\ 0, & R_{ij} > R_c \,, \end{cases} \tag{VIII.9}$$

with the free parameters η, η_{ang}, R_s, R_c and θ_s. The optimal choice leads to $R_c = 3\,\text{Å}$, $\eta = 20\,\text{Å}^{-2}$, $\eta_{\mathrm{ang}} = 80$, 6 equidistantly placed Gaussians centers R_s being distributed in radial direction between $0.5\,\text{Å}$ and $3\,\text{Å}$ in G_2 descriptor, 6 equidistantly placed Gaussians centers R_s being distributed in radial direction between $0.5\,\text{Å}$ and $3\,\text{Å}$ in G_5 descriptor, and 16 equidistantly Gaussians centers θ_s being placed between $\pi/32$ and $33/32\pi$. Together this leads to 102 Behler-Parrinello descriptors, histograms of a few of them which distinguish the respective phases the most are depicted in Fig. VIII.12.

Contrary to the work of Yoo et al., [181], who used Behler-Parrinello descriptors (or to be more precise their global average over the simulation cell) directly as a set of CVs, we take the approach of Rogal et al., [180] and Bilý [307], when the Behler-Parrinello descriptors are first passed to a small feed-forward neural network, see Eq. (VIII.10), where W^L is the matrix of weights and $\mathbf{b}^l$ is the vector of biases. The request of the small size of the network comes from the fact that in our approach the neural network is first evaluated for every atomic environment (every atom in the simulation cell) and only the output of the neural network is then globally averaged to yield the value of the CV.

$$\mathbf{a}^{l+1} = \sigma^l\left(W^l\mathbf{a}^l + \mathbf{b}^l\right) . \tag{VIII.10}$$

The output of the neural network is the vector $\mathbf{q}$ of length three (at the third layer, hence $\mathbf{q} = \mathbf{a}^{l=3}$), where the component of the vector is the similarity of the atomic environment with the respective phase, e.g. $q_{\mathrm{BC8}} = 0.8$ says that the atomic environment is with the probability of 80% similar to the BC8 phase. To fullfill the requirement of the small size of the neural network, we use a neural network with two hidden layers of 25 neurons and as an activation function σ we use the ReLU function. The only exception is the last layer when we use a so-called LogSoftmax activation function, see Eq. (VIII.11),

$$\sigma^{l=3}(a_i) = \log\left(\frac{\exp(a_i)}{\sum_j \exp(a_j)}\right) . \tag{VIII.11}$$

This ensures that the vector $\mathbf{q}$ can be interpreted as a probability. The vector $\mathbf{q}^i$ for the i-th atom is then globally averaged over the whole system to the value - $\overline{\mathbf{q}} = 1/N \sum_i \mathbf{q}^i$. We plan to use this globally averaged vector directly as the CV and limit the exploration of the CV space by means of harmonic constraints - `upper walls` and `lower walls` commands in PLUMED. If our approach works, we could selectively steer the transition from the cubic diamond phase towards simple cubic and BC8 phase separately by imposing a barrier to the other phase. Similarly, one can possibly steer the transition from the simple cubic phase towards cubic diamond and BC8 phase separately.

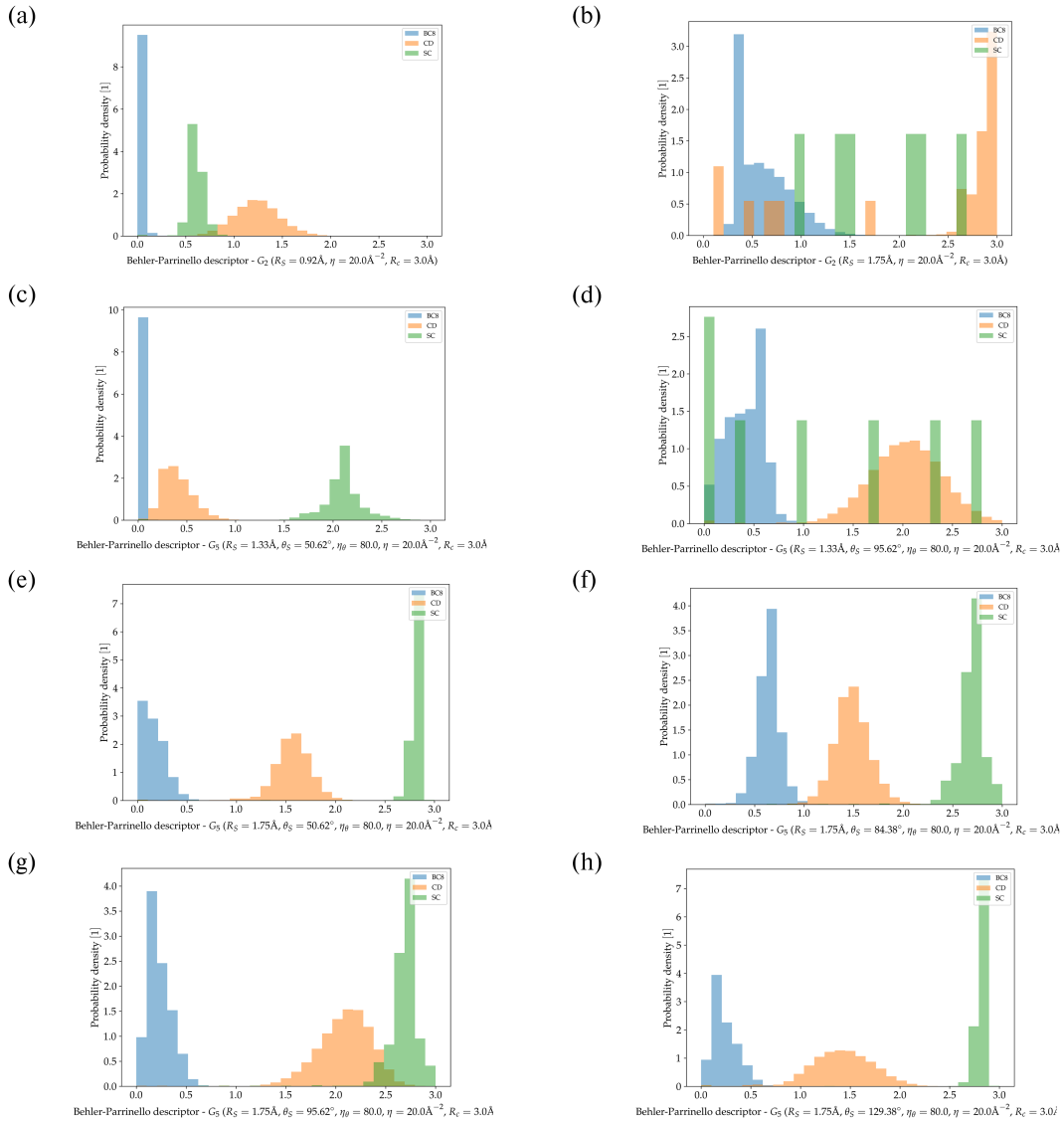

Figure VIII.12: A few selected BP descriptors whose values are significantly different from zero showing easiness of the distinguishing the simple cubic, cubic diamond and BC8 phase of carbon, with the respective parameters of the descriptors written below. Histograms of BC8 phase are from trajectory simulated at 250 GPa and 5 000 K, for cubic diamond phase at 2.5 TPa and 5 000 K, and for simple cubic phase at 3 TPa and 5 000 K. (Blue) BC8 phase (Orange) Cubic diamond phase (Green) Simple cubic phase.

If the above-mentioned approach does not work, we will employ PathCV variables, see Eq. (VIII.12) where the bias is deposited along the coordinate s which measures the progress along the path and a harmonic constraint is placed on the coordinate z - which is perpendicular to the chosen path. The only requirement is to specify the path $\mathbf{q}_K$ in advance.

$$s(\mathbf{q}) = \frac{1}{P-1} \frac{\sum_{K=1}^{P} (K-1) \exp\left(-\lambda |\mathbf{q} - \mathbf{q}_K|^2\right)}{\sum_{K=1}^{P} \exp\left(-\lambda |\mathbf{q} - \mathbf{q}_K|^2\right)},$$
$$z(\mathbf{q}) = -\frac{1}{\lambda} \ln\left(\sum_{K=1}^{P} \exp\left(-\lambda |\mathbf{q} - \mathbf{q}_K|^2\right)\right). \tag{VIII.12}$$

So far, we trained a neural network discriminator, see Fig. VIII.13 for the loss function and validation and training accuracy as the function of the epoch in the training. We have also already implemented, in a private modification of PLUMED, the calculation of the above mentioned Behler-Parrinello descriptors and the evaluation of the neural network using `TorchScript` file using C++ version of PyTorch - Libtorch. The last remaining step is to actually run the metadynamics calculations with the neural network discriminator. This private modification is as our private modification of the calculation of CN parallelized using a MPI-aware linked-cell neighbour list, and thus it also readily allows for simulations of large systems sizes.

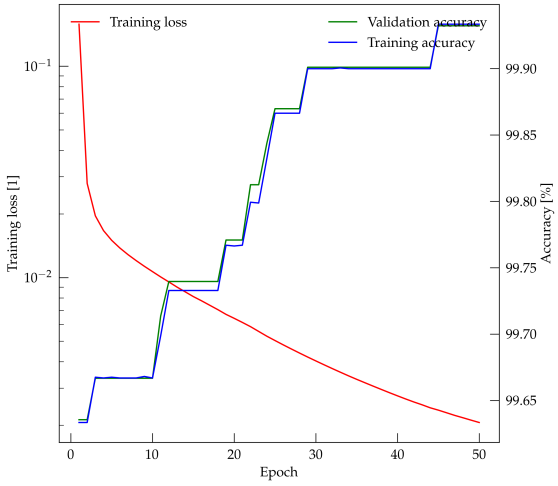

Figure VIII.13: Training loss, validation and training accuracy as the function of the number of epoch during the training with the stochastic gradient descent.

The dataset consists of 64 064 atomic environments for the BC8 phase obtained from the trajectory at 250 GPa and 5 000 K, 64 064 atomic environments for the cubic diamond phase obtained from the trajectory at 2.5 TPa and 5 000 K and 64 064 atomic environments for the simple cubic phase obtained from the trajectory at 3 TPa and 5 000 K. The higher temperature was chosen in order to sample the Behler-Parrinello descriptors with a higher variance. Thus the discriminator can be also readily used at lower temperatures, which however, does not necessarily work in the opposite direction, if one trains the discriminator from trajectories at low temperatures and applies it to a higher temperature. The dataset is randomly shuffled at the start of training and randomly split between the training and validation dataset with the split ratio 9:1. The network is trained for 50 epochs with the stochastic gradient descent with a fixed

learning rate of 10^{-4}, with a batch size of 100 examples, and a momentum equal to 0.9. The weights in the neural network are initialized from the Kaiming uniform distribution, except the weights in the last layer, which are initialized from the Xavier uniform distribution. As the loss function the negative log-likelihood is used. The train and validation accuracy reach 99.93%.

IX $\alpha \rightarrow \omega$ and $\omega \rightarrow \alpha$ transitions in Titanium

We have seen in the previous chapter that the simulation of nucleation for the graphite $\rightarrow$ diamond transition was not computationally feasible with the resources which we had access to, therefore, we wanted to investigate another covalent system which could be simulated using less resources, but still would allow for inclusion of structural defects such as dislocations[1]. We identified the temperature-induced ω (hexagonal) $\rightarrow \alpha$ (hcp) transition as a suitable candidate with Steinhardt's parameters used as collective variables. However, due to the time limitations we did not perform the study of nucleation in $\omega \rightarrow \alpha$ transition in titanium. We note that contrary to the literature which focuses into pressure driven $\alpha \rightarrow \omega$ transition, we were not able to find a suitable collective variables for this transition. Some unsuccessful attempts are also presented in this chapter.

IX.1 Summary of previous studies

Experimentally [22, 309–316], at room temperature, the $\alpha \rightarrow \omega$ transition is observed between 2 and 15 GPa, depending on the pressure environment and sample purity. The $\omega \rightarrow \alpha$ transformation is observed below 2 GPa. The $\alpha \rightarrow \omega$ pressure driven transition in pure titanium has significant technological implications for the aerospace industry since the ω-phase lowers toughness and ductility.

Trinkle et al. [24, 25] proposed a new mechanism (in 2003) for the pressure driven $\alpha \rightarrow \omega$ transition in pure titanium by means of methods used by Stokes and Hatch also for the case of NaCl [182, 183] (identifying common subgroups and proposing mechanisms within the common subgroup). They called this pathway TAO-1 mechanism and found it to proceed without a metastable intermediate phase. They found a barrier to be of an order of 10 meV/atom for the pressures in the range of 0 - 40 GPa. The estimated critical size of the nucleus for the homogeneous nucleation is 47 000 atoms with the critical barrier of 400 eV [317]. For the visualisation of the mechanism see Fig. IX.1.

Hennig et al. [23] showed that the presence of impurities (being interstitial oxygen, nitrogen or carbon) can increase the barrier for $\alpha \rightarrow \omega$ transition in titanium alloys by factor of 2 - 3. This result has a large technological importance, since the brittle ω phase is present in the form of defects in aerospace application of titanium.

Errandonea et al. [318] studied the effect of uniaxial stress on the $\alpha \rightarrow \omega$ transition and found that the onset of transition pressure rises from 4.9 GPa to 10.5 GPa if one uses argon as a pressure medium.

Cerreta et al. [319] experimentally studied the role of oxygen content to shock loading in the

[1] Inclusion of dislocation into the ionic system such as NaCl can lead to presence of so-called *jogs* - which lead to presence of locally charged regions [308].

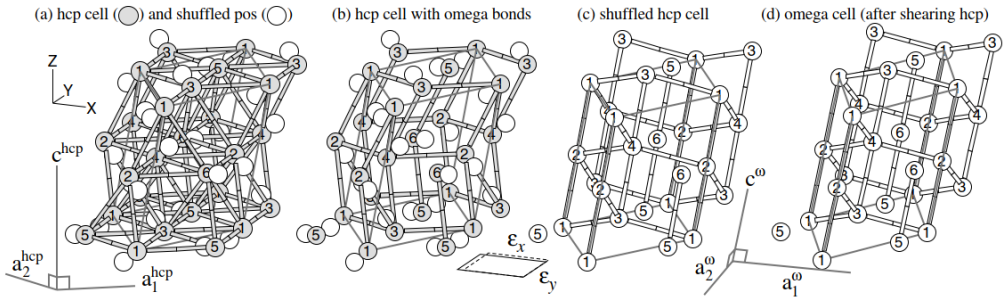

Figure IX.1: Visualization of the so-called TAO-1 mechanism proposed as the most optimal one for the $\alpha \rightarrow \omega$ transition in pure titanium. Adapted from Ref. [24].

$\alpha \rightarrow \omega$ transition. They found the transition is not observed for stresses up to 35 GPa in the alloy containing oxygen impurities (with the concentration of 3700 ppm) compared to the high purity titanium where the transition proceeded at 10.4 GPa.

In 2008, Hennig et al. [26] presented a classical MEAM potential trained on the DFT data which is able to computationally describe the α, ω and β phase of titanium including the transitions between them. The phase diagram of the potential is depicted in Fig. IX.2. However, the phase diagram presented in Ref. [26] was not constructed using any free energy integration method and thus, it suffers from hysteresis effects.

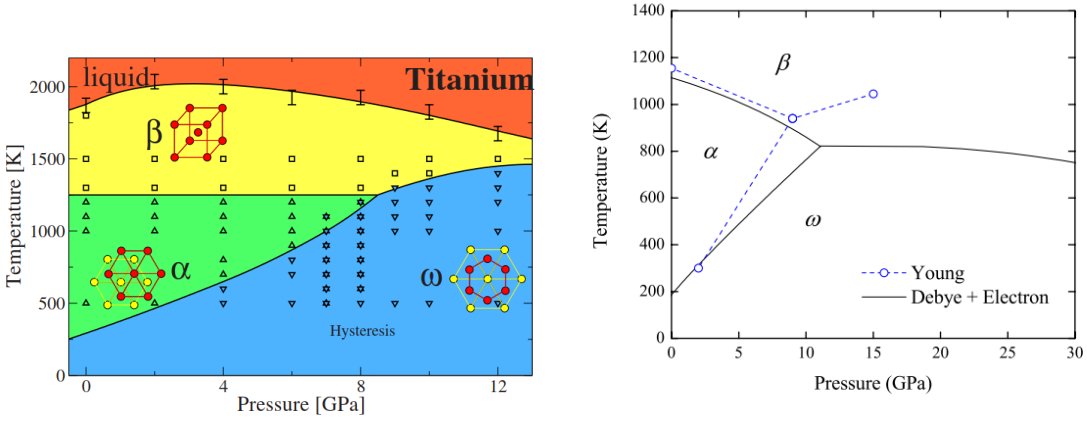

Figure IX.2: (Left) Phase diagram of the potential presented in Ref. [26]. Adapted from Ref. [26] (Right) Phase diagram calculated using quasi-harmonic approximation based on DFT data from Ref. [320].

Mei et al. [320] calculated in 2009 the phase diagram of titanium α, ω and β phases within quasi-harmonic approximation based on the DFT data.

Zong et al. [321] focused experimentally on the reverse $\omega \rightarrow \alpha$ transition in Zr and Ti. They found that the crystal orientational relationship for the reverse transition is in agreement with the originally proposed transition mechanism in Ti for the $\alpha \rightarrow \omega$ transition by Silcock [322]. Their simulation results for Ti supported nucleation on dislocations rather than interface migration-mediated growth.

Mendelev et al. [323] proposed in 2016 another EAM potential, targeting at the transformation between the β and ω phases. The melting temperature was determined using the Gibbs-Helmholtz integration method. However, the potential is not suited for the α-ω transitions.

Zarkevich and Johnson [324] performed a DFT+U study with a generalised solid-state nudged elastic band method [16] of the α-ω phase transformation and found a metastable body-centered orthorhombic phase with lower density than both α and ω phases. They found the barrier to be of an order of 15 meV/atom. Interestingly the intermediate structure was found to possess a stable phonon spectrum.

Zong et al. [61] studied the role of grain boundaries in the shock response (with shock of velocities of 0.8 km/s) of α phase upon transformation into the ω phase in MD simulations with supercell of 3 milions atoms using the MEAM potential of Hennig [26]. They found out that the elastic shock wave induced inelastic deformation (leading to transformation into the ω phase) that occurs on both sides of coherent twin boundaries but for the case on incoherent twin boundaries and asymetric tilt grain boundaries only at one side, see Fig 5, 6 and 7 in Ref [61].

Takahashi et al. [325] published in 2017 a new potential for titanium using linear regression on a set of radial and angular descriptors and showed that it outperforms the MEAM potential [26] based on phonon calculations of α(hcp) and β(bcc) phases and comparison of elastic constants and bulk modulus. However, this potential is not publicly available.

Dickel et al. [326] pointed out that both potentials of Hennig et al. [26] and Ko et al. [327] unsurprisingly overestimate the equilibrium transition temperature as the reported data relied on dynamic heating and cooling to observe transitions and no free energy integration method was employed.

Li et al. [328] focused at the role of metastable ω phase nuclei for the $\beta \rightarrow \alpha$ transition by means of transmission electron microscopy and ab-initio calculations. Their results suggest that the metastable ω phase does not necessarily act as a precursor for the α phase, but can reduce the energy barrier for the nucleation of the α phase inside the β phase.

Ferrari et al. [329] published a local-bond order potential for titanium, however, the predicted $E - V$ curves for α and ω phases deviated from the underlying DFT data, as well as when compared to the phonon diagrams of the respective phases.

Wen et al. [330] recently proposed a Deep-MD potential for titanium and show its applicability for the reconstruction of dislocation cores in titanium. The potential was trained for the hcp - α, bcc - β and fcc phases, however, missing the ω phase.

Nelasov et al. [331] developed an own machine learning potential and performed a MD simulation of the $\alpha \rightarrow \omega$ transformation upon loading conditions in supercell of 800 and 53 760 atoms to find that as the stress increases to 10 GPa the α phase partially transforms into a structure containing inclusions of ω phase. However, the α phase was preserved even when the pressure reached the value of 20 GPa and they concluded that an extra impact in addition to hydrostatic pressure is needed to initiate the $\alpha \rightarrow \omega$ transition.

Nitol et al. [332] recently published a neural network potential called RANN which aims to accurately model transitions between all three titanium phases - α, β, ω. The approach consists of a feed-forward neural network and a set of 45 descriptors of two body and three body order with a RMSE of energies of 1.77 meV/atom and RMSE on forces of 0.248 eV/Å. Besides the excellent agreement with the DFT $E - V$ curves, the potential also reasonably well describes the energetics of the dislocations. The phase diagram presented in Fig. IX.3 was constructed using thermodynamic integration.

Dang et al. [333] recently (2023) employed the MEAM potential of Hennig et al. [26] and studied the effect of dislocations and deviatoric stress on the stability of ω nucleus inside the α domain. They found out that the deviatoric stress reduces the critical radius of the ω nucleus and that such deviatoric stress can internally originate from the presence of prismatic edge dislocations, which are able to reduce the size of the critical ω nucleus by 10 to 16 %.

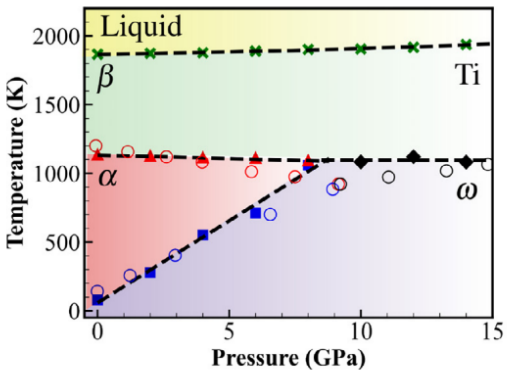

Figure IX.3: Phase diagram of the RANN potential presented in Ref. [332]. Adapted from Ref. [332].

IX.2 Model

To model the transition we chose to work with two potentials - the MEAM potential of Hennig et al. [26] and the neural network potential RANN of Nitol et al. [332].

In the MEAM formalism, the atomic energy is split into two parts, a pairwise interaction and an interaction dependent on the atomic density and a three body contribution which is a function of the relative angle θ_{ijk} between the central atom i and the neighbours j and k,

$$E = \sum_{ij} \phi(r_{ij}) + \sum_{i} U(\rho(i)) \,, \tag{IX.1}$$

$$\rho(i) = \sum_{j} \rho(r_{ij}) + \sum_{jk} f(r_{ij}) f(r_{jk}) g\left(\cos\left(\theta_{ijk}\right)\right) \,. \tag{IX.2}$$

The five functions $\phi(r)$, $U(\rho)$, $\rho(r)$, $f(r)$ and $g(\cos(\theta))$ are subjects to the potential fit and are usually parametrised in terms of cubic splines. Hennig et al. [26] fitted those functions with the goal that the MEAM potential E-V curves, see Fig. IX.4, for α, β and ω phases match those predicted by underlying DFT data within 5 meV/atom accuracy [26]. Hennig et al. [26] also compared the elastic constants of the α, β and ω phases to find that their deviation from the DFT data is of an order of 13%, with the maximum deviation of 29%. The phase diagram depicted in Fig. IX.2 was constructed simulating the supercells containing interfaces of respective pair of phases and observing within 1 ns to which phase the simulation proceeds. In particular, $\alpha \rightarrow \omega$ transition was simulated using the TAO-1 pathway as an interface between the α and ω phases. For the enthalpy vs pressure curve reproduced by the potential, see Fig. IX.5.

The descriptors in the RANN potential are similar to those in the MEAM potential. The RANN potential consists of a small feed-forward neural network (multi-layer perceptron) and a following set of pair (F_n) and angular descriptors ($G_{m,k}$) [334],

$$F_n = \sum_{j \neq i} \left(\frac{r_{ij}}{r_e} \right)^n e^{-\alpha_n \frac{r_{ij}}{r_e}} f_c \left(\frac{r_c - r_{ij}}{\Delta r} \right) S_{ij} \,, \tag{IX.3}$$

$$G_{m,k} = \sum_{j,k \neq i} \cos^m(\theta_{ijk}) e^{-\beta_n \frac{r_{ij}+r_{ik}}{r_e}} f_c \left(\frac{r_c - r_{ij}}{\Delta r} \right) f_c \left(\frac{r_c - r_{ik}}{\Delta r} \right) S_{ij} S_{ik} \,, \tag{IX.4}$$

where S_{ij} is given as

$$S_{ij} = \Pi_{k \neq i,j} f_c \left(\frac{C_{ijk} - C_{\min}}{C_{\max} - C_{\min}} \right) \,, \tag{IX.5}$$

where

$$C_{ijk} = 1 + 2 \frac{r_{ij}^2 r_{ik}^2 + r_{ij}^2 r_{jk}^2 - r_{ij}^4}{r_{ij}^4 - \left(r_{ik}^2 - r_{jk}^2 \right)^2} \,, \tag{IX.6}$$

and where f_c is suitable switching function and r_e, r_c, Δr, $C_{\min}$, $C_{\max}$, α_n, and β_n are the free parameters.

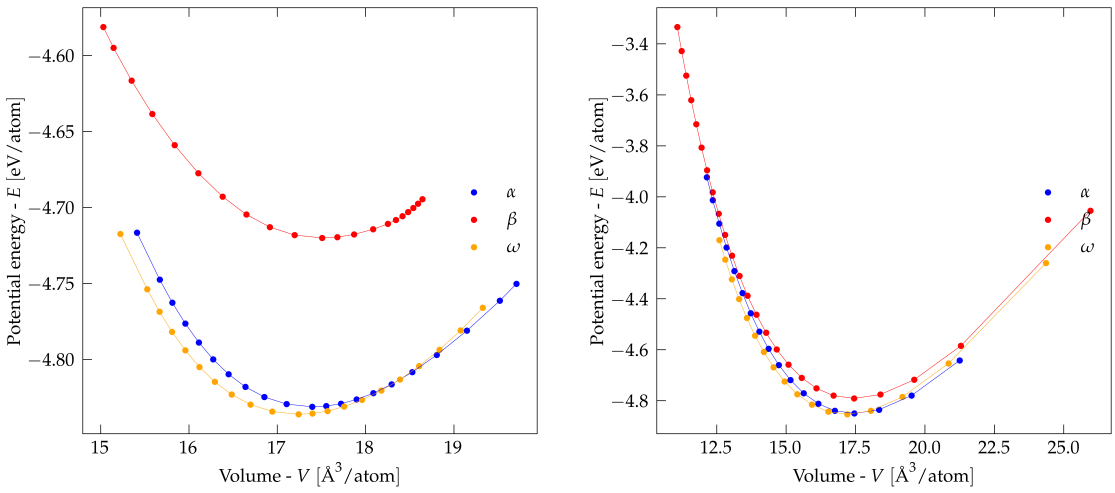

Figure IX.4: (Left) The E-V curve for the titanium α, β and ω phases for the MEAM potential [26]. (Right) The E-V curve for the titanium α, β and ω phases for the RANN potential [332].

For both potentials the temperature of dynamical instability (for $\omega \to \alpha$ transition) is found at 1100 K by means of unbiased molecular dynamics with a heating rate 2 K/ps. The value is actually quite close to the melting temperature towards the β phase. We note that the equilibrium transition temperature (for $\omega \to \alpha$ transition) is 79.62 K for the RANN potential.

IX.3 Results

In this section, we report the results obtained for the $\alpha \to \omega$ and $\omega \to \alpha$ transitions for various collective variables. In summary, we found the Steinhardt's parameters to represent a suitable pair of collective variables for $\omega \to \alpha$ transition, while we were not able to identify a suitable set of collective variables for the $\alpha \to \omega$ transition. Our unsuccessful attempts are also reported in this section.

Simulations were performed using LAMMPS [247, 248] and PLUMED [249, 250]. The

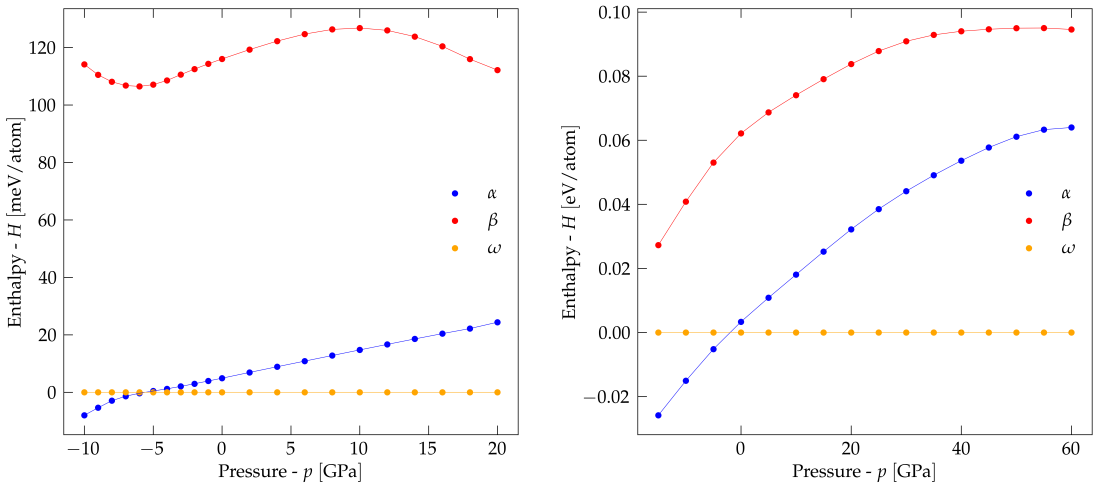

Figure IX.5: (Left) The H-p curve titanium α, β and ω phases for the MEAM potential [26]. (Right) The H-p curve titanium α, β and ω phases for the RANN potential [332].

integration step was set to 1 fs. Nosé-Hoover barostats and thermostats of chain length 3 with MTK correction terms [220] were used. The relaxation times of the barostat and thermostat were set to $0.5\,\mathrm{ps}$ and $0.25\,\mathrm{ps}$, respectively. For parameters of Gaussians, see respective sections.

IX.3.1 Steinhardt's parameters - Q_4 a Q_6

In this section, we summarise the results found when the Steinhardt's parameters are used as collective variables. To be more precise, we use the average of the locally calculated Steinhardt's parameters for the atoms. The Steinhardt's parameters (Q_4 and Q_6) are calculated as follows,

$$q_{lm}(i) = \frac{\sum_{j=1}^{N_i} \sigma(r_{ij}) Y_{lm}(r_{ij})}{\sum_{j=1}^{N_i} \sigma(r_{ij})}, \tag{IX.7}$$

$$Q_l(i) = \sqrt{\frac{4\pi}{2l+1} \sum_{m=-l}^{l} |q_{lm}(i)|^2}, \tag{IX.8}$$

where $\sigma(r_{ij})$ is a suitable switching function, e.g., of the same functional form as the one used for calculation of coordination number for NaCl,

$$\sigma(r_{ij}) = \left(1 + \left(\frac{r_{ij} - d_0}{r_0}\right)^6\right)^{-1}, \tag{IX.9}$$

where Y_{lm} is the spherical harmonic and N_i is the number of neighbours of the i-th atom.

A similar insight as for the case for NaCl, where the derivative of the switching function should overlap between the first and second coordination shell, can be drawn for titanium as well. The transition from the α phase to ω phase is accompanied by the transfer of two atoms from the third coordination shell of the α phase into the first coordination shell of the atom in the ω, and vice versa. Also note that in the α phase every atom in the unit cell has coordination of 12, whereas in the ω phase two atoms in the unit cell have the coordination of 11, and one

atom has the coordination of 14, see e.g Fig. IX.11.

Therefore, a suitable switching function, which have a derivative with a significant overlap between the first coordination shell of ω phase and the third coordination shell of the α phase. A suitable switching function has parameters $d_0 = 1.3$ Å and $r_0 = 2.1$ Å, see Fig. IX.6.

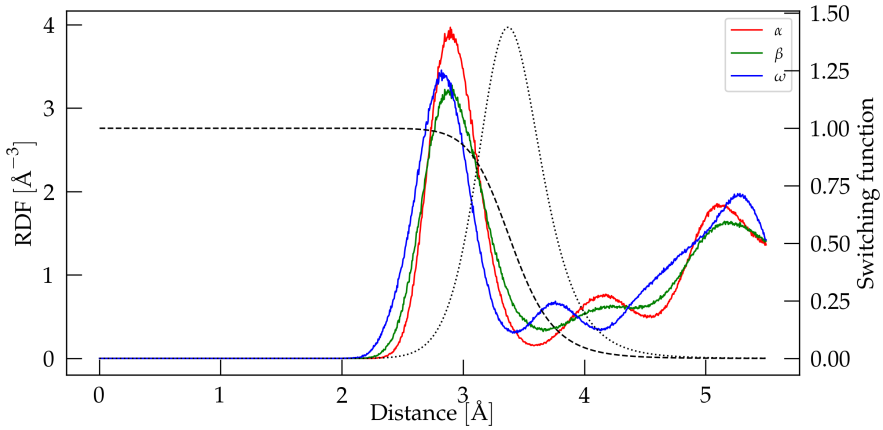

Figure IX.6: Radial distribution function of α phase at 1 000 K and 0 GPa (red), β phase at 1 500 K and 0 GPa (green), ω phase at 1000 K and 12 GPa (blue) and employed switching function used for the calculation of Steinhardt's parameters (dashed) and the absolute value of its derivative (dotted). Note that due to the smearing of the peaks of RDF the second visible peak of α phase actually represents the third coordination shell, as the peaks corresponding to the first and second coordination shell coalesce into an one peak.

The metadynamics simulations were run in supercell of 432 atoms, commensurate with both α and ω phases. The height of Gaussians were set to 0.048 meV/atom, and width 0.005 in both Q_4 and Q_6.

While for the $\omega \rightarrow \alpha$ transition the Steinhardt's parameters represent a set of suitable collective variables, the same is not true for the $\alpha \rightarrow \omega$ transition. For the $\omega \rightarrow \alpha$ transition one can easily extract the height of barrier, see Fig. IX.10, for the found reconstructive mechanism see Fig. IX.11 (which is the same for both the MEAM and the RANN potentials). The same is not true for the $\alpha \rightarrow \omega$ transition, where the nature of the time evolution of CVs hinders the task of the extraction of the barrier, see Fig. IX.7 for the time evolution of CVs for $\omega \rightarrow \alpha$ and $\alpha \rightarrow \omega$ transitions (the value of the CVs in the respective free energy basins have a significant overlap with the transition state as well). For the height of barriers in the collective mechanism for the $\omega \rightarrow \alpha$ transition for various temperatures, see Fig. IX.10. For the transition mechanism see Figs. IX.11 and IX.12.

IX.3.2 Q_4 and enthalpy or volume

Motivated by the success of the application of the coordination number and volume for the case of NaCl, and the success of the use of enthalpy and entropy for liquid-solid transition for sodium and aluminium [335] we tried a combination of Q_4 with volume and Q_4 with enthalpy. However, both combinations did not bring any substantial improvement with respect to the choice of Q_4 and Q_6. For the time evolution of the respective CVs during the metadynamics calculation see Figs. IX.13 and IX.14. One can clearly see that the original combination of Q_4 and Q_6 results in much more diffusive behaviour of the collective variables as these combinations,

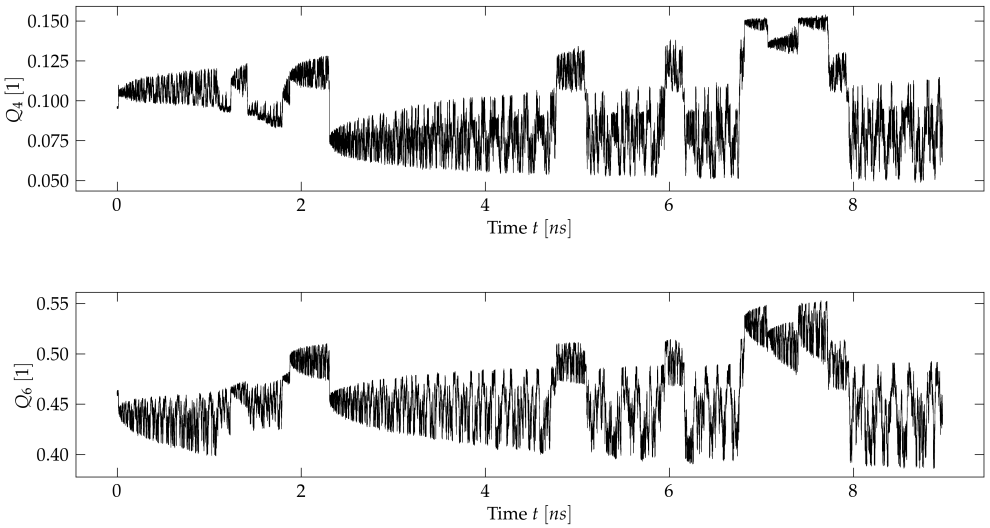

Figure IX.7: The time evolution of the collective variables for the simulation run at 500 K and 0 GPa for the $\omega \rightarrow \alpha$ transition.

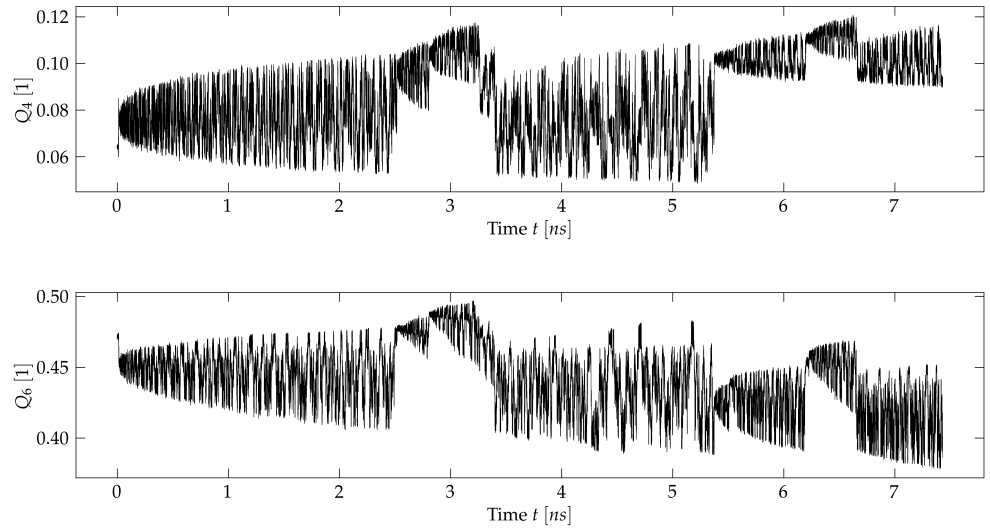

Figure IX.8: The time evolution of the collective variables for the simulation run at 500 K and 5 GPa for the $\alpha \rightarrow \omega$ transition.

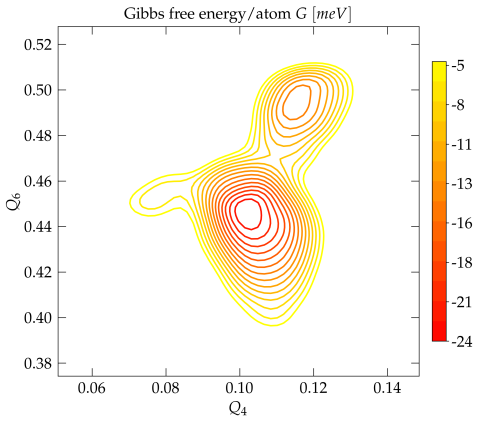

Figure IX.9: Example of free energy surface (FES) as reproduced by MEAM [26] potential just after the first transition to the α phase from the ω phase at T = 500 K and p = 0 GPa. The ω phase is represented on the FES as the major (deepest) minimum, the α phase lies in left and corresponds to the decrease of Q_4 variable (note the small jut on the left part of the FES), and the upper jut corresponds to the transitient structure, see time evolution of CVs in Fig. IX.7.

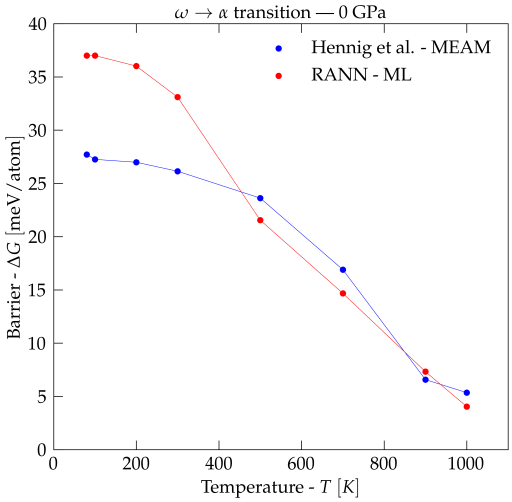

Figure IX.10: The barrier for the collective mechanism for the $\omega \rightarrow \alpha$ transition as found by the MEAM [26] and RANN [332] potentials.

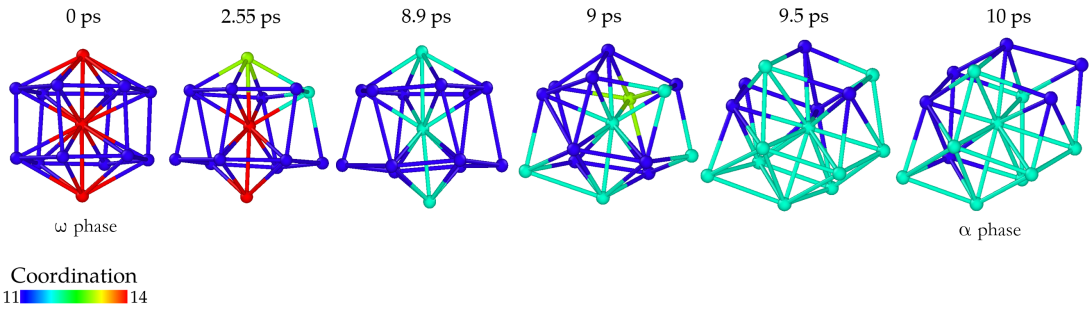

Figure IX.11: Microscopic transition mechanism for the $\omega \rightarrow \alpha$ transition found by the MEAM [26] as well as by the RANN [332] potential.

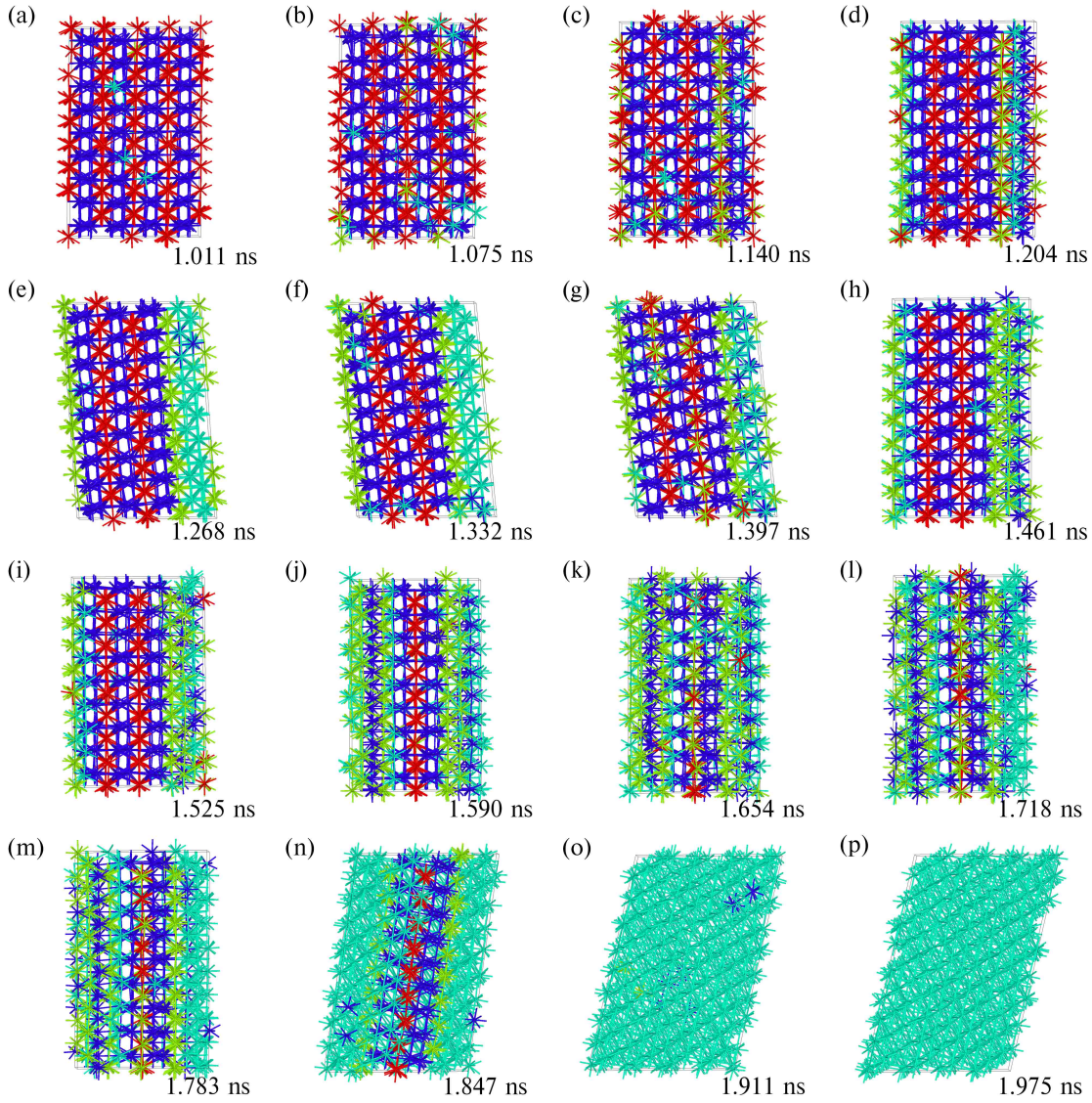

Figure IX.12: Evolution of the system of the size of 432 atoms near the point of the transition at 500 K and 0 GPa for the $\omega \rightarrow \alpha$ transition. (Blue) eleven coordinated atoms (red) fourteen coordinated atoms (green) twelve coordinated atoms.

see also the result on NaCl and the last chapter of this thesis.

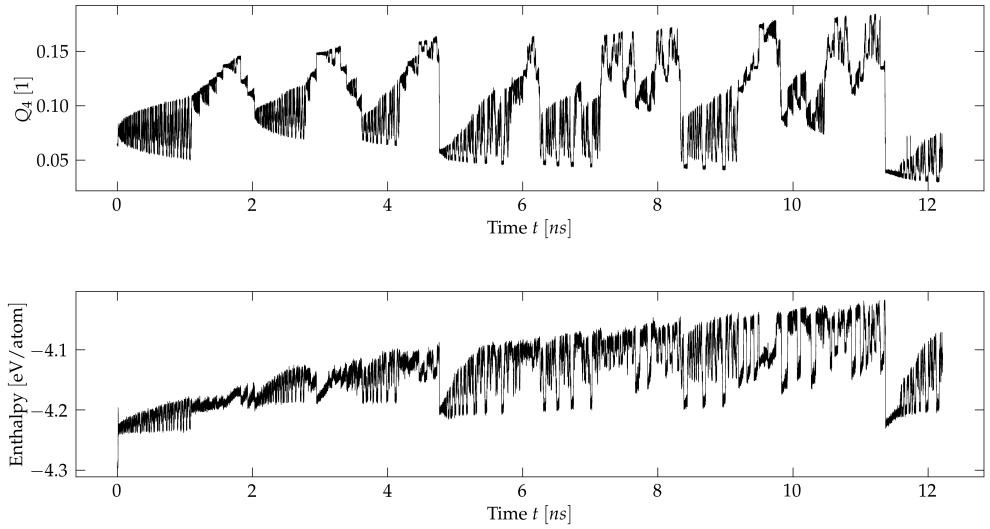

Figure IX.13: The time evolution of the collective variables for the simulation run at 500 K and 5 GPa for the $\alpha \rightarrow \omega$ transition.

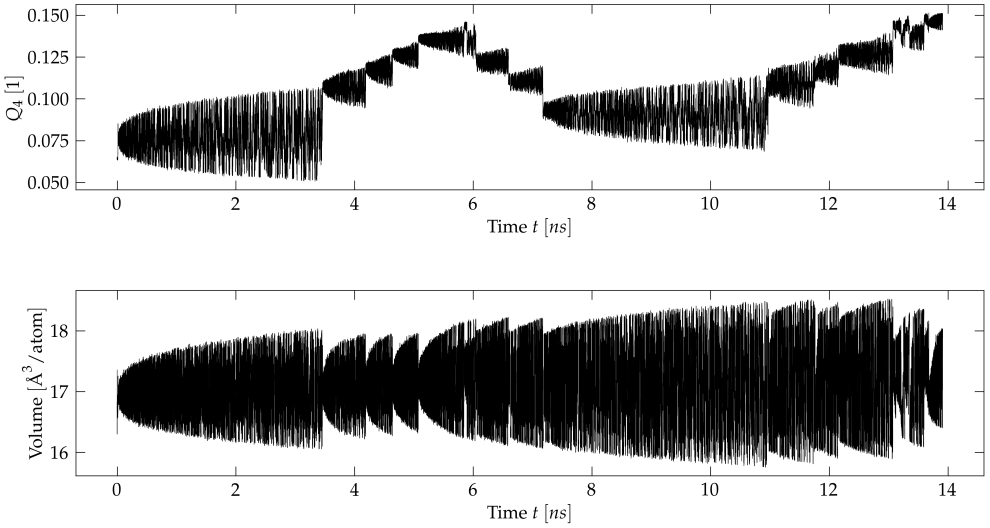

Figure IX.14: The time evolution of the collective variables for the simulation run at 500 K and 5 GPa for the $\alpha \rightarrow \omega$ transition.

The parameters for the metadynamics simulation were as follows. The height of Gaussians was set to 0.048 meV/atom in both cases. The width in the $\mathrm{enthalpy}$ direction was set to 50 meV, the width in the Q_4 direction to 0.005, and the width in volume direction was set to 0.15 $\text{Å}^3/\mathrm{atom}$. The Gaussians were deposited every 500 MD steps. The parameters of the switching function used for calculation of Q_4 was $d_0 = 1.3\,\text{Å}$ and $r_0 = 2.1\,\text{Å}$.

IX.3.3 Behler-Parrinello descriptors

For the task of creation of collective variable which would be able to distinguish the α and ω phase we tried to construct radial and angular Behler-Parrinello descriptors. The motivation behind this choice comes from the ability of the MEAM potential to describe these phases, which

is also based on the radial and the angular part. The second motivation comes from the work of Ackland [336], who showed that a bond-angle distribution related order parameter (ADOP), similar to the angular part of Behler-Parrinello descriptors, is able to differentiate bcc, fcc and hcp phases.

Namely, we tried to construct the Behler-Parrinello descriptors of the following form

$$G_2 = \sum_{i \neq j} e^{-\eta(R_{ij}-R_s)^2} f_c(R_{ij}) \,, \tag{IX.10}$$

$$G_5 = 2^{-22} \sum_{i \neq j,k} (1 + \cos(\theta_{ijk} - \theta_s))^{23} e^{-\eta(R_{ij}/2+R_{ik}/2-R_s)^2} f_c(R_{ij}) f_c(R_{ik}) \,, \tag{IX.11}$$

where

$$f_c(R_{ij}) = \begin{cases} \frac{1}{2}\left[1 + \cos\left(\frac{\pi R_{ij}}{R_c}\right)\right], & R_{ij} \leq R_c \\ 0, & R_{ij} > R_c \,, \end{cases} \tag{IX.12}$$

with the free parameters η, R_s, R_c and θ_s. The optimal choice leads to $R_c = 4\,\text{Å}$, $\eta = 20\,\text{Å}^{-2}$, 6 equidistantly placed Gaussians centers R_s being distributed in radial direction between 2 Å and 4 Å in G_2 descriptor, 6 equidistantly placed Gaussians centers R_s being distributed in radial direction between 2 Å and 4 Å in G_5 descriptor, and 8 equidistantly Gaussians centers θ_s being placed between $\pi/16$ and $17/16\pi$.

However, we found out that the Behler-Parrinello descriptors also do not represent a promising set of CVs for the $\alpha \rightarrow \omega$ transition. The problem is their degeneracy in terms of describing the α and ω phases, see e.g. a few selected histograms depicted in Fig. IX.15. This degeneracy comes from the fact that the nearest neighbour distances are very similar in the α and ω phases as well as the relative angles between the triplets of atoms.

IX.3.4 ACE descriptors

Since the description of the α and ω phases turned out to be degenerate in terms of Behler-Parrinello descriptors, we tried to employ a recently popular ACE formalism [130–138, 142, 143]. In the ACE formalism [130] the scalar quantity - such as the energy of atomic environment $E(\sigma)$ or such as here the scalar descriptor of atomic environment $\varphi(\sigma)$, is expanded in polynomials of basis functions $\phi(r_{ji})$,

$$\begin{aligned} \varphi_i(\sigma) = &\sum_j \sum_v c_v^{(1)} \phi_v(r_{ji}) + \frac{1}{2} \sum_{j_1 j_2} \sum_{v_1 v_2} c_{v_1 v_2}^{(2)} \phi_{v_1}(r_{j_1 i}) \phi_{v_2}(r_{j_2 i}) \\ &+ \frac{1}{3!} \sum_{j_1 j_2 j_3} \sum_{v_1 v_2 v_3} c_{v_1 v_2 v_3}^{(3)} \phi_{v_1}(r_{j_1 i}) \phi_{v_2}(r_{j_2 i}) \phi_{v_3}(r_{j_3 i}) + \dots \,. \end{aligned} \tag{IX.13}$$

In order to avoid the exponential scaling in the body order K - $\mathcal{O}(N^K)$, where N is the number of neighbours, the expansion is expressed in the atomic density - A_{iv},

$$A_{iv} = \sum_j \phi_v(r_{ji}) \,, \tag{IX.14}$$

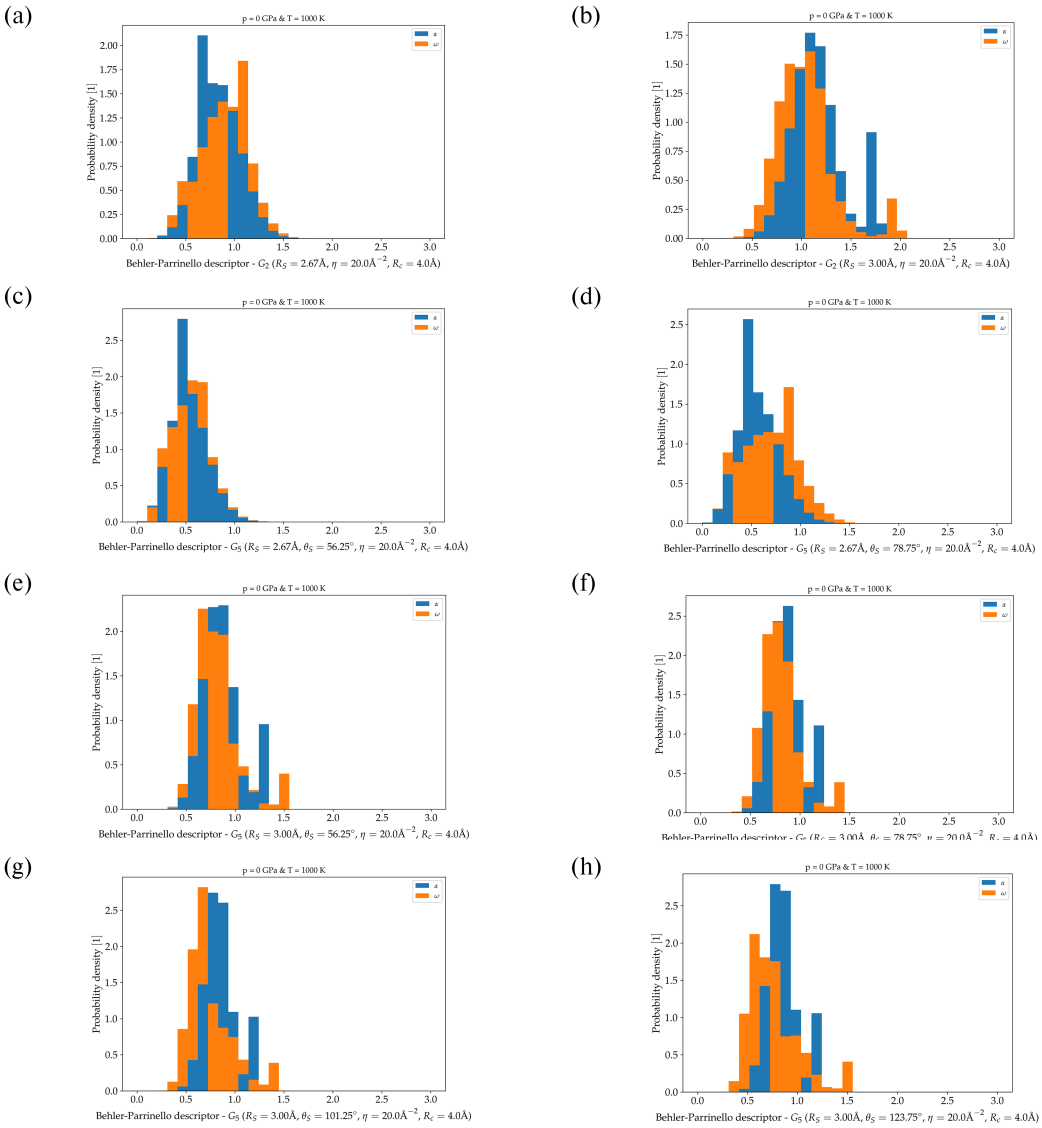

Figure IX.15: A few selected BP descriptors whose values are significantly different from zero showing their degeneracy in respect to the α and ω phases at p = 0 and T = 1 000 K, with the respective parameters of the descriptors written below. (Blue) α phase (Orange) ω phase.

so the expansion for $\varphi(\sigma)$ becomes

$$\varphi_i(\sigma) = \sum_v c_v^{(1)} A_{iv} + \sum_{v_1 v_2}^{v_1 \geq v_2} c_{v_1 v_2}^{(2)} A_{iv_1} A_{iv_2} + \sum_{v_1 v_2 v_3}^{v_1 \geq v_2 \geq v_3} c_{v_1 v_2 v_3}^{(3)} A_{iv_1} A_{iv_2} A_{iv_3} + \dots . \tag{IX.15}$$

The basis function are chosen in the form $\phi_v(\mathbf{r}) = \sqrt{4\pi} R_{nl}(r) Y_l^m(\mathbf{r}/r)$, where $v = (nlm)$, R_{nl} is the radial function and Y_l^m is the spherical harmonic. The radial functions are expanded in the complete set of polynomials,

$$\begin{aligned} R_{00}(r) &= g_0 = 1\,, \\ R_{0l}(r) &= 0 \,\text{for}\, l > 0\,, \\ R_{nl}(r) &= \sum_k c_{nlk} g_k(r) \,\text{for}\, n > 0\,, \end{aligned} \tag{IX.16}$$

where c_{nlk} are subject to optimisation or chosen as simple delta-functions $c_{nlk} = \delta_{nk}$ (as in our case). The functions $g_k(r)$ are chosen in the form

$$\begin{aligned} g_0(r) &= 1\,, \\ g_1(r) &= [1 + \cos(\pi r / r_c)]\,, \\ g_k(r) &= \frac{1}{4}\,[1 - T_{k-1}(x)]\,[1 + \cos(\pi r / r_c)]\,, \end{aligned} \tag{IX.17}$$

where x is the scaled distance $x = 1 - 2(e^{-\lambda(r/r_c - 1)} - 1)/(e^{\lambda} - 1)$, λ and r_c are the free parameters and T_k is the Chebyshev polynomial of the first kind.

The expansion given by Eq. (IX.15) is invariant to translation and inversion but not to rotation. Since the $\varphi(\sigma)$ is a scalar, only a combinations of A_{iv} leading to zero angular momentum (the basis functions $\phi_v(\mathbf{r})$ contain angular parts) can be present in the expansion. Therefore the final expansion leads to

$$\varphi_i(\sigma) = \sum_n c_n^{(1)} B_{in}^{(1)} + \sum_{n_1 n_2 l} c_{n_1 n_2 l}^{(2)} B_{in_1 n_2 l}^{(2)} + \sum_{n_1 n_2 n_3 l_1 l_2 l_3} c_{n_1 n_2 n_3 l_1 l_2 l_3}^{(3)} B_{n_1 n_2 n_3 l_1 l_2 l_3}^{(3)} + \dots\,, \tag{IX.18}$$

where the $\mathbf{B}$ are calculated as follows (the products of A_{iv} leading to zero angular momenta),

$$\begin{aligned} B_{in}^{(1)} &= A_{in00}\,, \\ B_{in_1 n_2 l}^{(2)} &= \sum_{m=-l}^{l} (-1)^m A_{in_1 lm} A_{in_2 l-m}\,, \\ B_{n_1 n_2 n_3 l_1 l_2 l_3}^{(3)} &= \sum_{m_1=-l}^{l} \sum_{m_2=-l}^{l} \sum_{m_3=-l}^{l} \begin{pmatrix} l_1 & l_2 & l_3 \\ m_1 & m_2 & m_3 \end{pmatrix} A_{in_1 l_1 m_1} A_{in_2 l_2 m_2} A_{in_3 l_3 m_3} \\ &\dots \end{aligned} \tag{IX.19}$$

the matrix elements of the Wigner 3j symbol can be found e.g., in the original work on ACE [130].

Due to time limitations, we implemented the ACE formalism only up to the fourth body order (since higher body orders will require implementation of coupling of angular momenta via generalized Clebsch-Gordan coefficients) in which one still found α and ω phases to be degenerate, see Fig. IX.16, even though the fourth body order descriptors are already beyond Behler-Parrinello descriptors (which are of second and third body order). We expect that this

degeneracy will diminish with higher order descriptors since the ACE formalism with body order up to five and hundreds of basis functions was successfully used in creation of machine learning potentials [130, 132, 133, 138, 142].

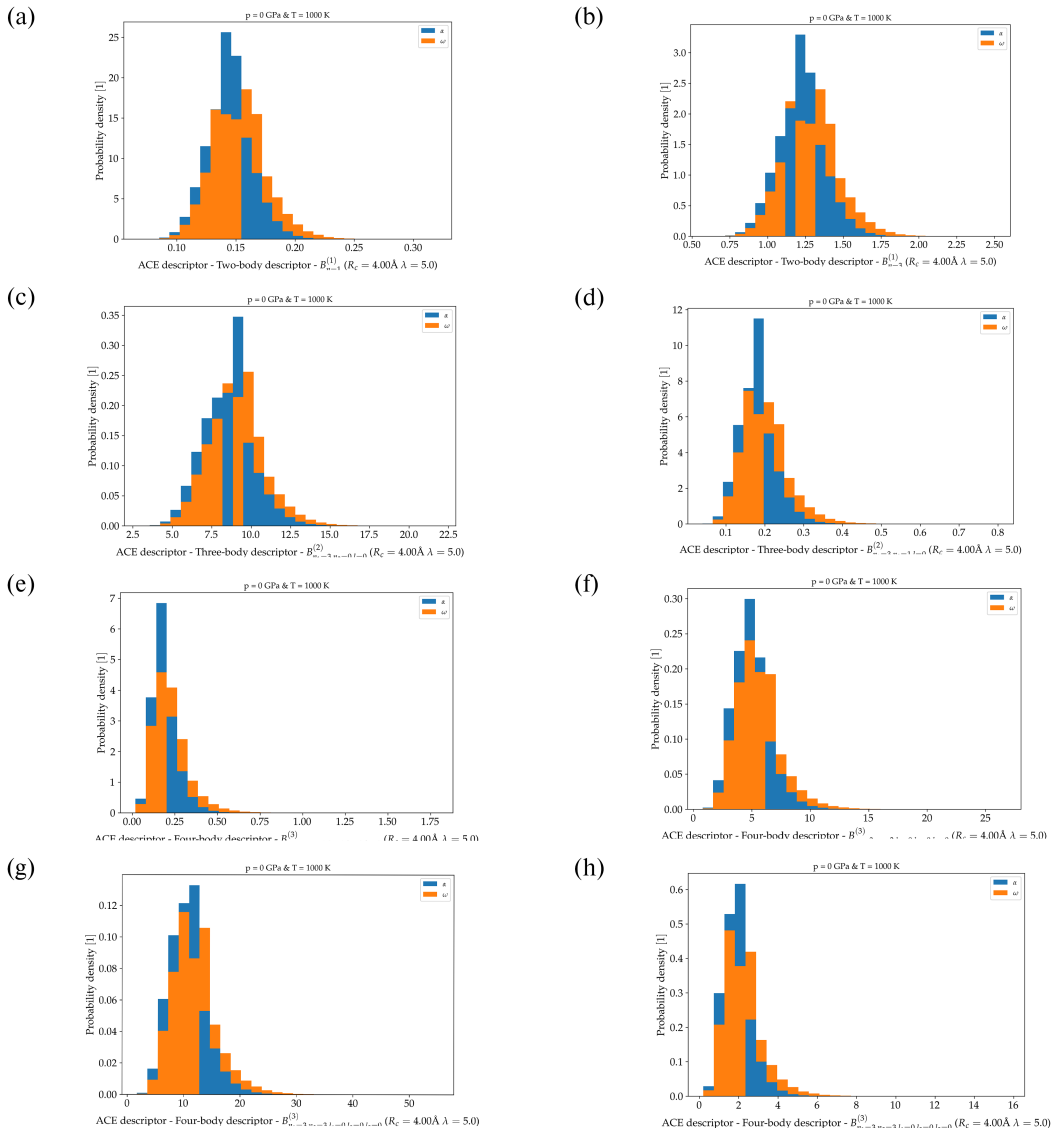

Figure IX.16: A few selected ACE descriptors (of second, third and fourth order) whose values are significantly different from zero showing their degeneracy in respect to the α and ω phases at p = 0 and T = 1 000 K, with the respective parameters of the descriptors written below. (Blue) α phase (Orange) ω phase.

X Assessment of the suitability of CVs for metadynamics simulations

In this last chapter of this thesis, we present yet unpublished results obtained in collaboration with prof. A. Laio on the assessment of the suitability of CVs in metadynamics simulations. The original motivation behind this algorithm was the success of the ability of the coordination number and volume to induce the structural transformation in NaCl and the "diffusiveness" of this combination in terms of their time evolution, see Ch. VI. In this chapter, we introduce a formal algorithm which can assess the suitability of CVs for metadynamics simulations via the inspection of their diffusive limit. We benchmark the approach on a model as well as on realistic situations - folding of alanine dipeptide and the mentioned B1-B2 transition in NaCl, see Ch. VI.

The success of not only metadynamics [148, 149] but also of other free energy estimation methods such as umbrella sampling [337], weighted histogram analysis method (WHAM) [338], adaptive biasing force method [339], or more recently, variationally enhanced sampling (VES) [340] and on-the-fly probability enhanced sampling (OPES) [341, 342] is contingent to the choice of collective variables. In most of these approaches, CVs should be able to distinguish all relevant metastable states, and all the transition states [149]. In the recent past, the choice and the explicit construction of the CVs was facilitated by unsupervised learning and machine learning techniques [151, 153, 154, 157–160, 180, 343–353], but the assessment of the quality of a CV is up to these days still performed largely based on domain experience, e.g., in metadynamics, by visual inspection of the trajectory followed by the CVs [149]. Moreover, while the particular choice of CVs can lead to convergence [150], the true free energy barrier can differ from the observed converged estimate [354].

Our approach is based on the monitoring of the diffusion properties of the CVs during a metadynamics run. Indeed, if the chosen set of CVs is correct, metadynamics should in a sufficiently long time fill all free energy minima and the metadynamics walker should start to diffuse in CV space [149, 150, 164, 355], see Fig. X.1 for illustration.

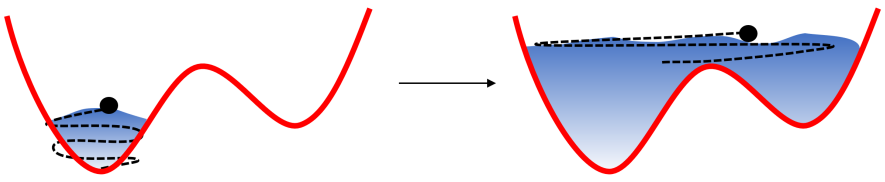

Figure X.1: Illustration of the filling of the free energy surface. In sufficiently long time all free energy minima should be filled, the free energy surface should be flat, except fluctuations, and the metadynamics walker should diffuse in the whole CV space.

We quantify the "diffusiveness" by measuring the discrepancy between the empirical Green function observed in the simulation and the Green function that should be observed if the dynamics of the CV corresponds to a genuine diffusion process. We quantify the "distance"

between the two Green functions by means of a Kolmogorov-Smirnov statistical test [356]. This allows accepting or rejecting the null hypothesis that the observed time-evolution of CVs follows a diffusion process and, as a consequence, deciding if the CV is appropriate or not.

X.1 Algorithm

We assume that metadynamics is performed using a n-dimensional collective variable $\mathbf{S}$ with reflective boundary condition (RBC) in every component of $\mathbf{S}$ as described in Ref. [150]. Later, we show that this assumption is not crucial and this procedure can be applied also to the cases when the metadynamics were not run with RBC. Assuming the metadynamics is run long enough, the metadynamics walker fills all free energy minima and starts to diffuse in CV space. Since after filling all free energy minima, the free energy profile is almost flat (except for fluctuations) [150], the dynamics, in ideal conditions, decouples to n independent diffusion processes in every component of $\mathbf{S}$.

Hence from now on, we consider, without loss of generality, a diffusion of a single scalar variable S, as a CV. We rescale first the collective variable S using its minimal S_{min} and maximal value S_{max} as $s(t) \equiv \frac{2S(t)-(S_{\text{max}}+S_{\text{min}})}{S_{\text{max}}-S_{\text{min}}}$, thus $s(t) \in \langle -1, 1\rangle$. Our approach for assessing convergence is based on monitoring the joint probability density $\mathrm{P}(s,t;s',0)$ of observing the CV at the time 0 at a position s' and at a time t at a position s. The joint probability density can be expressed using the stationary probability distribution $\mathrm{P}_{\text{st}}(s) = 1/2$ and the conditional probability $\mathrm{P}(s,t|s',0)$ as

$$\mathrm{P}(s,t;s',0) = \mathrm{P}(s,t|s',0)\mathrm{P}_{\text{st}}(s')\,. \tag{X.1}$$

In ideal conditions, when the dynamics is diffusive, the transition probability $\mathrm{P}(s,t|s',0)$ is the solution of a one-dimensional Fokker-Planck equation with a vanishing drift coefficient and a constant diffusion coefficient (Wiener process)

$$\frac{\partial \mathrm{P}}{\partial t} = \mathrm{D}\frac{\partial^2 \mathrm{P}}{\partial s^2}\,, \tag{X.2}$$

on a finite line of length 2 with RBCs ($\partial \mathrm{P}/\partial \mathrm{s}|_{\mathrm{s}=-1} = 0$ & $\partial \mathrm{P}/\partial \mathrm{s}|_{\mathrm{s}=+1} = 0$) and an initial condition $\mathrm{P}(s,0|s',0) = \delta(\mathrm{s}-\mathrm{s}')$.

To simplify the following analytical formula, we restrict to the transition probability at time τ of finding the metadynamics walker at position s, given we observe the walker at time 0 at position 0. We label this transition probability as $\mathrm{P}(s,t|0,0)$. This can be calculated by separation of variables $\mathrm{P}(s,t|0,0) = \phi(s)e^{-\lambda t}$. This gives

$$\mathrm{P}(s,t|0,0|D) = \frac{1}{2} + \sum_{n=1}^{\infty} \cos(\pi n s)\exp\left[-\pi^2 n^2 D t\right]. \tag{X.3}$$

Using this explicit solution we are able to infer the diffusion constant D from a series of numerically estimated histograms of observing the CV at position s after a time lag τ (see Sec. X.1.1). Next, by fixing the value of Dt to 0.1, see Sec. X.1.2, we verify the hypothesis that the dynamics is described by a diffusion process by a Kolmogorov-Smirnov statistical test. In short, this is done by comparing the empirical and theoretical Green functions and deciding if their difference can be described by statistical fluctuations.

X.1.1 Inference of D from metadynamics data

To infer the diffusion constant D from the metadynamics data - $s(t)$, we proceed as follows. First, we find in the CV trajectory $s(t)$ all the times t_i in which it crosses the $s = 0$ surface, namely such that $(s(t_{i-1}) < 0 \,\&\, s(t_i) > 0) \,|\, (s(t_{i-1}) > 0 \,\&\, s(t_i) < 0)$. We exclude from the analysis the first part of the dynamics, in which the free energy profile has not yet been filled with Gaussians. We then estimate the empirical probability density functions $\mathrm{P}_{\mathrm{emp}}(s, \tau|0, 0)$ of finding the walker at position s at the time $t_i + \tau$ given that $s = 0$ at time t_i.

If the CV follows a diffusion process and we know the underlying diffusion constant D, the empirical histograms $\mathrm{P}_{\mathrm{emp}}(s, \tau|0, 0)$ should match the theoretical one $\mathrm{P}(s, \tau|0, 0|D)$ (Eq. X.3) for any choice of τ. Note that the transition probability density function, $\mathrm{P}(s, \tau|0, 0|D)$, is the function of the product $D\tau$ only. For $D\tau \gg 1$, the transition probability is close to $1/2$ everywhere. On the contrary, for $D\tau \to 0$ the transition probability is close to the Gaussian-like peak around $s = 0$. In the intermediate regime, $D\tau \sim 0.1$, the transition probability is largely broadened from the Gaussian-like peak towards the reflective boundaries, see the last row of Fig. X.2 for illustration. Therefore, the deviations from the diffusivity on the empirical histogram can be expected to be most pronounced in the intermediate regime when $D\tau \sim 0.1$.

Thus, we can infer the diffusion constant D by minimizing the L_2 loss between the empirical and theoretical histograms for a suitable choice of $D\tau$, e.g., $D\tau = 0.1$,

$$L_2(D) = \int_{-1}^{1} \mathrm{d}s(\mathrm{P}_{\mathrm{emp}}(s, \tau = 0.1/D|0, 0) - \mathrm{P}(s, \tau = 0.1/D|0, 0))^2 \,. \tag{X.4}$$

The empirical histograms $\mathrm{P}_{\mathrm{emp}}(s, \tau_i|0, 0)$ are evaluated on a grid $s \in < -1, 1 >$ where the number of bins is set to the square root of the number of observations $s(t_i)$ from which the histogram is constructed.

X.1.2 Quantifying the deviation of the CV dynamics from a diffusion process

Once the diffusion constant D has been obtained we can compare the empirical histogram (based on the observed data) $\mathrm{P}_{\mathrm{emp}}(s, \tau|0, 0)$ with the theoretical probability density $\mathrm{P}(s, \tau|0, 0)$ (given by Eq. X.3) at a given time-lag τ. Note that given the hypothesis that the CV follows a diffusion process, they should match, except for statistical errors, for any choice of τ. To quantify the deviation from diffusivity, we compare a suitable representative pair of histograms, namely the histograms for which time lag τ yields the value $D\tau = 0.1$, by means of Kolmogorov-Smirnov (KS) statistical test [356].

We briefly review the KS statistical test [356]. For a desired value of statistical significance p of accepting a hypothesis (in our case that dynamics of the CV is described by diffusion), there is a critical maximal difference - d_p between the empirical cumulative density functions $F_{\mathrm{emp}}(s, \tau = 0.1/D)$ calculated from $\mathrm{P}_{\mathrm{emp}}(s, \tau = 0.1/D)$ and the cumulative density function $F(s, \tau = 0.1/D)$ corresponding to $\mathrm{P}(s, \tau = 0.1/D)$,

$$d = \sup_s |F_{\mathrm{emp}}(s, \tau = 0.1/D) - F(s, \tau = 0.1/D)| \,, \tag{X.5}$$

The critical maximal difference depends on p and on the number of observations N used for the empirical determination of $\mathrm{P}_{\mathrm{emp}}(s, \tau = 0.1/D)$ [356]. If $d < d_p(N)$ the hypothesis is accepted,

if $d > d_p(N)$ then it is rejected. The values of $d_p(N)$ are tabulated [356]. E.g., for $N > 40$ and $p = 0.01$, $d_{p=0.01}(N) \approx 1.63/\sqrt{N}$.

In order to minimize the effect of correlations, which are unavoidably present in the CV trajectory, we periodically decimate the times t_i at which the CV crosses the $s = 0$ manifold taking into account e.g. only every second point, every third point, etc., thus obtaining a set of $\mathrm{P}_{\mathrm{emp}}(s, \tau = 0.1/D)(N)$ which differ in the number of observations N from which they are constructed. For every empirical histogram $\mathrm{P}_{\mathrm{emp}}(s, \tau = 0.1/D)(N)$ we then calculate the result of KS test, thus obtaining a set of values $d(N)$. For small N, however, the histogram becomes noisy and therefore we inspect the limit of $d(N)$ for large N, e.g. the values for the 20 largest N, and compare it to $d_p(N)$. If $d(N) < d_p(N)$ the hypothesis that the dynamics of the CV is diffusive is accepted, if $d(N) > d_p(N)$ the hypothesis is rejected.

X.2 Benchmark on a model free energy surface (FES)

We illustrate our approach on a series of two-dimensional model free energy surfaces (FES), on which we perform an overdamped Langevin metadynamics using discrete equations presented in Eq. X.6, with the χ_x and χ_y being the random numbers sampled from a normal distribution, $\chi_x, \chi_y \in \mathcal{N}(0, 1)$, the $F_{\mathrm{MetaD}}(x)$ being a history-dependent metadynamics potential, given by Eq. X.7 (with height of Gaussians - H, width of Gaussians - w centered at positions $x(t_i)$), and the metadynamics being performed with RBCs on x, with boundaries at $x = -1$ and $x = +1$. The diffusion constant in pure Langevin MD D is set to the value $D = 0.1$ and the timestep is set to value $\Delta t = 0.01$.

$$
\begin{aligned}
x(t + \Delta t) &= x(t) + \sqrt{2D\Delta t}\chi_x - \frac{D\Delta t}{k_B T}\left(\frac{\partial F(x, y, \lambda)}{\partial x} + \frac{\partial F_{\mathrm{MetaD}}(x)}{\partial x}\right), \\
y(t + \Delta t) &= y(t) + \sqrt{2D\Delta t}\chi_y - \frac{D\Delta t}{k_B T}\left(\frac{\partial F(x, y, \lambda)}{\partial y}\right),
\end{aligned} \tag{X.6}
$$

The history-dependent metadynamics potential has the form,

$$
F_{\mathrm{MetaD}}(x) = \sum_{i; t_i < t} \mathrm{H} \cdot \mathrm{Exp}\left[-\frac{(x - x(t_i))^2}{2w^2}\right]. \tag{X.7}
$$

For the illustration of the algorithm we perform overdamped Langevin metadynamics described by Eq. X.6 in a hypothetical free energy surface (FES) given by Eq. X.8 with free parameter λ changing the position of free-energy minima and shape of FES, see Fig.X.2.

$$
\begin{aligned}
F(x, y, \lambda)/k_B T = -25 \cdot \mathrm{Exp}[-2((\mathrm{gX}(-1, 0, \lambda) - x)^2 + (\mathrm{gY}(-1, 0, \lambda) - y)^2 \\
+\lambda \cdot 0.07((\mathrm{gX}(-1, 0, \lambda) + \mathrm{gY}(-1, 0, \lambda)) - (x + y))^3 \\
-\lambda \cdot 0.9((-f(-x, -2) - \mathrm{gX}(-1, 0, \lambda))^3)] \\
-25 \cdot \mathrm{Exp}[-2((\mathrm{gX}(1, 0, \lambda) - x)^2 + (\mathrm{gY}(1, 0, \lambda) - y)^2 \\
-\lambda \cdot 0.07((\mathrm{gX}(1, 0, \lambda) + \mathrm{gY}(1, 0, \lambda)) - (x + y))^3 \\
+\lambda \cdot 0.9((f(x, -2) - \mathrm{gX}(1, 0, \lambda))^3)],
\end{aligned} \tag{X.8}
$$

where

$$\begin{aligned} \mathrm{gX}(x, y, \lambda) &= \cos(\pi\lambda/2) \cdot x - \sin(\pi\lambda/2) \cdot y \\ \mathrm{gY}(x, y, \lambda) &= \cos(\pi\lambda/2) \cdot x + \sin(\pi\lambda/2) \cdot y \end{aligned} \tag{X.9}$$

and

$$f(x, a) = g(x, a) \cdot \left(\frac{g(a + 0.0001, a)}{g(a - 0.0001, a)} + \left(-\frac{g(a + 0.0001, a)}{g(a - 0.0001, a)} + 1 \right) \cdot \Theta(x - a) \right) \tag{X.10}$$

where Θ is Heaviside theta function and $g(x, a)$ is a switching function of following form,

$$g(x, a) = \log(1 + \exp(x - a)) + a + (-a - \log(1 + \mathrm{e})) \cdot \Theta(-x + a) + (\mathrm{e} - 2.0) \cdot \Theta(-x + a) \tag{X.11}$$

The free parameter λ, smoothly changes the landscape from the case (panel a) ($\lambda = 0$) where the CV is able to distinguish an initial state, the transition state and the final state to the case where this is not true (panels b - e) ($0 < \lambda \leq 0.5$). The time evolution of the CV - X and the time evolution of the estimate of the barrier are shown in Fig.X.2. Note that as the parameter λ is increased the error in the reconstructed free energy barrier increases (the green vs. the blue lines in the third row in the Fig.X.2, see also Fig. X.3). This error rises by order of magnitude as λ approaches 0.5. For values of λ much larger than 0.5 the concept of free energy barrier becomes meaningless as the FES suffers from large hysteresis effects (only one minimum is present). Note that the error in the reconstructed free energy barrier shown in Figs. X.2 and X.3 was calculated as the cumulative time average of the instantaneous estimate.

In the last row, we plot the empirical histograms (leading to value $D\tau = 0.1$) together with the exact Green function (Eq. X.3). One can clearly see the "jumping behaviour" of time evolution of CV (see panel e - for $\lambda = 0.5$) which manifests in artifacts of the empirical histograms that deviate largely from the expected analytical result. Note, in particular, the presence of additional peaks for large λ values.

In Fig. X.3, we plot the error in the reconstruction of the free energy barrier (the difference between the green and blue lines in the third row in Fig. X.2) and the limit of $d(N)\sqrt{N}$ obtained from the analysis of d for the range $0 \leq \lambda \leq 0.5$. We see that the values of Kolmogorov-Smirnov statistics correlate with the errors of the reconstructed free energy barriers. In particular, the relative error remains smaller than ~ 3 % for all the values of λ for which the hypothesis that the CV dynamics is diffusive is accepted.

It is also worth to mention and show, how does the diffusion constant measured in the actual metadynamics simulation change comparing to the value of the diffusion constant in the underlying overdamped Langevin dynamics given e.g., by Eq. (X.6). For the sake of completness, we performed metadynamics simulations in a flat one-dimensional free energy surface and plotted the ratio of the measured diffusion constant D^* to the diffusion constant in the underlying overdamped Langevin dynamics - D_0 as the function of the parameters of the metadynamics in Fig. X.4.

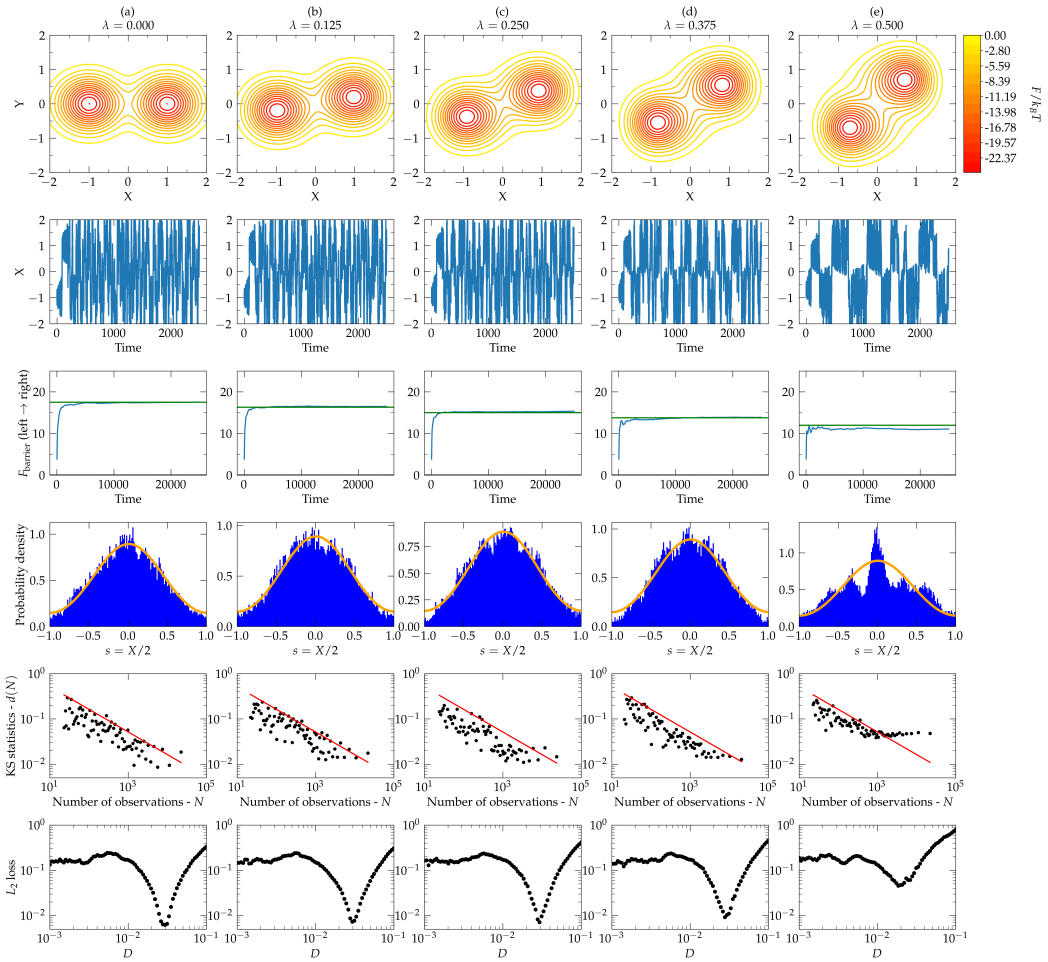

Figure X.2: (First row) Model free energy surface (FES) as function of variable λ. Increasing the parameter λ moves the free energy minima closer to each other in variable X and tilts the free energy surface. (Second row) Time evolution of variable X in metadynamics simulations biasing only the variable X. (Third row) Time evolution of the estimate of the free energy barrier (blue) vs. the true free-energy barrier in X-variable (after integrating out the y-variable) (green). (Fourth row) The empirical (blue) and exact (orange) Green function at the time τ providing the value $D\tau = 0.1$. Note the presence of additional peaks - artifacts as the λ is increased towards the value 0.5. (Fifth row) KS statistics d as the function of the number of observations N taken into account. (Sixth row) L_2 loss, see Eq. X.4, as the function of diffusion constant.

X.3 Further benchmarks of the algorithm

X.3.1 The B1-B2 transition in NaCl

First, we demonstrate the method on a pressure-induced structural phase transition in sodium chloride presented in Ch. VI.

We compare two situations - (a) when one uses the CN as the only CV and (b) when one uses both CN and volume as the CVs. Recall, that the suboptimality of using CN as the single CV has an underlying physical interpretation. Since, the parameters of switching function, see Eq. (VI.2),

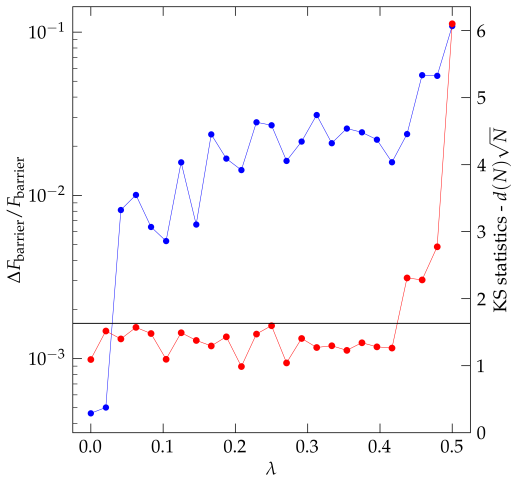

Figure X.3: The relative error on the barrier (blue) and the value of KS statistics (red) (obtained from a single simulation for every λ) for various metadynamics simulations biasing only the X-variable while changing the shape of 2D FES through the parameter λ. The critical line for acceptance of the hypothesis that the CV dynamics is diffusive is set to - $d_{p=0.01}(N)\sqrt{N} = 1.63$ (black line).

are not scaled with volume the structural phases are represented as rather long and narrow valleys on 2D FES. If CN is used as the only CV, the long and narrow valley, see Fig. VI.8 overlaps in the CN coordinate with the transition states, similarly as here the variable X on the hypothetical 2D FES when $\lambda > 0$, see Fig. X.2. Using the CN solely as CV thus cannot efficiently disentangle two different ways how the CN can change on 2D FES - by "breathing" (isotropic change of volume) of the crystal preserving the structure or by structurally changing the crystal structure.

The results of our method are presented in Fig. X.5. We note that since the metadynamics were not run with the RBCs, we choose smaller value of the phase $Dt = 0.02$, when the exact Green function does not reach the boundaries, to avoid potential artifacts which could be caused by a small steady exploration of the CV space as the simulation progresses. Our method rejects the diffusivity of CN in the case when it is used as the only CV and accepts CN as a suitable CV in the case when both CN and volume are used as the CVs. Thus, our method is able to point to the case of sub-optimality of use of CN as a single CV. Moreover, one is able to quantify this increase of diffusion constant of the CN - to find a factor 2.8 when one adds the volume as the second CV. We also stress that the smaller choice of phase factor Dt in the procedure can lead to successful application of our method also for the simulations run without the RBCs (as it is probably the case for a usual metadynamics simulation).

Simulation details

For the details of the metadynamics simulations of the B1-B2 transition in NaCl see Ch. VI. We compared two simulations, where both systems have the size of 512 atoms and were simulated at $p = 20\,\text{GPa}$ and $T = 300\,\text{K}$. In both types of simulations, the coordination number is calculated using the switching function of the form presented in Eq. (VI.2) with the choice of free parameters described in Ch. VI .

For the metadynamics simulations using the CN as the only CV, the parameters of Gaussians

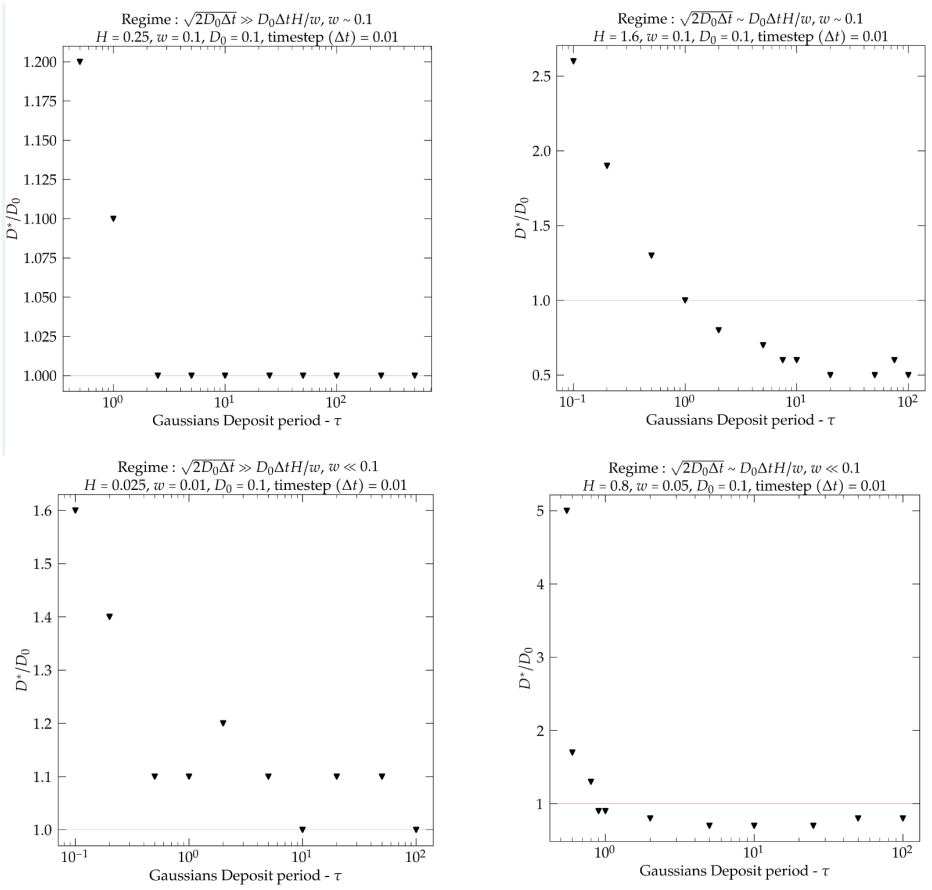

Figure X.4: Ratio of the measured diffusion constant D^* in the 1D metadynamics simulation with the flat free energy surface $F(x) = 0$ to the diffusion constant of the underlying overdamped Langevin metadynamics D_0 as the function of the Gaussian deposit rate. Height of Gaussians is expressed in multiplies of k_BT. Four regimes can be found. In some regimes the diffusion under presence of metadynamics is actually slower than unbiased overdamped Langevin dynamics. Note that in the limit of small deposit times the diffusion is always pronounced.

are $H = 0.41$ meV/atom and width of 0.03 in the CN-coordinate being deposited every 1000 MD steps (with a single MD step of 2 fs). For metadynamics simulations using both CN and volume as CVs, the parameters of Gaussians are $H = 0.41$ meV/atom and widths of 0.03 in the CN-coordinate and 0.03 Å^3/atom in the volume, being deposited also every 1000 MD steps (with a single MD step of 2 fs).

For time evolution of all variables in all respective simulations please see Figs. X.6.

X.3.2 Alanine dipeptide

To demonstrate the method further, we have chosen another paradigmatic model - alanine dipeptide. We compared three one-dimensional metadynamics simulations of alanine dipeptide (in a water solution of 744 molecules), namely, (a) using the Ramachandran angle ϕ as the only CV, (b) using the Ramachandran angle ψ as the only CV, and (c) using a path collective variable (with a fixed cyclic path joining the $C7_{eq}$ and $C7_{ax}$ states in the most optimal way) employed on the ϕ-ψ space using a method presented in Ref. [357], see Sec 5.3 there. We note that contrary to Ref. [357], we use only a single walker.

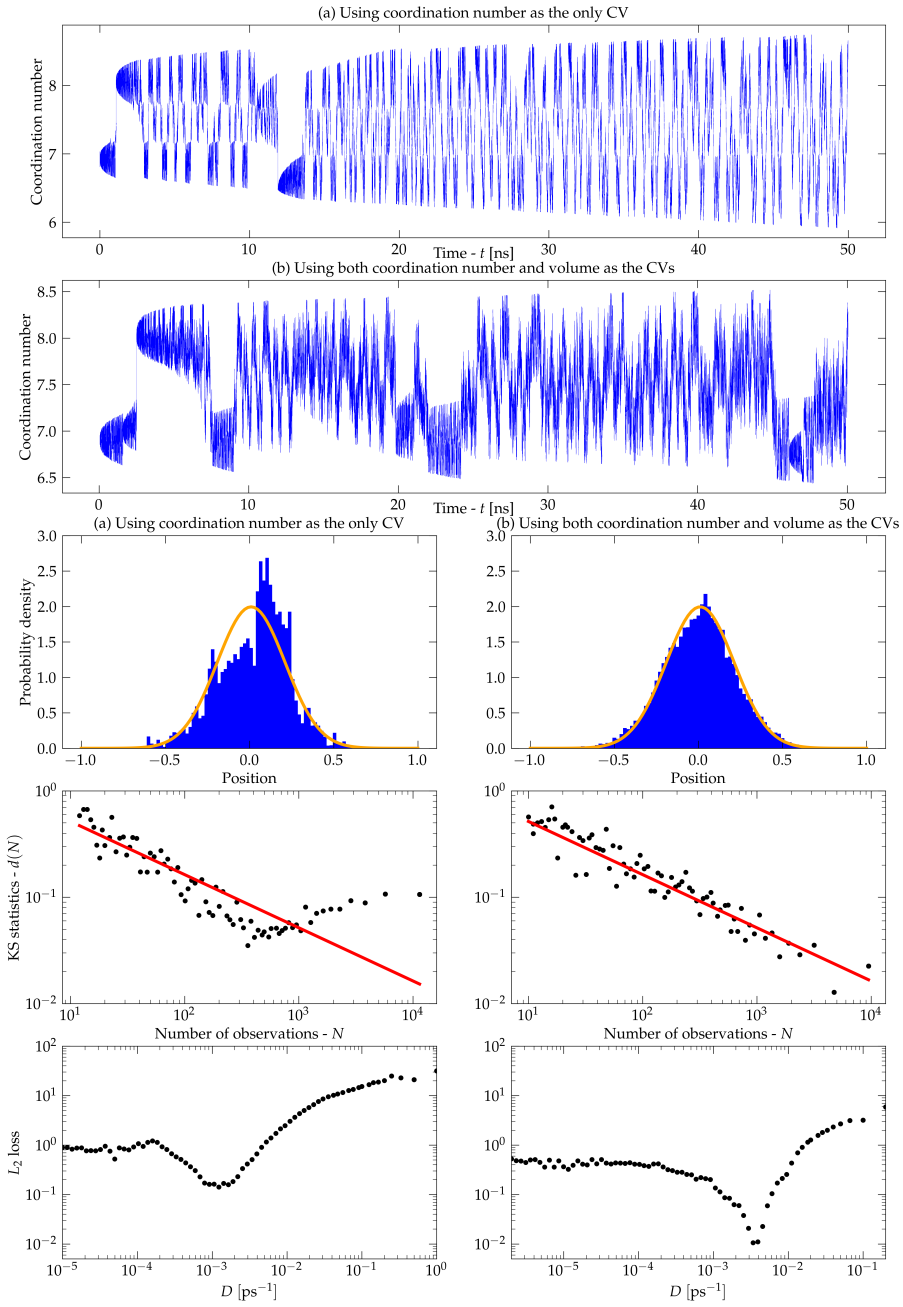

Figure X.5: (First row) Time evolution of coordination number (CN) in simulation which uses CN as the only CV. (Second row) Time evolution of CN in simulation which uses both CN & volume as the CVs. (Third row) The best fit empirical histograms and exact probability density functions (Green functions) for $Dt = 0.02$. Note the artefacts present for the simulations which uses the CN as the single CV. (Fourth row) KS statistics - d as the function of the number of observations N taken for the construction of the empirical histograms. (Fifth row) Obtained L2 loss (see Eq. X.4) as the function of diffusion constants. The inferred diffusion constants are $1.2 \cdot 10^{-3}\text{ps}^{-1}$ and $3.4 \cdot 10^{-3}\text{ps}^{-1}$, respectively.

We present the results of our method in Fig. X.7. We note that since the metadynamics were not run with the RBCs, we also chose a smaller value of the phase $Dt = 0.02$.

Our method rejects all three variables as the suitable CVs, even though the time evolution of

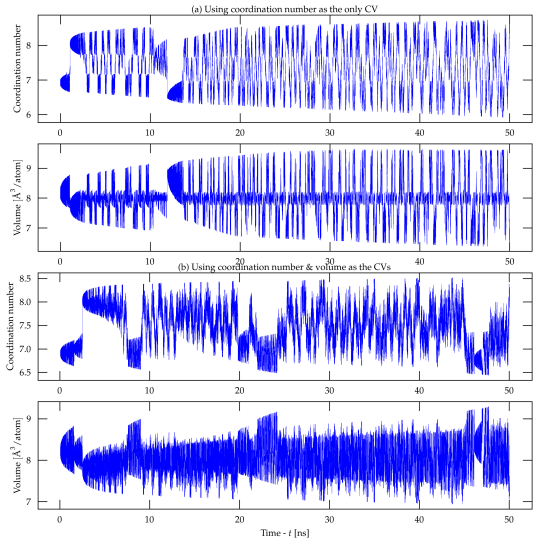

Figure X.6: (First row) Time evolution of CN in the simulation which uses CN as the only CV. (Second row) Time evolution of volume in the simulation which uses CN as the only CV. (Third row) Time evolution of CN in the simulation which uses both CN & volume as the CVs. (Fourth row) Time evolution of volume in the simulation which uses both CN & volume as the CVs.

respective CVs looks diffusive. The conclusion is not surprising for the angles ψ and ϕ alone, as the both angles ψ and ϕ are known to be a good set of CVs when used as CVs at the same time. However, the conclusion is surprising for the path-CV variable, when one would expect that the CV along the optimal path should be a good one-dimensional CV too. However, one should also note that the deviation from the diffusive limit is the smallest among the three studied for the path-CV. These results should be viewed as a limitation of the current form of our method.

Simulation details

For the metadynamics simulations of alanine dipeptide using the Ramachandran angle ψ as the single CV, the Gaussians of $H = 1.2\,\mathrm{kJ/mol}$ and $w = 0.2$ were used and being deposited every 500 MD steps. For the metadynamics simulations of alanine dipeptide using the Ramachandran angle ϕ as the single CV, the Gaussians of $H = 1.2\,\mathrm{kJ/mol}$ and $w = 0.2$ were used and being deposited every 500 MD steps.

For the metadynamics simulations of alanine dipeptide using the path CV the parameters were as follows. The path was first optimized in a separate 10 ns metadynamics run as described in Sec 5.3 in Ref. [357], this obtained path was the same as the path presented in Fig. A7 in Ref. [357]. Later, a metadynamics is run with the optimized path, using the path collective variable s which measures the progress along the path, with Gaussian height $H = 0.33\,\mathrm{kJ/mol}$, $w = 0.05$, and the Gaussians being deposited every 250 MD steps. To constrain the MD walker along the path, a harmonic well $(1/2\kappa z^2)$ is used with $\kappa = 209.2\,\mathrm{kJ/mol}$ using variable z - being perpendicular to the progress along the path.

AMBER99SB-ILDN and TIP3P force fields were used. Modified Berendsen barostats and thermostats were used. The relaxation times of the barostat and thermostat were set to 0.25 ps and 0.1 ps, respectively. Integration step of $2\,\mathrm{fs}$ were used. The cutoff for long-range interaction was set to $10\,\text{Å}$. Coulomb interactions were evaluated using the particle mesh Ewald method. Metadynamics calculations were performed using GROMACS [358] and PLUMED [249, 250].

For time evolution of all variables in all respective simulations please see Figs. X.8.

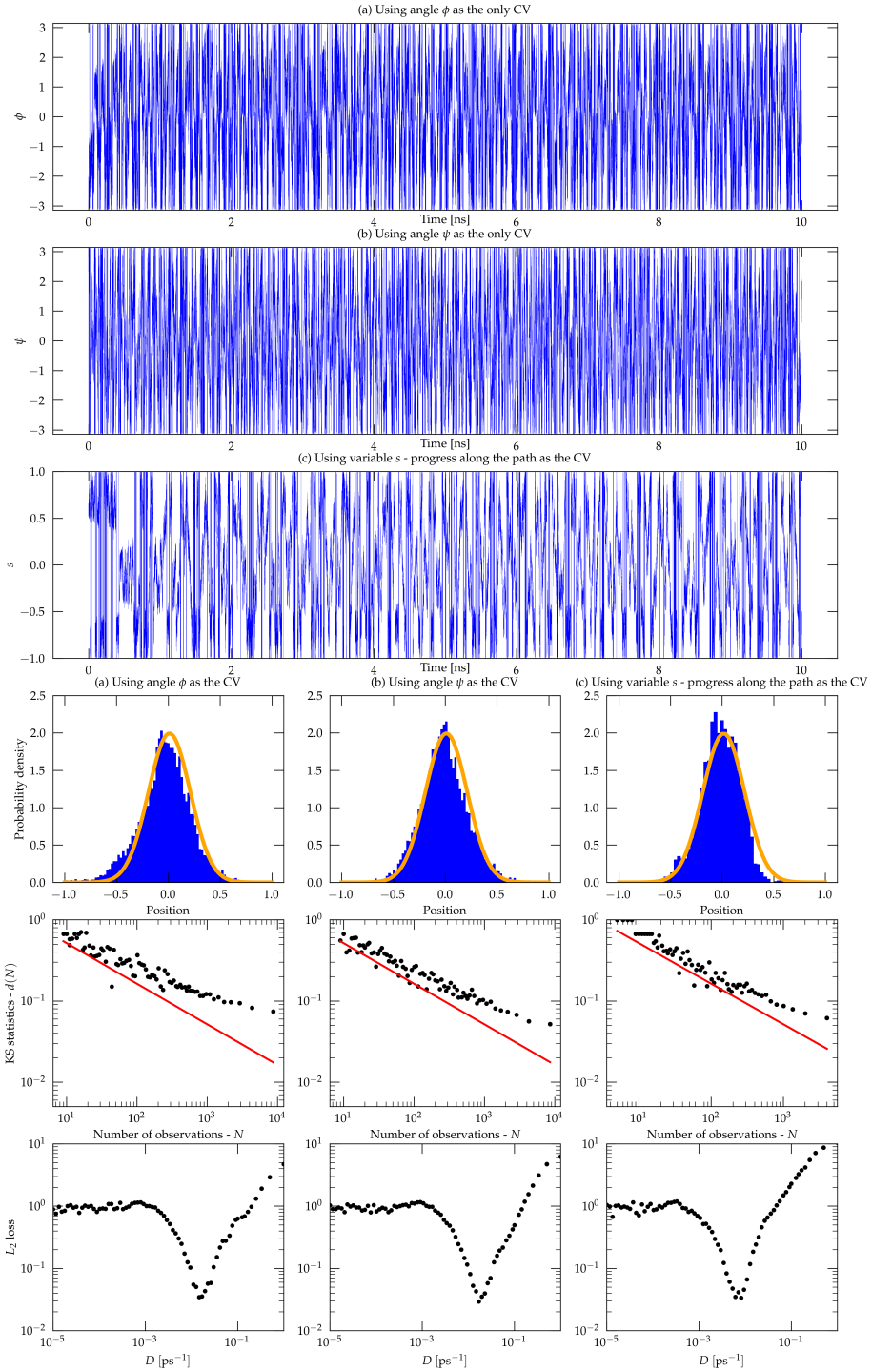

Figure X.7: (First row) Time evolution of angle ϕ in the simulation which uses only the angle ϕ as CV. (Second row) Time evolution of angle ψ in the simulation which uses only the angle ψ as CV. (Third row) Time evolution of variable s - the progress along the path in the simulation which uses path CV. (Fourth row) The best fit empirical histograms and exact probability density functions (Green functions) for $Dt = 0.02$. Note the artefacts present at all empirical histograms. (Fifth row) KS statistics - d as the function of the number of observation N taken for the construction of the empirical histograms. (Sixth row) Obtained L2 loss (see Eq. X.4) as the function of diffusion constants. The inferred diffusion constants are $1.47 \cdot 10^{-2}\text{ps}^{-1}$, $1.69 \cdot 10^{-2}\text{ps}^{-1}$ and $8.2 \cdot 10^{-3}\text{ps}^{-1}$, respectively.

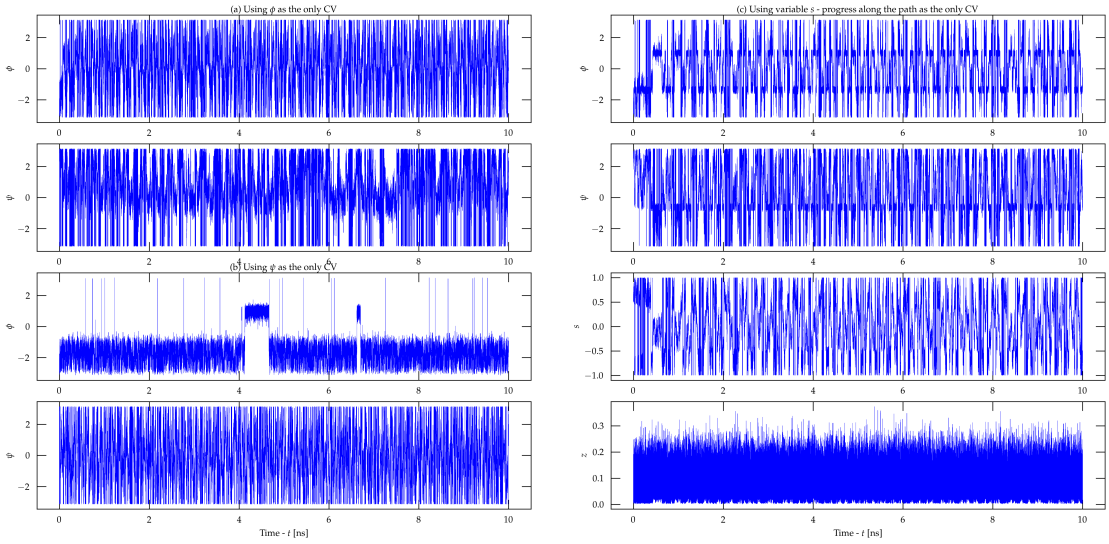

Figure X.8: (First row left) Time evolution of the angle ϕ in the simulation which uses ϕ as the only CV. (Second row left) Time evolution of the angle ψ in the simulation which uses ϕ as the only CV. (Third row left) Time evolution of the angle ϕ in the simulation which uses uses ψ as the only CV. (Fourth row left) Time evolution of the angle ψ in the simulation which uses ψ as the only CV. (First row right) Time evolution of the angle ϕ in the path-CV metadynamics. (Second row right) Time evolution of the angle ψ in the path-CV metadynamics. (Third row right) Time evolution of variable along the path - s in the path-CV metadynamics. (Fourth row right) Time evolution of variable perpendicular to the path - z in the path-CV metadynamics.

XI Conclusions and outlook

In the first part of this thesis, we presented an exhaustive overview of what is known about nucleation in a solid-solid transition. Based on that, we motivated the use of atomistic simulation methods in contrast to the well-studied phase field models and Ginzburg-Landau theories. We showed that the task of creation of a realistic Ginzburg-Landau theory for a solid-solid transition represents a rather cumbersome and expensive task. In contrast, the atomistic simulation methods, such as molecular dynamics, metadynamics and the use of machine-learning potentials based on DFT data, provide a useful alternative where the nucleation can be observed directly in a large system.

In the first part of the results chapters of this thesis we presented results already published in our work [57] for the case of homogeneous nucleation in NaCl for the well-studied B1-B2 transition. We demonstrated a simple, generic and well physically motivated metadynamics scheme using coordination number and volume as collective variables. Later, we tried to address the case of the heterogeneous nucleation in the B1-B2 transition focusing on the case of nucleation on grain boundaries. We show that the presence of grain boundaries can lower the pressure of dynamical instability at 300 K from 60 GPa, also found in Buerger's mechanism, to 40 GPa. At 35 GPa, we show that the barrier is largely lowered from the values above 90 eV to a few eV. While these results may seem positive a precaution is needed in their interpretation. It is very likely that at our system sizes 65k - 256k, the systems still suffered from the large finite size effects implied by periodic boundary effects and topology of the grain boundaries, in respect to their elastic self-interaction. These results should be thus viewed only as a proof of concept that such simulations are feasible using our method or any other similar atomistic simulation scheme.

In the next chapter, we moved our attention to the graphite to diamond transition in carbon. Employing the coordination number and volume as CVs, we tried to address the homogeneous nucleation of the graphite to diamond as studied in the past by Khaliullin et al. [146] or in metadynamics by Zipoli et al. [175]. Unfortunately, at all studied pressures we were not been able to induce the nucleation. Due to the CPU time cost of the machine learning potential of Shaidu et al. [197] our study was restricted to the system sizes of 64 000 atoms. In the collaboration with Dr. Yusuf Shaidu and prof. Stefano de Gironcoli we tried to speed-up their machine learning potential, albeit it led to less reliable neural network potentials, therefore we stuck to their original version. However, despite this limitation, we tried to see if the presence of dislocation loops can significantly lower the free-energy barrier. The answer is no. Also contrary to the work of to the Ref. [170], which studied transitions by ab-initio metadynamics in BN, no temperature dependence was found on the outcome of the graphite $\rightarrow$ diamond transition. The other plausible reason of not being able to induce nucleation may be an unoptimal choice of Gaussian parameters. Due to a recent availability of ACE potential by Qamar et al. [138], which is by an order of magnitude faster, we plan to resimulate some of our results.

In the third results chapter, we presented preliminary results on the application of metady-

namics to the transitions in the post-diamond phases of carbon using the recent SNAP potential of Willman et al. [198]. We showed that by application of the coordination number and volume as well as by the application of the tetrahedral order parameter [306] and volume as the CVs we are able to induce the transition from the cubic diamond phase into the simple cubic phase and vice versa. Moreover, we were able to calculate the barrier for the transition from the BC8 phase into the cubic diamond phase. However, we were not able to observe any transition into the BC8 phase, e.g. contrary to the work of Sun, Klug and Martoňák [167] who observed transition into the BC8 phase upon decompression from the simple cubic phase. In order to selectively steer the transition towards the BC8 phase upon decompression from the simple cubic phase and compression from the cubic diamond we are currently creating a set of machine learning CVs using a set of Behler-Parrinello descriptors and a small feed-forward neural network acting as a discriminator.

In the fourth part of the results chapter, we identified the $\alpha \rightarrow \omega$ and $\omega \rightarrow \alpha$ transition in titanium as a suitable covalent system for the study of the role of dislocations for nucleation. The fact that the system is covalent represents an advantage, since it eliminates the occurence of the charged regions near the dislocation jogs. For the transitions we identified two affordable (by orders of magnitude faster than for the case of carbon) force field descriptions. For the successfull application of the metadynamics, one also needs a suitable set of CVs.

In this task, we identified the Steinhardt's parameters as suitable CVs for the $\omega \rightarrow \alpha$ transition. For the (most studied in literature) $\alpha \rightarrow \omega$ transition we were not able to find a suitable set of CVs which would allow for the reconstruction of the free energy, even if some choices were able to induce the transition. We tried also to construct a set of Behler-Parrinello and ACE descriptors which turned out to be degenerate in the description of α and ω phases. It is likely that the problem of the degeneracy will diminish with high body order in the ACE formalism [130–138, 142, 143]. Thus we identified the $\alpha \rightarrow \omega$ transition as a suitable benchmark for the task of creation of machine learning CVs too as it represents a rather challenging task for a set of descriptors to distinguish the α and ω phases.

While the recent equivariant neural network architectures such as NequIP [140], Allegro [141], SE(3)-Transformers [144] or Equiformer [145] working in the regime of benign overfitting with millions of free parameters seems as suitable candidates for creation of such machine learning CV e.g. in a tandem with work of Bonati et al. [160], it is unlikely they will be successfull due to their high computational requirements unless the PLUMED code [249, 250] (or other code implementing metadynamics) is ported to the GPU. Therefore, as a suitable candidate the ACE formalism seems to be performant and efficient in the description of the structures. We believe that the higher order descriptors in the ACE formalism will be able to reduce the degeneracy of the respective structures. When successful in the induction of the $\alpha \rightarrow \omega$ transition, this transition may be used to study the role of dislocations for nucleation.

In the last chapter of the results part we presented an algorithm for the assessment of the suitability of CV for metadynamics simulations developed in collaboration with prof. A. Laio. This algorithm enables to quantify the "distance" between the actual behaviour of CVs and the diffusive limit, to which metadynamics should converge. Our method works well on a model scenario as well as it confirms the diffusivity of the coordination number and volume as CVs. In the case of alanine dipeptide more analyses and simulations are needed to come to a conclusive result. When the approach is finalised, it may open a way towards quantitative enhancement of the construction of the CVs, e.g., by creating a self-optimalising CV scheme in which the free paramaters of the CVs are optimised using algorithmic differentiation (thanks to having a metric

- the value from the KS test which can be optimised), e.g., by use of a JAX-MD framework [359].

References

[1] R.A. Cowley, W.J.L. Buyers, and G. Dolling. "Relationship of normal modes of vibration of strontium titanate and its antiferroelectric phase transition at 110°K". *Solid State Communications* 7.1 (1969), pp. 181–184.

[2] R. A. Cowley. "Soft Modes and Structural Phase Transitions". *Integrated Ferroelectrics* 133.1 (2012), pp. 109–117.

[3] Gernot Kostorz, ed. *Phase Transformations in Materials*. Wiley, 2001.

[4] R. H. Wentorf and J. S. Kasper. "Two New Forms of Silicon". *Science* 139.3552 (1963), pp. 338–339.

[5] Mungo Frost et al. "Novel high-pressure nitrogen phase formed by compression at low temperature". *Physical Review B* 93.2 (2016).

[6] Bertil Sundqvist. "Carbon under pressure". *Physics Reports* 909 (2021), pp. 1–73.

[7] R. Paul, S. X. Hu, and V. V. Karasiev. "Anharmonic and Anomalous Trends in the High-Pressure Phase Diagram of Silicon". *Physical Review Letters* 122.12 (2019).

[8] A Mujica et al. "High-pressure phases of germanium". *Journal of Physics: Condensed Matter* 13.1 (2000), pp. 35–42.

[9] V. Swamy et al. "A thermodynamic assessment of silica phase diagram". *Journal of Geophysical Research: Solid Earth* 99.B6 (1994), pp. 11787–11794.

[10] Liangzi Deng et al. "Pressure-induced high-temperature superconductivity retained without pressure in FeSe single crystals". *Proceedings of the National Academy of Sciences* 118.28 (2021), e2108938118.

[11] Artem R. Oganov and Colin W. Glass. "Crystal structure prediction using ab initio evolutionary techniques: Principles and applications". *The Journal of Chemical Physics* 124.24 (2006), p. 244704.

[12] Chris J. Pickard and R. J. Needs. "High-Pressure Phases of Silane". *Phys. Rev. Lett.* 97 (4 2006), p. 045504.

[13] Chris J Pickard and R J Needs. "Ab initio random structure searching". *Journal of Physics: Condensed Matter* 23.5 (2011), p. 053201.

[14] Yanchao Wang et al. "Crystal structure prediction via particle-swarm optimization". *Physical Review B* 82.9 (2010).

[15] Stefan Goedecker. "Minima hopping: An efficient search method for the global minimum of the potential energy surface of complex molecular systems". *The Journal of Chemical Physics* 120.21 (2004), pp. 9911–9917.

[16] Daniel Sheppard et al. "A generalized solid-state nudged elastic band method". *The Journal of Chemical Physics* 136.7 (2012).

[17] M. Cohen, G. B. Olson, and P. C. Clapp. In: *Proc. ICOMAT'79*. Cambridge (MA): MIT, 1979, p. 1.

[18] Kazuhiro Ōtsuka. *Shape memory materials*. Cambridge New York: Cambridge University Press, 1998.

[19] Paul McMullin. *Steel design*. New York: Routledge, 2018.

[20] A. Laio et al. "Physics of Iron at Earth's Core Conditions". *Science* 287.5455 (2000), pp. 1027–1030.

[21] Yang Sun et al. "Two-step nucleation of the Earth's inner core". *Proceedings of the National Academy of Sciences* 119.2 (2022), e2113059119.

[22] John C. Jamieson. "Crystal Structures of Titanium, Zirconium, and Hafnium at High Pressures". *Science* 140.3562 (1963), pp. 72–73.

[23] Richard G. Hennig et al. "Impurities block the α to ω martensitic transformation in titanium". *Nature Materials* 4.2 (2005), pp. 129–133.

[24] D. R. Trinkle et al. "New Mechanism for the α to ω Martensitic Transformation in Pure Titanium". *Physical Review Letters* 91.2 (2003).

[25] D. R. Trinkle et al. "Systematic pathway generation and sorting in martensitic transformations: Titanium α to ω". *Physical Review B* 72.1 (2005).

[26] R. G. Hennig et al. "Classical potential describes martensitic phase transformations between the α, β, and ω titanium phases". *Physical Review B* 78.5 (2008).

[27] R. G. Hennig et al. "Phase transformation in Si from semiconducting diamond to metallic β-Sn phase in QMC and DFT under hydrostatic and anisotropic stress". *Physical Review B* 82.1 (2010).

[28] Frank Reginald Nunes Nabarro. "The strains produced by precipitation in alloys". *Proceedings of the Royal Society of London. Series A. Mathematical and Physical Sciences* 175.963 (1940), pp. 519–538.

[29] John Douglas Eshelby. "The determination of the elastic field of an ellipsoidal inclusion, and related problems". *Proceedings of the Royal Society of London. Series A. Mathematical and Physical Sciences* 241.1226 (1957), pp. 376–396.

[30] Kenneth C. Russell. "Nucleation in solids: The induction and steady state effects". *Advances in Colloid and Interface Science* 13.3-4 (1980), pp. 205–318.

[31] G. B. Olson and M. Cohen. "CLASSICAL AND NONCLASSICAL MECHANISMS OF MARTENSITIC TRANSFORMATIONS". *Le Journal de Physique Colloques* 43.C4 (1982), pp. C4–75–C4–88.

[32] Brent Fultz. *Phase Transitions in Materials*. Cambridge University Press, 2020.

[33] Lei Zhang, Long-Qing Chen, and Qiang Du. "Morphology of Critical Nuclei in Solid-State Phase Transformations". *Physical Review Letters* 98.26 (2007).

[34] B. Moran, Y.A. Chu, and G.B. Olson. "Homogeneous nucleation of a solid-solid dilatational phase transformation". *International Journal of Solids and Structures* 33.13 (1996), pp. 1903–1919.

[35] P.J Clemm and J.C Fisher. "The influence of grain boundaries on the nucleation of secondary phases". *Acta Metallurgica* 3.1 (1955), pp. 70–73.

[36] John W. Cahn. "The kinetics of grain boundary nucleated reactions". *Acta Metallurgica* 4.5 (1956), pp. 449–459.

[37] K.C Russell. "Grain boundary nucleation kinetics". *Acta Metallurgica* 17.8 (1969), pp. 1123–1131.

[38] W. C. Johnson et al. "Influence of crystallography on aspects of solid-solid nucleation theory". *Metallurgical Transactions A* 6.4 (1975), pp. 911–919.

[39] G. B. Olson and Morris Cohen. "A general mechanism of martensitic nucleation: Part III. Kinetics of martensitic nucleation". *Metallurgical Transactions A* 7.12 (1976), pp. 1915–1923.

[40] P. E. Marth et al. "Application of heterogeneous nucleation theory to precipitate nucleation at GP zones". *Metallurgical Transactions A* 7.10 (1976), pp. 1519–1528.

[41] H. I. Aaronson et al. "Precipitation at interphase boundaries". *Metallurgical Transactions A* 9.3 (1978), pp. 363–371.

[42] J.K. Park and A.J. Ardell. "Precipitation at grain boundaries in the commercial alloy Al 7075". *Acta Metallurgica* 34.12 (1986), pp. 2399–2409.

[43] W. F. Lange, M. Enomoto, and H. I. Aaronson. "The kinetics of ferrite nucleation at austenite grain boundaries in Fe-C alloys". *Metallurgical Transactions A* 19.3 (1988), pp. 427–440.

[44] W. F. Lange, M. Enomoto, and H. I. Aaronson. "Precipitate nucleation kinetics at grain boundaries". *International Materials Reviews* 34.1 (1989), pp. 125–152.

[45] S. E. Offerman et al. "Grain Nucleation and Growth During Phase Transformations". *Science* 298.5595 (2002), pp. 1003–1005.

[46] H. Landheer et al. "The role of crystal misorientations during solid-state nucleation of ferrite in austenite". *Acta Materialia* 57.5 (2009), pp. 1486–1496.

[47] Philip C. Clapp. "Static and dynamic precursors of displacive transformations near crystalline defects". *Physica D: Nonlinear Phenomena* 66.1-2 (1993), pp. 26–34.

[48] John W Cahn. "Nucleation on dislocations". *Acta Metallurgica* 5.3 (1957), pp. 169–172.

[49] H.E Cook. "A lattice model of structural and dislocation transformations". *Acta Metallurgica* 21.10 (1973), pp. 1431–1444.

[50] G. B. Olson and Morris Cohen. "A general mechanism of martensitic nucleation: Part I. General concepts and the FCC → HCP transformation". *Metallurgical Transactions A* 7.12 (1976), pp. 1897–1904.

[51] G. B. Olson and Morris Cohen. "A general mechanism of martensitic nucleation: Part II. FCC → BCC and other martensitic transformations". *Metallurgical Transactions A* 7.12 (1976), pp. 1905–1914.

[52] M. Suezawa and H.E. Cook. "On the nucleation of martensite". *Acta Metallurgica* 28.4 (1980), pp. 423–432.

[53] B. Li et al. "Molecular dynamics simulations of the effects of defects on martensite nucleation". *Journal of Applied Physics* 95.4 (2004), pp. 1698–1705.

[54] A. Samanta et al. "Microscopic mechanisms of equilibrium melting of a solid". *Science* 346.6210 (2014), pp. 729–732.

[55] Valery I. Levitas, Hao Chen, and Liming Xiong. "Phase Transitions and Their Interaction with Dislocations in Silicon". In: *Proceedings of the International Conference on Martensitic Transformations: Chicago*. Springer International Publishing, 2018, pp. 83–87.

[56] Michael Marder. *Condensed Matter Physics*. Hoboken, N.J: Wiley, 2010.

[57] Matej Badin and Roman Martoňák. "Nucleating a Different Coordination in a Crystal under Pressure: A Study of the B1-B2 Transition in NaCl by Metadynamics". *Physical Review Letters* 127.10 (2021).

[58] P. C. Clapp. "A Localized Soft Mode Theory for Martensitic Transformations". *Physica Status Solidi (b)* 57.2 (1973), pp. 561–569.

[59] N. Lazarev et al. "Atomic-scale simulation of martensitic phase transformations in NiAl". *Materials Science and Engineering: A* 481-482 (2008), pp. 205–208.

[60] T Uehara, C Asai, and N Ohno. "Molecular dynamics simulation of shape memory behaviour using a multi-grain model". *Modelling and Simulation in Materials Science and Engineering* 17.3 (2009), p. 035011.

[61] Hongxiang Zong et al. "Twin boundary activated $\alpha \rightarrow \omega$ phase transformation in titanium under shock compression". *Acta Materialia* 115 (2016), pp. 1–9.

[62] H. Song and J.J. Hoyt. "A molecular dynamics study of heterogeneous nucleation at grain boundaries during solid-state phase transformations". *Computational Materials Science* 117 (2016), pp. 151–163.

[63] H. Song and J. J. Hoyt. "A molecular dynamics study of the nucleus interface structure and orientation relationships during the austenite-to-ferrite transformation in pure Fe". *Canadian Metallurgical Quarterly* 57.1 (2017), pp. 12–19.

[64] Jerome Meiser and Herbert M. Urbassek. "Martensitic transformation of pure iron at a grain boundary: Atomistic evidence for a two-step Kurdjumov-Sachs-Pitsch pathway". *AIP Advances* 6.8 (2016), p. 085017.

[65] Jerome Meiser and Herbert M. Urbassek. "Influence of grain boundaries on the austenitic and martensitic phase transitions in iron". *The European Physical Journal B* 92.2 (2019).

[66] Xueyang Zhang et al. "Effect of grain boundaries on shock-induced phase transformation in iron bicrystals". *Journal of Applied Physics* 123.4 (2018).

[67] Y.M. Jin, A. Artemev, and A.G. Khachaturyan. "Three-dimensional phase field model of low-symmetry martensitic transformation in polycrystal: simulation of $\zeta\prime 2$ martensite in AuCd alloys". *Acta Materialia* 49.12 (2001), pp. 2309–2320.

[68] A. Artemev, Yongmei Jin, and A. G. Khachaturyan. "Three-dimensional phase field model and simulation of cubic $\rightarrow$ tetragonal martensitic transformation in polycrystals". *Philosophical Magazine A* 82.6 (2002), pp. 1249–1270.

[69] Y. Sutou et al. "Effect of grain size and texture on pseudoelasticity in Cu–Al–Mn-based shape memory wire". *Acta Materialia* 53.15 (2005), pp. 4121–4133.

[70] Y CUI et al. "Simulation of hexagonal–orthorhombic phase transformation in polycrystals". *Acta Materialia* 55.1 (2007), pp. 233–241.

[71] Akinori Yamanaka, Tomohiro Takaki, and Yoshihiro Tomita. "Elastoplastic phase-field simulation of martensitic transformation with plastic deformation in polycrystal". *International Journal of Mechanical Sciences* 52.2 (2010), pp. 245–250.

[72] J.-Y. Cho et al. "Finite element simulations of dynamics of multivariant martensitic phase transitions based on Ginzburg–Landau theory". *International Journal of Solids and Structures* 49.14 (2012), pp. 1973–1992.

[73] A Malik et al. "Phase-field modelling of martensitic transformation: the effects of grain and twin boundaries". *Modelling and Simulation in Materials Science and Engineering* 21.8 (2013), p. 085003.

[74] Tae Wook Heo and Long-Qing Chen. "Phase-Field Modeling of Nucleation in Solid-State Phase Transformations". *JOM* 66.8 (2014), pp. 1520–1528.

[75] Mahmood Mamivand, Mohsen Asle Zaeem, and Haitham El Kadiri. "Shape memory effect and pseudoelasticity behavior in tetragonal zirconia polycrystals: A phase field study". *International Journal of Plasticity* 60 (2014), pp. 71–86.

[76] Ephraim Schoof et al. "Multiphase-field modeling of martensitic phase transformation in a dual-phase microstructure". *International Journal of Solids and Structures* 134 (2018), pp. 181–194.

[77] Hemantha Kumar Yeddu. "Phase-field modeling of austenite grain size effect on martensitic transformation in stainless steels". *Computational Materials Science* 154 (2018), pp. 75–83.

[78] Oleg Shchyglo et al. "Phase-field simulation of martensite microstructure in low-carbon steel". *Acta Materialia* 175 (2019), pp. 415–425.

[79] Jingming Zhu, Jun Luo, and Yuanzun Sun. "Phase field study of the grain size and temperature dependent mechanical responses of tetragonal zirconia polycrystals: A discussion of tension-compression asymmetry". *Computational Materials Science* 172 (2020), p. 109326.

[80] Cheikh Cissé and Mohsen Asle Zaeem. "An Asymmetric Elasto-Plastic Phase-Field Model for Shape Memory Effect, Pseudoelasticity and Thermomechanical Training in Polycrystalline Shape Memory Alloys". *Acta Materialia* 201 (2020), pp. 580–595.

[81] Shangbin Xi and Yu Su. "A phase field study of the grain-size effect on the thermomechanical behavior of polycrystalline NiTi thin films". *Acta Mechanica* 232.11 (2021), pp. 4545–4566.

[82] Bo Xu and Guozheng Kang. "Phase field simulation on the super-elasticity, elastocaloric and shape memory effect of geometrically graded nano-polycrystalline NiTi shape memory alloys". *International Journal of Mechanical Sciences* 201 (2021), p. 106462.

[83] Bhasker Paliwal et al. "Martensitic microstructure evolution in austenitic steel: A thermomechanical polycrystalline phase field study". *Journal of Materials Research* 36.6 (2021), pp. 1376–1399.

[84] Ling Fan et al. "Multigrain phase-field simulation in ferroelectrics with phase coexistences: An improved phase-field model". *Computational Materials Science* 203 (2022), p. 111056.

[85] Anup Basak. "Grain boundary- and triple junction-induced martensitic transformations: A phase-field study of effects of grain boundary width and energy". *International Journal of Solids and Structures* 277-278 (2023), p. 112308.

[86] Hamed Babaei, Raghunandan Pratoori, and Valery I. Levitas. "Simulations of multivariant Si I to Si II phase transformation in polycrystalline silicon with finite-strain scale-free phase-field approach". *Acta Materialia* 254 (2023), p. 118996.

[87] Hao Chen et al. "Nontrivial nanostructure, stress relaxation mechanisms, and crystallography for pressure-induced Si-I $\rightarrow$ Si-II phase transformation". *Nature Communications* 13.1 (2022).

[88] Long-Qing Chen. "Phase-Field Models for Microstructure Evolution". *Annual Review of Materials Research* 32.1 (2002), pp. 113–140.

[89] Heike Emmerich et al. "Phase-field-crystal models for condensed matter dynamics on atomic length and diffusive time scales: an overview". *Advances in Physics* 61.6 (2012), pp. 665–743.

[90] Philip C. Clapp. "Localized soft modes and ultrasonic effects in first order displacive transformations". *Materials Science and Engineering* 38.2 (1979), pp. 193–198.

[91] Y. A. Chu et al. "A model for nonclassical nucleation of solid-solid structural phase transformations". *Metallurgical and Materials Transactions A* 31.5 (2000), pp. 1321–1331.

[92] F Falk and P Konopka. "Three-dimensional Landau theory describing the martensitic phase transformation of shape-memory alloys". *Journal of Physics: Condensed Matter* 2.1 (1990), pp. 61–77.

[93] R. J. Gooding and J. A. Krumhansl. "Symmetry-restricted anharmonicities and the CsCl-to-7R martensitic structural phase transformation of the Ni_xAl_{1-x} system". *Physical Review B* 39.3 (1989), pp. 1535–1540.

[94] G. Guénin and P. F. Gobin. "A localized soft mode model for the nucleation of thermoelastic martensitic transformation: Application to the $\beta \rightarrow$ 9R transformation". *Metallurgical Transactions A* 13.7 (1982), pp. 1127–1134.

[95] J.A. Krumhansl. "Landau models for structural phase transitions: Are soft modes needed?" *Solid State Communications* 84.1-2 (1992), pp. 251–254.

[96] Valery I. Levitas and Dean L. Preston. "Three-dimensional Landau theory for multivariant stress-induced martensitic phase transformations. I. Austenite↔martensite". *Physical Review B* 66.13 (2002).

[97] Valery I. Levitas and Dean L. Preston. "Three-dimensional Landau theory for multivariant stress-induced martensitic phase transformations. II. Multivariant phase transformations and stress space analysis". *Physical Review B* 66.13 (2002).

[98] Valery I. Levitas, Dean L. Preston, and Dong-Wook Lee. "Three-dimensional Landau theory for multivariant stress-induced martensitic phase transformations. III. Alternative potentials, critical nuclei, kink solutions, and dislocation theory". *Physical Review B* 68.13 (2003).

[99] Hui She, Yulan Liu, and Biao Wang. "Phase field simulation of heterogeneous cubic→tetragonal martensite nucleation". *International Journal of Solids and Structures* 50.7-8 (2013), pp. 1187–1191.

[100] Valery I. Levitas. "Phase field approach to martensitic phase transformations with large strains and interface stresses". *Journal of the Mechanics and Physics of Solids* 70 (2014), pp. 154–189.

[101] Valery I. Levitas and James A. Warren. "Phase field approach with anisotropic interface energy and interface stresses: Large strain formulation". *Journal of the Mechanics and Physics of Solids* 91 (2016), pp. 94–125.

[102] Valery I. Levitas, Hao Chen, and Liming Xiong. "Lattice instability during phase transformations under multiaxial stress: Modified transformation work criterion". *Physical Review B* 96.5 (2017).

[103] Hamed Babaei and Valery I. Levitas. "Phase-field approach for stress- and temperature-induced phase transformations that satisfies lattice instability conditions. Part 2. simulations of phase transformations Si I↔ Si II". *International Journal of Plasticity* 107 (2018), pp. 223–245.

[104] Valery I. Levitas. "Phase field approach for stress- and temperature-induced phase transformations that satisfies lattice instability conditions. Part I. General theory". *International Journal of Plasticity* 106 (2018), pp. 164–185.

[105] A. Roy et al. "Simulation study of nucleation in a phase-field model with nonlocal interactions". *Physical Review E* 57.3 (1998), pp. 2610–2617.

[106] A. C.E. Reid, G. B. Olson, and B. Moran. "Dislocations in nonlinear nonlocal media: Martensitic embryo formation". *Phase Transitions* 69.3 (1999), pp. 309–328.

[107] Chen Shen, Ju Li, and Yunzhi Wang. "Finding Critical Nucleus in Solid-State Transformations". *Metallurgical and Materials Transactions A* 39.5 (2007), pp. 976–983.

[108] Y. Wang and A.G. Khachaturyan. "Three-dimensional field model and computer modeling of martensitic transformations". *Acta Materialia* 45.2 (1997), pp. 759–773.

[109] Lei Zhang et al. "Recent developments in computational modelling of nucleation in phase transformations". *npj Computational Materials* 2.1 (2016).

[110] D. M. Hatch et al. "Systematic Technique for the Study of Interphase Boundaries in Structural Phase Transitions". *Physical Review Letters* 76.8 (1996), pp. 1288–1291.

[111] Russell Hemley. *Ultrahigh-pressure mineralogy : physics and chemistry of the earth's deep interior*. Washington, DC: Mineralogical Society of America, 1998.

[112] Wojciech Grochala et al. "The Chemical Imagination at Work inVery Tight Places". *Angewandte Chemie International Edition* 46.20 (2007), pp. 3620–3642.

[113] Maosheng Miao et al. "Chemistry under high pressure". *Nature Reviews Chemistry* 4.10 (2020), pp. 508–527.

[114] Julia Dshemuchadse et al. "Moving beyond the constraints of chemistry via crystal structure discovery with isotropic multiwell pair potentials". *Proceedings of the National Academy of Sciences* 118.21 (2021), e2024034118.

[115] W. Kohn and L. J. Sham. "Self-Consistent Equations Including Exchange and Correlation Effects". *Physical Review* 140.4A (1965), A1133–A1138.

[116] Hans C. Andersen. "Molecular dynamics simulations at constant pressure and/or temperature". *The Journal of Chemical Physics* 72.4 (1980), pp. 2384–2393.

[117] M. Parrinello and A. Rahman. "Crystal Structure and Pair Potentials: A Molecular-Dynamics Study". *Phys. Rev. Lett.* 45 (14 1980), pp. 1196–1199.

[118] M. Parrinello and A. Rahman. "Polymorphic transitions in single crystals: A new molecular dynamics method". *Journal of Applied Physics* 52.12 (1981), pp. 7182–7190. eprint: https://doi.org/10.1063/1.328693.

[119] R. Car and M. Parrinello. "Unified Approach for Molecular Dynamics and Density-Functional Theory". *Physical Review Letters* 55.22 (1985), pp. 2471–2474.

[120] Joost VandeVondele, Urban Borštnik, and Jürg Hutter. "Linear Scaling Self-Consistent Field Calculations with Millions of Atoms in the Condensed Phase". *Journal of Chemical Theory and Computation* 8.10 (2012), pp. 3565–3573.

[121] Jörg Behler and Michele Parrinello. "Generalized Neural-Network Representation of High-Dimensional Potential-Energy Surfaces". *Physical Review Letters* 98.14 (2007).

[122] Albert P. Bartók et al. "Gaussian Approximation Potentials: The Accuracy of Quantum Mechanics, without the Electrons". *Physical Review Letters* 104.13 (2010).

[123] Frank Noé et al. "Machine Learning for Molecular Simulation". *Annual Review of Physical Chemistry* 71.1 (2020), pp. 361–390.

[124] Stefan Chmiela et al. "Towards exact molecular dynamics simulations with machine-learned force fields". *Nature Communications* 9.1 (2018).

[125] Jörg Behler. "Four Generations of High-Dimensional Neural Network Potentials". *Chemical Reviews* (2021).

[126] Volker L. Deringer et al. "Gaussian Process Regression for Materials and Molecules". *Chemical Reviews* 121.16 (2021), pp. 10073–10141.

[127] Felix Musil et al. "Physics-Inspired Structural Representations for Molecules and Materials". *Chemical Reviews* 121.16 (2021), pp. 9759–9815.

[128] Jörg Behler et al. "Metadynamics Simulations of the High-Pressure Phases of Silicon Employing a High-Dimensional Neural Network Potential". *Physical Review Letters* 100.18 (2008).

[129] Jing Zhang and Ming Chen. "Unfolding Hidden Barriers by Active Enhanced Sampling". *Physical Review Letters* 121.1 (2018).

[130] Ralf Drautz. "Atomic cluster expansion for accurate and transferable interatomic potentials". *Physical Review B* 99.1 (2019).

[131] Ralf Drautz. "Atomic cluster expansion of scalar, vectorial, and tensorial properties including magnetism and charge transfer". *Physical Review B* 102.2 (2020).

[132] Yury Lysogorskiy et al. "Performant implementation of the atomic cluster expansion (PACE) and application to copper and silicon". *npj Computational Materials* 7.1 (2021).

[133] Dávid Péter Kovács et al. "Linear Atomic Cluster Expansion Force Fields for Organic Molecules: Beyond RMSE". *Journal of Chemical Theory and Computation* 17.12 (2021), pp. 7696–7711.

[134] Anton Bochkarev et al. "Multilayer atomic cluster expansion for semilocal interactions". *Physical Review Research* 4.4 (2022).

[135] Anton Bochkarev et al. "Efficient parametrization of the atomic cluster expansion". *Physical Review Materials* 6.1 (2022).

[136] Geneviève Dusson et al. "Atomic cluster expansion: Completeness, efficiency and stability". *Journal of Computational Physics* 454 (2022), p. 110946.

[137] Ilyes Batatia et al. *The Design Space of E(3)-Equivariant Atom-Centered Interatomic Potentials*. 2022. eprint: arXiv:2205.06643.

[138] Minaam Qamar et al. "Atomic Cluster Expansion for Quantum-Accurate Large-Scale Simulations of Carbon". *Journal of Chemical Theory and Computation* (2023).

[139] Stephen R. Xie, Matthias Rupp, and Richard G. Hennig. *Ultra-fast interpretable machine-learning potentials*. 2021. eprint: arXiv:2110.00624.

[140] Simon Batzner et al. "E(3)-equivariant graph neural networks for data-efficient and accurate interatomic potentials". *Nature Communications* 13.1 (2022).

[141] Albert Musaelian et al. "Learning local equivariant representations for large-scale atomistic dynamics". *Nature Communications* 14.1 (2023).

[142] Ilyes Batatia et al. "MACE: Higher Order Equivariant Message Passing Neural Networks for Fast and Accurate Force Fields". In: *Advances in Neural Information Processing Systems*. Ed. by S. Koyejo et al. Vol. 35. Curran Associates, Inc., 2022, pp. 11423–11436.

[143] David Peter Kovacs et al. *Evaluation of the MACE Force Field Architecture: from Medicinal Chemistry to Materials Science*. 2023. eprint: arXiv:2305.14247.

[144] Fabian Fuchs et al. "SE(3)-Transformers: 3D Roto-Translation Equivariant Attention Networks". In: *Advances in Neural Information Processing Systems*. Ed. by H. Larochelle et al. Vol. 33. Curran Associates, Inc., 2020, pp. 1970–1981.

[145] Yi-Lun Liao and Tess Smidt. "Equiformer: Equivariant Graph Attention Transformer for 3D Atomistic Graphs". In: *International Conference on Learning Representations*. 2023.

[146] Rustam Z. Khaliullin et al. "Nucleation mechanism for the direct graphite-to-diamond phase transition". *Nature Materials* 10 (2011), pp. 693–697.

[147] Omar Valsson, Pratyush Tiwary, and Michele Parrinello. "Enhancing Important Fluctuations: Rare Events and Metadynamics from a Conceptual Viewpoint". *Annual Review of Physical Chemistry* 67.1 (2016), pp. 159–184.

[148] A. Laio and M. Parrinello. "Escaping free-energy minima". *Proceedings of the National Academy of Sciences* 99.20 (2002), pp. 12562–12566.

[149] Giovanni Bussi and Alessandro Laio. "Using metadynamics to explore complex free-energy landscapes". *Nature Reviews Physics* 2.4 (2020), pp. 200–212.

[150] Giovanni Bussi, Alessandro Laio, and Michele Parrinello. "Equilibrium Free Energies from Nonequilibrium Metadynamics". *Physical Review Letters* 96.9 (2006).

[151] Pratyush Tiwary and B. J. Berne. "Spectral gap optimization of order parameters for sampling complex molecular systems". *Proceedings of the National Academy of Sciences* 113.11 (2016), pp. 2839–2844.

[152] Letif Mones, Noam Bernstein, and Gábor Csányi. "Exploration, Sampling, And Reconstruction of Free Energy Surfaces with Gaussian Process Regression". *Journal of Chemical Theory and Computation* 12.10 (2016), pp. 5100–5110.

[153] James McCarty and Michele Parrinello. "A variational conformational dynamics approach to the selection of collective variables in metadynamics". *The Journal of Chemical Physics* 147.20 (2017), p. 204109.

[154] Mohammad M. Sultan and Vijay S. Pande. "tICA-Metadynamics: Accelerating Metadynamics by Using Kinetically Selected Collective Variables". *Journal of Chemical Theory and Computation* 13.6 (2017), pp. 2440–2447.

[155] Ilaria Gimondi, Gareth A. Tribello, and Matteo Salvalaglio. "Building maps in collective variable space". *The Journal of Chemical Physics* 149.10 (2018), p. 104104.

[156] Alex Rodriguez et al. "Computing the Free Energy without Collective Variables". *Journal of Chemical Theory and Computation* 14.3 (2018), pp. 1206–1215.

[157] Mohammad M. Sultan and Vijay S. Pande. "Automated design of collective variables using supervised machine learning". *The Journal of Chemical Physics* 149.9 (2018), p. 094106.

[158] Dan Mendels et al. "Folding a small protein using harmonic linear discriminant analysis". *The Journal of Chemical Physics* 149.19 (2018), p. 194113.

[159] Valerio Rizzi et al. "Blind Search for Complex Chemical Pathways Using Harmonic Linear Discriminant Analysis". *Journal of Chemical Theory and Computation* 15.8 (2019), pp. 4507–4515.

[160] Luigi Bonati, GiovanniMaria Piccini, and Michele Parrinello. "Deep learning the slow modes for rare events sampling". *Proceedings of the National Academy of Sciences* 118.44 (2021), e2113533118.

[161] Dongdong Wang et al. "Efficient sampling of high-dimensional free energy landscapes using adaptive reinforced dynamics". *Nature Computational Science* 2.1 (2021), pp. 20–29.

[162] R. Martoňák, A. Laio, and M. Parrinello. "Predicting Crystal Structures: The Parrinello-Rahman Method Revisited". *Physical Review Letters* 90.7 (2003).

[163] Roman Martoňák et al. "Simulation of structural phase transitions by metadynamics". *Zeitschrift für Kristallographie - Crystalline Materials* 220.5/6 (2005).

[164] Paolo Raiteri, Roman Martoňák, and Michele Parrinello. "Exploring Polymorphism: The Case of Benzene". *Angewandte Chemie International Edition* 44.24 (2005), pp. 3769–3773.

[165] Roman Martoňák et al. "From four- to six-coordinated silica: Transformation pathways from metadynamics". *Physical Review B* 76.1 (2007).

[166] Clive Bealing, Roman Martoňák, and Carla Molteni. "Pressure-induced structural phase transitions in CdSe: A metadynamics study". *The Journal of Chemical Physics* 130.12 (2009), p. 124712.

[167] Jian Sun, Dennis D. Klug, and Roman Martoňák. "Structural transformations in carbon under extreme pressure: Beyond diamond". *The Journal of Chemical Physics* 130.19 (2009), p. 194512.

[168] Yansun Yao et al. "Structural Prediction and Phase Transformation Mechanisms in Calcium at High Pressure". *Physical Review Letters* 103.5 (2009).

[169] J. Sun et al. "High-pressure polymeric phases of carbon dioxide". *Proceedings of the National Academy of Sciences* 106.15 (2009), pp. 6077–6081.

[170] Liliana Hromadová and Roman Martoňák. "Pressure-induced structural transitions in BN fromab initiometadynamics". *Physical Review B* 84.22 (2011).

[171] Dušan Plašienka and Roman Martoňák. "Transformation pathways in high-pressure solid nitrogen: From molecular N2 to polymeric cg-N". *The Journal of Chemical Physics* 142.9 (2015), p. 094505.

[172] Qunchao Tong et al. "Machine learning metadynamics simulation of reconstructive phase transition". *Physical Review B* 103.5 (2021).

[173] Roman Martoňák. "Simulation of Structural Phase Transitions in Crystals: The Metadynamics Approach". In: *Modern methods of crystal structure prediction*. Ed. by A. R. Oganov. Wiley-VCH, Berlin, 2011, pp. 107–130.

[174] R. Martoňák. "Atomistic simulations of pressure-induced structural transformations in solids". *The European Physical Journal B* 79.3 (2011), pp. 241–252.

[175] F. Zipoli, M. Bernasconi, and R. Martoňák. "Constant pressure reactive molecular dynamics simulations of phase transitions under pressure: The graphite to diamond conversion revisited". *The European Physical Journal B* 39.1 (2004), pp. 41–47.

[176] S. Pipolo et al. "Navigating at Will on the Water Phase Diagram". *Physical Review Letters* 119.24 (2017).

[177] Ilaria Gimondi and Matteo Salvalaglio. "CO2 packing polymorphism under pressure: Mechanism and thermodynamics of the I-III polymorphic transition". *The Journal of Chemical Physics* 147.11 (2017), p. 114502.

[178] Samuel Alexander Jobbins, Salah Eddine Boulfelfel, and Stefano Leoni. "Metashooting: a novel tool for free energy reconstruction from polymorphic phase transition mechanisms". *Faraday Discussions* 211 (2018), pp. 235–251.

[179] Dan Mendels et al. "Searching for Entropically Stabilized Phases: The Case of Silver Iodide". *The Journal of Physical Chemistry C* 122.3 (2018), pp. 1786–1790.

[180] Jutta Rogal, Elia Schneider, and Mark E. Tuckerman. "Neural-Network-Based Path Collective Variables for Enhanced Sampling of Phase Transformations". *Physical Review Letters* 123.24 (2019).

[181] Dongsun Yoo et al. "Metadynamics sampling in atomic environment space for collecting training data for machine learning potentials". *npj Computational Materials* 7.1 (2021).

[182] Harold T. Stokes and Dorian M. Hatch. "Procedure for obtaining microscopic mechanisms of reconstructive phase transitions in crystalline solids". *Physical Review B* 65.14 (2002).

[183] Harold T. Stokes et al. "Mechanisms for the reconstructive phase transition between the B1 and B2 structure types in NaCl and PbS". *Physical Review B* 69.17 (2004).

[184] Pedro A. Santos-Florez et al. "Size-Dependent Nucleation in Crystal Phase Transition from Machine Learning Metadynamics". *Physical Review Letters* 129.18 (2022).

[185] Xiaoyuan Li and Raymond Jeanloz. "Measurement of theB1-B2 transition pressure in NaCl at high temperatures". *Physical Review B* 36.1 (1987), pp. 474–479.

[186] H Shoji. "Geometric relations between the modied variations of a substance". *Zeitschrift Fur Kristallographie* 77 (1931), pp. 381–410.

[187] M. J. Buerger. *Phase transformations in solids*. Ed. by R. Smoluchowski and J.E. Mayer. John Wiley, Sons, and Hapman Hall Ltd., 1951.

[188] M. Watanabe, M. Tokonami, and N. Morimoto. "The transition mechanism between the CsCl-type and NaCl-type structures in CsCl". *Acta Crystallographica Section A* 33.2 (1977), pp. 294–298.

[189] B.G. Hyde and M. O'Keeffe. "On the mechanism of B1-B2 structural transformation". In: *Phase Transitions*. Ed. by L. E. Cross. Pergamon, Oxford, 1973, pp. 345–349.

[190] Nobuyuki Nakagiri and Motoyuki Nomura. "Theoretical Study of Hysteresis Phenomena of Pressure-Induced Polymorphic Transition in Alkali Halides". *Journal of the Physical Society of Japan* 51.8 (1982), pp. 2412–2418.

[191] Y. A. Nga and C. K. Ong. "Mechanism of pressure-induced polymorphic transition in NaCl". *Physical Review B* 46.17 (1992), pp. 10547–10553.

[192] A. Martin Pendas et al. "Pressure induced B1-B2 phase transition in alkali halides: General aspects from first-principles calculations". *Physical Review B* 49.5 (1994), pp. 3066–3074.

[193] C. E. Sims et al. "Thermodynamics and mechanism of theB1-B2phase transition in group-I halides and group-II oxides". *Physical Review B* 57.18 (1998), pp. 11164–11172.

[194] P. Tolédano et al. "Phenomenological theory of the reconstructive phase transition between the NaCl and CsCl structure types". *Physical Review B* 67.14 (2003).

[195] Dirk Zahn and Stefano Leoni. "Nucleation and Growth in Pressure-Induced Phase Transitions from Molecular Dynamics Simulations: Mechanism of the Reconstructive Transformation of NaCl to the CsCl-Type Structure". *Physical Review Letters* 92.25 (2004).

[196] Y. Y. Zhang et al. "Ultrafast X-Ray Diffraction Visualization of B1-B2 Phase Transition in KCl under Shock Compression". *Physical Review Letters* 127.4 (2021).

[197] Yusuf Shaidu et al. "A systematic approach to generating accurate neural network potentials: the case of carbon". *npj Computational Materials* 7.1 (2021).

[198] Jonathan T. Willman et al. "Machine learning interatomic potential for simulations of carbon at extreme conditions". *Physical Review B* 106.18 (2022).

[199] Raymond Jeanloz et al. "B1-B2 Transition in Calcium Oxide from Shock-Wave and Diamond-Cell Experiments". *Science* 206.4420 (1979), pp. 829–830.

[200] Hongxiang Zong et al. "Free electron to electride transition in dense liquid potassium". *Nature Physics* 17.8 (2021), pp. 955–960.

[201] Simone Anzellini and Silvia Boccato. "A Practical Review of the Laser-Heated Diamond Anvil Cell for University Laboratories and Synchrotron Applications". *Crystals* 10.6 (2020), p. 459.

[202] R. F. Smith et al. "Ramp compression of diamond to five terapascals". *Nature* 511.7509 (2014), pp. 330–333.

[203] Hosung Ki et al. "Ultrafast X-Ray Crystallography and Liquidography". *Annual Review of Physical Chemistry* 68.1 (2017), pp. 473–497.

[204] Xanthippi Markenscoff. "Eshelby instability pressure for nucleation of a phase change defect". *Journal of the Mechanics and Physics of Solids* 143 (2020), p. 104054.

[205] John W. Cahn and John E. Hilliard. "Free Energy of a Nonuniform System. III. Nucleation in a Two-Component Incompressible Fluid". *The Journal of Chemical Physics* 31.3 (1959), pp. 688–699.

[206] Lula Rosso et al. "On the use of the adiabatic molecular dynamics technique in the calculation of free energy profiles". *The Journal of Chemical Physics* 116.11 (2002), pp. 4389–4402.

[207] G. J. Ackland et al. "Computer simulation of point defect properties in dilute Fe-Cu alloy using a many-body interatomic potential". *Philosophical Magazine A* 75.3 (1997), pp. 713–732.

[208] H Song and J J Hoyt. "An atomistic simulation study of the crystallographic orientation relationships during the austenite to ferrite transformation in pure Fe". *Modelling and Simulation in Materials Science and Engineering* 23.8 (2015), p. 085012.

[209] D.Z. Li et al. "Growth modes of individual ferrite grains in the austenite to ferrite transformation of low carbon steels". *Acta Materialia* 55.18 (2007), pp. 6234–6249.

[210] Philip C. Clapp. "Pretransformation effects of localized soft modes on neutron scattering, acoustic attenuation, and Mössbauer resonance measurements". *Metallurgical Transactions A* 12.4 (1981), pp. 589–594.

[211] G. R. Barsch and J. A. Krumhansl. "Nonlinear and nonlocal continuum model of transformation precursors in martensites". *Metallurgical Transactions A* 19.4 (1988), pp. 761–775.

[212] J. A. Krumhansl and R. J. Gooding. "Structural phase transitions with little phonon softening and first-order character". *Physical Review B* 39.5 (1989), pp. 3047–3053.

[213] F. Schwabl and U. C. Täuber. "Elastic phase transitions in inhomogeneous media". *Phase Transitions* 34.1-4 (1991), pp. 69–103.

[214] Sivan Kartha et al. "Spin-glass nature of tweed precursors in martensitic transformations". *Physical Review Letters* 67.25 (1991), pp. 3630–3633.

[215] A. Saxena and G.R. Barsch. "Pretransformation strain modulations in proper ferroelastics". *Physica D: Nonlinear Phenomena* 66.1-2 (1993), pp. 195–204.

[216] Sivan Kartha et al. "Disorder-driven pretransitional tweed pattern in martensitic transformations". *Physical Review B* 52.2 (1995), pp. 803–822.

[217] M. A. Fradkin. "External field in the Landau theory of a weakly discontinuous phase transition: Pressure effect in the martensitic transitions". *Physical Review B* 50.22 (1994), pp. 16326–16339.

[218] Shuichi Nosé and M.L. Klein. "Constant pressure molecular dynamics for molecular systems". *Molecular Physics* 50.5 (1983), pp. 1055–1076.

[219] Shuichi Nosé. "A unified formulation of the constant temperature molecular dynamics methods". *The Journal of Chemical Physics* 81.1 (1984), pp. 511–519.

[220] Glenn J. Martyna, Douglas J. Tobias, and Michael L. Klein. "Constant pressure molecular dynamics algorithms". *The Journal of Chemical Physics* 101.5 (1994), pp. 4177–4189.

[221] M. P. Allen. *Computer simulation of liquids*. Oxford England New York: Clarendon Press Oxford University Press, 1987.

[222] Daan Frenkel. *Understanding molecular simulation : from algorithms to applications*. San Diego: Academic Press, 2002.

[223] Mark Tuckerman. *Statistical mechanics : theory and molecular simulation*. Oxford: Oxford University Press, 2010.

[224] J. Tersoff. "Empirical interatomic potential for silicon with improved elastic properties". *Physical Review B* 38.14 (1988), pp. 9902–9905.

[225] M. I. Baskes. "Application of the Embedded-Atom Method to Covalent Materials: A Semiempirical Potential for Silicon". *Physical Review Letters* 59.23 (1987), pp. 2666–2669.

[226] M. I. Baskes. "Modified embedded-atom potentials for cubic materials and impurities". *Physical Review B* 46.5 (1992), pp. 2727–2742.

[227] F.G. Fumi and M.P. Tosi. "Ionic sizes and born repulsive parameters in the NaCl-type alkali halides—I". *Journal of Physics and Chemistry of Solids* 25.1 (1964), pp. 31–43.

[228] M.P. Tosi and F.G. Fumi. "Ionic sizes and born repulsive parameters in the NaCl-type alkali halides—II". *Journal of Physics and Chemistry of Solids* 25.1 (1964), pp. 45–52.

[229] Jianwei Sun, Adrienn Ruzsinszky, and John P. Perdew. "Strongly Constrained and Appropriately Normed Semilocal Density Functional". *Physical Review Letters* 115.3 (2015).

[230] Albert P. Bartók and Jonathan R. Yates. "Regularized SCAN functional". *The Journal of Chemical Physics* 150.16 (2019), p. 161101.

[231] Riccardo Sabatini, Tommaso Gorni, and Stefano de Gironcoli. "Nonlocal van der Waals density functional made simple and efficient". *Physical Review B* 87.4 (2013).

[232] James Kirkpatrick et al. "Pushing the frontiers of density functionals by solving the fractional electron problem". *Science* 374.6573 (2021), pp. 1385–1389.

[233] Kieron Burke. "Perspective on density functional theory". *The Journal of Chemical Physics* 136.15 (2012), p. 150901.

[234] Axel D. Becke. "Perspective: Fifty years of density-functional theory in chemical physics". *The Journal of Chemical Physics* 140.18 (2014), 18A301.

[235] Kurt Lejaeghere et al. "Reproducibility in density functional theory calculations of solids". *Science* 351.6280 (2016).

[236] Michael G. Medvedev et al. "Density functional theory is straying from the path toward the exact functional". *Science* 355.6320 (2017), pp. 49–52.

[237] Gabriel R Schleder et al. "From DFT to machine learning: recent approaches to materials science–a review". *Journal of Physics: Materials* 2.3 (2019), p. 032001.

[238] Richard Martin. *Interacting electrons: Theory and computational approaches*. New York, NY: Cambridge University Press, 2016.

[239] Richard Martin. *Electronic structure: Basic theory and practical methods*. Cambridge, UK New York: Cambridge University Press, 2004.

[240] Feliciano Giustino. *Materials modelling using density functional theory: Properties and predictions*. Oxford: Oxford University Press, 2014.

[241] Alessandro Barducci, Giovanni Bussi, and Michele Parrinello. "Well-Tempered Metadynamics: A Smoothly Converging and Tunable Free-Energy Method". *Phys. Rev. Lett.* 100 (2 2008), p. 020603.

[242] Sergey N. Pozdnyakov et al. "Incompleteness of Atomic Structure Representations". *Physical Review Letters* 125.16 (2020).

[243] Jamshed Anwar, Daan Frenkel, and Massimo G. Noro. "Calculation of the melting point of NaCl by molecular simulation". *The Journal of Chemical Physics* 118.2 (2003), pp. 728–735.

[244] Michiel Sprik. "Coordination numbers as reaction coordinates in constrained molecular dynamics". *Faraday Discussions* 110 (1998), pp. 437–445.

[245] D. Bochicchio, A. Videcoq, and R. Ferrando. "Study of the B1-B2 transition in colloidal clusters". *The Journal of Chemical Physics* 140.2 (2014), p. 024911.

[246] Roman Martoňák et al. "Crystal structure transformations in SiO2 from classical and ab initio metadynamics". *Nature Materials* 5.8 (2006), pp. 623–626.

[247] Steve Plimpton. "Fast Parallel Algorithms for Short-Range Molecular Dynamics". *Journal of Computational Physics* 117.1 (1995), pp. 1–19.

[248] *LAMMPS Molecular Dynamics Simulator*.

[249] Gareth A. Tribello et al. "PLUMED 2: New feathers for an old bird". *Computer Physics Communications* 185.2 (2014), pp. 604–613.

[250] Massimiliano Bonomi et al. "Promoting transparency and reproducibility in enhanced molecular simulations". *Nature Methods* 16.8 (2019), pp. 670–673.

[251] Shiddartha Paul, Kasra Momeni, and Valery I. Levitas. "Shear-induced diamondization of multilayer graphene structures: A computational study". *Carbon* 167 (2020), pp. 140–147.

[252] Yang Gao et al. "Shear driven formation of nano-diamonds at sub-gigapascals and 300K". *Carbon* 146 (2019), pp. 364–368.

[253] E. Sanz et al. "Homogeneous Ice Nucleation at Moderate Supercooling from Molecular Simulation". *Journal of the American Chemical Society* 135.40 (2013), pp. 15008–15017.

[254] Pierre Hirel. "Atomsk: A tool for manipulating and converting atomic data files". *Computer Physics Communications* 197 (2015), pp. 212–219.

[255] Paul S. DeCarli and John C. Jamieson. "Formation of Diamond by Explosive Shock". *Science* 133.3467 (1961), pp. 1821–1822.

[256] F. P. Bundy. "Direct Conversion of Graphite to Diamond in Static Pressure Apparatus". *The Journal of Chemical Physics* 38.3 (1963), pp. 631–643.

[257] R. H. Wentorf. "The Behavior of Some Carbonaceous Materials at Very High Pressures and High Temperatures". *The Journal of Physical Chemistry* 69.9 (1965), pp. 3063–3069.

[258] Masao Wakatsuki, Kazuaki Ichinose, and Toshio Aoki. "Notes on Compressible Gasket and Bridgman-Anvil Type High Pressure Apparatus". *Japanese Journal of Applied Physics* 11.4 (1972), pp. 578–590.

[259] S. Naka et al. "Direct conversion of graphite to diamond under static pressure". *Nature* 259.5538 (1976), pp. 38–39.

[260] H. Yusa et al. "Direct transformation of graphite to cubic diamond observed in a laser-heated diamond anvil cell". *Applied Physics Letters* 72.15 (1998), pp. 1843–1845.

[261] Akifumi Onodera, Koji Higashi, and Yasushi Irie. "Crystallization of amorphous carbon at high static pressure and high temperature". *Journal of Materials Science* 23.2 (1988), pp. 422–428.

[262] Corentin Le Guillou et al. "Nanodiamond nucleation below 2273K at 15GPa from carbons with different structural organizations". *Carbon* 45.3 (2007), pp. 636–648.

[263] F. P. Bundy and J. S. Kasper. "Hexagonal Diamond: A New Form of Carbon". *The Journal of Chemical Physics* 46.9 (1967), pp. 3437–3446.

[264] F.P. Bundy et al. "The pressure-temperature phase and transformation diagram for carbon updated through 1994". *Carbon* 34.2 (1996), pp. 141–153.

[265] Yohei Sato et al. "Heterogeneous diamond phases in compressed graphite studied by electron energy-loss spectroscopy". *Diamond and Related Materials* 64 (2016), pp. 190–196.

[266] D. Kraus et al. "Nanosecond formation of diamond and lonsdaleite by shock compression of graphite". *Nature Communications* 7.1 (2016).

[267] Stefan J. Turneaure et al. "Transformation of shock-compressed graphite to hexagonal diamond in nanoseconds". *Science Advances* 3.10 (2017).

[268] Travis J. Volz and Y. M. Gupta. "Graphite to diamond transformation under shock compression: Role of orientational order". *Journal of Applied Physics* 125.24 (2019), p. 245902.

[269] Michael R. Armstrong et al. "Highly ordered graphite (HOPG) to hexagonal diamond (lonsdaleite) phase transition observed on picosecond time scales using ultrafast x-ray diffraction". *Journal of Applied Physics* 132.5 (2022), p. 055901.

[270] S. Scandolo et al. "Pressure-Induced Transformation Path of Graphite to Diamond". *Physical Review Letters* 74.20 (1995), pp. 4015–4018.

[271] Y. Tateyama et al. "Constant-pressure first-principles studies on the transition states of the graphite-diamond transformation". *Physical Review B* 54.21 (1996), pp. 14994–15001.

[272] Christopher J. Mundy et al. "Ultrafast transformation of graphite to diamond: An ab initio study of graphite under shock compression". *The Journal of Chemical Physics* 128.18 (2008), p. 184701.

[273] Jian-Tao Wang, Changfeng Chen, and Yoshiyuki Kawazoe. "Low-Temperature Phase Transformation from Graphite tosp3Orthorhombic Carbon". *Physical Review Letters* 106.7 (2011).

[274] Salah Eddine Boulfelfel, Artem R. Oganov, and Stefano Leoni. "Understanding the nature of superhard graphite". *Scientific Reports* 2.1 (2012).

[275] Penghao Xiao and Graeme Henkelman. "Communication: From graphite to diamond: Reaction pathways of the phase transition". *The Journal of Chemical Physics* 137.10 (2012).

[276] Xiao Dong et al. "An ab initio study on the transition paths from graphite to diamond under pressure". *Journal of Physics: Condensed Matter* 25.14 (2013), p. 145402.

[277] Hongxian Xie et al. "Mechanism for direct graphite-to-diamond phase transition". *Scientific Reports* 4.1 (2014).

[278] Shen Li Qiu. "Hexagonal graphite to cubic diamond transition from equilibrium lines and barrier calculations". *The European Physical Journal B* 87.7 (2014).

[279] Yao-Ping Xie, Xiao-Jie Zhang, and Zhi-Pan Liu. "Graphite to Diamond: Origin for Kinetics Selectivity". *Journal of the American Chemical Society* 139.7 (2017), pp. 2545–2548.

[280] Matthew P. Kroonblawd and Nir Goldman. "Mechanochemical formation of heterogeneous diamond structures during rapid uniaxial compression in graphite". *Physical Review B* 97.18 (2018).

[281] Stefano Signetti et al. "Atomistic modelling of the hypervelocity dynamics of shock-compressed graphite and impacted graphene armours". *Computational Materials Science* 170 (2019), p. 109152.

[282] Duan Luo et al. *Atomistic Evidence of Nucleation Mechanism for the Direct Graphite-to-Diamond Transformation*. 2021. eprint: arXiv:2111.13382.

[283] Jinjin Wang et al. "A deep learning interatomic potential developed for atomistic simulation of carbon materials". *Carbon* 186 (2022), pp. 1–8.

[284] Srilok Srinivasan et al. "Machine learning the metastable phase diagram of covalently bonded carbon". *Nature Communications* 13.1 (2022).

[285] S. Amelinckx and P. Delavignette. "Electron Optical Study of Basal Dislocations in Graphite". *Journal of Applied Physics* 31.12 (1960), pp. 2126–2135.

[286] P. Delavignette and S. Amelinckx. "Dislocation patterns in graphite". *Journal of Nuclear Materials* 5.1 (1962), pp. 17–66.

[287] M. T. Yin and Marvin L. Cohen. "Will Diamond Transform under Megabar Pressures?" *Physical Review Letters* 50.25 (1983), pp. 2006–2009.

[288] M. T. Yin. "Si-III (BC-8) crystal phase of Si and C: Structural properties, phase stabilities, and phase transitions". *Physical Review B* 30.4 (1984), pp. 1773–1776.

[289] R. Biswas et al. "Stability and electronic properties of complex structures of silicon and carbon under pressure: Density-functional calculations". *Physical Review B* 35.18 (1987), pp. 9559–9568.

[290] S. Fahy and Steven G. Louie. "High-pressure structural and electronic properties of carbon". *Physical Review B* 36.6 (1987), pp. 3373–3385.

[291] Giulia Galli et al. "Melting of Diamond at High Pressure". *Science* 250.4987 (1990), pp. 1547–1549.

[292] C. Mailhiot and A. K. McMahan. "Atmospheric-pressure stability of energetic phases of carbon". *Physical Review B* 44.21 (1991), pp. 11578–11591.

[293] S. J. Clark, G. J. Ackland, and J. Crain. "Theoretical stability limit of diamond at ultrahigh pressure". *Physical Review B* 52.21 (1995), pp. 15035–15038.

[294] S. Scandolo, G. L. Chiarotti, and E. Tosatti. "SC4: A metallic phase of carbon at terapascal pressures". *Physical Review B* 53.9 (1996), pp. 5051–5054.

[295] Matthew P. Grumbach and Richard M. Martin. "Phase diagram of carbon at high pressures and temperatures". *Physical Review B* 54.22 (1996), pp. 15730–15741.

[296] Yury G. Gogotsi, Andreas Kailer, and Klaus G. Nickel. "Pressure-induced phase transformations in diamond". *Journal of Applied Physics* 84.3 (1998), pp. 1299–1304.

[297] W. J. Nellis, A. C. Mitchell, and A. K. McMahan. "Carbon at pressures in the range 0.1–1 TPa (10 Mbar)". *Journal of Applied Physics* 90.2 (2001), pp. 696–698.

[298] Xiaofei Wang, Sandro Scandolo, and Roberto Car. "Carbon Phase Diagram from Ab Initio Molecular Dynamics". *Physical Review Letters* 95.18 (2005).

[299] Alfredo A. Correa, Stanimir A. Bonev, and Giulia Galli. "Carbon under extreme conditions: Phase boundaries and electronic properties from first-principles theory". *Proceedings of the National Academy of Sciences* 103.5 (2006), pp. 1204–1208.

[300] Alfredo A. Correa et al. "First-principles multiphase equation of state of carbon under extreme conditions". *Physical Review B* 78.2 (2008).

[301] D. G. Hicks et al. "High-precision measurements of the diamond Hugoniot in and above the melt region". *Physical Review B* 78.17 (2008).

[302] D. K. Bradley et al. "Diamond at 800 GPa". *Physical Review Letters* 102.7 (2009).

[303] Miguel Martinez-Canales, Chris J. Pickard, and Richard J. Needs. "Thermodynamically Stable Phases of Carbon at Multiterapascal Pressures". *Physical Review Letters* 108.4 (2012).

[304] A. Lazicki et al. "Metastability of diamond ramp-compressed to 2 terapascals". *Nature* 589.7843 (2021), pp. 532–535.

[305] Kien Nguyen-Cong et al. "Billion atom molecular dynamics simulations of carbon at extreme conditions and experimental time and length scales". In: *Proceedings of the International Conference for High Performance Computing, Networking, Storage and Analysis*. ACM, 2021.

[306] P.-L. CHau and A. J. Hardwick. "A new order parameter for tetrahedral configurations". *Molecular Physics* 93.3 (1998), pp. 511–518.

[307] Ondrej Bilý. "Application of machine-learning-based collective variables to identification of structural phases in solids". Master thesis. Comenius University in Bratislava, 2021.

[308] N. Loutat and C. A. Johnson. "The behaviour of jogs in dislocations". *Philosophical Magazine* 7.84 (1962), pp. 2051–2057.

[309] A. Jayaraman, W. Klement, and G. C. Kennedy. "Solid-Solid Transitions in Titanium and Zirconium at High Pressures". *Physical Review* 131.2 (1963), pp. 644–649.

[310] Y.K. Vohra et al. "Impurity effects and reaction kinetics of the pressure-induced $\alpha \rightarrow \omega$ transformation in Ti". *Journal of Physics and Chemistry of Solids* 38.11 (1977), pp. 1293–1296.

[311] L.-c. Ming, M.H. Manghnani, and K.W. Katahara. "Phase transformations in the Ti-V system under high pressure up to 25 GPa". *Acta Metallurgica* 29.3 (1981), pp. 479–485.

[312] Hui Xia et al. "Crystal structures of group IVa metals at ultrahigh pressures". *Physical Review B* 42.10 (1990), pp. 6736–6738.

[313] G T Gray III, C E Morris, and A C Lawson. "Omega phase formation in titanium and titanium alloys" (1992).

[314] Yuichi Akahama, Haruki Kawamura, and Tristan Le Bihan. "New δ (Distorted-bcc) Titanium to 220 GPa". *Physical Review Letters* 87.27 (2001).

[315] Yogesh K. Vohra and Philemon T. Spencer. "Novel γ-Phase of Titanium Metal at Megabar Pressures". *Physical Review Letters* 86.14 (2001), pp. 3068–3071.

[316] Rajeev Ahuja et al. "Titanium metal at high pressure: Synchrotron experiments and ab initio calculations". *Physical Review B* 69.18 (2004).

[317] Dallas Rhea Trinkle. "A theoretical study of the hcp to omega martensitic phase transition in titanium". PhD thesis. The Ohio State University, 2003.

[318] Daniel Errandonea et al. "Pressure-induced transition in titanium metal: a systematic study of the effects of uniaxial stress". *Physica B: Condensed Matter* 355.1-4 (2005), pp. 116–125.

[319] E. Cerreta et al. "The influence of oxygen content on the α to ω phase transformation and shock hardening of titanium". *Journal of Applied Physics* 100.1 (2006), p. 013530.

[320] Zhi-Gang Mei et al. "Density-functional study of the thermodynamic properties and the pressure-temperature phase diagram of Ti". *Physical Review B* 80.10 (2009).

[321] Hongxiang Zong et al. "The kinetics of the ω to α phase transformation in Zr, Ti: Analysis of data from shock-recovered samples and atomistic simulations". *Acta Materialia* 77 (2014), pp. 191–199.

[322] J.M Silcock. "An X-ray examination of the to phase in TiV, TiMo and TiCr alloys". *Acta Metallurgica* 6.7 (1958), pp. 481–493.

[323] M. I. Mendelev, T. L. Underwood, and G. J. Ackland. "Development of an interatomic potential for the simulation of defects, plasticity, and phase transformations in titanium". *The Journal of Chemical Physics* 145.15 (2016), p. 154102.

[324] N. A. Zarkevich and D. D. Johnson. "Titanium α-ω phase transformation pathway and a predicted metastable structure". *Physical Review B* 93.2 (2016).

[325] Akira Takahashi, Atsuto Seko, and Isao Tanaka. "Conceptual and practical bases for the high accuracy of machine learning interatomic potentials: Application to elemental titanium". *Physical Review Materials* 1.6 (2017).

[326] D Dickel et al. "Mechanical instabilities in the modeling of phase transitions of titanium". *Modelling and Simulation in Materials Science and Engineering* 26.6 (2018), p. 065002.

[327] Won-Seok Ko, Blazej Grabowski, and Jörg Neugebauer. "Development and application of a Ni-Ti interatomic potential with high predictive accuracy of the martensitic phase transition". *Physical Review B* 92.13 (2015).

[328] Dongdong Li et al. "Experimental and DFT characterization of interphase boundaries in titanium and the implications for ω-assisted α phase precipitation". *Acta Materialia* 151 (2018), pp. 406–415.

[329] Alberto Ferrari et al. "Phase transitions in titanium with an analytic bond-order potential". *Modelling and Simulation in Materials Science and Engineering* 27.8 (2019), p. 085008.

[330] Tongqi Wen et al. "Specialising neural network potentials for accurate properties and application to the mechanical response of titanium". *npj Computational Materials* 7.1 (2021).

[331] I V Nelasov et al. "Molecular dynamics simulation of the behavior of titanium under high-speed deformation". *Modelling and Simulation in Materials Science and Engineering* 29.6 (2021), p. 065007.

[332] Mashroor S. Nitol, Doyl E. Dickel, and Christopher D. Barrett. "Machine learning models for predictive materials science from fundamental physics: An application to titanium and zirconium". *Acta Materialia* 224 (2022), p. 117347.

[333] Khanh Dang, Carlos N. Tomé, and Laurent Capolungo. "The role of deviatoric stress and dislocations on the α to ω phase transformation in Ti". *Acta Materialia* 244 (2023), p. 118510.

[334] D. Dickel, M. Nitol, and C.D. Barrett. "LAMMPS implementation of rapid artificial neural network derived interatomic potentials". *Computational Materials Science* 196 (2021), p. 110481.

[335] Pablo M. Piaggi, Omar Valsson, and Michele Parrinello. "Enhancing Entropy and Enthalpy Fluctuations to Drive Crystallization in Atomistic Simulations". *Physical Review Letters* 119.1 (2017).

[336] G. J. Ackland and A. P. Jones. "Applications of local crystal structure measures in experiment and simulation". *Physical Review B* 73.5 (2006).

[337] G.M. Torrie and J.P. Valleau. "Nonphysical sampling distributions in Monte Carlo free-energy estimation: Umbrella sampling". *Journal of Computational Physics* 23.2 (1977), pp. 187–199.

[338] Shankar Kumar et al. "THE weighted histogram analysis method for free-energy calculations on biomolecules. I. The method". *Journal of Computational Chemistry* 13.8 (1992), pp. 1011–1021.

[339] Eric Darve and Andrew Pohorille. "Calculating free energies using average force". *The Journal of Chemical Physics* 115.20 (2001), pp. 9169–9183.

[340] Omar Valsson and Michele Parrinello. "Variational Approach to Enhanced Sampling and Free Energy Calculations". *Physical Review Letters* 113.9 (2014).

[341] Michele Invernizzi and Michele Parrinello. "Rethinking Metadynamics: From Bias Potentials to Probability Distributions". *The Journal of Physical Chemistry Letters* 11.7 (2020), pp. 2731–2736.

[342] Michele Invernizzi, Pablo M. Piaggi, and Michele Parrinello. "Unified Approach to Enhanced Sampling". *Physical Review X* 10.4 (2020).

[343] Davide Branduardi, Francesco Luigi Gervasio, and Michele Parrinello. "From A to B in free energy space". *The Journal of Chemical Physics* 126.5 (2007), p. 054103.

[344] Mary A. Rohrdanz et al. "Determination of reaction coordinates via locally scaled diffusion map". *The Journal of Chemical Physics* 134.12 (2011), p. 124116.

[345] Gareth A. Tribello, Michele Ceriotti, and Michele Parrinello. "Using sketch-map coordinates to analyze and bias molecular dynamics simulations". *Proceedings of the National Academy of Sciences* 109.14 (2012), pp. 5196–5201.

[346] Grisell Dıaz Leines and Bernd Ensing. "Path Finding on High-Dimensional Free Energy Landscapes". *Physical Review Letters* 109.2 (2012).

[347] GiovanniMaria Piccini, Daniela Polino, and Michele Parrinello. "Identifying Slow Molecular Motions in Complex Chemical Reactions". *The Journal of Physical Chemistry Letters* 8.17 (2017), pp. 4197–4200.

[348] Wei Chen and Andrew L. Ferguson. "Molecular enhanced sampling with autoencoders: On-the-fly collective variable discovery and accelerated free energy landscape exploration". *Journal of Computational Chemistry* 39.25 (2018), pp. 2079–2102.

[349] Christoph Wehmeyer and Frank Noé. "Time-lagged autoencoders: Deep learning of slow collective variables for molecular kinetics". *The Journal of Chemical Physics* 148.24 (2018), p. 241703.

[350] GiovanniMaria Piccini and Michele Parrinello. "Accurate Quantum Chemical Free Energies at Affordable Cost". *The Journal of Physical Chemistry Letters* 10.13 (2019), pp. 3727–3731.

[351] Baron Peters, Gregg T. Beckham, and Bernhardt L. Trout. "Extensions to the likelihood maximization approach for finding reaction coordinates". *The Journal of Chemical Physics* 127.3 (2007), p. 034109.

[352] Luigi Bonati, Valerio Rizzi, and Michele Parrinello. "Data-Driven Collective Variables for Enhanced Sampling". *The Journal of Physical Chemistry Letters* 11.8 (2020), pp. 2998–3004.

[353] Vojtěch Spiwok and Blanka Králová. "Metadynamics in the conformational space nonlinearly dimensionally reduced by Isomap". *The Journal of Chemical Physics* 135.22 (2011), p. 224504.

[354] Peter G Bolhuis et al. "Transition path sampling: throwing ropes over rough mountain passes, in the dark". en. *Annu. Rev. Phys. Chem.* 53.1 (2002), pp. 291–318.

[355] Alessandro Laio et al. "Assessing the Accuracy of Metadynamics†". *The Journal of Physical Chemistry B* 109.14 (2005), pp. 6714–6721.

[356] N. Smirnov. "Table for Estimating the Goodness of Fit of Empirical Distributions". *The Annals of Mathematical Statistics* 19.2 (1948), pp. 279–281.

[357] Alberto Pérez de Alba Ortíz and Bernd Ensing. *Simultaneous sampling of multiple transition channels using adaptive paths of collective variables*. 2021. eprint: arXiv:2112.04061.

[358] Mark James Abraham et al. "GROMACS: High performance molecular simulations through multi-level parallelism from laptops to supercomputers". *SoftwareX* 1-2 (2015), pp. 19–25.

[359] Samuel S Schoenholz and Ekin D Cubuk. "JAX, M.D. A framework for differentiable physics". *Journal of Statistical Mechanics: Theory and Experiment* 2021.12 (2021), p. 124016.